

Yordan Kyosev
Boris Mahltig
Anne Schwarz-Pfeiffer *Editors*

Narrow and Smart Textiles

 Springer

Narrow and Smart Textiles

Yordan Kyosev · Boris Mahltig
Anne Schwarz-Pfeiffer
Editors

Narrow and Smart Textiles

 Springer

Editors

Yordan Kyosev
Faculty of Textile and Clothing Technology
Niederrhein University Applied Sciences
Mönchengladbach
Germany

Anne Schwarz-Pfeiffer
Faculty of Textile and Clothing Technology
Niederrhein University Applied Sciences
Mönchengladbach
Germany

Boris Mahltig
Faculty of Textile and Clothing Technology
Niederrhein University Applied Sciences
Mönchengladbach
Germany

ISBN 978-3-319-69049-0 ISBN 978-3-319-69050-6 (eBook)
<https://doi.org/10.1007/978-3-319-69050-6>

Library of Congress Control Number: 2017957682

© Springer International Publishing AG 2018

This work is subject to copyright. All rights are reserved by the Publisher, whether the whole or part of the material is concerned, specifically the rights of translation, reprinting, reuse of illustrations, recitation, broadcasting, reproduction on microfilms or in any other physical way, and transmission or information storage and retrieval, electronic adaptation, computer software, or by similar or dissimilar methodology now known or hereafter developed.

The use of general descriptive names, registered names, trademarks, service marks, etc. in this publication does not imply, even in the absence of a specific statement, that such names are exempt from the relevant protective laws and regulations and therefore free for general use.

The publisher, the authors and the editors are safe to assume that the advice and information in this book are believed to be true and accurate at the date of publication. Neither the publisher nor the authors or the editors give a warranty, express or implied, with respect to the material contained herein or for any errors or omissions that may have been made. The publisher remains neutral with regard to jurisdictional claims in published maps and institutional affiliations.

Printed on acid-free paper

This Springer imprint is published by Springer Nature
The registered company is Springer International Publishing AG
The registered company address is: Gewerbestrasse 11, 6330 Cham, Switzerland

Preface

This book presents recent developments in the area of narrow and smart textiles, presented during the “International Week of Narrow and Smart Textiles 19–23.02.2018” in Mönchengladbach, Germany. The week combines three scientific events—Braiding Colloquium, Narrow Weaving Colloquium, and Smart Textiles Colloquium. Around the event are organized two courses—for patterning in the braiding and multilayer shuttle weaving. More as the half of the presenters on these events are coming directly from the world leading machinery and technology development centers and companies. They as usual are obligated to keep their secrets far from the publicity and do not participate with manuscripts in this book. Nevertheless, this book presents 23 new developments—new machine concepts, solar cells, simulation of light transmitting polymers, new finishes, 3D textiles, and some more, which we hope to be interesting for the readers.

Mönchengladbach, Germany

Yordan Kyosev
Boris Mahltig
Anne Schwarz-Pfeiffer

Contents

Part I Narrow Weaving and Knitting

Connected Ribbons-Design as a Key to Service’s Materiality	3
Florence Bost	
Modelling of Light Emission in Tapes Woven with Polymer Optical Fibres	11
Lisa de Mol, Harm Wisselink, Niels Gardenier and Edwin Lamers	
Interesting Mechanical Properties of 3D Warp Interlock Fabrics	21
F. Boussu, S. Picard and D. Soulat	
Fibers and Textiles for Fully Bio-Based Fiber Reinforced Materials	33
Thomas Grethe, Boris Mahltig, Haoqian Miao, Thomas Kick, Hajo Haase, Mark Kopietz and Sergiy Grishchuk	
Investigation of the Elastic Properties of Weft-Knitted Metal-Reinforced Narrow Composites	49
J. Kaufmann, Y. Kyosev, H. Rabe, K. Gustke and H. Cebulla	

Part II Braiding

Investigation About the Properties of HMHT Fibre Ropes and New Machine for Continuous Production of Ropes with Connection Between Core and Mantle	61
Andreas Kretschmer and Christoph Müller	
Interlacement Variations in the Alternative Covering Technology D-3F	69
Daniel Denninger, Maik Berger and Yordan Kyosev	
Development of Machine Configuration for T- and I-Profiles and Their Topological Modelling	81
Yordan Kyosev and Katalin Küster	

Modeling of Braided Structures Based on Secondary Helix	91
Fanggang Ning, Nick O Hear, Rong Zhou, Chuan Shi and Xin Ning	
Investigation of PET-Braided Vascular Stents Potential Compared with Commercial Metallic Stents	109
Hiba Jaziri, Sofiene Mokhtar, Khawla Aguir and Saber Ben Abdessalem	
Experimental and Numerical Investigation of Triaxial Braid Reinforcements	123
Boris Duchamp, Yordan Kyosev, Xavier Legrand and Damien Soulat	
Fibre-Rope-Driven Parallel Handling Device	141
Christoph Müller, Markus Helbig and David Holschemacher	
Pattern Design with the Variation Braider VF of Company Herzog GmbH	149
Peter Gleßner and Yordan Kyosev	
Ultrasonic Dip Coating of Fibre Ropes with Large Diameters	159
David Häser, Klaus Nendel, Christoph Müller and Markus Helbig	
Overlay Finishes and Coatings for Improving Abrasion Resistance in Braided Polyarylate Fiber Ropes	167
Loet Hoppe, Koen van Goethem, Hans-Gunter Kluczik, Forrest Sloan, Jens Mammitzsch and Markus Michael	
 Part III Smart Textiles	
Metal-Textile Hybrid Carrier Modules with Integrated Functions Based on Textile Sensors	175
Enrico Putzke, Andreas Müller and André Riedel	
4D Textiles: Hybrid Textile Structures that Can Change Structural Form with Time by 3D Printing	189
David Schmelzeisen, Hannah Koch, Chris Pastore and Thomas Gries	
Functional Nanofiber Mats for Medical and Biotechnological Applications	203
Robin Böttjer, Timo Grothe and Andrea Ehrmann	
Sensorized Woven Tapes and Their Testing	215
W. Scheibner, A. Neudeck, K. Ullrich, A. Kraher, H. Oschatz, M. Weiser and U. Möhring	
Integration of Solar Cells and Other Electronic Components into Clothes	229
Susanna Fafenrot, Paul Silbermann, Nils Grimmelsmann, Johannes Assig and Andrea Ehrmann	

Washing and Abrasion Resistance of Conductive Coatings for Vital Sensors	241
Patricia Schäl, Irén Juhász Junger, Nils Grimmelsmann, Hubert Meissner and Andrea Ehrmann	
Resource-Efficient Production of a Smart Textile UV Sensor Using Photochromic Dyes: Characterization and Optimization	251
Sina Seipel, Junchun Yu, Aravin P. Periyasamy, Martina Viková, Michal Vik and Vincent A. Nierstrasz	
Direct Printing of Light-Emitting Devices on Textile Substrates	259
Inge Verboven and Wim Deferme	

Part I
Narrow Weaving and Knitting

Connected Ribbons-Design as a Key to Service's Materiality

Florence Bost

Abstract Since the arrival of electronics in the textile field, the ribbon transformed into e-ribbon inaugurates its functionalities with two unseen features in hand: it joins together physically and electronically different worlds, arriving to the transformation of itself into an electrical component, in other words, materializing the service. The e-garments, as well as e-ribbons, intimately ally esthetics with utility. Halfway between product design and fashion, it is obliged to integrate the end user's opinion and think about new services to offer to the digital world. Going from connectivity through clients support and new marketing strategies, E-ribbons are getting their way in shaking the secular habits of a dynamic field, and yet, a linear one. The narrow textiles have a pioneer and strategic role to play NOW.

Keywords E-ribbon · Design · Materiality · Flexible connectics

1 E-Ribbons, an Ecosystem in Itself

Since the arrival of electronics the ribbon, then e-ribbon, opens its functionality with two key unprecedented features: harmonization (of different elements, often disparate, battery, and electrical device in the least case) and its transformation from the status of an ornament to that of a true electrical component (sensors and even actuators). Its flexibility, physical as well as of implementation, was only the beginning of a chameleon-like transforming ability. Nothing magical, however, if it is not a textile-bound solid based history and a long time organic role in its applications. Ribbons always had the task of assembling and putting together different universes; oscillating at ease between these two worlds, ribbons acquire today a mediator scope.

F. Bost (✉)

Sable Chaud, 5 Place de La Porte de Champerret, 75017 Paris, France

e-mail: florence@sablechaud.eu

URL: <https://www.sablechaud.eu>

1.1 E-Ribbon, More Than a Ribbon, an Artery

Because of their applications, ribbons have always went with textile's transformation. They may be rigid, semi or totally flexible at the occasion. Their use is, among other reasons, about joining (facing), holding (strap), to protect (tubular bandage) or yet, be the discreet support of a system (zipper). Most often the ribbon is associated to a technical function and its adaptability, ease to personalize and low cost, position it as indispensable. Getting hold of it by a service linked to the digital world, allows it to become the main artery of a network, discreet or not discreet, and makes ribbons ambassadors to technology. It actually materializes services' presence and longevity.

1.2 E-Ribbon, the Electronical Support of the Near Future?

The booming applications are those with radically electronic oriented functions. E-ribbons place themselves in the comfortable position of being the soles in both families of electronic devices which are sensors and actuators, to propose a flexible solution in a rigid or at its best semi-rigid universe. Thus, a ribbon that sensors humidity or a connected zipper (Fig. 1), join flexibility, functioning security, ease of implementation and maintenance. In this context, the ribbon is the modest component of an invisible and complicated architecture. The digital world is familiar with this transversal organization, but not the textile field, used to a more linear operating. The textile field learns that electronics engineers, programmers, data analysts, signal processing specialists, Ux designers, etc. ... that they all work in parallel, specifications interfering between them. E-ribbon's force might be that of being the visible support of this whole operation. It may propose or even implement, if it gives itself the means, a textile logic with a new approach of electronical conception.

1.3 E-Ribbon, the Service's Materiality

What does materializing a service mean? The sunken part of the iceberg brings upon important and practical notions such as simplicity, after-sales services (ASS), ergonomics, but also more sensible ones as the security of data circulation, optimal data captation, handicap or supra-performance perception, longevity of the device, technological limits, humanity and ethical approach. The e-ribbon almost becomes a product in itself, where the personality, as discreet as it may be, will provide as much information to the end user as to the different actors in the manufacturing process (fashioning, maintenance and care, repairs ...). The designer's know-how in this field is a keystone whose technicality has nothing to envy to that of

Fig. 1 Connected zipper «Zip and go®» - Génius Objects-2017



engineers' skills. For example, making electrical network apparent or not is a choice which may facilitate understanding how the system functions, simplify the ASS. And the availability of efficient technical surface treatments goes in this direction, as is the case today for conductive embroidery.

2 Design Methods, Understand Each Other to Work Together

What do you judge when you buy clothing: esthetics. What do you look for when you purchase a product: usefulness. E-textiles and in particular e-garments bring together both. If esthetics seems to vanish beneath technique it is that e-clothing is clothing that has features. It needs for a product design which brings together actors in the design, production and commercial fields such as engineers, developers, stylists, designers, marketing agents, ... but most of all, the final user. This does not

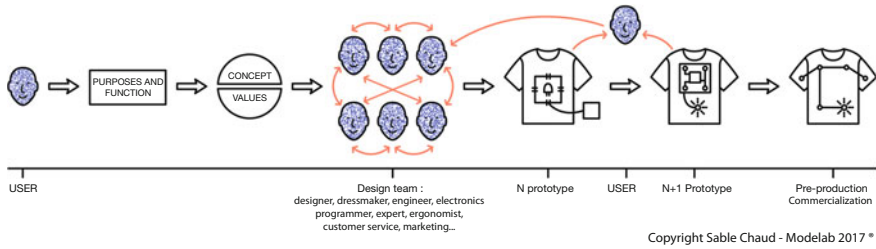


Fig. 2 Exchanges during an e-garment creation process

mean they will all work together at the same time, but it does mean that they will all be implicated since the beginning of the project and will assure the smart and conception of a useful product (Fig. 2). The development process of E-ribbons follows the same pattern and demands the coordination of the different corporations who struggle still today to agree. Well, in order to work together one must be conscious of the others' skills. Which electrical engineer, programmer or marketing agent has stepped into a knitted production chain, or a weaving one, or a dressmaking workshop? Which stylist or textile engineer has initiated itself into programming? At Fablab times, excuses are no longer admitted. Here is a brief on the process of creation for designers, engineers, and fashion designers.

2.1 *Engineering, a Team Centered on Industrial Feasibility*

The development of portable electronic device results from precise specifications being previously given by a client. They differ highly in accordance to technical choices (analogue, digital, communication protocols, types of sensors, etc.). Their setting up is complicated and each step has to be tested before proceeding to a pre-series production. Professions interlink and work in parallel: electronics, computers (for programming and algorithms) sometimes even outside experts (in the medical field). Their abundant exchanges (Fig. 3) take place between professions who work in the same way, step by step, joined by unavoidable equipment costs. This process often needs from 2 to 3 years.

2.2 *Fashion, a Team at the Service of a Personality*

If the collections of sportswear, medical and EPI (functional garments) are related because of their strong technical constraints and submitted to a particular product design whose process is described later, the ready-to-wear collections are mostly oriented by a personality: the fashion designer. He is designer of a universe, he tells

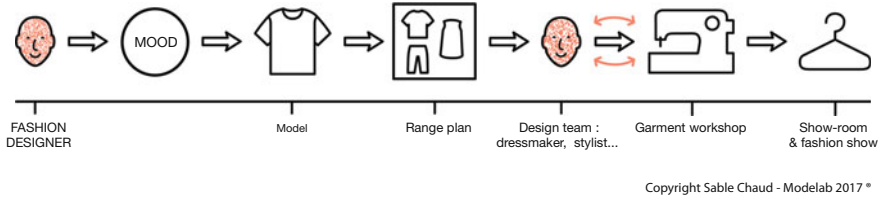


Fig. 3 Exchanges while creating a fashion collection

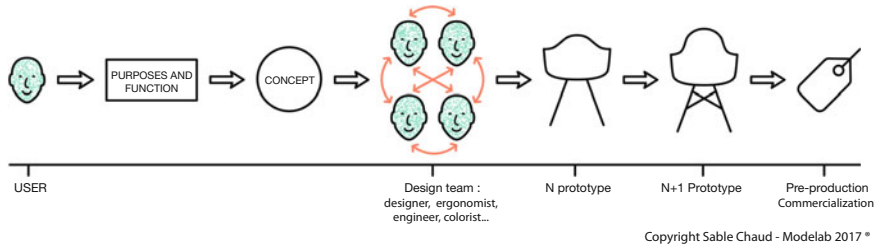


Fig. 4 Exchanges during a product design creation

a story that is going to link together all the pieces in his collection. The models of his plan for the collection are being adjusted as indications are being given to the chief of the workshop by the fashion designer. The garments are assembled in the chosen materials in order to establish the real manufacturing costs (minutage, poses, accessories, and marges). Then a pre-series with repetitions are made in order to present the models at a fashion show and to the brand’s showrooms. In short, there is someone who gives the orders and a series of performers with their back and forths for validation (Fig. 4), all this on a seasonal basis, sometimes monthly.

2.3 The Product, a Team Around the End User

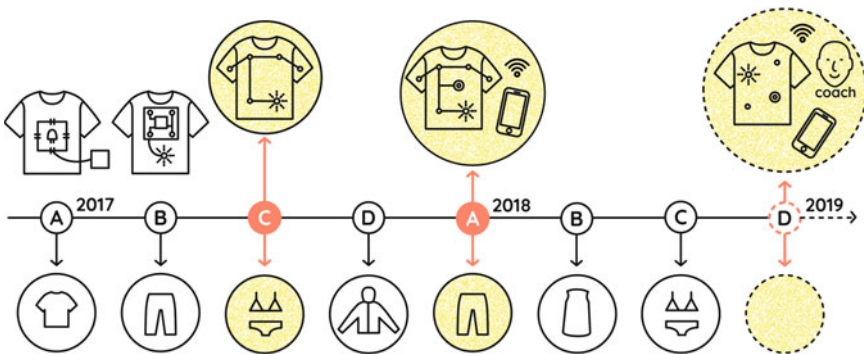
In the case of product design, use and the end user are placed at the center of the design process. Priority is given to functionality, ergonomics and products’ esthetics. All actors make several back and forths between them adapting constantly according to end users feedback. Product design may last for 2 or 3 years following the complexity of the project. The team is composed of a multitude of skills going from the engineer to the designer, the ergonomist, plastics specialist, color specialist, the designer Ux, and so on.

3 Collaborative Innovation’s Future

The ribbon industry has good days ahead with the condition that she builds collaborative alliances with similar industries as well as complementary ones. The ribbon’s narrow and long surface is an increased link of the flexible world (textiles) and the rigid one (electronics). It adapts to all commercial situations, from prototyping to small, medium, and large-scale series. It has a role to play in the life as well as the product’s maintenance. But in order to master the market, the ribbon industry has open into following its clients and the creation of new services as are after-sales services and connection. Two fields to which she is quite hermetical for the moment.

3.1 Marketing, a Time-Table Strategy

In all the clothing sectors taken together, the e-garment’s success is also related to the coherence of design and marketing, joined efforts from now on. Performance is crucial to the success of these hybrid products. Marketing has to have, on one side, the market’s acceptance of new services, in a direct manner or by means of a partner (start-up, updates, ASS). It has on the other side to compile an opportune time-table that will transform development’s time gaps (manufacturing, engineering) into assets (Fig. 5). Thus, a mature and progressive marketing will comfort the customer about the services that are being proposed to him. The customer is not credulous. The integration of a new technology does not betray, it shows in a flash the real implication of society in understanding its needs. This reality concerns the product collections for the public (B to C) as much as it does the B to B.



Copyright Sable Chaud - Modelab 2017 *

Fig. 5 Time coordination between technical maturity and the collection’s time-table

3.2 Client Support, a Novelty for the Textile World

The e-textile industry and even more the e-ribbon industry have to understand that they cannot sell just a textile product but a complete variety of services. In order to anticipate the technical demands but also to help the neophyte clients, those services go from the anticipation of technical demands up to the realization of half-finished products. Pre-connected ribbons, that is, passing through a true support to the client's project. Establish the technical specifications with the client in a precise and realistic way, is a starting point that guarantees at least a good development of the product. It is also the customer's fidelity assurance and a natural protection since it is difficult to copy know-hows based on a cross-experience between different fields without taking the same path. Last but not least, it is an obvious opening to new markets.

3.3 Flexible Connectivity, the Key to Success

In the digital world, all systems need connectivity. It is also its weakness and the delight of after-sale's services. It is expensive, ugly, and least ergonomic seen from the textile's point of view. Flexible connectivity remains to be completely invented. To believe that it is not the responsibility of the textile industry and the narrow textile's in particular, is allowing the electronics to impose their logic, the finish, its prices, but most of all, definitely close the commercial opportunities which may also be the profit to others.

Flexible connectivity design is a strategic turning point for the textile world in order to guarantee the rising of new markets. As for the narrow textile, this becomes an emergency at various levels:

- Guarantee commercial longevity giving nonexistent key-in-hand solutions.
- To integrate the dressmaking logic in the electronical process
- To inaugurate new markets by the alliance of electrical performances and flexibility (suppleness, torsion, personalisation, washable ...)

4 Conclusion

Mark Weiser, father of the concept of ubiquity, writes in the article of reference « The computer for the twenty-first Century » [1]:

« The most profound technologies are those that disappear. They weave themselves into the fabric of everyday life until they are indistinguishable from it »

An important task for industrials, researchers, and designers remains undone in order to give fluid design and marketing of flexible connected textiles back. The complexity and the natural inertia of the textile field are however its interior intelligence and formidable assets in front of recent technologies lacking sometimes of an overall perspective.

So, it has never been more crucial to gather efficient transversal teams and bring the end user at the heart of the process, since the competition is reactive. The narrow textiles have a pioneer and strategic role to play ... NOW

References

1. Weiser, M. (1991). The Computer for the 21st Century. *Scientific American* 265(3), 94–104, Ubicomp Paper after Sci Am editing, http://wiki.daimi.au.dk/pca/_files/weiser-orig.pdf.
2. Modelab n°4, outils d'expert: la conception de e-vêtements, 66–67 (2017), www.modelab.fr.

Modelling of Light Emission in Tapes Woven with Polymer Optical Fibres

Lisa de Mol, Harm Wisselink, Niels Gardenier and Edwin Lamers

Abstract For the treatment of dermatologic diseases such as actinic keratosis with photodynamic therapy (PDT), a light emitting fabric (LEF) is developed. The light emission of the LEF should be as homogenous as possible to assure a successful and pain-reduced treatment. The considered LEFs are tapes, that are woven with polymer optical fibres (POFs). The light emission varies for different weaves. A prediction of the light emission by modelling and simulation is expected to give insight in the processes and help with the investigation of finding a tape with the most homogenous light emission. In this paper, a modelling procedure is presented, with which the light emission can be regarded based especially on the weave type and setting. The modelling procedure incorporates weaving simulations as well as ray tracing simulations. To discuss the importance of weave settings on the light emission, tapes that are woven with different warp tensions are regarded. The applicability of the modelling procedure to predict light emission of complete weaves is shown.

1 Introduction

A light emitting fabric (LEF) is developed for the use in photodynamic therapy (PDT) for the treatment of dermatological diseases, such as actinic keratosis. The treatment requires light with a certain wavelength. In Europe, red light (630 nm) is used, while in the USA, blue light (450 nm) is the standard (see [9]). Currently in PDT, the patient is treated by light-emitting diodes (LED), which leads to a non-uniform distribution of light on the patient's body. A more homogenous distribution of light on the human body is desired, since in this way the light intensity and thus the sensation of pain can be decreased. The more homogenous distribution will be realized by the application of LEF in PDT. The use of a fabric, instead of a fixed panel of LEDs, has also practical advantages, such as portability. The LEF has light input from two sides.

L. de Mol (✉) · H. Wisselink · N. Gardenier · E. Lamers
Reden BV, F. Hazemeijerstraat 800, 7555RJ Hengelo, The Netherlands
e-mail: l.demol@reden.nl
URL: <http://www.reden.nl/>

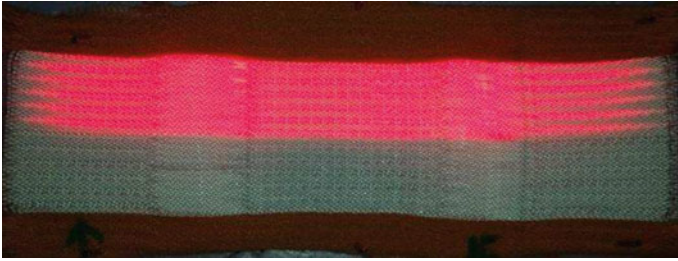


Fig. 1 Photography of a light emitting fabric with light input from two sides, [7]

An example of an LEF is shown in Fig. 1. Some research still needs to be conducted to find the type of fabric that produces the most homogenous light output. More information on PDT and LEF can be found in [9].

An optical fibre is a cylindrical waveguide that transmits light along its axis. It consists of a core surrounded by a cladding layer. Light that enters the optical fibre is propagated through the core and the cladding which is described by Snell's and Fresnel's laws. The location where the light leaves the fibre can be influenced by bending the fibre. This is called macro-bending. This means that the desired light output can be controlled by the shape of the POF. The LEFs regarded in this paper are biaxial weaves, where the fill yarns are polymer optical fibres. The polymer optical fibre (POF) used here is a Toray Polymer Optical Fibre PGR-FB250.

A modelling procedure is set up to predict the light output of a tape based on the shapes of the POFs. These shapes are extracted from weaving simulations of the tape. Modelling and simulation are expected to help understand the phenomena of light propagation in LEF and assist in developing a type of fabric with the most homogenous light output.

2 Modelling Procedure

In order to predict the irradiance of light emitting textiles, several modelling steps are considered. First, a weaving simulation with the POFs is conducted. The simulation is capable of modelling any biaxial weave. From the weaving simulation, the fibre paths of the POFs are extracted. These fibre paths then serve as input for a ray tracing program. Here, light rays are propagated through a POF geometry and light emission is calculated.

3 Weaving Simulation

An explicit finite element weaving simulation is conducted in ESI PAMCRASH (ESI Virtual Performance Solution [5]) to extract a POF's path in any biaxial weave. Since the fibre shape is not only dependent on the type of weave but also on all process setting during weaving, the simulation mimics the real weaving process. A more thorough discussion on the weaving simulations itself and the importance of the weave setting on the final shape are discussed in [10].

One of the weave settings is the tension on the warp yarns. This tension is controlled via a weight per yarn in real weaving (see [8]). It is also taken into account in the weaving simulations. The cases 40, 63 and 87 g per warp yarns are regarded. After weaving, the tensions on the yarns are released. Plasticity is taken into account because of its effect on the shape of the yarns after tension release.

The fill yarns used in the weaving simulation are PMMA Toray (250 μm) and the warp yarns Polyester Sinterama (330 dTex) with a density of 20 per cm, which are also used in [9]. The optical fibre is a monofilament yarn and modelled with beam elements, whereas the warp yarns are multifilament yarns, consisting of several filaments per yarn, each modelled with bar elements.

As output of the simulation, the shape of the yarns within one unit cell should suffice. With a unit cell, which is the smallest repetitive element within a structure, weaves of any requested size can be created by translation of this unit cell. However, to diminish the influence of boundary effects on the regarded unit cell, it is found better to weave 3×3 unit cells and regard only the central one. Exemplary results of a weaving simulation of a satin 4 weave are shown in Fig. 2.

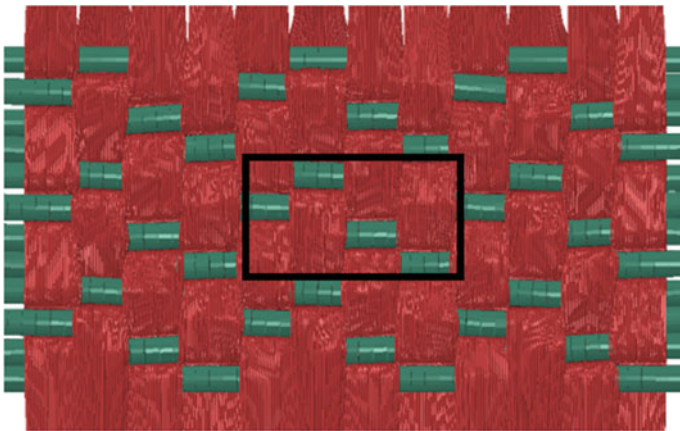


Fig. 2 Example of a satin 4 (87 g) weave. The POFs (fill yarns) are green, the warp yarns are red. The central unit cell is marked by a black box. 3×3 unit cells can be recognized

The monofilament POFs (green) can be distinguished from the multifilament warp yarns (red). In the picture, the 3×3 unit cells are recognizable with the central unit cell marked by a black box.

4 Data Preparation

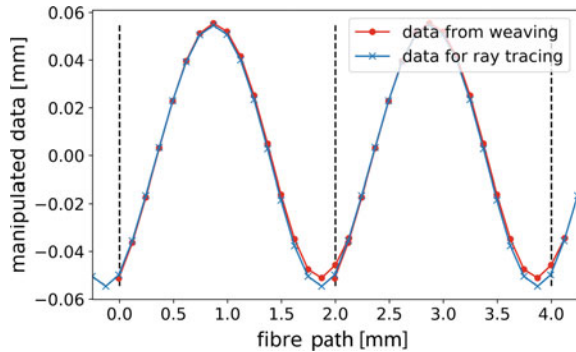
As already mentioned, the output from the weaving simulation is the POF shape in a unit cell. Before it can serve as input for the ray tracing program, the unit cell data has to be translated to the requested fibre length. To do so, the unit cell needs to contain a periodic set of data. This means that after translation of the unit cells, the data at the interface between two unit cells should describe a continuous and smooth curve.

The POF is discretized in nodes and elements. As data points, the nodal coordinates are regarded. The nodes will not lie exactly on the unit cell's edges and so the data set is not periodic as shown in Fig. 3. So from the existing data set, a periodic data set needs to be created in order to be able to describe a fibre at its full length.

This data set is obtained by a rotation and translation of the complete set of nodal coordinates. Additionally, a Fourier transformation and its inverse are conducted to get a periodic data set. The data is transformed into the frequency domain (Fourier transform), where its high, in this case disturbing, frequencies are deleted before it is transformed back (inverse Fourier transform).

The resulting data set, that can be used to describe a full length of a POF, is also shown in Fig. 3.

Fig. 3 POF's path as extracted from weaving simulation, as well as after data preparation for ray tracing. The unit cell has a length of 2 mm and is marked by the vertical striped lines. The x-axis is the axis in POF direction, the y-axis is the out of plane direction



5 Ray Tracing Simulations

Snell's law (Eq. 1) describes the relationship between the angles of incidence θ_1 and refraction θ_2 , when light passes a boundary between two media with refractive indices n_1 and n_2 .

$$n_1 \sin \theta_1 = n_2 \sin \theta_2 \quad (1)$$

When light travels from a medium with a high refractive index towards a medium with a lower refractive index, then Snell's law predicts that rays with incident angles larger than the critical angle θ_c will be completely reflected. Rays incident with an angle below θ_c will be partially reflected and refracted. The Fresnel equations describe the fraction of the incident power of the split ray, which is reflected and refracted, as shown in Fig. 4.

An optical fibre is a cylindrical waveguide that transmits light along its axis and consists of a core surrounded by a cladding layer. Because the refraction index of the cladding is lower than the refraction index of the core, the rays remain inside the core of the fibre due to total internal reflection (TIR). However, when the POF has been bent, some of these rays leave the core as the angle of incidence becomes larger than the critical angle (Fig. 5). This phenomenon is called macro-bending. The attenuation due to macro-bending depends on the refractive index difference of core and cladding, the radius of bend (curvature), the number of bends and the length under bend.

Ray tracing can be used to follow a ray of light in a multimode step index fibre as used in this project [6]. A ray tracing program has been developed in order to predict the propagation and emission of light through an arbitrarily shaped POF. The ray tracing program uses Snell's law and the Fresnel equations to calculate the path of a ray at every reflection point. It is assumed that the light is unpolarized. The ray tracing program follows the rays in the core and cladding. Rays hitting the core/cladding or cladding/air interface may be split at every reflection/refraction and will be radiated gradually as rays inside the cladding are 'leaky'.

In order to model the 'leaky' cladding, a loss factor is introduced in the model. For every ray hitting the cladding–outside interface, a fraction of the light is

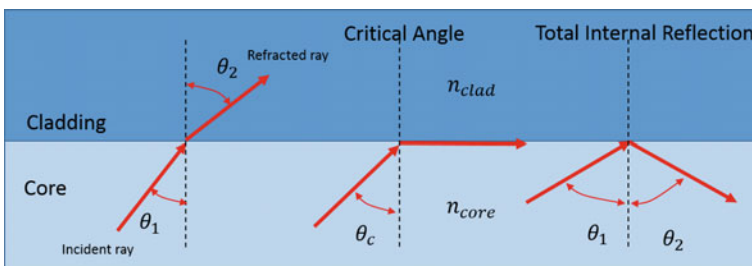
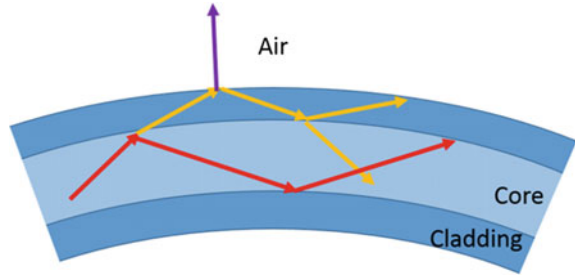


Fig. 4 Reflection, refraction and total internal reflection of light between two media ($n_1 > n_2$) (Wikipedia)

Fig. 5 Light leaving fibre due to macro-bending [3]



radiated perpendicular to the POF surface, independently of the Snell/Fresnel equations. This accounts for other loss mechanisms such as micro-bending and impurities inside the fibre. In micro-bending, an edge emitting fibre is obtained due to a slightly inefficient core/cladding boundary caused by high frequency perturbations of the waveguide.

With a Monte Carlo analysis many rays, with randomly varying initial position, angle, etc., are traced inside the POF. The calculation time depends on the number of rays and the shape and length of the POF.

The properties of the POF, the diameter and refractive indices, can be varied. The shape of the POF is described by a collection of points on the POF centreline. A smooth cubic spline is used to interpolate these points resulting in a smooth description of the POF with continuous curvatures. These points can be obtained from analytical functions, measurements or in our case from finite element simulations of a weaving process as described in the previous section.

The output of the program is the intensity of light inside the POF and the light leaving the POF can be measured using detector planes.

The results of the ray tracing model are explained using a typical result for a 180° bent fibre with a bending radius of 2.5 mm shown in Fig. 6. Here,

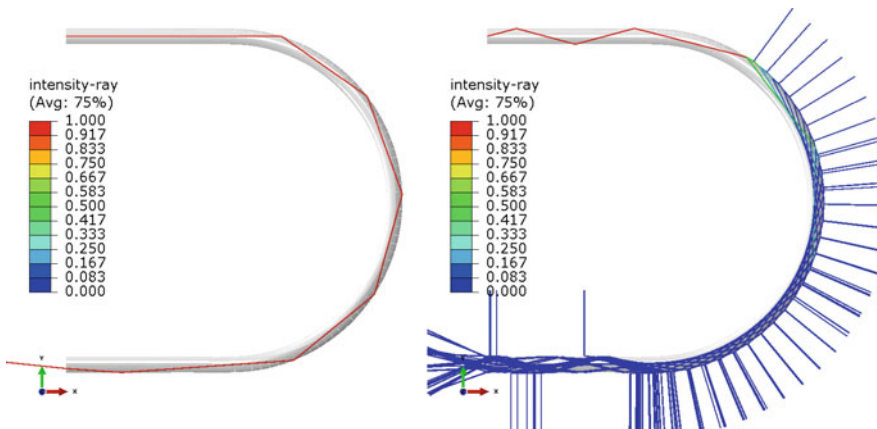


Fig. 6 Examples of a guided ray (left) and a scattered ray (right) in a bended POF

two typical rays are shown with a different initial angle. One ray is able to pass the bend without any loss. The other ray is guided in the initial straight part but enters the cladding in the curve. Here, this ray splits into many rays each with a lower intensity. Part of the light is emitted to the surroundings.

A Monte Carlo analysis with typically at least 1000 rays is performed. The rays enter the POF with equal intensity but with a random angle and random position within the core. The intensity of the light is presented in Fig. 7. The sum of the intensities of all rays entering the POF is scaled to 1. It can be seen that the intensity of light inside the core is decreasing. Light is transferred from the core to the cladding just after the injection of light and directly after the transition from straight to curved. The light in the cladding is not emitted to its surroundings immediately, but slowly emitted over some distance after the curvature change.

POFs with a constant curvature (as shown in Fig. 7) do not lose light anymore after some distance. To be able to emit all light, an undulating shape as in weaving is required. Simulations show that the light lost in a bend depends on the distribution of the rays before the bend, which was also seen by [4]. This means that ray tracing cannot be applied on a unit cell to predict the emission of a complete weave and therefore the fibre with its full length needs to be included in the ray tracing simulation.

6 Ray Tracing Validation on Single POF

The ray tracing results have been compared with numerical and experimental results from literature [1], [2], [4]. The general trends agree qualitatively.

Tests have been carried out on a single POF using white LED light. Some specially designed fixtures are used to control the exact shape of the POF, one with

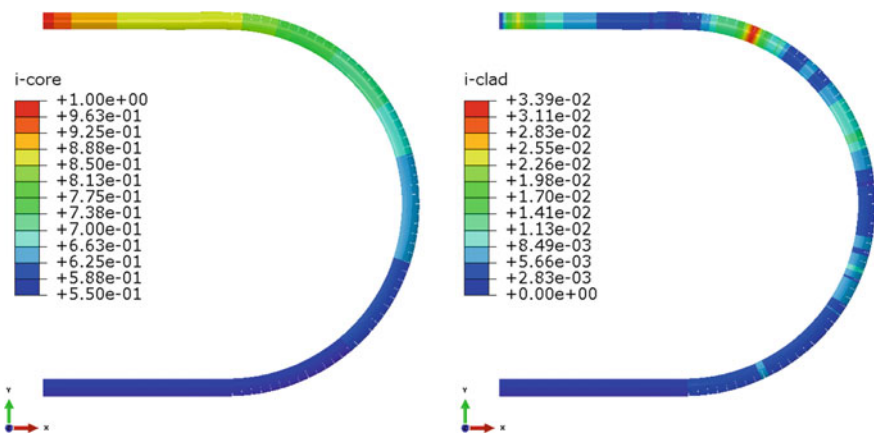


Fig. 7 Intensity of light inside the core and cladding of the POF

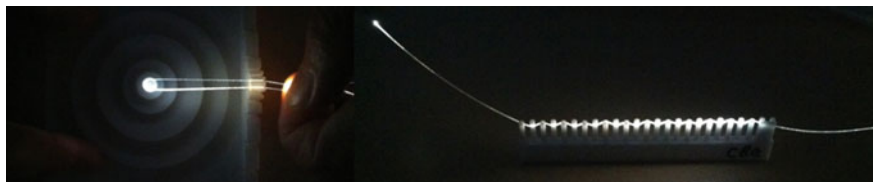
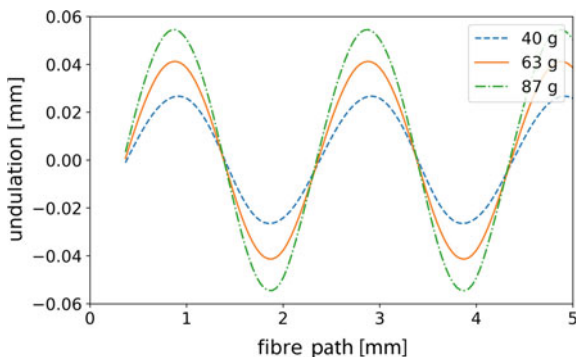


Fig. 8 POF experiment with constant curvature (left) and with cyclic curvature (right)

Fig. 9 POF's shape used in the ray tracing simulations. 5 mm of a total of 22 mm length is shown



a number of constant radii and one with a cyclic bending pattern, which mimics the weaving pattern (Fig. 8). Here, the light intensity leaving the fibre at the end has been measured before and after bending the fibre. Again, the major trends were captured well by the ray tracing simulations.

7 Results

To show the importance of weave settings on the fibre shape and on the final light output of the fabric, results of simulations with varying tension on the warp fibres are discussed. A satin 4 weave, which is shown in Fig. 2, is woven with 40, 63 and 87 g tension on the warp yarns. All other weave settings are unchanged.

It is expected, that a higher tension on the warp yarns, will cause more undulation in the fill yarns, in this case the POF. Figure 9 confirms this hypothesis. Here, the POF's shape is shown after data preparation for ray tracing. The POF that is regarded is the first one from the bottom with the unit cell shown in Fig. 2. The POF in the 87 g weave do indeed have a higher amplitude.

The weave settings do not only influence the POF's shape, but also the light emission. Figure 10 shows the cumulative light emission as a fraction of the light input. So at 0 no light is emitted and at 1 all the incident light is emitted.

A relation between the weave settings, the POF shape and the light output can be seen. The higher the tension on the warp yarns, the higher the undulation of the POFs and the faster the POF emits light.

The existing results do already contain enough information to describe the light emission of a complete weave. The POF with the complete length of the weave is used as input for the ray tracing program. The unit cell's character can now also be used to translate the results in warp direction. So the existing four POFs of the unit cell could describe a weave with any requested length in warp direction. As an example, Fig. 11 shows the cumulative light emission of a complete weave with the length of 15 unit cells in warp direction. Only the first 50 mm in fill direction are plotted.

The boundary effects in a real weave on the POF's shape at the weave's edges are not taken into account yet.

Fig. 10 Cumulative light emission as a fraction of light input over the first 50 mm of the POF's path, taken from the satin 4 (87 g) weave

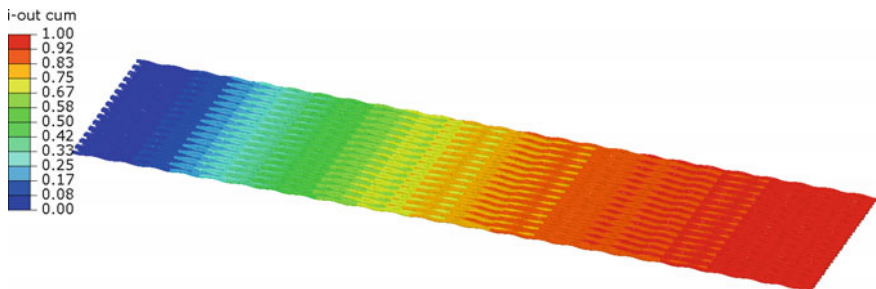
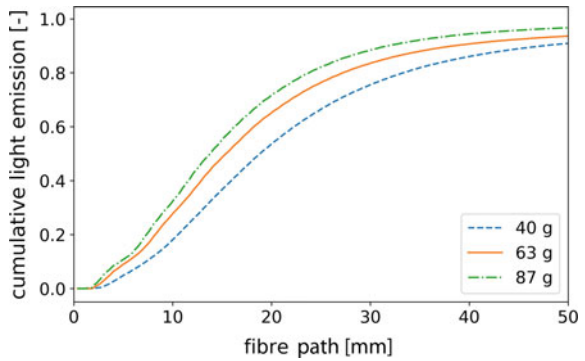


Fig. 11 Contour plot of the cumulative light emission as a fraction of light input over the first 50 mm of the satin 4 (87 g) weave with the length of 15 unit cells in warp direction

8 Summary and Outlook

A modelling procedure was set up to predict light output in a light emitting fabric. This procedure consists of a weaving simulation, the extraction of the fibre shape from this simulation and a ray tracing simulation based on this shape. Results from the ray tracing program are validated against numerical and experimental literature results, as well as against a set of test. The results are qualitatively in good agreement. It is then shown that the weave settings matter for the light output. The light output of single POF of a weave with varying tension on the warp fibres is investigated. A clear correlation between warp fibre tension, the POF shape and the light output is presented.

With the modelling procedure, light output from a complete weave can now be predicted. The weave type and the weave settings, which lead to the most homogenous light output, are now being investigated. The simulation results will be compared to experimental data.

Acknowledgements This study is supported by the European Commission through the project PHOS-ISTOS (621103) titled ‘Development of biophotonic device based on flexible light emitting textile dedicated to the monitoring and treatment for dermatologic diseases and carcinoma’. We would especially like to thank the project partners Ensait and Inserm.

References

1. Achenbach, C., & Cobb, J. (2003). Computational studies of light acceptance and propagation in straight and curved multimodal active fibres. *Journal of Optics A: Pure and Applied Optics*, vol. 5.
2. Arrue, J., Zubia, J., Fuster, G., & Kalymnios, D. (1998). Light power behaviour when bending plastic optical fibres. *IEE Proc Optoelectron, Fed.*, 145(6).
3. Durana, G., Zubia, J., Arrue, J., Aldabaldetrek, G., & Mateo, J. (2003). Dependence of bending losses on cladding thickness in plastic optical fibres. *Applied Optics*, 42(6).
4. Endruweit, A., Long, A., & Johnson, M. (2008). Textile composites with integrated optical fibres: Quantification of the influence of single and multiple fibre bends on the light transmission using a Monte Carlo ray-tracing method. *Smart Materials and Structures*, 17.
5. ESI Virtual Performance Solution. (2015).
6. Jiménez, F., Arrue, J., Aldabaldetrek, G., & Zubia, J. (2004). Numerical simulation of light propagation in plastic optical fibres of arbitrary 3D geometry. *WSEAS Transactions on Mathematics*, 4(3), 824–829.
7. Oguz, Y. (2017). Conception et réalisation de structures textile lumineuses pour le traitement et le monitoring de la thérapie Photo Dynamique, PhD thesis.
8. Oguz, Y., Cochrane, C., Koncar, V., & Mordon, S. (2016). Doehlert experimental design applied to optimization of light emitting textile structures. *Optical Fiber Technology*, 30.
9. Oguz, Y., Koncar, V., Cochrane, C., & Mordon, S. (2017). Light-emitting woven fabric for treatment with photodynamic therapy and monitoring of actinic keratosis. In *Photomedicine - Advances in Clinical Practice*.
10. Russcher, L., Lamers, E., Dufour, C., Boussu, F., Wang, P., & Soulat, D. (2013). Modelling the microstructure of Multilayer Woven Fabrics. In *13th Autex world textile conference*.

Interesting Mechanical Properties of 3D Warp Interlock Fabrics

F. Boussu, S. Picard and D. Soulat

Abstract The purpose of this study is to analyse the influence of weaving parameters of 3D warp interlock fabrics on their mechanical properties. Using the same yarns in the warp and weft direction, four main product and process parameters have been chosen as the weave diagram, the weft density and positions of stuffer and linking warp yarns inside the woven structure. Based on several 3D warp interlock architecture produced on the same dobby loom, the mechanical characterization of these fabrics have been performed by unidirectional tensile and bending tests, both in the warp and weft directions. Thanks to this complete protocol; a comparison between 3D warp interlock woven architectures has been done to reveal the influence of process and product parameters on their mechanical performances.

1 Introduction

The 3D warp interlock fabrics have demonstrated higher mechanical properties than 2D fabrics stacked together as laminates as fibrous reinforcement for composite material. Dedicated scientific review, added by our own research results [1–6], have enabled us to cross-check and confirm the results of the mechanical properties of 3D warp interlock fabrics. These structures, because of their specific consolidation method in the thickness, exhibit advantageous mechanical properties [7]. Recurrently, 3D warp interlock fabrics increase resistance to delamination [8–13] and the impact resistance [8–11, 14–23]. Episodically, some researches have shown improved properties of resistance to crack propagation, damage tolerance and dimensional stability [15].

Despite all of these research results, the link between the 3D warp interlock fabrics product parameters and their resulted mechanical properties appears not yet revealed. Thus, the purpose of this study tries to answer these two main questions.

F. Boussu (✉) · S. Picard · D. Soulat
ENSAIT, GEMTEX, Université de Lille 1, 59100 Roubaix, France
e-mail: francois.boussu@ensait.fr

First: Considering the same weaving loom, what are the differences between the geometrical model and the real geometry of the 3D warp interlock fabrics?

Second: What are the main differences in mechanical properties between several 3D warp interlock architectures?

2 Experimental Approach

According to our definition of 3D warp interlock fabrics [24], four architectures have been chosen to reflect the four different family types of 3D fabrics, as described in Hu [25]. The distinction of these four family types is led by the evolution of the binding warp yarn as Orthogonal or Angle coupled with its thickness depth as layer-to-layer or through-the-thickness.

For this study, the following 3D warp interlock fabrics architectures have been defined as:

- (a) O-L 3 4-2 twill 5 weave, 28 picks/cm, 10 ends/cm, without stuffer warp yarns
- (b) A-L 4 3-2 twill 4 weave, 70 picks/cm, 10 ends/cm, with stuffer warp yarns
- (c) O-T 4 3-4 3 by 3 basket weave, 20 picks/cm, 10 ends/cm, with stuffer warp yarns
- (d) A-T 4 5-4 twill 6 shaped weave, 40 picks/cm, 10 ends/cm, with stuffer warp yarns

For instance, the fabric O-L 3 4-2 twill 5 weave corresponds to an Orthogonal architecture with a Layer-to-layer binding yarn on three layers, linking with a step of four weft yarns columns and thickness depth penetration of two layers, and finally following the twill 5 weave diagram.

All these fabrics have been woven on the same dobby weaving loom and with the same warp and weft yarns as a Twaron 2000 filaments/yarn, 336 Tex, 60 twists/m.

Taking into account these produced fabrics, observations of the real geometry in the two directions have been first done.

3 Geometrical Comparison

Based on these four different 3D warp interlock fabrics architectures, a low-speed resin infusion process has been applied to each of these fibrous reinforcements in order to keep as safe as possible their initial geometry. Then, 3D fabric slices have been obtained both in the warp and weft directions to be compared with geometric scheme made on Wisetex software [26].

The first fabric, labelled (a), does not contain any stuffer warp yarns on the three weft yarns layers; while the others, labelled (b), (c) and (d) include stuffer warp yarns between each of the four weft yarns layers.

- (a) O-L 3 4-2 twill 5 weave, 28 picks/cm, 10 ends/cm, without stuffer warp yarns
- (b) A-L 4 3-2 twill 4 weave, 70 picks/cm, 10 ends/cm, with stuffer warp yarns
- (c) O-T 4 3-4 3 by 3 basket weave, 20 picks/cm, 10 ends/cm, with stuffer warp yarns
- (d) A-T 4 5-4 twill 6 shaped weave, 40 picks/cm, 10 ends/cm, with stuffer warp yarns

The geometrical model of each of the 3D warp interlock fabrics is represented in Table 1, with cross-section of weft yarns and warp yarns evolutions.

The 3D views of each of the 3D warp interlock fabrics architectures are given in Table 2.

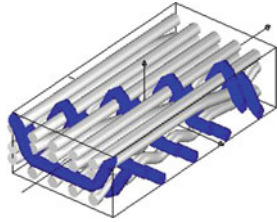
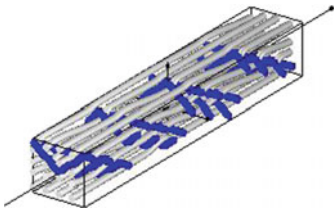
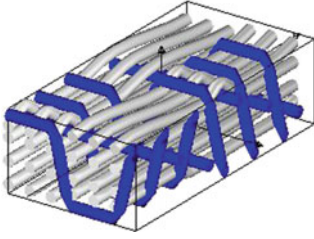
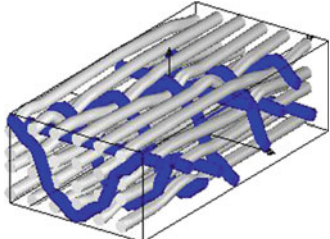
3.1 Observations in the Warp Direction

The real and modelled geometries of the four 3D warp interlock fabrics are represented in Table 3 using weft cross-section views.

Table 1 Weft cross-section views of the geometrical representation of the four 3D warp interlock fabrics

	Orthogonal (a)	Angle (b)
Layer to layer		
Through the thickness		

Table 2 3D views of the geometrical representation of the four 3D warp interlock fabrics (warp yarns in blue and weft yarns in grey)

	Orthogonal (a)	Angle (b)
Layer to layer		
Through the thickness		

Comparing the following fabrics, 3D warp interlock O-L 3 4-2 twill 5 weave and 3D warp interlock O-T 4 3-4 3 by 3 basket weave, similar geometries with real and simulated models can be observed. The warp yarns evolutions, inside the real 3D warp interlock fabric, follow the same path as the one mentioned in the simulated geometry.

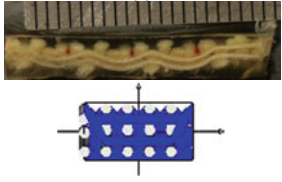
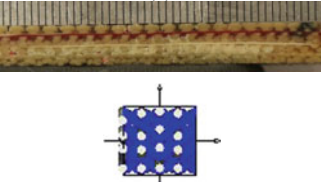
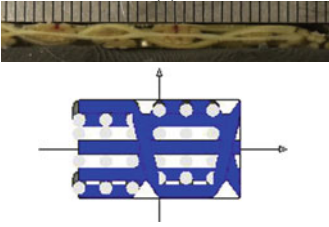
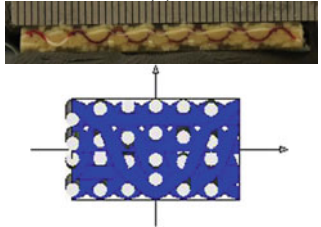
On the contrary, considering the other fabrics, 3D warp interlock A-L 4 3-2 twill 4 weave and 3D warp interlock A-T 4 5-4 twill 6 shaped weave, the warp yarns evolutions are slightly different from the geometrical models.

3.2 Observations in the Weft Direction

The real and modelled geometries of the four 3D warp interlock fabrics are represented in Table 4 using warp cross-section views.

None of these fabrics have a similar weft yarns evolutions by comparing the real and modelled geometries. It can be highlighted a crimp evolution of the weft yarns more pronounced for the real geometry than for the modelled geometry especially for the 3D warp interlock fabric A-L 4 3-2 twill 4 weave.

Table 3 Evolutions of warp yarns inside each 3D warp interlock fabrics architectures

Weft cross section view	Orthogonal	Angle
Layer to layer	<p>(a)</p> 	<p>(b)</p> 
Through the thickness	<p>(c)</p> 	<p>(d)</p> 

4 Mechanical Comparison

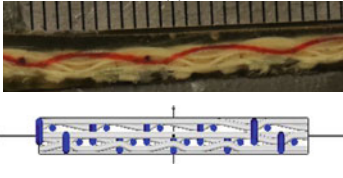
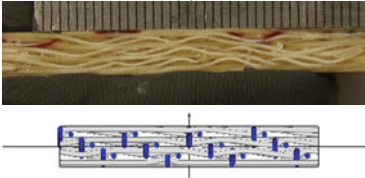
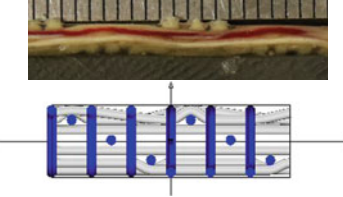
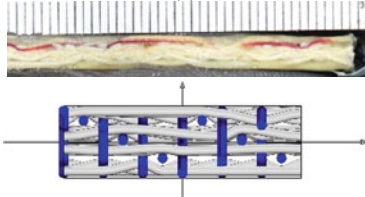
The same testing protocol has been applied on all these four 3D warp interlock fabrics. One of the performed mechanical characterizations is a uniaxial tensile test done in the two directions of the fabric. During these tests, the deformation speed has been fixed to 100 mm/min with a pre-charge of 2 N. In order to compare all these results between the different architectures of fabrics with different end and pick densities, the force applied on the fabric has been divided by the number of yarns in the direction of the test (in N/yarn) with respect to the elongation (%). Based on these results given for each of the four architectures and both in the warp and weft directions, the loss of crimp, the elastic behaviour, the maximal strain and the corresponding elongation at its maximum value are revealed. For each of these 3D warp interlock fabrics, five specimens have been tested in each warp and weft direction with a 5 cm width as regards the dimensions provided by the standard EN ISO 13934-1.

Considering the force–elongation curve represented in Fig. 1, different parts of this curve can be divided to explain the different 3D fabrics behaviour.

The first part of the curve corresponds to the loss of crimp and warp and weft re-arrangements inside the 3D warp interlock fabric structure.

The second part displays the elastic behaviour of warp yarns during the tensile test.

Table 4 Evolutions of weft yarns inside each 3D warp interlock fabrics architectures

Warp cross section view	Orthogonal	Angle
Layer to layer	<p>(a)</p> 	<p>(b)</p> 
Through the thickness	<p>(c)</p> 	<p>(d)</p> 

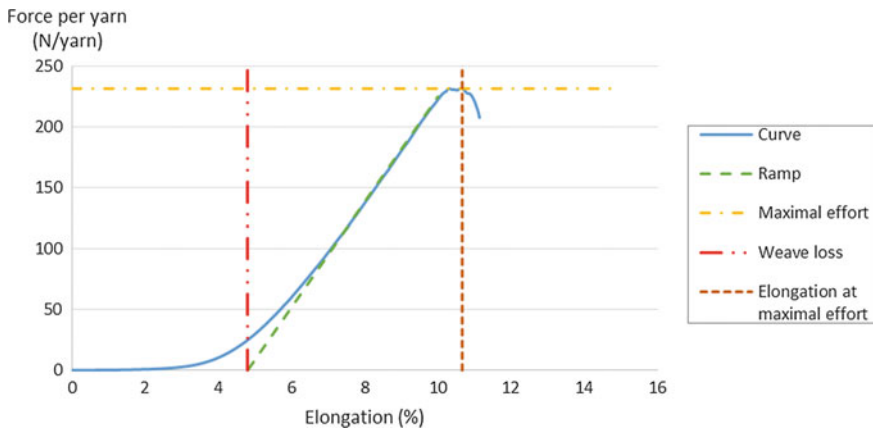
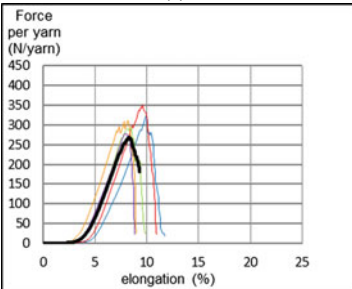
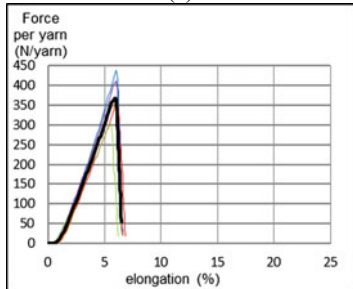
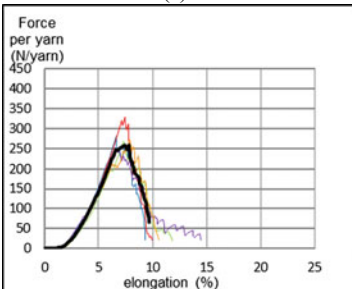
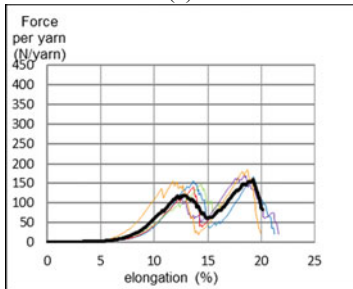


Fig. 1 3D warp interlock fabric force versus elongation curve during a tensile test

Thanks to these graphs, three comparison parameters can be evaluated as:

- The loss of crimp
- The elongation at break
- The maximal force.

Table 5 Comparison of tensile tests applied in the warp direction

Warp direction	Orthogonal	Angle
Layer to layer	(a) 	(b) 
Trough to thickness	(c) 	(d) 

4.1 Mechanical Comparison in the Warp Direction

In Table 5, the force–elongation average curves of each of the four 3D warp interlock fabrics are represented for tensile tests done in the warp direction.

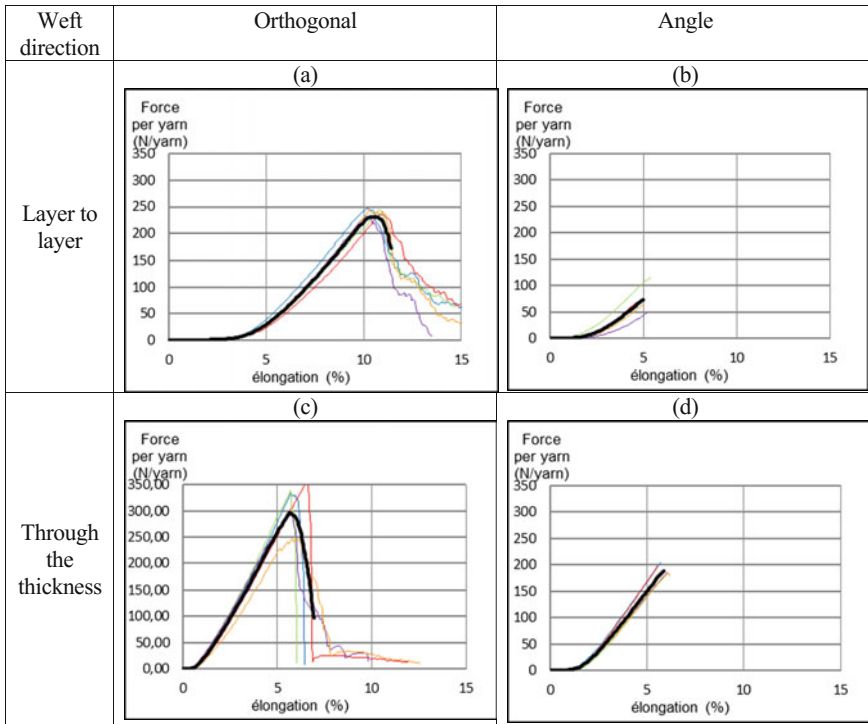
Considering the 3D warp interlock fabric O-L 3 4-2 twill 5 weave (labelled (a)), the crimp loss appears after an elongation value of 4% and the standard deviation of the average curve seems to be the highest of the four different types of architecture.

Considering the 3D warp interlock fabric A-L 4 3-2 twill 4 weave (labelled (b)), the crimp loss has been revealed as the lowest value and the maximum force at break the highest value. This can be directly linked to the straight positions of stuffer warp yarns inside the structure as revealed in Table 3 (label (b)).

Considering the 3D warp interlock fabric O-T 4 3-4 3 by 3 basket weave (labelled (c)), the average curve is quite similar to the 3D warp interlock fabric O-L 3 4-2 twill 5 weave (labelled (a)), with a slight increase of stiffness due to the straight position of stuffer warp yarns inside the structure as observed in Table 3 (label (c)).

Considering the 3D warp interlock fabric A-T 4 5-4 twill 6 shaped weave (labelled (d)), the lowest value of maximum force is obtained but with the highest

Table 6 Comparison of tensile tests applied in the weft direction



value of elongation before break. By the same, the equal distribution of the binding and stuffer warp yarns with respectively undulated and straight position inside the 3D fabric architecture, as observed in Table 3 (label (d)), can mainly explain these two pics of mechanical behaviour.

The difference of weave evolution between stuffer yarns and binding yarns can primarily affect the fabric behaviour in the warp direction and second the third part of the curve. A high weave difference of these yarns can create a second pic during the tensile test (third part of the curves). For the case where all the evolutions of warp yarns are straight inside the fabric, the fabric stiffness seems to be higher (as for labelled curve (b)).

When the difference of crimp has a low value, where all the yarns are not straight, a certain amount of yarns will be first involved in the tensile resistance before the others; which lead to distinguishing two cases.

In the first case, the second part of the warp yarns can work before the break of the first yarns, so a structure stiffening can be observed during the test (as for labelled curve (c)). In the second case, the second part of the warp yarns can work after the break of the first yarns, so a second pic can be observed during the test (as for labelled curve (d)).

4.2 Mechanical Comparison in the Weft Direction

In Table 6, the force–elongation average curves of each of the four 3D warp interlock fabrics are represented for tensile tests done in the weft direction.

Considering the 3D warp interlock fabrics A-L 4 3-2 twill 4 (labelled (b)) and A-T 4 5-4 twill 6 shaped (labelled (d)), with respectively, 70 and 40 picks/cm, the tensile tests measurement has not been able to register all the force–elongation curve mainly due to highest values of pick densities which reach the limit of our tensile bench.

Considering the 3D warp interlock fabric O-L 3 4-2 twill 5 weave (labelled (a)), the highest values of crimp loss and elongation can be also explained by the undulated position of weft yarns inside the structure, as revealed in Table 4 (label (a)). However, the variation of values around the average curve seems lower than the standard deviation previously observed in the warp direction.

Considering the 3D warp interlock fabric O-T 4 3-4 3 by 3 basket weave (labelled (c)), the straight position of weft yarns inside the structure, as revealed in Table 4 (label (c)), mainly explained the observed stiffness of the fabric with higher value of force resistance and lower value of elongation.

In the weft direction, the influence of the binding appears less sensible than in the warp direction, but most of the mechanical properties depend on the resulted geometry given by the 3D warp interlock fabric architecture.

5 Conclusion

This research work aims at highlighting the main influence of the binding and resulted geometry of 3D warp interlock fabrics on their mechanical behaviours.

The binding can affect the crimp loss value correlated with the elongation value, both in the warp and weft directions. But the binding is not the only parameter which can affect the mechanical properties of 3D warp interlock fabrics. A high pick density value can also affect the geometry of the fabrics and lead to an equilibrium of floats.

An additional research study based on the other product parameters can be useful to improve the knowledge on the mechanical behaviour of these 3D warp interlock fabrics.

References

1. Nauman, S. (2008). *Modélisation Géométrique de tissu 3D Interlock*. Roubaix, France, Master report: Laboratoire GEMTEX.
2. Nauman, S. (2011). Geometrical modelling and characterization of 3D warp interlock composites and their on-line structural health monitoring using flexible textile sensors, University of Lille 1, Lille, Ph-D thesis. <http://www.theses.fr/en/2011LIL10010>, 24/03/2011.

3. Lapeyronnie, P. (2010). Mise en œuvre et comportement mécanique de composites organiques renforcés de structures 3D interlocks. Université de Lille 1, Douai, France, Thèse de doctorat <http://www.theses.fr/en/2010LIL10126>, 14/12/2010.
4. Ha-Minh, C. (2011). Comportement mécanique des matériaux tissés soumis à un impact balistique: approches expérimentale, numérique et analytique. Université de Lille 1, Lille, France, Thèse de doctorat <http://www.theses.fr/en/2011LIL10184>, 17/11/2011.
5. Lefebvre, M. (2011). Résistance à l'impact balistique de matériaux composites à renforts Interlocks tissés. Application au blindage de véhicules. Université de Valenciennes, Valenciennes, Thèse de doctorat <http://www.theses.fr/en/2011VALE00030>, 07/12/2011.
6. Provost, B. (2013). Étude et Réalisation d'une solution à renfort tissé interlock pour la protection balistique de véhicule. Université de Valenciennes, Valenciennes, Thèse de doctorat <http://www.theses.fr/en/2013VALE00003>, 14/01/2013.
7. Cristian, I., Boussu, F., & Nauman, S. (2010). Interesting parameters of 3D warp interlock fabrics influencing the mechanical properties of the final composite structures. In *10th World textile conference*, Vilnius, Lithuania, 21–23 June, 2010.
8. Tong, L., Mouritz, A. P., & Bannister, M. K. (2002). *3D fibre reinforced composite materials*. London: Elsevier Applied Science. ISBN 978-0-08-043938-9.
9. Hu, J. (2008). *3D fibrous assemblies, properties applications and modelling of three dimensional textile structure*. Woodhead Publishing, vol. 74. ISBN-978-1-84569-377-0.
10. Sheng, S. Z., & Hoa, S. V. (2003). Modelling of 3D angle interlock woven fabric composites. *Journal of Thermoplastic Composite Materials*, 16(1), 45–59. <https://doi.org/10.1177/0892705703016001206>.
11. Mouritz, A. P., Bannister, M. K., Falzon, P. J., & Leong, K. H. (1999). Review of applications for advanced three-dimensional fibre textile composites. *Composites Part A Applied Science and Manufacturing*, 30(12), 1445–1461. [https://doi.org/10.1016/S1359-835X\(99\)00034-2](https://doi.org/10.1016/S1359-835X(99)00034-2).
12. Nauman, S., Boussu, F., Cristian, I., & Koncar, V. (2009). Impact of 3D woven structure onto the high performance yarn properties. In *Second conference on intelligent textiles and mass customisation, textile composites workshop*, Casablanca, Morocco, 12–14th November 2009.
13. Brandt, J., Drechsler, K., Arendts, F.J. (1996). Mechanical performance of composites based on various three dimensional woven fibre preforms. *Composites Sciences and Technology*, 56(3), 381–386. doi:10.1016/0266-3538(95)00135-2.
14. Lapeyronnie, P., Le Grogne, P., Binetruy, C., & Boussu, F. (2010). Angle-interlock reinforcements: Weaving and the mechanical properties of composites. *JEC Composites*, 58, 58–59.
15. Tan, P., Tong, L., & Steven, G. P. (1999). Micromechanics models for mechanical and thermomechanical properties of 3D through-the-thickness angle interlock woven composites. *Composites: Part A*, 30(5), 637–648. [https://doi.org/10.1016/S1359-835X\(98\)00176-6](https://doi.org/10.1016/S1359-835X(98)00176-6).
16. Tsai, K. H., Chiu, C. H., & Wu, T. H. (2000). Fatigue behaviour of 3D multi-layer angle interlock woven composite plates. *Composites Science and Technology*, 60, 241–248. [https://doi.org/10.1016/S0266-3538\(99\)00120-7](https://doi.org/10.1016/S0266-3538(99)00120-7).
17. Baucom, J.N., & Zikry, M.A. (2003). Evolution of failure mechanisms in 2D and 3D woven composite systems under quasi-static perforation. *Journal of Composite Materials*, 37(18), 651–1674, 01/01 2003. doi:10.1177/0021998303035178.
18. Tanzawa, Y., Watanabe, N., & Ishikawa, T. (1999). Interlaminar fracture toughness of 3-D orthogonal interlocked fabric composites. *Composites Science and Technology*, 59(8), 1261–1270. doi:10.1016/S0266-3538(98)00167-5.
19. Chen, F., & Hodgkinson, J.M. (2009). Impact behaviour of composites with different fibre architecture. *Proceedings of the Institution of Mechanical Engineers, Part G: Journal of Aerospace Engineering*, 223(7), 1009–1017, 01/11 2009.
20. Naik, N. K., Azad, S. K., Durga Prasad, N. M., & Thur, P. (2001). Stress and failure analysis of 3D orthogonal interlock woven composites. *Journal of Reinforced Plastics and Composites*, 20(17), 1485–1523. <https://doi.org/10.1177/073168401772679110>.

21. Padaki, N.V., Alagirusamy, R., Deopura, B.L., & Figueiro, R. (2010). Influence of preform interlacement on the low velocity impact behavior of multilayer textile composites. *Journal of Industrial Textiles*, 40(2), 171–185, 26/05 2010. DOI:[10.1177/1528083710366723](https://doi.org/10.1177/1528083710366723).
22. Tung, P.S., & Jayaraman, S. (1991). Three dimensional multilayer woven preforms for composites. In *High-tech fibrous materials*. Washington, DC, Washington, USA: ACS Publisher, vol. 457, Chap. 4, pp. 53–80. DOI:[10.1021/bk-1991-0457.ch004](https://doi.org/10.1021/bk-1991-0457.ch004).
23. Coman, F., Herszberg, L., & Bannister, M. (1996). Design and analysis of 3D woven preforms for composite structures. *Science and Engineering of Composite Materials*, 5(2), 83–96.
24. Boussu, F., Cristian, I., & Nauman, S. (2015). General definition of 3D warp interlock fabric architecture. *Composites: Part B*, 81, 171–188. <https://doi.org/10.1016/j.compositesb.2015.07.013>.
25. Hu, J. (2008). 3D fibrous assemblies, properties applications and modelling of three dimensional textile structure. Woodhead Publishing, vol. 74.
26. Lomov, S., Gusakov, A. V., Huysmans, G., Prodromou, A., & Verpoest, I. (2000). Textile geometry preprocessor for meso-mechanical models of woven composites. *Composites Science and Technology*, 60, 2083–2095.

Fibers and Textiles for Fully Bio-Based Fiber Reinforced Materials

Thomas Grethe, Boris Mahltig, Haoqian Miao, Thomas Kick,
Hajo Haase, Mark Kopietz and Sergiy Grishchuk

Abstract Textile materials and their modifications for use in bio-based fiber reinforced materials are presented. Main results are related to hydrophobic and antimicrobial functionalization, to make the natural fiber materials more suitable for application in composite materials. To realize a fully bio-based composite, it is the challenge to evaluate also bio-based finishing agents offering the wished properties.

1 Introduction

Fiber reinforced materials are useful in several fields of construction and are part of daily life nowadays. These materials are used in construction in different areas, as e.g., aircraft, automotive, bicycle, energy production, etc. [1–5]. In a simple view, they are built up by a textile construction and a polymer matrix surrounding the textile. For many high-performance applications, the textile is made from inorganic fibers, as carbon- or glass fibers. The polymer matrix is made of synthetic polymers.

In comparison, a fully bio-based reinforced material contains both textiles and polymer matrix from renewable resources. Of course, with view on the fiber strength, the use of natural fibers is disadvantageous compared to composites containing inorganic fibers. However, the use of natural fibers in composite materials offers several advantages. These advantages are based on material,

T. Grethe · B. Mahltig (✉) · H. Miao · T. Kick
Faculty of Textile and Clothing Technology, Hochschule Niederrhein,
Webschulstr. 31, 41065 Mönchengladbach, Germany
e-mail: boris.mahltig@hs-niederrhein.de

H. Haase
Technische Universität Berlin, Institut für Lebensmitteltechnologie und Lebensmittelchemie,
Gustav-Meyer Allee 25, 13355 Berlin, Germany

M. Kopietz · S. Grishchuk
Institut für Verbundwerkstoffe GmbH, Erwin-Schroedinger-Str. 58,
67663 Kaiserslautern, Germany

economic and ecologic reasons. The material advantage of natural fibers is related to their low density especially compared to glass fibers, so composite materials of lower weight can be realized [5, 6]. The economic advantage of natural fibers is related to their price which is quite low compared to glass and carbon fibers [7, 8]. The ecologic advantage of natural materials is that their recycling is easily possible compared to composite materials containing inorganic fibers [3, 5, 9].

However, for application in composites, natural fibers have mainly two disadvantages, both are related to their hydrophilicity. Natural fibers can take up significant amounts of water [10–12]. This uptake of water can lead to changes in fiber volume, which can promote crack formation in the matrix of the composite material. Also, the presence of water can promote the growth of fungi and bacteria, which can be part of a biocorrosion of the composite material.

For this, it is important to modify natural fibers used in composites with hydrophobic and antimicrobial properties. Of course in a fully bio-based composite, these hydrophobic and antimicrobial properties should be realized by using also bio-based agents.

2 Pretreatment of Natural Fibers

2.1 *Hydrophobization of Textile Fabrics*

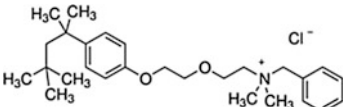
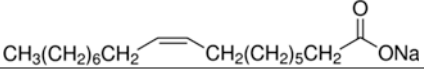
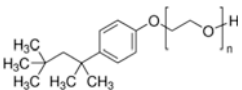
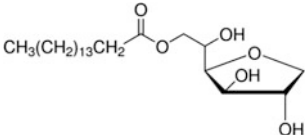
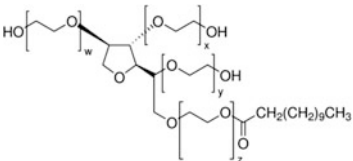
For realization of hydrophobic properties, the textile fabrics are treated with different hydrophobic finishing agents, containing chemical components as Tung oil, natural oils, amino acids or suspensions of polyisoprene. These chemicals are bio-based and evaluated in their application as water-based recipes. These hydrophobic components are partly cross-linked after application onto the fibers and covalently bonded to the fiber surface. Application onto the fabrics is done by padding, which is followed by thermal drying and fixation.

2.1.1 Application of Natural Oils

Natural oils can be used to apply hydrophobic properties onto textiles. These natural oils are not applied as pure substances. Instead of this, they are part of a water-based finishing agent, which is containing also other components. Important components are surfactants which are necessary to stabilize the water/oil recipe against phase separation. Oxidative agents as sodium persulfate are added to improve cross-linking after application on the textile surface [13].

Best results are gained in actual investigations by usage of the Tung oil, which is a natural oil produced from the Tung tree originated in China and an established agent for the treatment of wooden materials [14–16]. The Tung oil containing recipes are applied onto linen fabrics by padding.

Table 1 Overview on selected surfactants

Surfactant	Charge	HLB value	Biodegradable y/n	Chemical structure
Hyamin 1622	Cationic	7.6	n	
Hexadecyltrimethylammonium-bromide	Cationic	8.8	n	$\text{H}_3\text{C}(\text{H}_2\text{C})_{15}\text{N}^+(\text{CH}_3)_3 \text{Br}^-$
Tetradecyltrimethylammonium-bromide	Cationic	9.75	n	$\text{CH}_3(\text{CH}_2)_{12}\text{CH}_2\text{N}^+(\text{CH}_3)_3 \text{Br}^-$
Sodium oleate	Anionic	18	y	
Sodium dodecyl sulfate	Anionic	40	n	$\text{CH}_3(\text{CH}_2)_{10}\text{CH}_2\text{O}\text{S}(=\text{O})(\text{O}^-)\text{Na}^+$
Triton X 100	Neutral	13.6	n	
Sorbitanmono-palmitat Span 40	Anionic	8.4	y	
Polyoxyethylen-sorbitanmonolaurat Tween 20	Neutral	16.7	y	

For recipe formulation, the surfactants Triton X 100, sodium dodecyl sulfate (SDS) and sodium oleate are evaluated. An overview on several surfactants and their properties is given in Table 1. Best results for suspension stability and gained hydrophobic effect are reached by addition of sodium oleate (see Fig. 1). The positive result gained with sodium oleate could be explained by an oxidative cross-linking to the Tung oil components, so the added surfactant is finally incorporated and covalent bonded to the hydrophobic finishing [13].

Further experiments are done with aqueous recipes containing Tung oil, sodium peroxodisulfate, and sodium oleate. Sodium peroxodisulfate is added to improve oxidative cross-linking between the Tung oil components after application onto the textile. However, high concentrations of sodium peroxodisulfate damage the treated textile and lead to decreased textile strength. The addition of sodium peroxodisulfate in small amounts to the finishing recipe can even improve the strength of

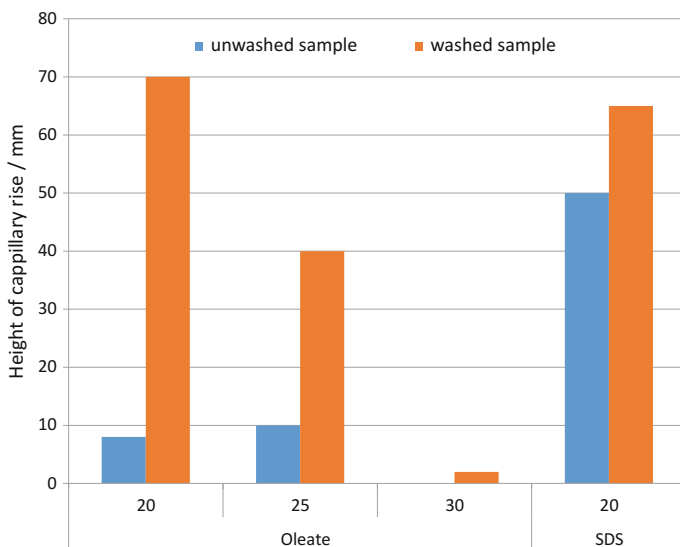


Fig. 1 Capillary rise after 15 min. On linen fabrics treated with Tung oil. Compared are samples containing different surfactants and Tung oil concentrations in g/100 ml. The capillary rise is given for samples directly after preparation and after rinsing with water

the fiber material. However, this effect strongly depends on the intensity of thermal after treatment (Fig. 2). Also, the hydrophobic properties of treated fiber samples are improved as a function of sodium peroxodisulfate concentration in the finishing recipe (Figs. 3 and 4). This statement is especially strengthened by the contact angle measurements done with water drops on the textile samples (Fig. 4). For this preparation, a Tung oil concentration of 30% is chosen and the sodium peroxodisulfate concentration is increased up to values of 20 g/100 mL.

The presence of this cross-linker leads to an increase of hydrophobicity of the treated textiles. With increased cross-linker concentration also the hydrophobic effect is present after a washing process (Fig. 4). Probably the sodium peroxodisulfate leads to a cross-linkage of Tung oil components between each other but also to the hydrophilic fiber surface. Also, recipes with increasing Tung oil concentration are evaluated for textile treatment. As expected, the hydrophobic properties of the treated textiles increase as a function of Tung oil concentration (Fig. 5).

Alternatively to Tung oil, also two other natural oils are evaluated as hydrophobic additive—oil from sunflowers and oil from rapeseed. These natural oils are applied in similar recipe composition as done with Tung oil before. Both natural oils contain as well unsaturated fats, so a cross-linking reaction as proposed for the Tung oil should be expected. However, as seen in Figs. 6 and 7, the hydrophobic properties of textiles gained by application of these natural oils are low and not competitive to the effects gained by Tung oil applications. One explanation could be that both used natural oils contain a certain amount of Vitamin E, which can act as radical catcher. By this, the cross-linking reactions are probably hindered.

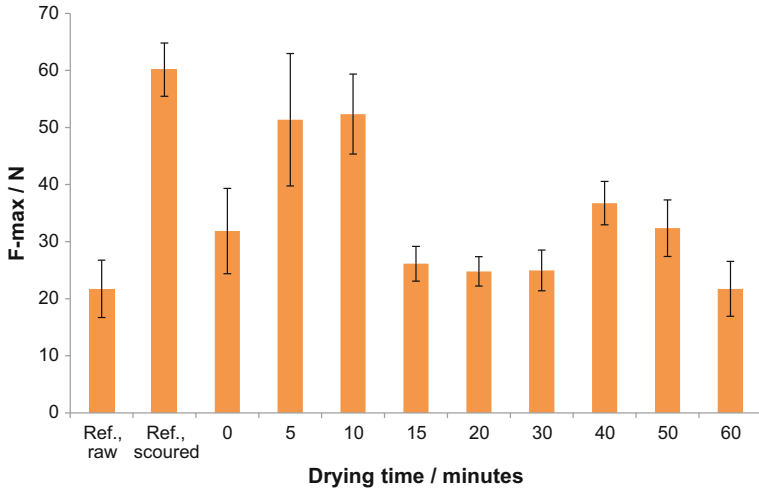


Fig. 2 Maximum tensile strength of linen fabrics treated with Tung oil and sodium oleate under addition of sodium persulfate. The results are shown for increasing drying duration after recipe application

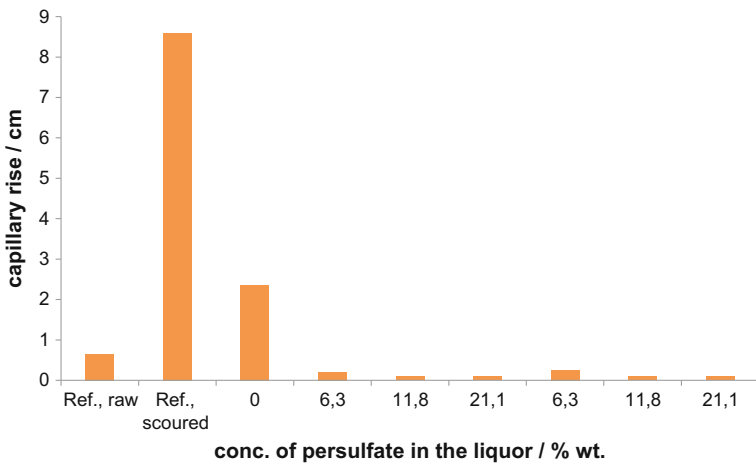


Fig. 3 Capillary rise on linen fabrics treated with Tung oil recipe containing different amounts of sodium persulfate

2.1.2 Application of Polyisoprene

As an alternative approach, recipes containing polyisoprene are evaluated to realize hydrophobic textile surfaces. For this, suspensions of latex are applied in undiluted and in dilution with water. Also, a recipe containing 50 mL latex suspension, 50 mL distilled water, and 5 g sodium peroxodisulfate is applied. The hydrophobic

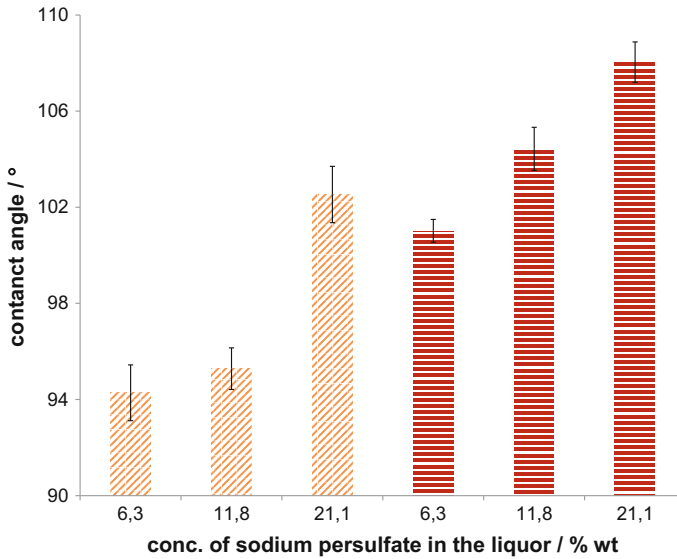


Fig. 4 Contact angle measurements (with water) on Tung oil treated linen fabrics. The Tung oil is applied in presence of different sodium persulfate concentrations—yellow/left: measurements directly after the finishing/red/right: measurements after rinsing with water and the surfactant Triton-X 100

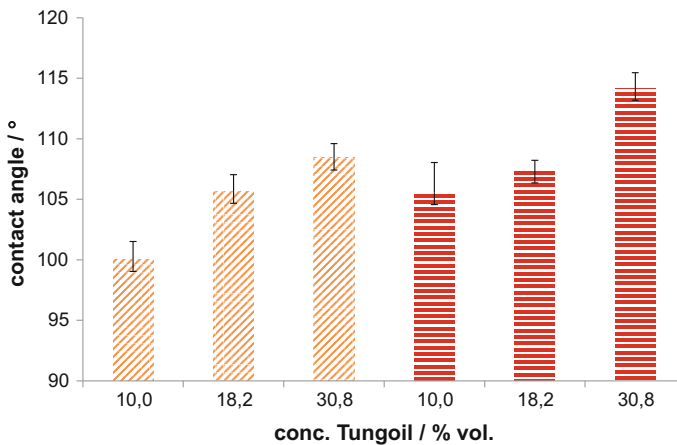


Fig. 5 Contact angle measurements (with water) on Tung oil treated linen fabrics. The Tung oil is applied with increasing concentrations—yellow/left: measurements directly after the finishing/red/right: measurements after rinsing with water and the surfactant Triton-X 100

properties of the realized textiles are tested directly after preparation and after a rinsing procedure. Only with the undiluted latex suspension, a significant hydrophobic effect can be introduced to the textile samples (Fig. 8). Also, the addition of the cross-linker does not improve the results.

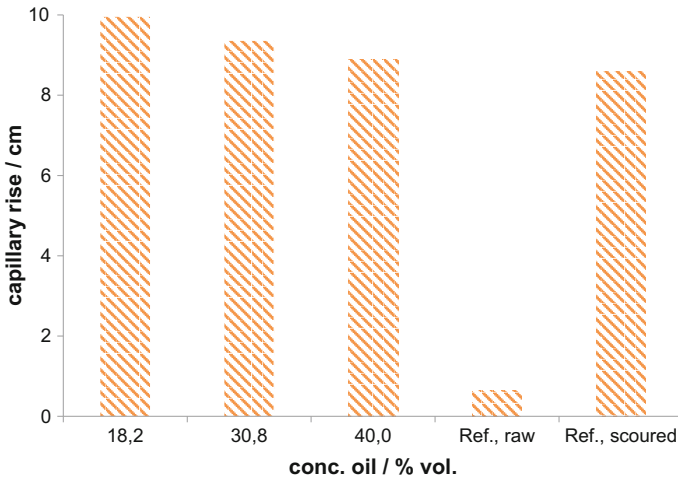


Fig. 6 Capillary rise on linen fabrics treated with oil from sunflowers of increasing concentration

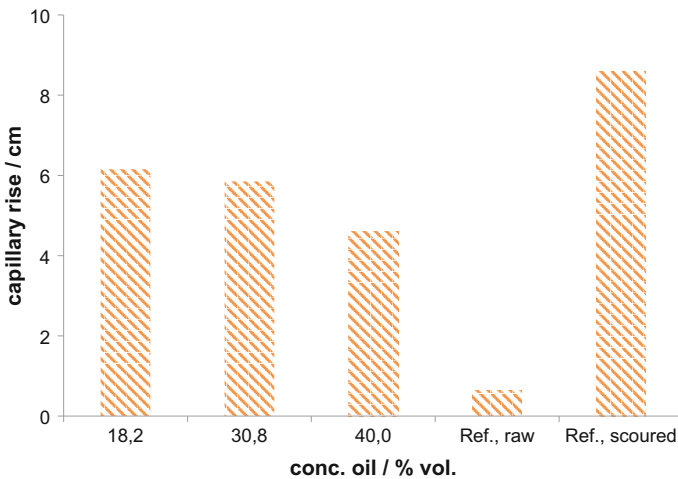


Fig. 7 Capillary rise on linen fabrics treated with oil from rapeseed of increasing concentration

The air permeability of the treated textiles is summarized in Fig. 9. It is clearly seen, that the application of polyisoprene containing recipes drastically reduces the air permeability compared to the untreated textile samples. In comparison, with application of the oil containing recipes, the air permeability is nearly on the same level as the untreated textile.

In summary, the application of polyisoprene recipes seems not to be the adequate method for pretreatment of fiber materials used in bio-based fiber-reinforced materials.

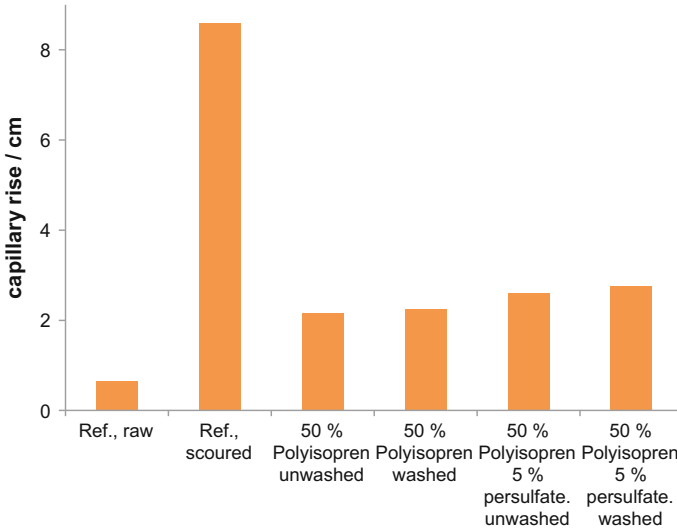


Fig. 8 Capillary rise of linen fabrics after finishing with different polyisoprene containing recipes

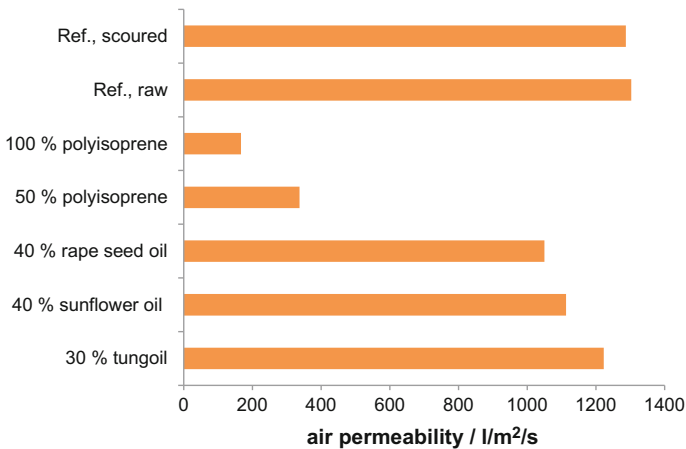


Fig. 9 Air permeability of fiber felts after different treatments. The air permeability is tested with 200 Pa. The concentrations are given in related to the finishing bath

2.1.3 Application of Surfactants

Surfactants contain both a hydrophilic and a hydrophobic part. For this, surfactants could be a promising category of compounds useful for hydrophobic treatment of textiles. This approach is especially attractive because the surfactants can be used as single component in a water-based recipe without addition of further additives.

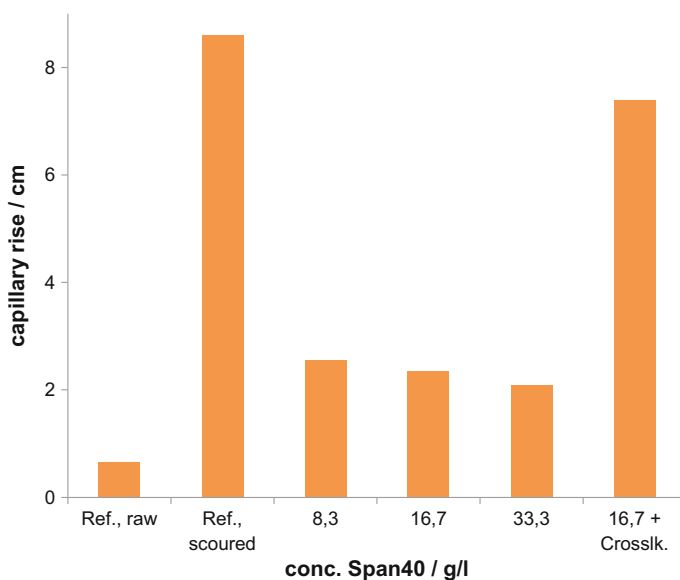


Fig. 10 Capillary rise of linen fabrics treated with different recipes containing the surfactant Span40

In actual investigations following three surfactants are evaluated: Span40, Tween20 and sodium oleate. These surfactants are solved in water and applied onto textiles by padding. Following, a drying step is performed at 100 °C.

Besides the application of pure surfactant solutions, also the addition of cross-linkers is investigated. This is done especially with the aim to bond the surfactants covalently to the fiber surface. For the surfactant sodium oleate, sodium persulfate is used as cross-linker. For the surfactants Span40 and Tween20, butanetetracarboxylic acid is used. However, for all applied recipes, this addition of cross-linkers leads to lower hydrophobic values on the treated textiles (Figs. 10, 11 and 12). Altogether, most suitable results related to the reached hydrophobicity are gained by recipes containing the surfactant Span40.

An alternative approach using natural components with hydrophilic and hydrophobic structural elements, is the application of hydrophobic amino acids, as Valin, Leucin, and Phenylalanin. The intensive investigation of those three amino acids for hydrophobic treatment of textiles is published elsewhere [17].

2.1.4 Hydrophobization of Staple Fibers

Besides textile fabrics, also staple fibers are evaluated in current investigations. These fiber materials are at first enzymatically treated for cleaning purposes and to remove unwished components from fiber surface. For this enzymatic cleaning

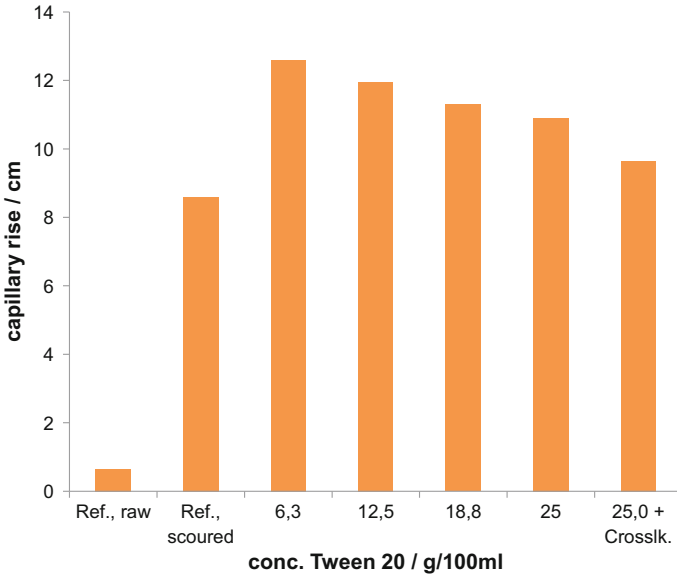


Fig. 11 Capillary rise of linen fabrics treated with different recipes containing the surfactant Tween20

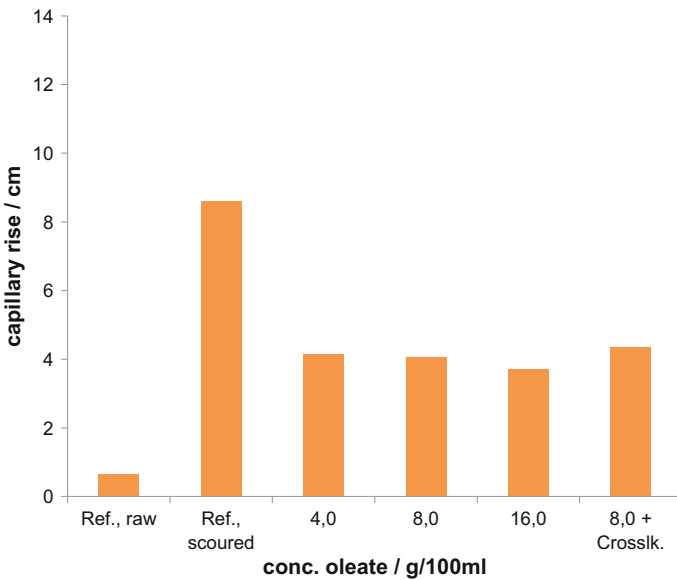


Fig. 12 Capillary rise of linen fabrics treated with different recipes containing sodium oleate

procedure, commercially products from the company Dr. Petry (Germany) are used—Perizym DBS, Perlavin NIC, Periplex AHL, Kollasol OCE.

The hydrophobic treatments of cleaned fibers are done by recipes containing fat alcohols. These fat alcohols are cross-linked with butanetetracarboxylic acid to alcohol groups on the fiber surface. The related cross-linking reaction is driven at temperatures of 180 °C. For this, the application of the aqueous recipe and the following drying at 100 °C can be separated from the cross-linking reaction. The cross-linking can be performed after use of the staple fibers for textile production or after incorporation into the reinforced material. A similar process with use of butanetetracarboxylic acid as cross-linker is described in the literature for cyclodextrin containing finishing solutions [18].

The alcohols dodecanol and octadecanol are used as hydrophobic component in the water-based finishing agent. Butanetetracarboxylic acid is added as cross-linker. Surfactants are applied to stabilize the suspension, evaluated are here the surfactants Tween 20, TritonX-100, Span40, sodium oleate, and sodium docedylsulfate. To reach also an improved sterical stability stabilization of the suspensions, also layered silicates (Laponite RD) are added to the recipes.

Finally, a finishing recipe containing besides octadecanol as hydrophobic agent also Laponite RD, sodium oleate, and butanetetracarboxylic acid are used, because of best stability properties.

2.2 Antimicrobial Finishing

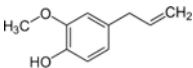
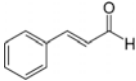
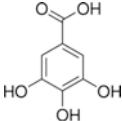
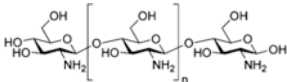
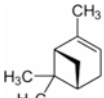
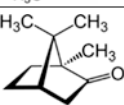
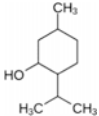
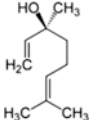
Different natural compounds are evaluated for antimicrobial finishing. These compounds belong to the classes of terpenoids, phenylpropanoids, and tannins (see Table 2). Also chitosan as a polymer from natural resources and antimicrobial properties is taken into account.

The antimicrobial activity of treated textiles is determined by using a testing system based on the dye Methyltetrazolium. The testing procedure is described earlier in detail [19]. Actual investigations are performed with bacteria suspensions of *E. Coli* and *S. Warneri*. The results are given in remaining bacterial viability [%] after contact with the textile samples in comparison with the bacterial viability without the presence of textile sample.

From the class of terpenoids, the compounds pinene and camphor are evaluated for their antimicrobial properties. These compounds are applied as ethanolic solutions or water-based dispersions in high concentrations. However, even after application of high concentrated recipes, no significant antimicrobial effect was observed. Probably the high vapor pressure of both compounds is responsible for this result, because due to this, after application onto the textile the concentration present on the textile is decreased rapidly.

From the class of phenylpropanoids, the compounds cinnamaldehyde and linalool are evaluated for their antimicrobial properties. Both compounds are used in a concentration of 10% and are stabilized in the aqueous recipe by addition of sodium

Table 2 Overview on natural substances with antimicrobial properties

Substance	Chemical structure	Type/comment
Eugenol		Phenyylpropanoid
Cinnamon aldehyde		Phenyylpropanoid
Gallic acid		Plant-based tannin
Chitosan		Modified polymer from natural resources
Pinene		Terpenoid
Camphor		Terpenoid
Menthol		Terpenoid
Linalool		Terpenoid

oleate. After application of cinnamaldehyde, the treated textiles exhibit a small antimicrobial effect—for *E. Coli* of 10 and 17% (for application onto linen- or cotton fabrics) and for *S. Warneri* of 38 and 40%.

From the class of tannins, the gallic acid is evaluated for its antimicrobial properties (Figs. 13 and 14). The gallic acid is applied with concentration in the range of 2.5–20 wt%. The solution is prepared with hot water and no further additive is necessary for stabilization. The reached antimicrobial effect is significant and increased with increased applied gallic acid. The determined effect is observed for both investigated bacteria but it is stronger against *E. Coli*.

In comparison with the other actually investigated antimicrobial agents, the gallic acid exhibits the best performance. In conclusion, antimicrobial treatments based on gallic acid could be recommended as part of a production process for bio-based fiber reinforced materials.

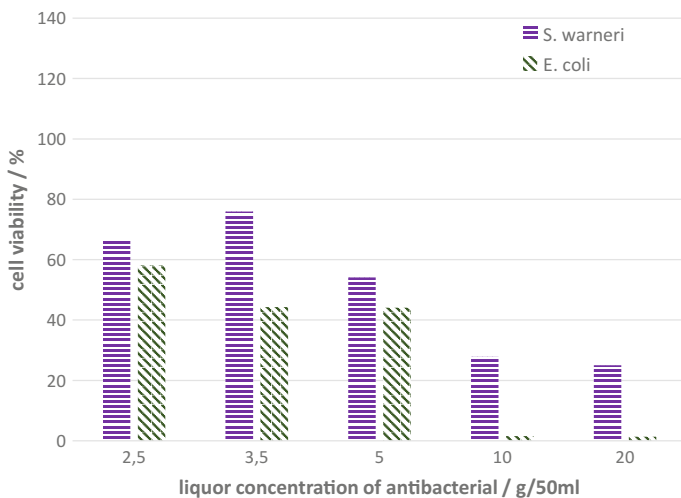


Fig. 13 Bacterial viability after contact with cotton fabrics treated with recipes of increasing concentration of gallic acid

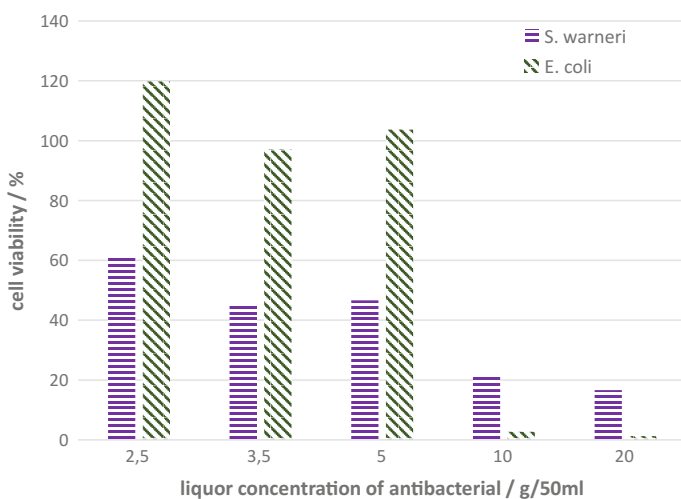


Fig. 14 Bacterial viability after contact with linen fabrics treated with recipes of increasing concentration of gallic acid

3 Developments Related to Textile Structures

3.1 Fiber Felts

Flax fibers are used to produce fiber felts. Before felt production, the staple fibers are enzymatically cleaned and finished with solutions of the surfactants Span 40 to gain hydrophobic properties. Altogether, two different fiber felts are realized. First, a thinner felt containing one layer and a weight of 160 g/m². Second, a felt containing a double layer and a higher weight of 208 g/m². By these experiments, it is shown, that also staple fibers from flax treated with the surfactant Span40 can be used in production of fiber felts. The hydrophobic properties of realized felts are determined by the capillary rise (Table 3). By this, the hydrophobic properties of produced fiber felts are clearly determined.

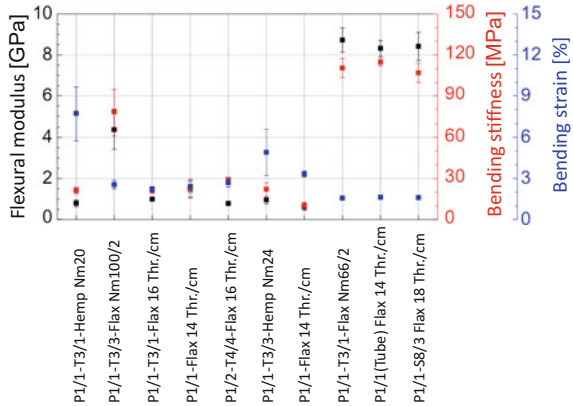
3.2 Fabric Production

The aim of investigations on fabric production is to realize a textile fabric construction containing a good wettability and adhesion to the polymer matrix in the composite material. For this, the production of a flat fabric is aimed, which can be regularly covered by the matrix. Here the cross points of warp and weft yarns should be in the same height as over parts of the fabric. Beside single layer fabrics, also double layer fabrics are investigated. The textiles are produced as narrow fabrics. As weft yarn, a cotton yarn is chosen, while as warp yarn flax is used. Different double layered fabrics are prepared and used for composite production. The mechanical properties of the produced composites are given in Fig. 15. Testing was accomplished by a method derived from DIN EN ISO 178, testing speed was 2 mm/min and sample dimensions were 80 by 10 by 4 mm. Bending modulus was calculated between 0.05 and 0.25% deformation. Each series consisted of five samples. The composites containing combined double Layer structures either from plain and twill or plan and satin show remarkable better mechanical performance data than the other combinations. However, on sample produced with the same weave but from hemp rather than flax showed poorer performance. Furthermore, the density of weft yarns and the yarn count seem to have a significant influence on the result, as can be seen by the twill satin combination. The much better

Table 3 Capillary rise of fiber felts treated with the surfactant Span40 in comparison with an untreated reference felt made of natural fibers

Time/capillary rise in mm	1 min	5 min	15 min	30 min
Single-layered felt	1	1.5	2	2
Double-layered felt	0	0.5	1	2
Reference	28	40.5	59	67.5

Fig. 15 Mechanical properties of composites prepared with differently constructed textile narrow fabrics (without finishing) and different weft threads, P: plain weave, T: twill weave, S: satin weave; warp was always cotton



performance of a plain hose compared to a doubled plain weave is remarkable, but cannot be completely explained. Possibly the relocatability of the layers during composite fabrication may lead to beneficial composite structures.

4 Summary and Conclusions

It can be concluded that natural fibers can be prepared in different ways to apply them in fiber reinforced composites. First, hydrophobic finishing to accomplish the requirements of the polymeric matrix can be applied easily by hydrophobic detergents but also with natural oils, if a more water stable hydrophobization is necessary. Antibacterial agents of a natural origin are suitable substances to mitigate biocorrosion in such textiles. Especially tannins turned out to be promising, due to their low vapor pressure, easy applicability, and surprisingly good effectiveness.

Finishing of textile surfaces can be achieved by the above-mentioned methods as well as finishing of staple fibers, so fiber felts from these pretreated fibers can be manufactured for the application in fiber reinforced composites.

Also, the structure of woven narrow fabrics has a significant influence on the mechanical properties of the resulting composites. Beside the weave pattern, the yarn number and material seems to be crucial as well. However, these effects cannot easily be explained.

Finally, the presented methods, chemicals, and concepts pave the way to fiber reinforced composites made from renewable and natural resources.

Acknowledgements This work is supported by the programme “Zentrales Innovationsprogramm Mittelstand” of the German Federal Ministry for Economic Affairs and Energy.

References

1. Soutis, C. (2005). Fibre reinforced composites in aircraft construction. *Progress in Aerospace Sciences*, 41, 143–151.
2. Trimble, B.J. (1989). Composite bicycle frame and production method US Patent, US4,850,607.
3. Cherrington, R., Goodship, V., Meredith, J., Wood, B. M., Coles, S. R., Vuillaume, A., et al. (2012). Producer responsibility: Defining the incentive for recycling composite wind turbine blades in Europe. *Energy Policy*, 47, 13–21.
4. Thakur, V. K., & Thakur, M. K. (2014). Processing and characterization of natural cellulose fibers/thermoset polymer composites. *Carbohydrate Polymers*, 109, 102–107.
5. Wambua, P., Ivens, J., & Verpoest, I. (2003). Natural fibres: can they replace glass in fibre reinforced plastics? *Composites Science and Technology*, 63, 1259–1264.
6. Schürmann, H. (2005). *Konstruieren mit Faser-Kunststoff-Verbunden*. Berlin: Springer-Verlag.
7. Bogoeva-Gaceva, G., Avella, M., Malinconico, M., Buzarovska, A., Grozdanov, A., Gentile, G., et al. (2007). Natural fiber eco-composites. *Polymer Composites*, 28, 98–107.
8. Pico, D., Wilms, C., Seide, G., & Gries, T. (2011). Natural volcanic rock fibers. *Chemical Fibers International*, 61, 90–91.
9. Larsen, K. (2009). Recycling wind turbine blades. *Renewable Energy Focus*, 9, 70–73.
10. Behr, D. (1991). *Wirkerei und Strickerei Technik*, 41, 7.
11. Textor, T., & Mahltig, B. (2010). A sol-gel based surface treatment for preparation of water repellent antistatic textiles. *Applied Surface Science*, 256, 1668–1674.
12. Erdumlu, N., & Ozipek, B. (2008). Investigation of regenerated bamboo fibre and yarn characteristics. *Fibres & Textiles in Eastern Europe*, 16, 43–47.
13. Kick, T., Grethe, T., & Mahltig, B. (2017). A Natural Based Method for Hydrophobic Treatment of Natural Fiber Material. *Acta Chimica Slovenica*, 64, 373–380.
14. Allen, S. (2011). *Oberflächenbehandlung von Holz*. Vincentz Network GmbH, Hannover: Klassische Techniken und Rezepte.
15. Schönemann, A., Eisbein, M., Unger, A., Dellmour, M., Frenzel, W., & Kenndler, E. (2008). Historic Consolidants for Wooden Works of Art in Saxony. *Studies in Conservation*, 53, 118–130.
16. Trueb, L. F. (2015). *Pflanzliche Naturstoffe*. Stuttgart: Borntraeger Verlagsbuchhandlung.
17. Grethe, T., Kick, T., & Mahltig, B. (2017). Sustainable controlling of hydrophilic properties of cotton and linen by application of amino acids. *The Journal of the Textile Institute*, 108, 436–439.
18. Martel, B., Weltrowski, M., Ruffin, D., & Morcellet, M. (2002). Polycarboxylic acids as crosslinking agents for grafting cyclodextrins onto cotton and wool fabrics: study of the process parameters. *Journal of Applied Polymer Science*, 83, 1449–1456.
19. Mahltig, B., Reibold, M., Gutmann, E., Textor, T., Gutmann, J., Haufe, H., et al. (2011). Preparation of silver nanoparticles suitable for textile finishing processes to produce textiles with strong antibacterial properties against different bacteria types. *Zeitschrift für Naturforschung B Chemical Sciences*, 66B, 905–916.

Investigation of the Elastic Properties of Weft-Knitted Metal-Reinforced Narrow Composites

J. Kaufmann, Y. Kyosev, H. Rabe, K. Gustke and H. Cebulla

Abstract Weft-knitted structures are very suitable for draping of different 3D forms because of their flexibility and the possibility to change the sizes of the different loops redistributing the yarn lengths at the different loops. The FEM analysis of such 3D forms requires the knowledge of the elastic behaviour and particularly the elasticity modulus and Poisson's numbers of the single cell at the different regions of the structure after the deformation. This work presents a method for numerical prediction of these values and experimental validations. The numerical prediction is based on several steps. First, the 3D geometry of the loop is generated based on a geometrical model for the loops. This geometry is then used, together with the properties of the yarns (wires) and the matrix for homogenisation calculations. The geometrical model is implemented into C++ Software tool within the TexMind suite, which exports it into WiseTex-XML format. This is then used within the TexComp software for homogenisation, where the method of inclusions is used to then compare the results with the experimental ones.

This paper was initially presented during the '7th World Conference 3D Fabrics and their applications, 2016, Ensait, Roubaix, France'.

J. Kaufmann · H. Rabe · K. Gustke · H. Cebulla (✉)
Department for Textile Technologies, Technische Universität Chemnitz,
Reichenhainer Straße 31-33, 09126 Chemnitz, Germany
e-mail: holger.cebulla@mb.tu-chemnitz.de

J. Kaufmann
e-mail: joerg.kaufmann@mb.tu-chemnitz.de

Y. Kyosev
Fachbereich Textil- Und Bekleidungstechnik, Forschungsinstitut Für Textil Und Bekleidung,
Hochschule Niederrhein, Webschulstr. 31, 41065 Mönchengladbach, Germany
e-mail: yordan.kyosev@hs-niederrhein.de

1 Introduction

Weft knitting is a long-known textile technology that is used for several fabrics for fibre-reinforced plastic parts and structures. Such weft-knitted structures are very suitable for draping of different 3D forms because of their flexibility and possibility to change the sizes of the different loops redistributing the yarn lengths at the different loops.

For producing weft-knitted fabrics usually glass or carbon fibres are used. These reinforcement fibres or rovings are often used as a weft yarn. In such cases, the warp yarn is mostly made of a thin polymer yarn like polyamide because of the insignificant mechanical impact of the resulting structure of the unidirectional single layer of the fibre-reinforced plastic (FRP).

Beside this classic reinforcement yarns also metal wires could be used for the reinforcement of a reinforced plastic. This material group is then called a metal wire-reinforced plastic (MRP). The significant advantage of such a material is the ductile material failure of the metal components instead of the brittle behaviour of classic reinforcement products. By combining different types of MRP with FRP with the relevant matrices systems the failure could be optimised between the two states of brittle and ductile. In this paper, a numerical model for calculating the quasi-static engineering constants of a single layer of a metal wire-reinforced plastic is shown and verified with first experimental data.

This FEM analysis of such weft-knitted 3D forms requires the knowledge of the elastic behaviour and particularly the elasticity modulus and Poisson's numbers of the wire material and the single cell inside the polymer matrix at the different regions of the structure after the deformation. This work presents a method for numerical prediction of these values for different wire volume fractions and includes a first experimental validation. Hence, the numerical prediction and the experimental validation is based on several steps. First, the E-Modulus of the wire is measured according to DIN EN ISO 6892-1 and the Poisson's number is assumed according to literature data. After that, the 3D geometry of the weft loop is generated based on a geometrical model for the loops. This geometry is then used, together with the properties of the yarns (wires) and the matrix for homogenisation calculations. The geometrical model is implemented into C++ Software tool WeftKnit3D within the TexMind suite [1], which exports it into WiseTex-XML format [2–4]. This is then used within the TexComp software for homogenisation [5], where the method of inclusions is used for computation of the elasticity parameters. The computed values are compared with the experimental results.

2 Material Data

For the weft-knitted structure, a wire made of aluminium AlMg5 with a diameter of 0.2 mm is used. The matrix system is a bio-based epoxy resin (entropy super sap CPM/CPF-CPL) that cures with additional temperature. The mechanical properties

Table 1 Mechanical properties of the semi-finished products

	E	G_{12}	μ_{12}
Wire	70.0	26.1	0.34
Epoxy	2.5	0.9	0.35

of these semi-finished products were determined according to DIN EN ISO 6892-1 and DIN EN ISO 527-4 in the linear elastic zone with 70.0 GPa for the aluminium and 2.5 GPa for the epoxy resin. The Poisson’s number of the wire is assumed with 0.34 and the shear modulus of this isotropic semi-finished product is then calculated with 26.1 GPa. Regarding the epoxy resin, the Poisson’s number was also experimentally determined with 0.35 and the shear modulus was calculated with 0.9 GPa (see. Table 1).

3 Modelling

The geometry of the weft-knitted structure is created with a geometrical model as explained in [6, 7]. This model gives more flexibility about the definition of the loop geometry compared to the classical models proposed in [8–12]. The distances between the key points of the loop can be defined as presented in Fig. 1 (Fig. 1 left side). It is based on the definition of the contact points between the yarns and the width and height of the loops as they can be measured from the weft-knitted sample per graph paper (Fig. 1 right side). The model is implemented as a C ++ code within the TexMind suite at the software WeftKnit3D.

Figure 2 presents modelled 3D geometry of 4×4 loops of the aluminium wire structure. This can be exported in the XML Format of WiseTex software [2, 3] as presented in Fig. 3.

The WiseTex file can then be used for calculation of the elastic properties—elasticity modulus and Poisson’s numbers of composite material using TexComp software [5] based on the method of inclusions.

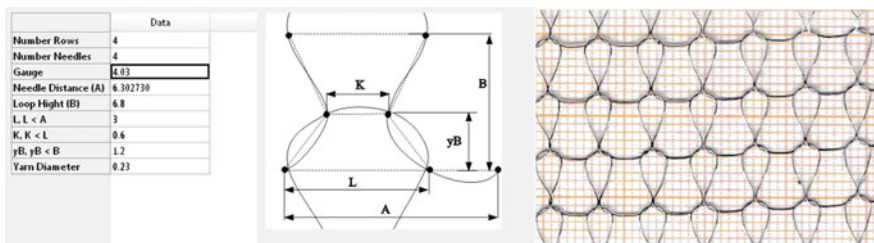


Fig. 1 Geometrical model and its parameters as entered in the WeftKnit3D (left side). Determination of the geometrical parameters per graph paper (right side)

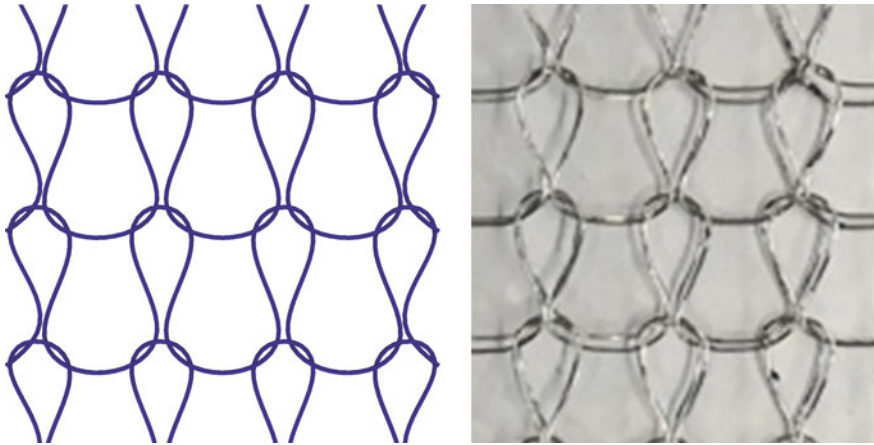


Fig. 2 3D geometry of 4×4 loops created with TexMind WeftKnit3D and photo of the real structure

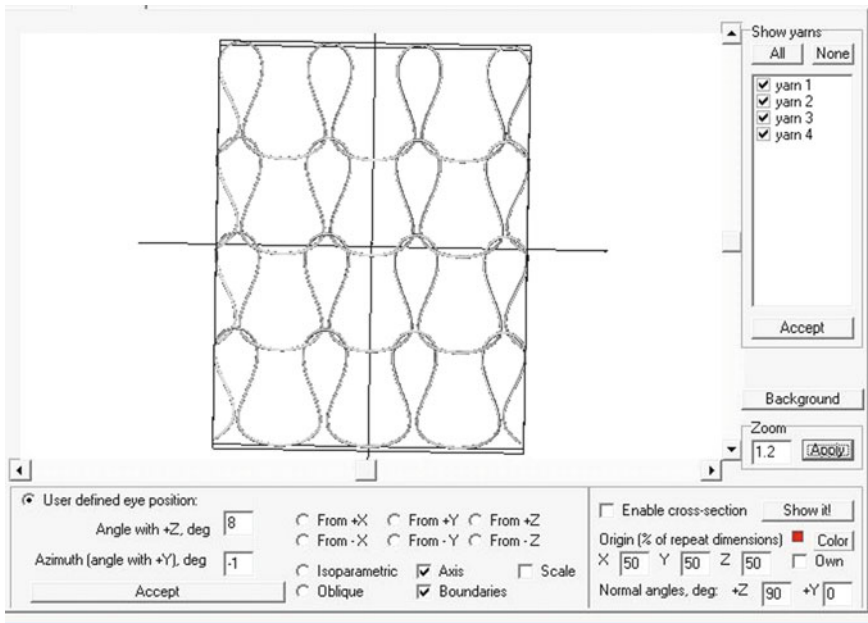


Fig. 3 3D geometry of 4×4 loops imported in WiseTex

In the practical case, several layers of weft-knitted wire structures are placed one after another in the composite material, as visualised by LamTex (Fig. 4). As the layers are based on the same geometry, these are considered later through the different wire volume fractions during the homogenisation.

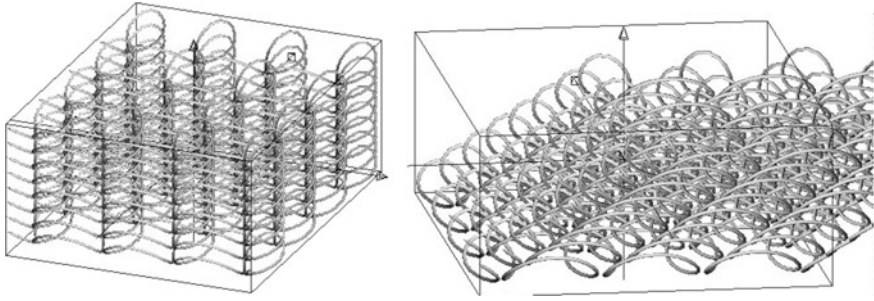


Fig. 4 Multi-layered weft-knitted structure, visualised by LamTex on the base of the created model. Left—eight layers, right—eight layers by maximal nesting

4 Numerical Results

The homogenisation was performed using the standard method of inclusions, implemented in the TexComp software. Figure 5 presents the simulated Poisson's number ν_{12} of the structure, as function of the wire volume fraction, according to which, with increasing the volume fraction, the Poisson's number slightly reduces.

The elastic modulus (E_1) of the composite in the main direction increases linearly with the increasing volume fraction (Fig. 6).

The simulated wire-reinforced plastic with a wire volume fraction of 35% shows a very low anisotropy with varying values between 3.801 and 3.805 MPa, which could be negligible and an isotropic behaviour could be assumed (Fig. 7).

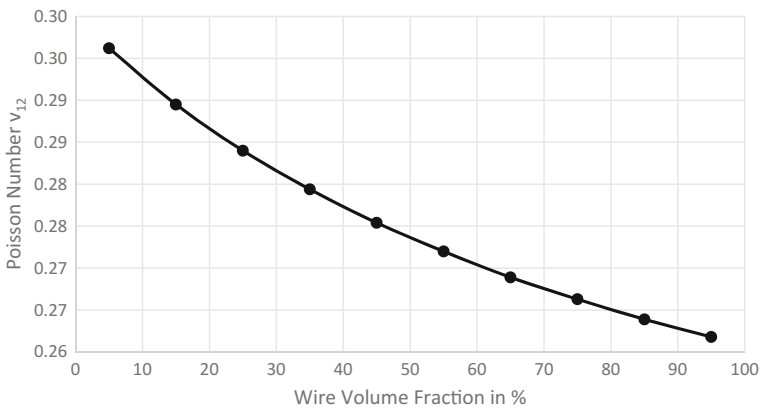


Fig. 5 Calculated by homogenisation (Method of Inclusions within TexComp) Poisson Number ν_{12} at different volume fractions

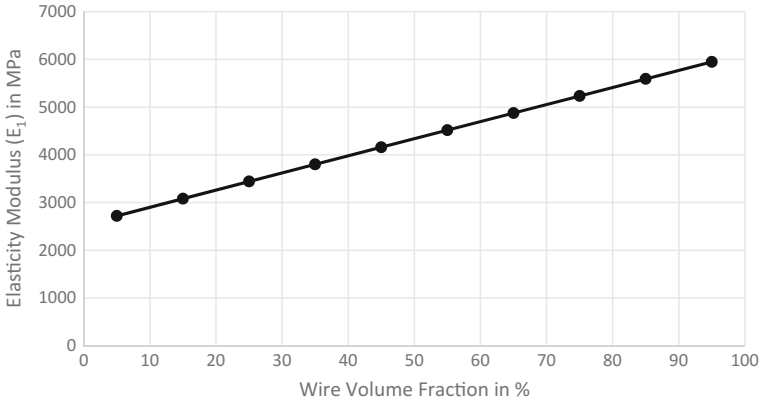


Fig. 6 Elasticity modulus (E_1) calculated by homogenisation (Method of Inclusions within TexComp) at different volume fractions

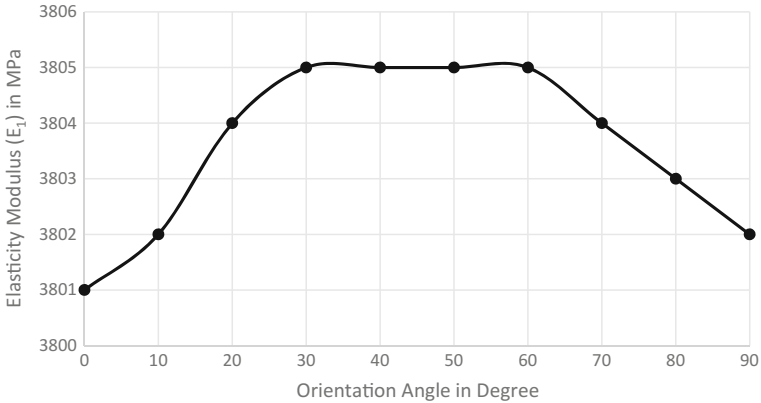


Fig. 7 Elasticity modulus as a function of the orientation of the testing direction—Calculated by homogenisation (Method of inclusions within texcomp)

5 Sample Production

In the first step, the aluminium circular weft-knitted structures (see. Fig. 8) were produced by using a circular knitting machine ‘Harry Lucas RR2-Z-10’. Process-related thin oil film is added on the metal wire that had to be removed afterwards in a bath of acetone for having a good adhesion between the wire and the epoxy resin.

The cleaned wire weft-knitted structures are processed in a manual wet lamination process and cured in a hot press with 85 °C and 3 bar for 60 min. For producing the test specimens, the circular weft-knitted structure is flattened; hence, the MRP consists of two layers of wire structure. From each of the resulting MRP

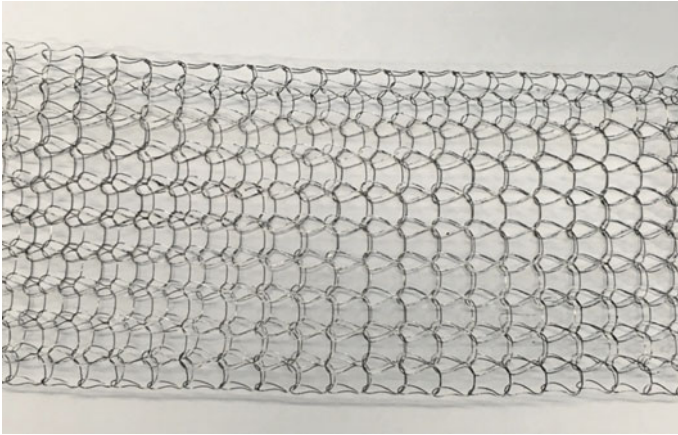


Fig. 8 Sample of 0.2 mm aluminium circular weft knitted structure with a diameter of 8.0 mm

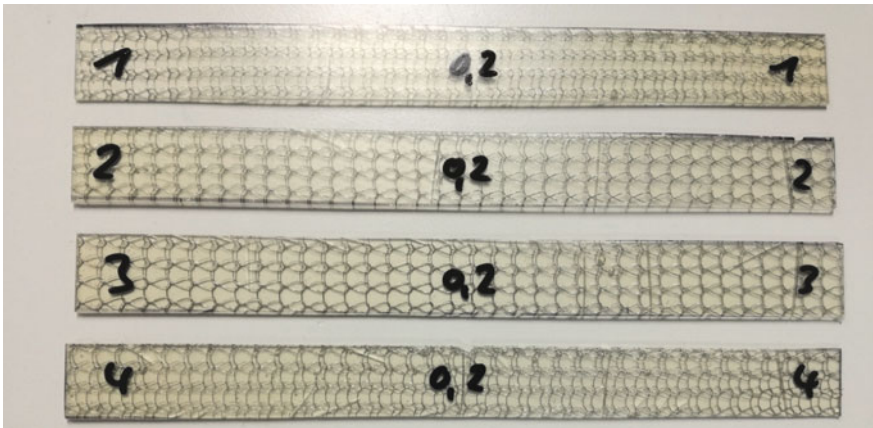


Fig. 9 Sample of 0.2 mm aluminium circular weft-knitted structure with epoxy matrix for machinery testing with a width of 25 mm and a length of 250 mm

parts, two test samples with the dimension of 25 mm × 250 mm (see Fig. 9) were cut by using water jet-cutting technology. Due to the big true stain at the border zone of the flattened weft-knitted fabric, the two samples are cut from the middle of the structure for having less influence on the mechanical properties.

6 Experimentation

The experimental setup consists of a tension testing machine Zwick Z100 where the test specimens are fixed at both sides with a resulting test length of 150 mm and a measuring area of 25 mm × 50 mm. With a testing speed of 2 mm/min and a start

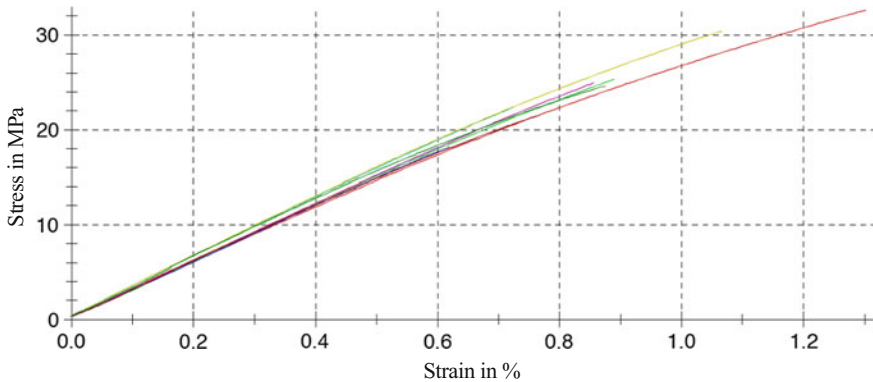


Fig. 10 Stress–strain curve of the tested wire-reinforced polymer

force of 10 N, the samples were loaded until failure. The resulting stress–strain curves for the 12 samples are shown in Fig. 10.

The resulting E-Modulus of the experiment is 3.050 MPa with a standard deviation of 124 MPa and the measured wire volume content is approximately 5%. According to the calculation performed in Chap. 4 and Fig. 6, a simulated E-Modulus of 2.720 MPa is resulting for the supposed MRP and a deviation of 10%.

7 Conclusions

The simulation model is a robust and valid method for calculation of the mechanical properties of a metal wire-reinforced plastic made of a circular weft-knitted fabric. With this numerical model, parameters like wire thickness, wire volume fraction and orientation angle could be calculated. First, experimental tests show that the FEA model describes the material behaviour of a metal wire-reinforced plastic with a sufficient accuracy.

In further material tests, samples with a different amount of weft-knitted layers and wire thickness should be investigated. This is necessary to have a further validation of the models accuracy for other parameters. Furthermore, samples with different orientation angles of the weft-knitted fabric should be analysed.

References

1. Kyosev, Y. TexMind WeftKnit3D, Product Information. www.texmind.com
2. Lomov, S. V., et.al. (2012). Wisetex, department MTM, KU Leuven. <http://www.mtm.kuleuven.be/Onderzoek/Composites/software/wisetex>

3. Lomov, S., Gusakov, A., Huysmans, G., Prodromou, A., & Verpoest, I. (2000). Textile geometry preprocessor for meso-mechanical models of woven composites. *Composites Science and Technology*, 60(11), 2083–2095.
4. Lomov, S., et.al.(2013). Meso-level textile composites simulations: Open data exchange and scripting. *Journal of Composite Materials, Online First*. doi:[10.1177/0021998313476327](https://doi.org/10.1177/0021998313476327)
5. Huysmans, G., Verpoest, I., & Van Houtte, P. (1998). A poly-inclusion approach for the elastic modelling of knitted fabric composites. *Acta Materials*, 46(9), 3003–3013.
6. Moesen, M., Lomov, S., Verpoest, I. (2003). Modelling of the geometry of weft-knit fabrics. In: Tech—Textil Symposium. Frankfurt.
7. Kyosev, Y., & Renkens, W. (2009). Modelling and visualization of knitted fabrics. In X. Chen (Ed.), *Modelling and predicting textile behaviour*, (Series 94). Woodhead Publishing Limited.
8. Leaf, G. A. V., & Glaskin, A. (1955). The geometry of a plain knitted loop. *Journal of the Textile Institute*, 45, T587–605.
9. Göktepe, O., & Harlokc, S. C. (2002). Three-dimensional computer modelling of warp knitted structures. *Textile Research Journal*, 72, 266–272.
10. Hart, K., De Jong, S., & Postle, R. (1985). Analysis of the single bar warp knitted structure using an energy minimization technique: Part I: Theoretical development. *Textile Research Journal*, 55(8), 489–498.
11. Wu, W. L., Hamada H., & Maekawa, Z. (1994). *Journal of Textile Institute*, 85(2), 199–213.
12. Choi, K., & Lo, T. (2003). An energy model of plain knitted fabric. *Textile Research Journal*, 73(8), 739–748.

Part II

Braiding

Investigation About the Properties of HMHT Fibre Ropes and New Machine for Continuous Production of Ropes with Connection Between Core and Mantle

Andreas Kretschmer and Christoph Müller

Abstract The intention of this paper is to give a short overview of the results of the doctoral thesis of Dr.-Ing. Andreas Kretschmer. The scope of the work includes among others two predominant parameters of the braiding process with major influence on the rope's bending properties. Furthermore, a newly designed braiding machine is introduced.

1 Introduction

Modern fibre ropes, made of High-Modulus-High-Tenacity (HMHT) fibres, are used in a wide array of fields. They are utilised in sports like climbing and sailing as well as in various industries like fishing and mooring lines for offshore oil rigs or ships. Recent applications, that start to utilise the benefits of high-performance fibre ropes, are the replacement of wire ropes in conveying applications and robotics. Each application has its own needs. Thus, special rope constructions for individual purposes are very useful. The aspects/parameters that predominantly influence the characteristics of the product are the following.

- Basic construction of the rope (single layer or multilayer construction, nominal diameter)
- Stranding operation (laid or braided)
- Type of machinery
- Number of strands, floating length, twist angle of the strands, braiding or laying angle

A. Kretschmer (✉)

Faculty of Mechanical Engineering, University of Technology Chemnitz,
Chemnitz, Germany
e-mail: andreas.kretschmer@mb.tu-chemnitz.de

C. Müller

Professorship of Materials Handling and Conveying Engineering, 09126 Chemnitz, Germany

- Strand-twisting-method (direction, opening or closing in the braiding process)
- Yarn properties (fibre thickness, yarn count), yarns per strand
- Fibre materials, coating of the yarn, strand and/or the rope

However, still more influencing parameters can be found. Even minor changes to some of these parameters can result in major deviations of the end products' properties, like breaking load, elongation, flexibility/bendability and cyclic-bending-over-sheave (CBOS) lifetime. Thus, a lack of exchangeability between different rope manufacturers is obvious. Even if the ropes of two manufacturers are of the same material, diameter and design, there is no guarantee that they have comparable characteristics. Therefore, the authors did a research to figure out the underlying reasons. For this study, interviews with several fibre-rope manufacturers were carried out. The following questions have been asked.

Q.1 'Do you have a special production standard for each of your ropes?'

Q.2 'Is this your own standard?'

Q.3 'Does the fibre producer give you advice how to use the different fibres?'

Q.4 'In which direction do you produce your rope, do the braids get opened or more closed?'

The following sums up the frequently given answers.

A.1 Yes, for our default ropes we use standards, but our clients tell us what the rope should look like, how it should feel, which elongation it should have and which breaking strength it should have. For these parameters, we got our own catalogue, based on our experiences. Otherwise, we would have to do numerous experiments to get the wanted properties.

A.2 For default ropes we use our own standards. There is no DIN Standard for e.g. the twist angle of the strands.

A.3 The fibre producers do not give detailed advice. Sometimes we buy the strand ready for braiding only with a safety twist applied on it or with a specific twist we or our customer wanted. Sometimes we turn the strand on our own or we use parallel untwisted yarns as a strand.

A.4 Mostly we produce the ropes by opening the strands. This means that the strand is overtwisted. During the braiding process, the strand is turned back to the angle desired. The customers often wish for a special handling. They generally do want a 'round' rope with a big breaking load or an extra smooth surface. Specific studies were not carried out often. Frequently rope design is done by experience. This knowledge is passed from generation to generation and rarely can be found in standards or books.

Keeping that in mind, it is obvious that ropes of different origin cannot have identical properties. More studies have to be conducted, taking into account the stated determining parameters. The present study is only a starting point. And the customer must know that not only the handling has to be well. Good handling does not come with long CBOS lifetime automatically, especially in conveying applications.

2 Predominant Parameters: Twist Angle (Yarns and Strands) and Floating Length

Heinze showed in 2013 that there is an optimal yarn-twist-angle in terms of abrasive resistance (Fig. 1) [1]. This twist angle was assumed to be adequate for the implementation in fibre ropes of the respective yarn type. Kretschmer transferred the results in 2016 to the strand-twist-angle approach [2]. Furthermore, a comparison of ropes with floating length two or three was conducted. For the latter, a specific braiding machine was designed and implemented. This braiding machine also allows the simultaneous braiding of core and mantle as well as an in-between connection in a quasi-continuous process.

To analyse the effects of the strand-twist-angle the following method was applied. In order to reach the optimal strand-twist-angle, the strand needs to be pre-twisted with regard to the subsequent braiding process. The strands undergo an additional twist each time the carrier of the spool makes one round on the braiding machine. As an example for a braiding length of $f = 40$ mm, the carrier of the spool will take 25 rounds for one metre. Consequentially, the strand undergoes 25 additional twists per metre (tpm). So, a strand with 30 tpm (in the rope) is theoretically reached by two ways. On the one hand, a pre-twisted strand with 5 tpm can be subsequently turned further in the braiding process to the 30 tpm. Or, on the other hand, an overtwisted strand with 55 tpm is opened back up to the 30 tpm. However, since the working space of the available twister is limited (20 tpm up to 140 tpm), strands with low tpm numbers can only be achieved by twisting back the strand in the braiding process.

Fig. 1 Yarn-on-Yarn test cycles over the twist angle of Technora® T221 [1]

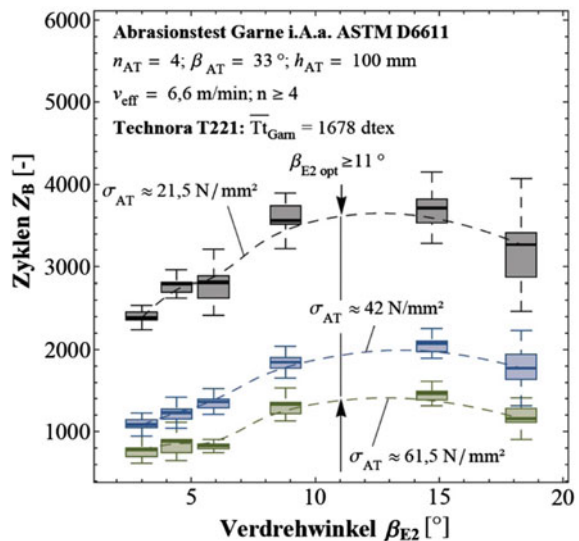


Table 1 CBOS testing parameters referring to Fig. 2

General Setup (parameters kept constantly):						
Yarn type Technora® T221, yarn count $T_{\text{yarn}} = 1670$ dtex, Nominal diameter $d_n = 6$ mm, 12-strand-rope with 11 yarns per strand, braiding length $f = 40$ mm, Load $F_p = 10$ % of F_B						
Specific Setup (parameters varied):						
Label	G1	G2	G3	G4	G5	G6
Floating length	two	two	two	two	three	three
Twist of the strand β_2	11°	11°	11°	11°	11°	11°
Braiding direction of the strands	N.A.	opened closed	closed	closed	closed	closed
Profile of the sheave	round	round	round	Optimized	round	Square
Rope orientation on the sheave	N.A.	N.A.	0° 180°	180°	N.A.	N.A.

For the analysis of both, floating length and strand-twist-angle, several ropes were produced and analysed in terms of CBOS testing. While the optimal yarn-twist-angle $\beta_2 = 11^\circ$ (Fig. 1) equals 49 tpm for the respective yarn type, it was uncertain if the opening or closing in the braiding process is of influence to the end product. Therefore, two different pre-twists on the strands had been added. For comparison of the floating length, a control group of ropes (floating length two) was manufactured on a different braiding machine. The latter and its design were chosen in accordance with [1]. The general setup for all produced ropes, irrespective of the floating length, was used (Table 1).

3 Results of the CBOS Testing

The analysis starts with the parameter set G1 (Fig. 2) which refers to the so-called control group (floating length two, optimised strand twist) and does neither distinguish the braiding direction nor the rope orientation on the sheave.¹ It can be seen that the median of the group reaches up to almost 23 k bending cycles. Also, the box and the whiskers show a considerable deviation of the data.

In the parameter set G2 the differing performance of the ropes with different twisting strategies in the strands (opening versus closing) is obvious. It can be seen that clustering the data of G1 according to the twisting strategy shows no intersection of the two groups. The green upper group refers to a closed twisting within the braiding process whereas the lower red group refers to an opened twisting.

In parameter set G3 only the values of set G2 are contained, where the twisting was closed. A further clustering of the data according to its rope orientation on the sheave shows a clear separation into two split groups again. The 180°-side on the

¹As it will be stated below, the rope orientation on the testing sheave is of major influence since the ropes cross section is not symmetric.

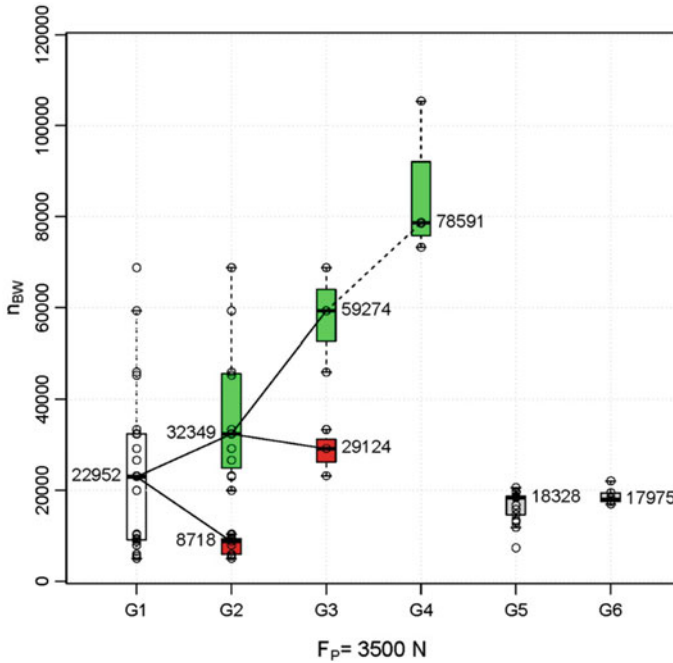


Fig. 2 Global comparison of all ropes tested, referring to Table 1 [2]

sheave proves of better performance as the 0° -side of the rope. While testing it became obvious that there are two different sides in the closed-strand-manufactured rope (denoted 0° and 180° , Fig. 3a–c). A simple test of the flexibility/bendability of the rope proofed this assumption (Fig. 3d–f). The 180° -side shows better bendability, which is assumed the cause for the better performance in CBOS testing.

Parameter set G4 represents data obtained from measurements of closed strands and the 180° -side of the rope in combination with an adapted sheave groove geometry. The CBOS lifetime increased to a median of 78.6 k cycles, which was expectable due to the gentle bending in the optimised groove.

Parameter sets G5 and G6 only distinguish within the operated sheave, more precisely within the groove geometry. As it can be seen from (Fig. 4a) the cross section of the rope with the floating length three is more of a quadratic shape. Therefore, in the set G6 an adapted groove geometry, namely a square groove, was operated. However, no significant difference in between G5 and G6 can be observed. In general, the floating length three ropes only around 18 k bending cycles, which is within the box values control group G1. In accordance to [2] (Fig. 1) an optimal strand-twist-angle of $\beta_2 = 11^\circ$, which equals 49 tpm, was verified also for floating length three (Fig. 4b).

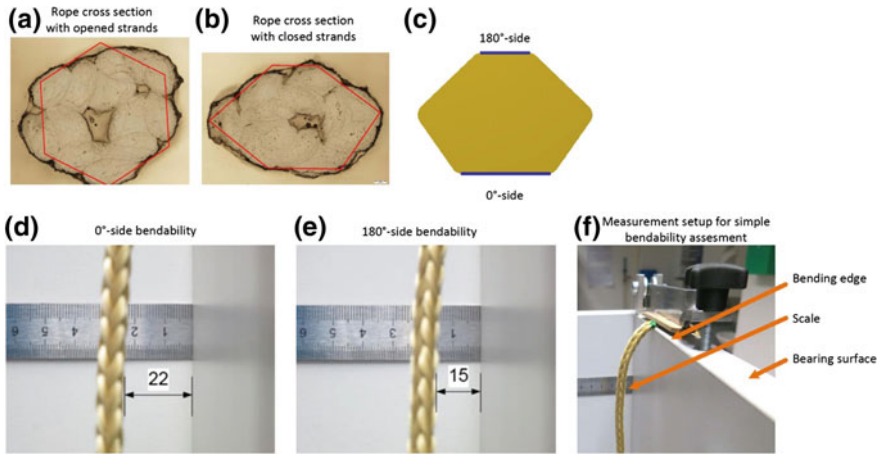


Fig. 3 Bendability and side dependency in a braided rope [2]

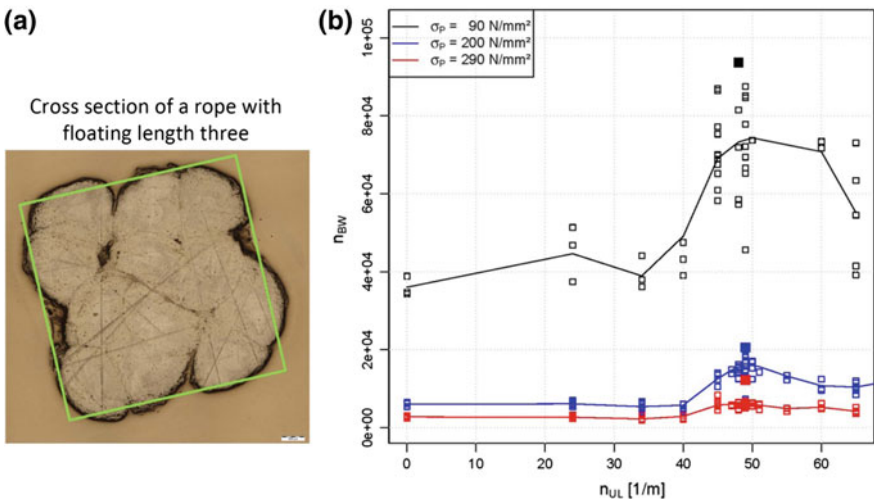


Fig. 4 Cross section of a rope with floating length three and CBOS cycles over strand twist (tpm)

4 Simultaneous Core-Mantle-Braiding Machine

For the purpose of this study, a braiding machine was designed for floating length three. It is now possible to produce a core rope, a core-mantle rope simultaneously and a core-mantle rope with a connection in between. The machine is fully implemented and in use at University of Technology Chemnitz to produce special ropes with floating length three or to give ropes an additional mantle.

5 Conclusions

The present study shows that the floating length is of major influence on the possible lifetime of ropes in CBOS testing. Another major influence was determined with the twisting angle of the strands in the braided rope and the way it is reached; by opening or closing the strands. The authors show that closing the strands is beneficial in terms of bending lifecycles. Also, the optimal twisting angle is limited to a narrow range.

Another finding was the two sides of the rope with major influence on bendability and therefore on CBOS lifetime. The symmetrical (or unsymmetrical) ropes cross section resulting from the braiding process as well as its general shape was identified as important in terms of both, handling and lifetime. Hence, this subject should be focused in further research. A necessity, therefore, is the integral assessment of the process parameters like production speed, tension of the strands, rope forming after the braiding-point and several others.

Acknowledgements The study was granted by the BMBF via the 'Unternehmen Region' program. Financial support is gratefully acknowledged.

References

1. Heinze, T. (2013). *Zug-und biegewechselbeanspruchte Seilgeflechte aus hochfesten Polymerfasern*. Doctoral thesis.
2. Kretschmer, A. (2016). *Einflussfaktoren auf die Lebensdauer laufender Faserseile*. Doctoral thesis.

Interlacement Variations in the Alternative Covering Technology D-3F

Daniel Denninger, Maik Berger and Yordan Kyosev

Abstract The following study deals with the main interlacement variations and possibilities of the new covering technology D-3F. There are well-known processing technologies for the covering of extruded hoses or other tubular cores in order to increase their radial stiffness, like braiding or spiraling. The main disadvantage of the spiraling layers is the limitation in stability of the single windings, caused by missing interlacements. An advantage might be the fiber deflections and the resulting directed mechanical properties in combination with the achieved productivity. On the other hand, it is impossible to cover cores with changing diameters and resulting local angles higher than the friction angle of the current materials. These forming cores or profiles are often covered by the more suitable braiding technology. Braided structures can be produced stably based on proper interlacement between the two or three thread systems inside. In fact, the braiding technology has its limitations concerning the productivity. The interlacement of the thread, which stabilizes the structure from one side, is the reason for broken filaments as a result of the deflection of the threads from the other side. The number of broken filaments is proportionally increasing with the speed of the braiding process. In order to combine the advantages of both spiraling and braiding into a new productive and fiber-friendly technology, a new machine concept was developed and patented. The new weaving-like binding structure “D-3FG” (“Denninger-3Faden Geflecht”) combines the properties of two layers and weaving-like interlacements.

D. Denninger (✉) · M. Berger
Technical University Chemnitz, Professorship of Assembly and Handling Technology,
Reichenhainer Straße 70, 09126 Chemnitz, Germany
e-mail: daniel.denninger@mb.tu-chemnitz.de

Y. Kyosev
Faculty of Textile and Clothing Technology, Hochschule Niederrhein,
Research Institute of Textile and Clothing, Webschulstrasse 31,
41065 Mönchengladbach, Germany
e-mail: yordan.kyosev@hs-niederrhein.de

1 Introduction

1.1 *State of the Art—Covering Processes*

The idea of fiber reinforced rubber or plastic materials evolved in bionics. In such composites, different materials are combined in a purpose-oriented manner in order to obtain improved or new macroscopic properties against the starting constituents and to control undesirable side effects. Humankind recognized the outstanding potential of fiber composite materials as a construction element from early on. For example, already 10,000 years ago, a combination of fiber materials (straw or reeds) and matrix (clay) served as a building material [1, 2].

Today, especially hose or preform applications require the use of high-performance fibers in order to withstand numerous mechanical and thermal, and often also chemical and electrical stresses. There are established extruding technologies for the manufacturing of tubular semifinished fiber reinforced rubber or plastic products. These products are usually shaped, assembled, and finished in follow-up processes. Depending on the expected stresses, different textile covering technologies are used for the reinforcement of these intermediates [3].

In order to increase the pressure resistance or radial stiffness, the individual high-performance fibers are initially combined, as rovings or yarns. They are fed to the chosen textile process on specific bobbins and applied in its characteristic manner. Depending on the chosen method, these have process-related binding structures and therefore variable mechanical properties as well as different shaping and handling ability. Particularly for the production of profile-shaped or final-contoured hoses or preforms, only a few textile processes could be established [1, 4]:

- knitting (meshed systems)
- wrapping/winding/spiraling (non-mesh systems, without interlacements)
- braiding (non-mesh systems, with interlacements)

The knitting processes are not taken into account for all further. Although the knitted fabrics are distinguished by a comparatively good handling ability as well as damage resistance, due to potential fiber stretching, the multiple fiber deflections, and changing fiber orientations lead to proportionally decreasing mechanical properties. In addition, the production speed is comparatively low.

In contrast, especially the multilayered spiraled hoses or wound preforms have a constant fiber orientation per layer. These layers are characterized by minimal fiber deflections on the micro- and mesoscopic level and can, therefore, be ideally force-flow-oriented to increase the mechanical properties of a hose or component. The main disadvantage of spiraling is the limitation in stability of the single windings caused by missing interlacements. The shaping and handling of these intermediates is therefore only ensured to a limited extent since the individual layers tend to slip. Regarding the fiber deflections and the resulting mechanical properties in these intermediates that may be an advantage. On the other hand, it is impossible

to cover profiles with changing diameters and in the same local angles higher than the friction angle of the current materials. For a more detailed look at the winding process, please refer to the relevant technical literature at this point [2–4].

Forming cores with cross section changes or hoses for high-pressure applications are often covered by the more suitable braiding technology. Braided or weaving-like structures can be produced stable based on proper interlacement between the two or three thread systems inside. Weaving-like structures essentially include the tissues and braids. In theory, they are also defined by a concrete number of layers. In contrast to the spiraling, these layers are interconnected by crossings (interlacements). These interlacements are the reason for significantly higher fiber deflections. With these deflections, proportionally decreasing mechanical properties with simultaneously good resistance to damage are to be expected due to potential fiber stretching and easy handling. Above all, the slipping can be largely avoided, but not completely eliminated, with the corresponding configuration of the braiding parameters. The advantage of a braided structure is relative shape stability even without a core [5].

In particular, the braiding process offers excellent conditions for the gentle processing of high-performance and synthetic fibers for the economical covering of extruded hoses, other tubular cores or even semi-finished fiber products or final-contoured preforms. The comparatively high fiber deposits of the braiding technique are ideally combined by the layer-wise overlapping of forming cores with a simultaneously large production repertoire for geometrically flexible design. For the realization of a reproducible and force-oriented fiber orientation, three thread systems are usually processed into a triaxial UD braid [6].

Main part of conventional production processes are circular or radial braiding machines, based on the maypole system with mechanically forcible laying of threads. In fact, braiding has its limitation concerning the productivity. The interlacement of the threads, which is stabilized by the structure from one side, is the result for broken filaments. The number of broken filaments is proportionally increasing with the speed of the braiding process [7].

Rotary braiding machines—especially lever arm braiding machines in accord with the system “Horn”—are not used. The advantage of the system “Horn” as opposed to the maypole system, is the constant tangential bobbin arrangement in combination with the characteristic laying of the threads as well as the accompanying fiber friendly and position-parallel processing of the braiding material. At the same time, the increased braiding speed, due to the machine concept with the opposite rotational movement of two rotors, is an enormous advantage for economical serial production [8].

1.2 Interlaced Composites Winding Technology D-3F

The technological synthesis for integrating a third thread system lead to a novel and textile-technological manufacturing process with a new weaving-like binding

structure as a combination of laying and braiding or weaving, “D-3FG” (see Fig. 1). Mentioned binding structure combines the properties of two layers and weaving-like interlacements. Through the interlacements, these layers are arranged one inside the other and fixed in their respective orientation. In analogy to the braiding angle, the angle of the laying threads can be varied in some manner over the take-off speed and can thus be used for the orientation of the reinforcing fibers [9]. Along with that, the drive concept of the new rotor braiding system D-3F was patented (file reference 102014016832.8) with the title “*Flechtvorrichtung und Flechtverfahren zum Überflechten eines Flechtkerns*” [10].

The result of the logical interpretation of the new laying technique in a rotary braider system, based on the system “Horn”, is shown in the following Fig. 2. The rotary braiding system “D-3F” matches a targeted combination of all characteristics typical for braiding in a system concept that is suitable for covering extruded hoses, other tubular cores or even preforms with a tangential alignment of bobbins and parallel laying of threads. Thus, the covering of cores are produced by “over-braiding” with the new weaving-like bonding structure.

In the proposed system concept, the weft thread bobbin carriers are fastened to slides, which are mounted on guide rails and are again mounted on a fixed slide track at a defined distance from one another. To enable the shedding of the warp threads, the slider web must be provided with slots at equidistant intervals. The openings of the opposing slots are aligned with each other, Fig. 3. For the production of the new weaving-like binding structure, warp threads are provided by the third thread system. These warp threads are drawn off from an outer and stationary filament carrier set by an individual thread positioning element. These elements are oscillating from a lower to a higher latitude with a collision-free passage of the weft bobbin carriers and are thereby laid above or below the intersection points of the weft threads. The opening and closing of a compartment take place in the time windows in which the slides are not guided over the slits of the guide rails.

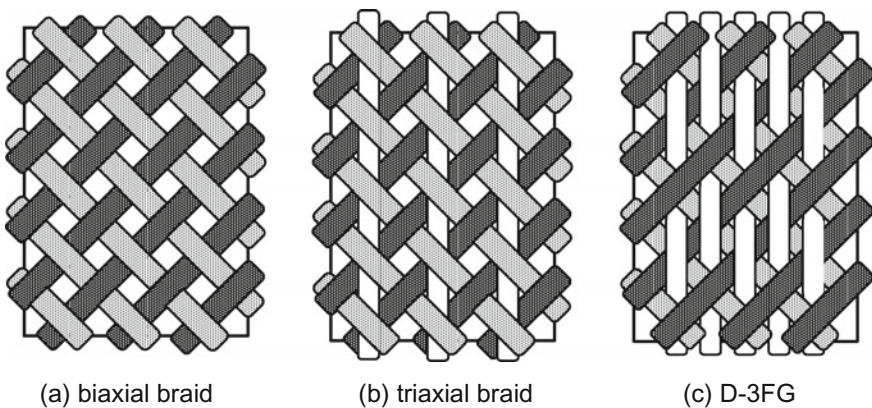


Fig. 1 Biaxial, triaxial, and new D-3FG

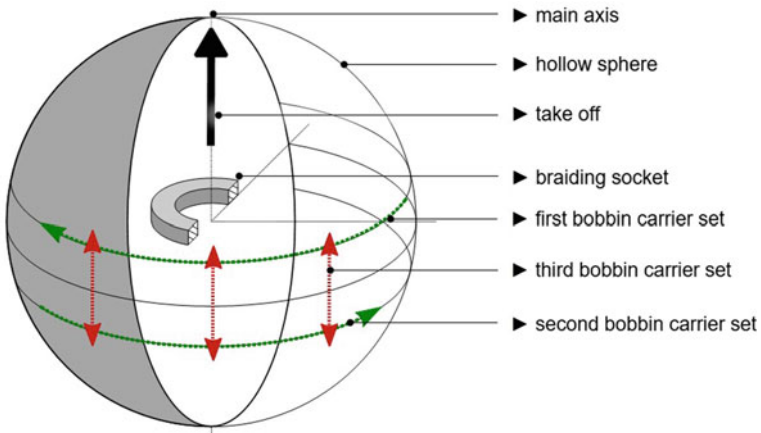


Fig. 2 Rotary braiding system “D-3F”

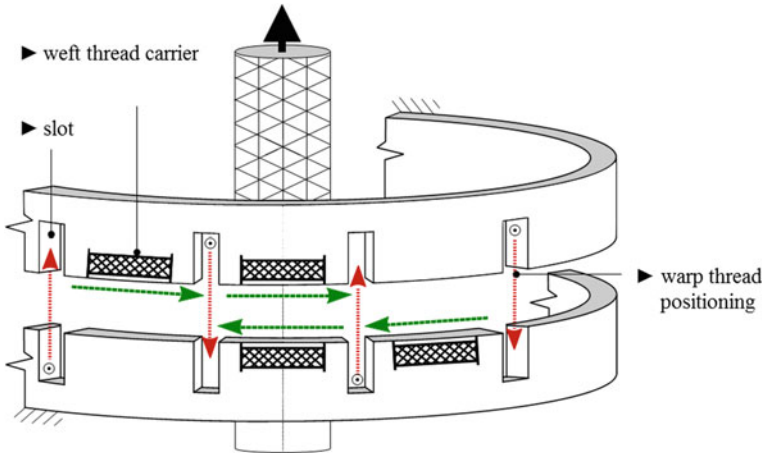


Fig. 3 Schematic structure of the rotary braiding system D-3F

2 Design Studies and Possibilities of D-3F

2.1 Basic Winding Options

In addition to the synthesis and simulation of the rotary braiding system D-3F, design studies have been performed to evaluate further possible binding structures and their potential applications. In particular, the variation of the movement of the warp threads permits a defined range of configurations for the binding variation of the alternative covering technology. However, such design studies lead to a

nonpractical computational effort in the used CAE/CAD system. On these grounds, the development of an effective solution for the design and visualization of the possible binding structures became necessary.

Due to the existing functionalities for the calculation and visualization of braided products with known binding structures, the software TexMind Braider [11] was used as a basis for development. The clear analytical description of the thread paths leads to a real-time calculation of chosen settings. In addition to the image of braided products, known binding structures can be set variably, taking the parameter configurations such as braidiness, cross sections, number of fibers, coloring, etc. into consideration. Furthermore, the generated 3D geometries can be exported in FEM tools and processed for computations. Calculations for the output quantity, taking into account the parameter settings and other machine-specific feasibility estimates, are already implemented.

Figure 4 shows the prototypical version of the TexMind Braider D-3F, based on the conventional calculation core. This toolbox already provides all necessary functionalities for the design of theoretically possible binding structures with three thread systems. This allows the mapping of the whole bandwidth of the alternative covering technology by neglecting machine-specific restrictions. Therefore, the implementation of the binding variables is built up systematically, using a matrix-based input. The superimposed layers of oppositely oriented weft thread systems are generally present (Fig. 4: red, green).

In principle, an interlacement with the aid of a warp thread from the warp thread system is possible at each intersection of these opposing threads. Each column of the matrix corresponds to a series of intersections in a horizontal arrangement. By filling the matrix, the binding structure takes place over a defined number of rows according to the following definition:

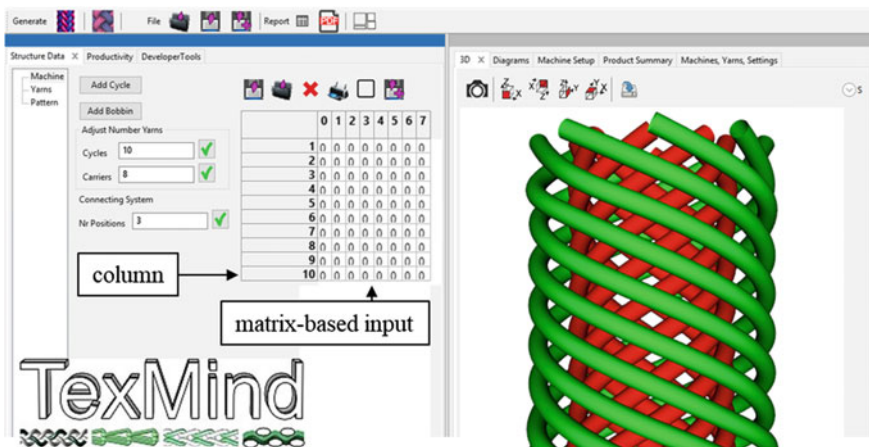


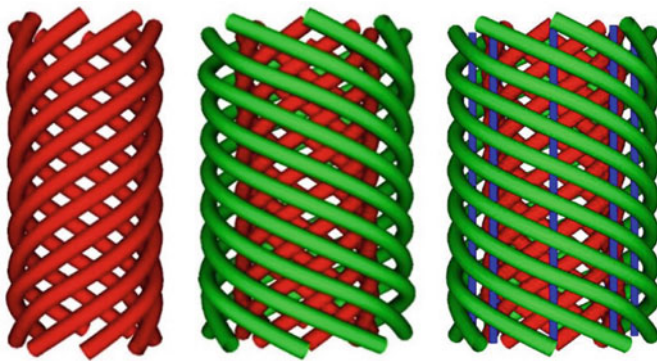
Fig. 4 Using the new toolbox in TexMind Braider for design studies of the textile structures

- 0 means no interlacement
- 1 means the interlacement of one warp thread system
- 2 means the interlacement of both warp thread systems.

The structure of the rotary braiding system D-3F allows the fabrication of a variety of weaving-like binding structures as well as the winding or spiraling of a guided core with rotating warp thread systems (spiraling carriers). The weft thread system can also be used with the aid of an appropriately fixed position of the thread, laying units for the removal of noninterlaced 0 degree threads as shown in Fig. 5. Consequently, the following general options of thread laying without interlacements are given:

- one thread system (winding single layer with multiple carriers)
- two thread system (winding two layers S, Z)
- two thread system (winding one layer S or Z and 0 degree without interlacement)
- three thread system (winding two layers S, Z, and 0 degree without interlacement)

In addition to the shown options for the processing of three thread systems, it is generally possible to build up structures for the processing of an arbitrary number of thread systems. The applicable restrictions are derived from the technical and economic boundary conditions and their feasibility. Especially the size of the bobbins and their carrier arrangements are responsible for the kinematic and kinetic effects which are used for the constructive design. However, there is no general technological restriction.



(a) one layer, z (b) two layers, z & s (c) two layers & 0 degree

Fig. 5 General options without interlacements based on three thread systems

2.2 Adding Interlacements Between Layers

An important advantage of the rotary braiding system D-3F is the stationary arrangement of the warp thread system. In particular, this stationary arrangement permits the use of large bobbins with an appropriate thread supply for the compensation of undesirable thread length and thread tension changes. This controlled thread supply is required for high process speeds with low fiber damage due to friction-related relative movements on the thread guide elements by the laying devices.

In order to combine the advantage of windings and weaving-like structures, the two layers (Fig. 5b) have to be fixed by adding interlacements with these weft threads. General options with interlacements, based on three thread systems, are shown in the following figures:

Figure 6: One weft thread system placed on a ring is winding by rotating and one stationary warp thread system is interlacing by going up and down

Figure 7: Two weft thread systems placed on rings are winding **by rotating in opposite directions** and one stationary warp thread system is interlacing both rotating systems

Figure 8: Two weft thread systems placed on rings are winding **by rotating in opposite directions** and one stationary warp thread system is interlacing both rotating systems in a softer way

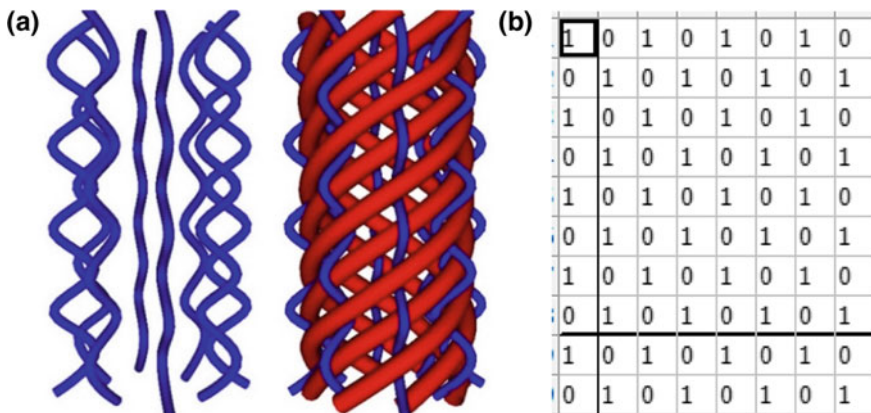


Fig. 6 a 3D Model with one layer interlaced with the second system completely through the thickness b column for the structure

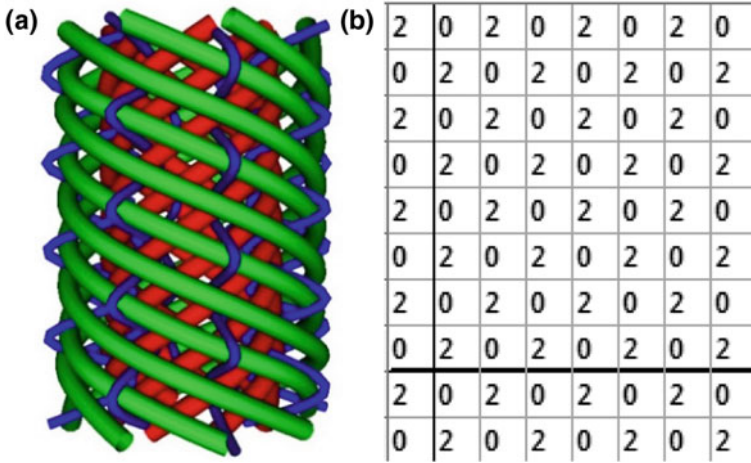


Fig. 7 a Two layers interlaced with the third system completely through the thickness b column

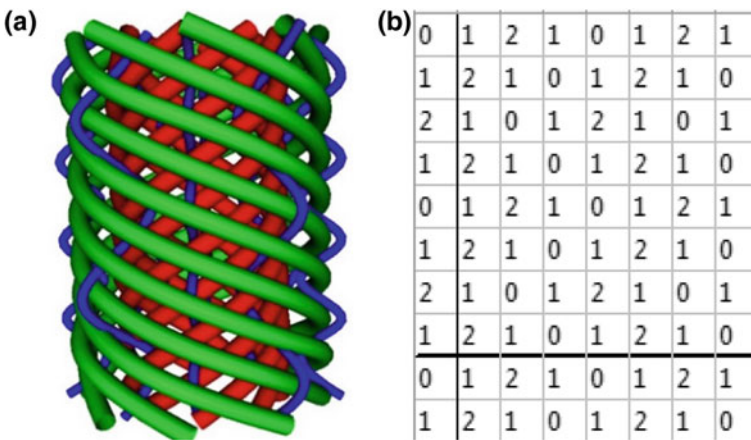


Fig. 8 a Two layers with intermediate interlacement, similar to the English weave b column

2.3 Possible Applications and Economical Aspects

As the previous figures and examples demonstrate, the D-3F technology is able for covering extruded hoses or other tubular cores by spiraling with two thread systems in its basic counter rotational configuration. By using the additional warp thread system for interlacing these two layers, the advantages of both spiraling and braiding can be combined. For this combination, the warp thread system could consist of very thin connecting threads. With this method, the interlacements will

not integrate countable crimp, similar to the triaxial UD braid. The interlacing threads will keep the covering structure stable and the two layers will be connected to each other.

Concerning the design of a prototype and the necessary exploration of the rotary braiding system D-3F, it is planned to apply servomotor drives for the laying devices of the warp threads. With these motion controlled systems, the frequency and the depth of the interlacements can be selected and adjusted according to the matrix-based input of the TexMind Braider D-3F. In order to keep the structure stable, the binding structure could be adjusted by building up more interlacements during the covering process of cores with conical cross sections. Main advantage of the rotary braiding systems is the technical implementation of the braiding process by mentioned laying devices. In contrast to the conventional maypole braiding machines, the bobbin carriers—which have a high and dynamically moving mass—are only performing in a constant rotational motion. The necessary changes of the moving direction for the production of interlacements are carried out by laying devices. For that reason, the rotary braiding machines can show a significantly higher productivity rate than conventional maypole braiding machines.

Another advantage to be mentioned is the constant tangential bobbin arrangement. The rotary braiding system D-3F was developed especially with a focus on the bobbing arrangement, space between the carriers possible calibers. Thereby, weft threads with comparatively high diameters could be used. Therefore, the system is designed to achieve an economically and technologically effective machine to cover even medium diameters of composite profiles for pultrusion or later lamination. This advantage is accompanied by a significant disadvantage. The system D-3F has a more stringent limit on its potential size. The braiding machine D3F with its current conceptual design and constant tangential carrier arrangement would, as a consequence, not be ergonomic, if it has to handle 48 or more carriers. That is why the overbraiding of thicker profiles will probably remain an area of the radial braiding machines with 144, 288, and more carriers.

3 Conclusions

This paper showed the main interlacement variations and possibilities of the new covering technology D-3F. This alternative covering process with a new circular drive concept to generate an innovative shifting motion is a result of the recombination of required sub-functions which are needed to manufacture the best possible and ideal binding structure. The technological synthesis for integrating a third thread system led to a novel and textile-technological manufacturing process with a new weaving-like binding structure as a combination of laying and braiding or weaving. Several structures are visualized with a new module of the TexMind Suite—named TexMind Braider D-3F. The analysis of the virtual samples shows, that the D-3F has potential in replacing spiraling, braiding or even composite winding in some class of composites, where the braiding diameter is not too high and where the

interlacement between two layers can improve the stability of the structure. The investigation of the economical and mechanical efficiency of the D-3F machine and the resulting covering or composite structures still have to be verified with experimental investigations, which include the realization of a prototype of the machine and the production of samples. For this upcoming task, the authors are open for cooperation.

References

1. Cherif, C. (2011). *Textile Werkstoffe für den Leichtbau—Techniken—Verfahren—Materialien—Eigenschaften* (1 Aufl). Heidelberg/ Dordrecht/ London/ New York: Springer-Verlag. ISBN 978-3-642-17991-4.
2. AVK-Industrievereinigung Verstärkte kunststoffe. (2014). *Handbuch Faserverbundkunststoffe/ Composites: Grundlagen, Verarbeitung, Anwendungen* (4 Aufl). Wiesbaden: Springer-Verlag. ISBN: 978-3-658-02754-4.
3. Ehrenstein, G. W. (2006). *Faserverbund-Kunststoffe—Werkstoffe—Verarbeitung—Eigenschaften* (2 Aufl). München/Wien: Carl Hanser Verlag GmbH & Co. KG. ISBN 978-3-446-22716-3.
4. Ermanni, P. (2007). *Composites technologien* (Version 4.0). Zürich: Vorlesung Eidgenössische Technische Hochschule Zürich.
5. Birkefeld, K. (2013). *Virtuelle Optimierung von Geflecht-Preforms unter Berücksichtigung von Fertigungsaspekten*. Dissertation, Universität Stuttgart—Fakultät für Luft-und Raumfahrttechnik und Geodäsie, Stuttgart.
6. Erber, A., Birkefeld, K. & Drechsler, K. (2009). The Influence of Braiding Configuration on Damage Tolerance of Drive Shafts. In *SEICO 09*, Paris.
7. Kyosev, Y. (2014). *Braiding technology for textiles* (1st ed.). Woodhead Publishing Series in Textiles. London: Elsevier Science & Technology. ISBN: 978-0-85709-135-2.
8. Douglass, W. A. (1964). *Braiding and braiding Machinery*. London: Cleaver-Hume-Press Ltd.
9. Denniger, D. (2016). Prozessorientierte Synthesemethodik am Beispiel der neuartigen Verlege-technik “D-3F” zum Überflechten mit drei Fadensystemen. Dissertation, TU Chemnitz—Fakultät für Maschinenbau, Chemnitz. ISBN 978-3-944640-80-8.
10. Denniger, D., & Berger, M. (2016). Flechtvorrichtung und Flechtverfahren zum Überflechten eines Flechtkeims. Patentschrift, TU Chemnitz, Deutsches Patent-und Markenamt, 2016-01-28, DE 10 2014 016 832 B3.
11. Texmind UG—Software and Consulting for textiles. (2017). *Home*. verfügbar unter <http://www.texmind.com/wp/> (Zugriff 27 May 2017).

Development of Machine Configuration for T- and I-Profiles and Their Topological Modelling

Yordan Kyosev and Katalin Küster

Abstract This work presents a numerical investigation about the production and simulation of braided products with complex cross section. The geometrical modelling of tubular and flat braids is already well described in the literature and implemented in several scripts and commercial software like TexMind Braider. In the literature are reported as well several works about the modelling of 3D braided structures, created using different 3D braiding techniques. For the case of complex maypole braiding machine with horn gears are reported some works with the software TexMind Braiding Machine Configurator, which emulates the carrier motion for the creation of the 3D geometry of the braids. This work presents evaluation of the possibilities of the software for designing machines with large number of horn gears in custom arrangements and at the same time presents the results of a large set of tests of the possible combinations for arrangements of horn gears with different size for the production of complex multilayer braided structures like T-, and double-T-profiles. The investigation shows, that the possibilities for carrier arrangement are directly connected with the topology of the tracks of these carriers and for structures with multiple tracks more empty places in the arrangement is required. For the cases, where for such structures suitable machine configuration and carrier arrangement is found, an simplistic 3D geometry of the braid is generated and can be used for FEM calculations, relaxation and other computations of the properties.

Y. Kyosev (✉) · K. Küster

Faculty of Textile and Clothing Technology, Research Institute of Textile and Clothing (FTB), Hochschule Niederrhein—University of Applied Sciences, Mönchengladbach, Germany
e-mail: yordan.kyosev@hs-niederrhein.de

K. Küster

e-mail: katalin.kuester@hs-niederrhein.de

1 Introduction

The most common uses of the braiding are for flat and tubular braiding, where the tubular braiding becomes very popular in the form of radial braiding for covering of mandrels of different form (overbraiding). The braiding of solid profiles, in the contrary, is less developed and used mainly for gaskets and only single reports and patents about production of larger solid braids are known in the literature [1, 2]. An extended, very detailed overview of the development of the 3D braiding technique can be found in the recently published chapter of Bogdanovich [3]. Some steps of the development of 3D maypole braiding machines are reported in [4–6] as well as Cartesian braiding [7], and hexagonal (lace-type) braiding [8].

The well-known 3D maypole braiding machine build by August Herzog [6] have a setup of horn gears with four slots, where each switch and gear has individual drive. This technique gives a high flexibility but is too expensive. In the patent literature and some conferences, machines can be found with horn gears, placed in special configuration, different from tubular or flat, so that profiles can be produced. In [1] some initial states of software of the company TexMind are reported, which allows emulation of the machine configuration with arbitrary placement of the horn gears. The algorithms and next development of this ‘Braiding Machine Configurator’ are reported in [9].

The current paper presents numerical experiments, performed with the current version of the TexMind Braiding Machine Configurator [10] with the goal to determine possible configurations of maypole braiding machines with constant paths for production of profiles with complex cross section for composites. On several patents, for paths of such machines, the carriers are seldom given. The arrangement of carriers for complex paths is not a trivial task, but in the current case this can be solved using simulation and checking each configuration.

2 Simulation Model Fundamentals

The basic principle of the Configurator is explained in [9]. Each part of the machine, which participates in the braid building is created virtually as an object, which is programmed in C++ language. For this, the classes Carrier, HornGear, Switch and YarnType are defined.

The class HornGear defines the properties of the gears, like coordinates of the centrum, angular velocity, radius and number slots. Each horn gear can carry only one carrier per slot. The carrier keeps the information about the yarn type which is placed in it. The switch is a connection place between two horn gears and can have ‘transfer’ or ‘keep’ state. The object ‘Machine’ consists of lists of horn gears,

carriers, yarn types and switches and has algorithms for saving, loading and plotting of the current state of the machine, but its most important part for the simulation is the algorithm for emulation of the motion of the machine. The algorithm moves the carrier in the time depending on the angular velocity of the horn gears until one switch is found. If the switch is in 'transfer' state, the carrier is removed from its current slot and transferred to the corresponding slot of the connected gear. Swiping the carrier coordinates in the vertical direction allows creation of simplistic 3D braid. This virtual braid is not dense enough to be used for mechanical properties simulation using FEM Method for instance, but good enough to evaluate the directions and positions of the yarns and to be used for evaluation of the machine configuration.

3 Graphical User Interface

The graphical user interface is created with the wxWidgets platform [11] using wxCrafter as IDE [12] (Fig. 1). It allows placement of the gears with different number of slots at any position, their rotation and motion with the mouse, as well of carriers with different colours. Macros for setting the gears of tubular and flat braiding machines and machines with rectangular arrangement of the gears are provided as well.

4 Concept and Simulation of Machine for T-Profile

The configuration of standard *flat* braiding machines is used as basic part for the concept and simulation of machines for T-profiles. The flat braiding machine has one track and builds a braid, which is placed in one plane. An example of such machine is presented in Fig. 2 and the idealized braid for this configuration in Fig. 3.

The track for the flat braid from Fig. 2 can be extended at each of the gears, placing an extension with several four-slot gears and turning gear at the end with five (or three) slots. Figure 4 presents such a configuration with arrangement of the carries 1Full–1 Empty, which would lead to a structure with floating length of two [1]. Actually, the configuration in this way would not work, because before filling all the carriers around the complete track, one carrier should be placed in a position, which is currently free, but will be used from a carrier in a neighbour staying gear (red carrier). In this meaning 1Full–1 Empty arrangement will lead to collision and is not possible for this configuration (Fig. 4, left). Carrier arrangement 1Full–3 Empty can be applied for this configuration (Fig. 4, right) and the simulated 3D

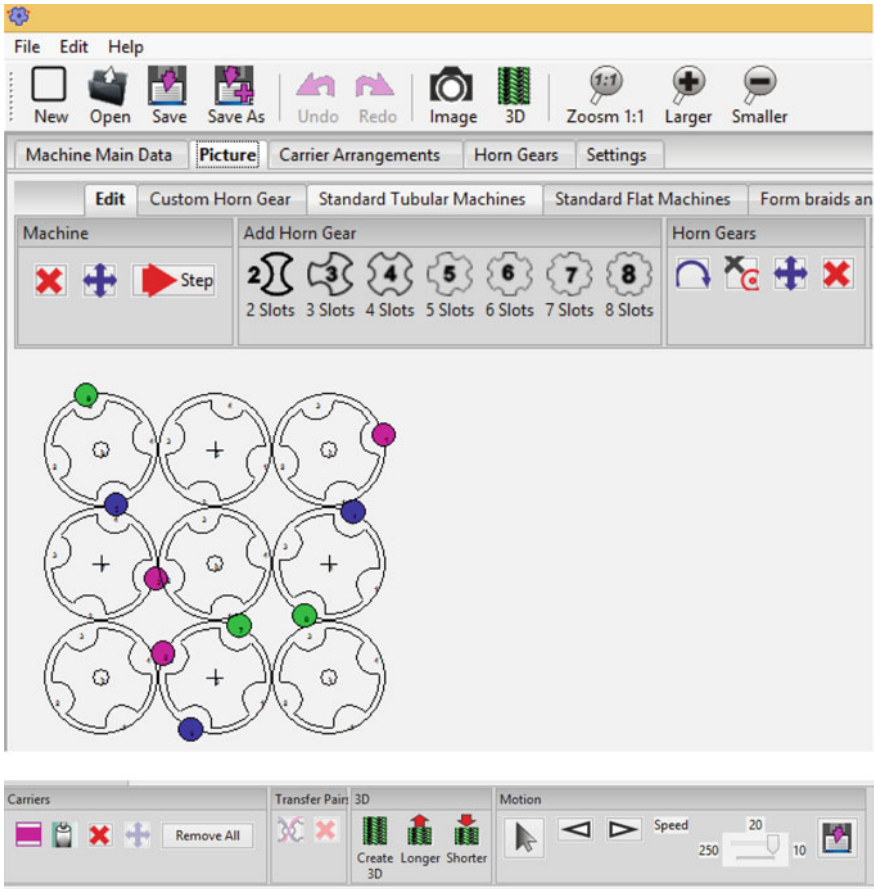


Fig. 1 Graphical User Interface of the TexMind Braiding Machine Configurator. Up—the common view with the machine and gear commands; down—the right-hand side part of the menu with tools for placement of carriers, creation of 3D braid and motion emulation

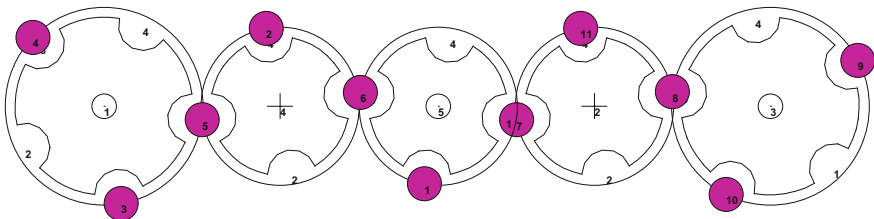


Fig. 2 Configuration of a flat braiding machine with 5-4-4-4-5 Slot gears with 11 carriers

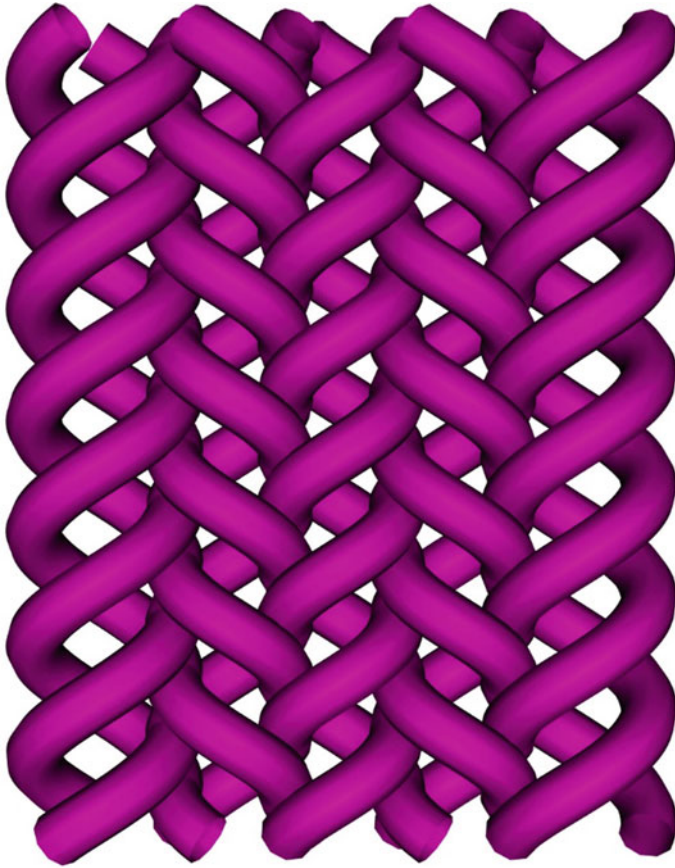


Fig. 3 Simulated braid for the configuration of Fig. 2

geometry of the braids is presented in Fig. 5 in top and side view. There are two disadvantages using 1Full–3 Empty carrier arrangement for this configuration. First—less numbers of carriers are available for the braiding, so for production of profiles with required dimension double more gears and respectively machine size are required compared to the case, 1Full–1 Empty would be possible. Second—at arrangement 1Full–1 Empty and four-slot horn gears the pattern will be with floating length of one—like a plain braid. This means, that the yarns have the largest possible undulations at the interlacement points. As well known, carbon, glass and basalt fibres have significant lower properties in crimped state, so this should be taken into account and investigated before building such machine.

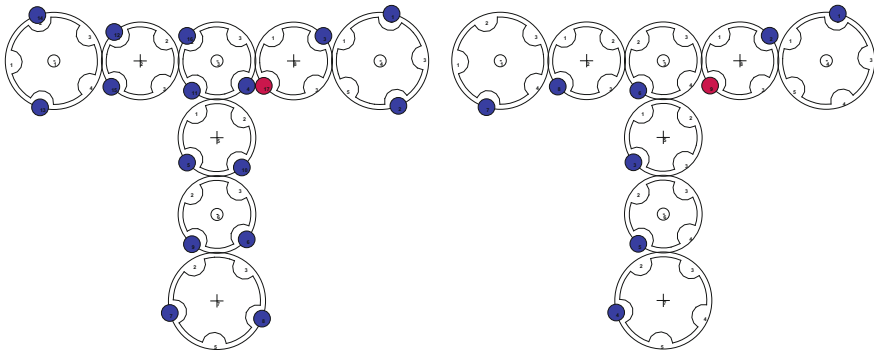


Fig. 4 Configuration for T-profile, based on an extension of a flat braid. Left—trial to arrange the carriers 1Full–1 Empty, which leads to collision and is not possible. Right—arrangement of carriers 1Full–3 Empty, which can be used

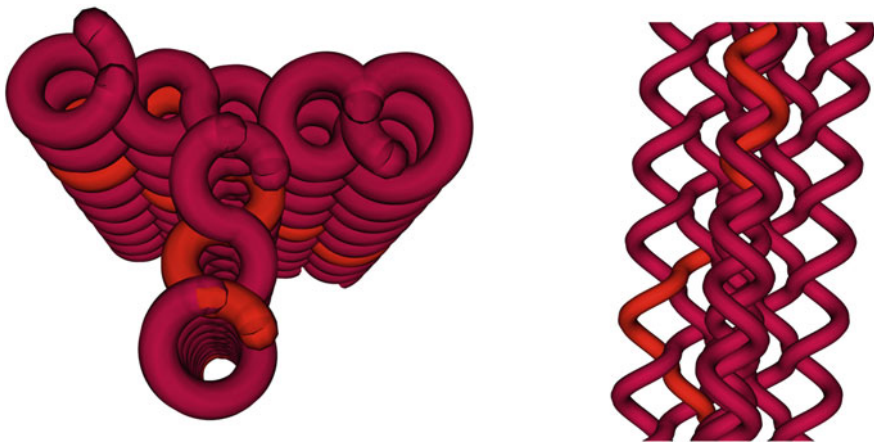


Fig. 5 Simulated idealized braid 3D geometry with the T-configuration and 1Full–3 Empty carrier arrangement (Fig. 4) in top and side view

5 Concept and Simulation of Machine for Double-T-Profile

The configuration for T-profile can be extended with additional flat branch in order to receive a double-T-profile (Figs. 6 and 7). This will still have one track.

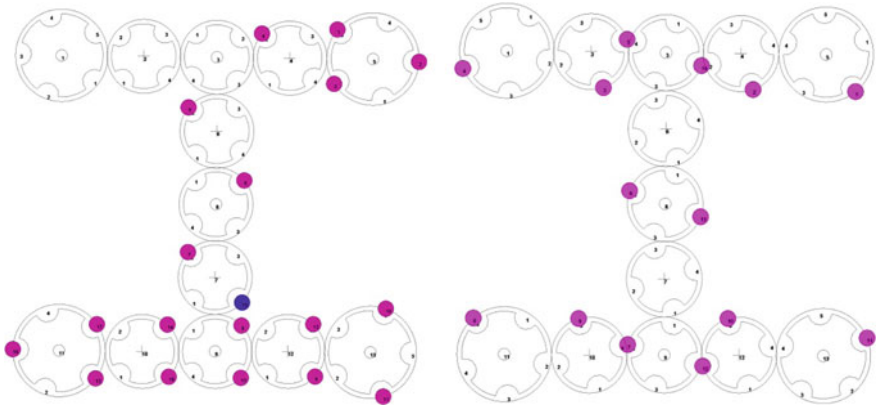


Fig. 6 Configuration for double-T-profile, based on an extension of a T-braid. Left—trial to arrange the carriers 1Full-1 Empty, which leads again to collision. Right—configuration with 1Full-3 Empty

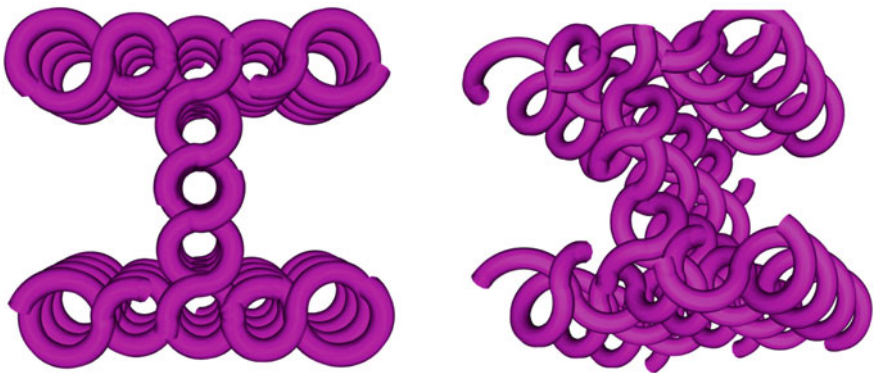


Fig. 7 Simulation of braided double-T-profile in top and side view

6 Outline

The realized configuration will produce thin-walled braids, which are based on one thin flat structure. Using the software configurator as a tool, it is possible to investigate variety of track and carrier arrangements as for instance, for two columns of gears as presented in Fig. 8. Ideas of such configurations are reported in several works and patents like from Brookstein et al. [13], Uozomi et al. [14], Temple [15], Akiyama, Hamada et al. [16] and more. In several of these technical drawings and patents, the carrier arrangement is not specified explicitly, because at that time it was not possible to simulate this behaviour on computer adequately.

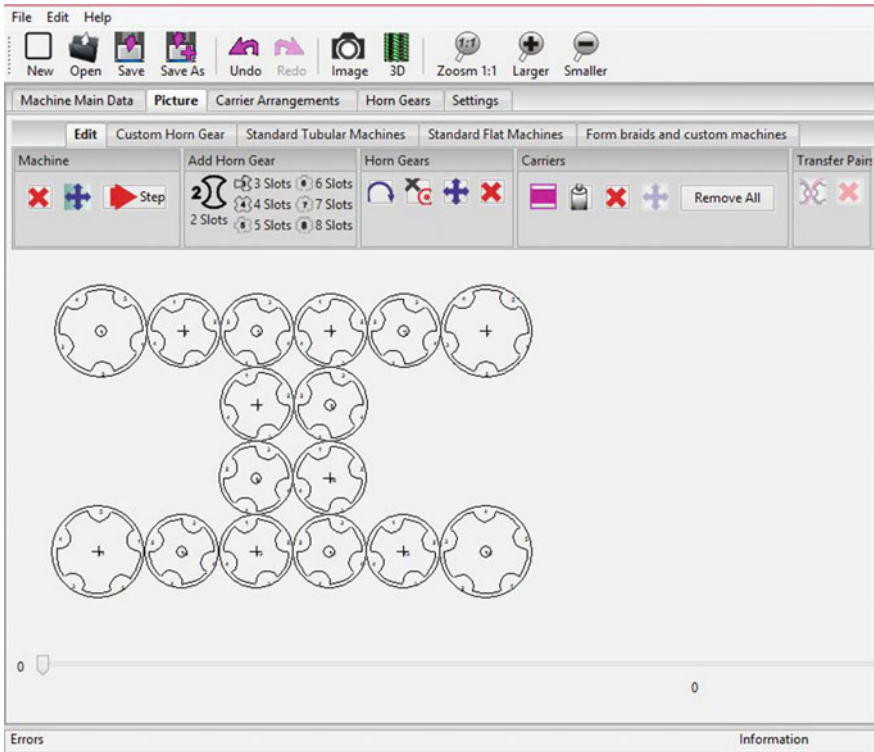


Fig. 8 Possible configuration for creation of thicker middle layer

7 Conclusions

This paper presents numerical evaluation of some configurations of maypole braiding machines for production of T- and double-T-profiles. Configuration of flat braiding machines is taken as basis and extended to a T-profile and double-T-profile. The carrier arrangement check with the software ‘Texmind Braiding Machine Configurator’ shows, that the carrier arrangement 1Full–1 Empty, which would lead to regular structure with floating length of two is not possible for the T- and double-T-configurations. Partial carrier occupation with 1Full–3 Empty can be applied for both configurations and can be used for production of the braided profiles. The simulated 3D geometries of the braids can be used for evaluation of the machine configuration and as well for approximated estimation of the properties of the structures.

References

1. Kyosev, Y. K. (2014). *Braiding technology for textiles: Principles, design and processes* (1st ed.). Woodhead Publishing Series in Textiles No. 158, Woodhead Publishing Limited.
2. Kyosev, Y. K. (Ed.). (2016). *Advances in braiding technology: Specialized techniques and applications*. Woodhead Publishing Limited.
3. Bogdanovich, A. E. (2016). An overview of three-dimensional braiding technologies. In *Advances in braiding technology* (pp. 3–78). Elsevier.
4. Schneider, M. (2000). *Konstruktion von dreidimensional geflochtenen Verstärkungstextilien für Faserverbundwerkstoffe. Berichte aus der Werkstofftechnik*. Aachen: Shaker Verlag.
5. Büsgen, A. (1993). *Neue Verfahren zur Herstellung von dreidimensionalen Textilien für den Einsatz in Faserverbundwerkstoffen*. Dissertation.
6. Lengersdorf, M., & Gries, T. (2016). Three-dimensional (3D)-maypole braiding. In *Advances in braiding technology* (pp. 89–105). Elsevier.
7. Bilisik, K. (2016). Cartesian 3D braiding. In *Advances in braiding technology* (pp. 107–145). Elsevier.
8. Schreiber, F. (2016) Three-dimensional hexagonal braiding. In *Advances in braiding technology* (pp. 79–88). Elsevier.
9. Kyosev, Y. K. (2014). Machine configurator for braided composite profiles with arbitrary cross section. In *16th European Conference on Composite Materials ECCM 16*. Seville, Spain.
10. Kyosev, Y. K. (2016). TexMind braiding machine configurator. TexMind UG.
11. Smart, J., Roebling R., Zeitlin, V., et al. (2015). wxWidgets cross platform GUI Library. wxWidgets.
12. Ifrah, E. (2016). wxCrafter <https://wxcrafter.codelite.org/>.
13. Brookstein, D., Dent, R., Dent, J., Rose, D., & Skelton, J. (1994). Solid braid structure. Google Patents <https://www.google.es/patents/US5357839>.
14. Uozomi, T., Iwahori, Y., Iwasawa, S., et al. (2001) Braiding technologies for airplane applications using RTM process. In *Proceedings of the Seventh Japan International SAMPE Symposium*. Tokyo, Japan.
15. Temple, S. Woven tubular structure. E.P. Patent No. 19,830,307,321.
16. Akiyama, Y., Hamada, H., Maekawa, Z., Uratani, Y., & Yokoyama, A. (1995) Braid and braiding method. Google Patents <http://www.google.es/patents/US5385077>.

Modeling of Braided Structures Based on Secondary Helix

Fanggang Ning, Nick O Hear, Rong Zhou, Chuan Shi and Xin Ning

Abstract In this paper, the relationship among primary helix, secondary helix and braiding curve is discussed and it concludes that the braiding curve is the projection of secondary helix on the braiding surface. Based on this conclusion, the equation of braiding curve is derived using Frenet frame. The geometrical models of braided strands are realized by two methods, one is based on the mathematical models; the braiding curves are obtained by their equations directly. The other is based on the projective relationship using SolidWorks™. A projective surface has been built and employed to realize the projection of secondary helix on the helical surface, the braiding curve is obtained by the intersection of projective surface and the helical surface. For both methods, the strands are built by sweeping the cross section along the braiding curve. The modeling methods introduced are not confined by the braiding angle and cross section of strand and could be used to simulate different braided structures.

1 Introduction

Braiding is a traditional technique normally employed for producing rope-like structures [1], while as the development of composites, it has been extended as the enforcement of composites. Even by using mandrels of different cross-sectional shapes, 3D-braided structures can be obtained. In order to perform engineering analysis of the structures, it is important to develop mathematical and geometrical models. The mathematical models are the accurate descriptions of the space morphology of braiding strands and the relative position of strands in both directions and also provide the theoretical base for the geometrical modeling. The results and

F. Ning (✉) · R. Zhou · C. Shi · X. Ning
Industrial Research Institute of Nonwovens & Technical Textiles, College of Textile and Clothing, Qingdao University, Qingdao 266071, China
e-mail: edward1654@163.com

N. O Hear
Tension Technology International, Schoonhoven 2871, NA, The Netherlands

effects of geometrical models reflect the accuracy of the corresponding mathematical models and build the relationship between the machine parameters and the geometry of the braids. In addition, the geometry of the braid structure, whether to be used alone or as a reinforcement in the composite, is also the starting point for the manufacture of the braids. Therefore, both mathematical and geometrical models are of great meanings for the research on braid.

The relevant researches on the mathematical modeling started in the 1950s; the initial researches analyzed the braided structures without considering the crimp. Brunnschweiler [2] was one of the first researchers to report on the mechanics of braid structures. Du and Ko [3] developed geometric models for 3D braids using a unit cell approach. Du and Popper [4] developed a detailed model of the complex braiding process by over braiding a contoured mandrel. Zhang et al. [5] analyzed two-dimensional braid geometry and gave the results that cover factor depends on braid angle, helical length, and braid diameter. Rawal [6, 7] discussed the equations of yarn paths mapping on different structures including circular cylinder, circular cone, elliptical cone, square prism, etc. without considering the crimp structures. With the deepening of the research, the crimp of braid was considered by researchers. Carey et al. [8] considered a sinusoidal trajectory to give a 2D configuration for only the undulation of the braiding yarns. Hristov et al. [9] studied the mechanical behavior of hybrid circular braids without a core under tensile loads and developed a predictive model of the mechanical response of the braids. Lomov et al. [10] studied flat braids and proposed a geometrical model by giving the paths of the yarn centerlines within a predetermined unit cell. Alpyildiz [11] gave a kind of descriptive equation of braiding strands based on a series of assumptions; the theoretical models included the diamond braid, regular braid, and hercules braid. Based on Alpyildiz's mathematical models, Rawal [12] improved his previous work [7] by introducing the crimp structures and presented the mathematical models of yarns mapped on revolving bodies. Besides Alpyildiz's mathematical model, some researchers used different geometrical methods to describe the strand curve and gave a total equation of braiding strands. Liao [13] presented a general mathematical method for braiding curve and built the real braided structures, while in their paper, the specific equations were not given. Wu [14] gave the mathematician models based on the discussion on the double-braiding structures.

The researches on the modeling methods of braided structures are simultaneous with the mathematical modeling. As the development of computer-aided design (CAD) techniques, it become possible to build CAD models based on mathematical equations. Adanur [15] presented three-dimensional models of fabric reinforcements for composite components by using computer-aided geometric design techniques. Two years later, Liao and Adanur [13] focused on the geometrical modeling of braided structures and built a series of braided models of revolving bodies. Recently, Kyosev [16–18] developed a computer-aided braid software named TexMind braider which could realize the modeling of tubular and flat braids

conveniently. Vu [19] presented a different modeling method. In their work, yarn of the rope is represented by a finite strain beam model. All these modeling methods could realize the modeling process and all of them need specialized knowledge on computer programming.

The author of this paper also focused on the mathematical and geometrical studies of braided structures. In our published papers [20, 21], the mathematical models of braided strand are given based on the generalized rose curve and the braided structures were realized by the intersection of braiding surface and helical surface. As to this paper, it presents a novel method to derive the equations of braided strand based on the projective relationship between secondary helix and braiding curve by Frenet frame. Based on this, two kinds of modeling methods were presented: one method is to obtain the braiding curve directly based on the equations and the other is to obtain the braiding curve based on the projective relationship between secondary helix and braiding curves by SolidWorks™. After obtaining the braiding curve, the braiding strand could be realized by sweeping a certain cross section along the braiding curve.

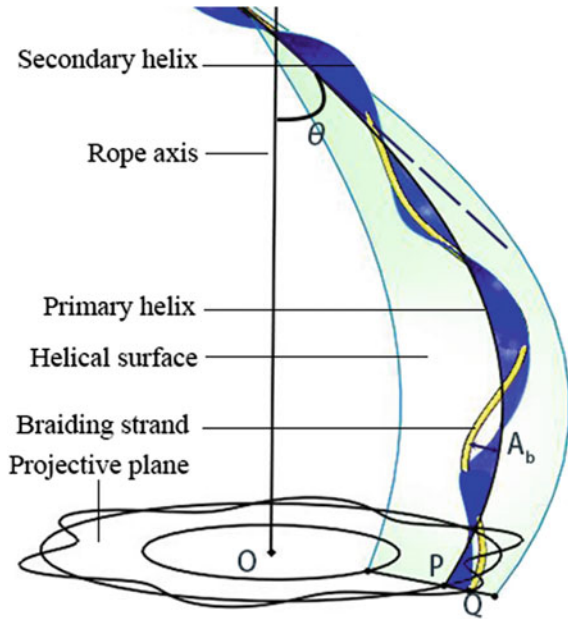
2 Geometric Analysis of Braided Structures

In braided structures, there are two sets of yarns, respectively, moving along a closed sinuous curve in clockwise and anticlockwise directions, and they alternatively pass through the crossing points of these two sinuous curve to form the interlacing structures. During this process, the number of cross points equals to the times of intersection. At the same time, the braided strands are drawn out by take-up roller continuously to form braided structures, the take-up speed, together with number of cross points depend on the density of crossing points on the tubular structures. The morphology of strands in braided structures is the result and records of these two motions.

Taking anticlockwise as an example, as shown in Fig. 1, the helical sinuous curve is the path of braiding strand which is formed by fluctuating the point P around the primary helix. The helical sinuous curve lies on the helical surface formed by helically sweeping OP along the primary helix.

In order to describe the relationship between braiding curve and secondary helix, it is necessary to give a description of the formation of the secondary helix. Secondary helix is also formed by sweeping a segment along a line, while this line is a single helix. If the centerline of helical sinuous curve and secondary helix coincide with each other and the amplitude of sinuous curve is the same with that of the secondary helix, it can be obtained that the projection of the secondary helix on the sweeping surface is the helical sinuous curve. On the helical surface, the helical sinuous curve runs in and out along the centerline of braiding structure, which will form the interlacing structure with yarns in another direction.

Fig. 1 Braiding path and helical surface



3 Mathematical Modeling of Braiding Strands

3.1 Basic Assumptions and Definition of Geometrical Parameters

In order to obtain the coordinate equation of the braiding strand, the following assumptions could be made:

- (a) The braiding strands are represented by their central curves, the radius and cross section of strands are not considered here;
- (b) These central curves follow local sinusoidal paths corresponding to their nominal helical paths;
- (c) The braiding curves are the projection of secondary helix on the braiding surface; and
- (d) All braiding yarns lie on the braiding paths, no slip happened during braiding process, and there is no interaction between adjacent strands.

3.2 Definition of Geometrical Parameters of a Braided Structure

The geometrical nomenclatures of a traditional braiding strand used in this paper are provided in Fig. 1 and the definitions of some key terms are specified as follows:

- (a) Radius of primary helix(R_p)
 R_p , the radius of primary helix, is defined as the radius of projected circle of single helix on the cross section of braided strands and it represents the thickness of braided structures. As shown in Fig. 1, the length of OP is the R_p .
- (b) Radius of secondary helix(R_s)
 The radius of secondary helix (R_s) refers to the length of line segment which is employed to helically sweep along the primary helix. R_s is the length of PQ in Fig. 1.
- (c) Amplitude of crimps (A_b)
 The amplitude of crimp refers to the maximum of amplitude of braiding curve. For braided structures, the amplitude of crimp mainly depends on the diameter of strands and the braiding patterns. Because the braiding curve is the projection of secondary helix, so the amplitude of crimp of braiding curve is the same as the radius of secondary helix (R_d).
- (d) Helical angle (θ_p, θ_s).
 Helical angle is defined as the angle among helix and corresponding axis. For primary helix, the helical angle (θ_p) refers to the angle between primary helix and the axis of braid, for secondary helix, the helical angle (θ_s) refers to the angle between primary helix and secondary helix.
- (e) Braiding angle (θ_b)
 The initial position is the starting position of strands on the cross section.
- (f) Initial position(φ)
 In the same structures, the braiding angle (θ_b) is defined as the angle among tangent line of braiding curve and braiding axis. For the braiding curve lies on the helical surface, the braiding angle equals to the helix angle (θ_p).
- (g) Direction parameter(λ)
 parameter λ is employed to characterize the direction of helix and braiding curve, for anticlockwise, $\lambda = 1$ and for a clockwise, $\lambda = -1$.

3.3 Primary Helix and Frenet Frame

In braided structures, the centerline of helical sinuous curve is a primary helix, as shown in Fig. 2. For a primary helix with an initial strand position angle of 0 at $z = 0$ and a right-hand lay direction, the vector equation of the central axis is

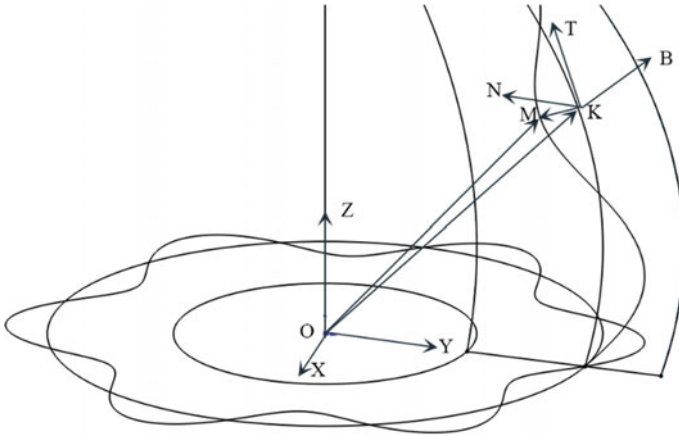


Fig. 2 Braiding path and Frenet frame

$$X_s(t) = \begin{cases} R_p \cos t_p \\ R_p \sin t_p \\ R_p t_p / \tan \theta_p \end{cases} \tag{1}$$

Where t_p is the position parameter of primary helix.

In order to analyze braiding elements in space, it is convenient to use a local coordinate system at each point of its central axis. The tangent (**T**), normal (**N**), and binormal (**B**) vectors are defined at each point. The Frenet formulas describe the geometric properties of the curve, as shown in Fig. 2.

T: The unit vector tangent to the curve, pointing in the direction of motion; **B**: The normal unit vector, the derivative of **T** with respect to the arc length parameter of the curve, divided by its length. **T**: The binormal unit vector, the cross product **T** and **N**.

The position vector of a point on the central axis is presented in global Cartesian coordinates by

$$X(t) = x(t)i + y(t)j + z(t)k \tag{2}$$

The derivation of this with respect to the variable parameterizing the curve is

$$X(t) = x(t)i + y(t)j + z(t)k \tag{3}$$

If the curve is parameterized by the angle of rotation, the distance dS between two nearby points on the curve is given by

$$ds = \mathbf{X}(t) dt \tag{4}$$

This is

$$ds = \sqrt{(x(t))^2 + (y(t))^2 + (z(t))^2} dt \quad (5)$$

The arc length between two points between $t = a$ and $t = b$ is given by

$$S = \int_a^b \|X(t)\| dt \quad (6)$$

In Frenet frame, some useful calculating expressions are shown below:

$$\mathbf{T} = \frac{\dot{x}}{\|X(t)\|} \mathbf{i} + \frac{\dot{y}}{\|X(t)\|} \mathbf{j} + \frac{\dot{z}}{\|X(t)\|} \mathbf{k} \quad (7)$$

$$\mathbf{B} = \frac{X(t) \otimes X(t)}{\|X(t) \otimes X(t)\|} \quad (8)$$

$$\mathbf{N} = \mathbf{B} \otimes \mathbf{T} \quad (9)$$

Where

$$\|X(t)\| = \sqrt{\left(\frac{dx}{dt}\right)^2 + \left(\frac{dy}{dt}\right)^2 + \left(\frac{dz}{dt}\right)^2} \quad (10)$$

$$\|X(t)\| = \sqrt{\left(\frac{d^2x}{dt^2}\right)^2 + \left(\frac{d^2y}{dt^2}\right)^2 + \left(\frac{d^2z}{dt^2}\right)^2} \quad (11)$$

and \otimes denote the cross product.

3.4 Secondary Helix and Braiding Curve

Secondary helix is formed by helically sweeping a segment along a primary helix, as shown in *Fig. 3*. From the description, it can be obtained that in Frenet frame, the secondary helix could be obtained by helically sweeping a segment on TB surface along a primary helix.

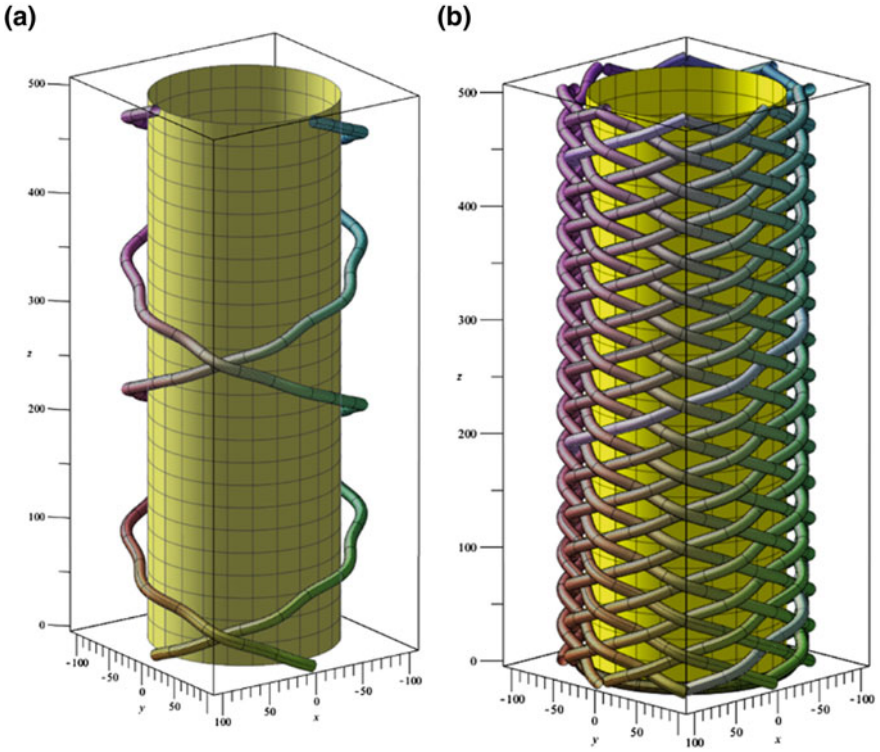


Fig. 3 Braided structures based on mathematical equations

According to the Frenet frame,

$$X_p(t) = \begin{cases} -R_p \sin(t_p) \\ R_p \cos \lambda(t_p) \\ R^p / \tan \theta_p \end{cases} \quad (12)$$

$$X_p(t) = \begin{cases} -R_p \cos(t_p) \\ R_p \sin \lambda(t_p + \varphi) \\ 0 \end{cases} \quad (13)$$

So, according to Eqs. (7), (8), and (9), the vectors of \mathbf{T} , \mathbf{N} , and \mathbf{B} can be expressed as follows:

$$T = -\sin \theta_p \sin(t)i + \sin \theta_p \cos(t)j + \sin \theta_p \tan \alpha k \quad (14)$$

$$N = -\cos(t)i - \sin(t)j + 0k \quad (15)$$

$$B = \sin \theta_p \sin(t)i + \sin \theta_p \cos(t)j + \cos \theta_p k \quad (16)$$

According to the relationship between secondary helix and primary helix, it can be obtained that secondary helix has components in both \mathbf{T} and \mathbf{N} .

According to the primary helix, the equation of the secondary helix in global coordinate is

$$X_s(t) = X_p(t_p) + R_s(\cos(t_s)N + \sin(t_s)B) \quad (17)$$

Combining Eqs. 2, 14, 15, 16, and 17, the equation of secondary helix in global coordinate can be expressed as follows:

$$X_s(t) = \begin{cases} R_p \cos 2\pi t_p + R_s(\sin \theta_p \sin t_p \sin t_s - \cos t_p \cos t_s) \\ R_p \sin t_p + R_s(\sin \theta_p \cos t_p \sin t_s - \sin t_p \cos t_s) \\ 2\pi R_p t_p / \tan \theta_p + R_d \cos \theta_p \sin t_s \end{cases} \quad (18)$$

Where t_p is the position variable of primary helix and t_d is the position variable of secondary helix, $t_p = t_s \sin \theta_p$

As described, the braiding curve is the projection of secondary helix on the helical surface, and the curve of braiding yarn only has component in \vec{N} . So the equation of braiding yarn curve can be expressed as

$$X_b(t) = X_p(t_p) + A_b \cos(t_s)N \quad (19)$$

So, Eq. (17) can be changed to

$$X_b(t) = \begin{cases} (R_p - A_b \cos t_s) \cos t_p \\ (R_p - A_b \cos t_s) \sin t_p \\ R_p / \tan \theta_p t_p \end{cases} \quad (20)$$

Let $\omega = 1/\sin(\theta_s)$ and also considering the initial position (φ), the difference between strands in two directions (κ) and direction of strand (λ), the equation of braiding strand could be rewritten as

$$X_b(t) = \begin{cases} (R_p - \kappa A_b \cos \omega t_p) \cos \lambda(t_p + \varphi) \\ (R_p - \kappa A_b \cos \omega t_p) \sin \lambda(t_p + \varphi) \\ R_p \tan \theta_p t_p \end{cases} \quad (21)$$

This equation is the expression of braiding curve in terms of t_p .

4 Geometric Modeling of Braiding Strand

4.1 Geometric Modeling Based on the Mathematical Model

Based on the equations of braiding curve, it could be easy to obtained geometrical structure of single strand by inputting the equations in CAD software, such as SolidWorks™ to get 3D braiding curve directly. In this case, the match of strands in two directions and the relative position of strands in the same direction would be the key factors to realize the whole braided structure.

In braiding process, the positions of strands in clockwise and anticlockwise at the same angle are symmetrical with respect to the projective circle of primary helix, which means that the positions of strands in two directions are always opposite. The reflection of this feature in the equations would be that the κ is always opposite for strands in two directions. If $\kappa = 1$ for strands in clockwise, then $\kappa = -1$ for strands in anticlockwise and vice versa.

For strands in the same direction, all strands are arranged equally, and the only difference lies on the different initial positions. For a braid with 2 N strands, the number of strands in the same direction would be N; all these N strands would arrange equally around a circle, so the phase difference would be shown as Eq. (22)

$$\Delta_\varphi = 2\pi/N \quad (22)$$

So, the equation of strands in anticlockwise would be expressed as

$$X_{ba}(t) = \begin{cases} (R_s - A_b \cos \omega t_s) \cos (t_s + i\Delta_\varphi) \\ (R_s - A_b \cos \omega t_s) \sin (t_s + i\Delta_\varphi) \\ R_s / \tan \theta_s t_s \end{cases} \quad i = 1, 2, \dots, N \quad (23)$$

Then, the corresponding equation of strands in clockwise would be

$$X_{bc}(t) = \begin{cases} (R_s + A_b \cos \omega t_s) \cos (-(t_s + i\Delta_\varphi)) \\ (R_s + A_b \cos \omega t_s) \sin (-(t_s + i\Delta_\varphi)) \\ R_s / \tan \theta_s t_s \end{cases} \quad i = 1, 2, \dots, N \quad (24)$$

Based on these two equations, the braided structure would be realized as shown in Fig. 3. Figure 3a shows strands in two directions and (b) shows a whole braid with diamond pattern.

From Fig. 3b, it could be observed that the model could reflect the interlacing feature of braid. So the mathematician models based on the secondary helix would be reasonable.

4.2 Geometrical Modeling Based on Secondary Helix

The realization of secondary helix and helical surface

Besides the mathematical methods, the projection of secondary helix could also be realized by CAD software. In this paper, the SolidWorks™ was employed to realize this process, while for other similar CAD software, such as Pro-e™ and UG™, etc., could also be used to realize this process based on the same modeling process.

In SolidWorks™, there is tool to generate the helix directly. So it is easy to generate the primary helix. At first, draw the projected circle on the sketch and use “helix and spiral” tool to define the helix with direction/pitch length/helical angle. Then, the primary helix can be obtained.

The secondary helix is obtained by helically sweeping a segment along the primary helix. During this process, the “swept surface” tool is employed. At first, a sketch which passes an endpoint of primary helix and is norm to the tangent line is generated. The method is to draw a reference plane. On this reference plane, taking the endpoint of primary helix as an endpoint, draw a segment as long as the amplitude of crimp of braiding yarn, then take this sketch as sweeping plane and the primary helix as sweeping path to generate a secondary helical surface, and the sideline of this surface is the secondary helix.

In order to get the path of braiding yarn, it is necessary to generate the helical surface. During the process to generate the helical surface, the “swept surface” tool is employed again. At first, draw a segment on the sketch which passes the original point and the starting point of primary helix, and it is longer than the diameter of projected circle. Then, use sweeping tool to generate the helix surface taking the segment as profile and the centerline of braid as path and at the same time, setting the sweeping style as “twist along path” and the turn as 1. Then, the helical surface can be obtained.

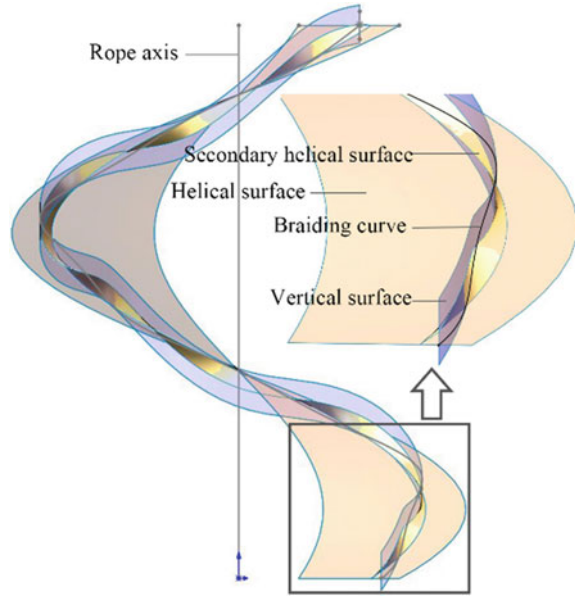
The next task is how to project the secondary helix to the helical surface. In all CAD softwares, there are no tools that can project a space curve on a space surface. So solving this difficulty becomes the key step to realize this model-building process.

The realization of projection and braiding curve

According to the definition of projection, as shown in Fig. 4, the projective surface is always normal to the helical surface and passes the secondary helix. The intersection of projective surface and the helical surface could be the projection of secondary helix on the braiding surface, which is the braiding curve. So the realization of projective surface would be the key for this modeling method. In SolidWorks™, the projective surface is realized by sweeping method, and the specialized steps are as follows:

- (a) A sketch would be built at first which is always normal to the single helix. The auxiliary plane is built taking the endpoint of helix and the primary helix as the references.

Fig. 4 Generation of vertical surface



- (b) On this auxiliary plane, draw a vertical segment, the length of which is longer than $2A_b$. Set that the midpoint of this segment is a kind of “make piece” relationship with the secondary helix which makes sure that when sweeping, the midpoint of this segment would always lie on the secondary helix.
- (c) The projective surface could be obtained by “swept surface” tool taking the sketch as the profile, the primary helix as the path, and the secondary helix as the guide curve, as shown in Fig. 4.

Then the “intersection curve” tool is employed again to obtain the intersection of projective surface and helical surface. The intersection of these two surfaces is the braiding curve.

After getting the path of braiding yarns, the yarns can be obtained by sweeping the cross section of yarn along its path. First, an auxiliary plane is needed to draw the sketch. The auxiliary plane should pass the endpoint of the braiding curve and be norm to the tangent line of the braiding curve at the endpoint. Then, draw a circle taking the endpoint of the braiding curve as the center and the diameter of braiding yarn as diameter. At last, the braiding yarn was generated by sweeping the sketch along the braiding curve using sweeping tool. Considering the phase difference in the same direction as Eq. (22) and the difference between strands in different directions as Eqs. (23) and (24), it is not difficult to obtain the model of yarns in another direction. The final model of this braiding structure is shown in Fig. 5.

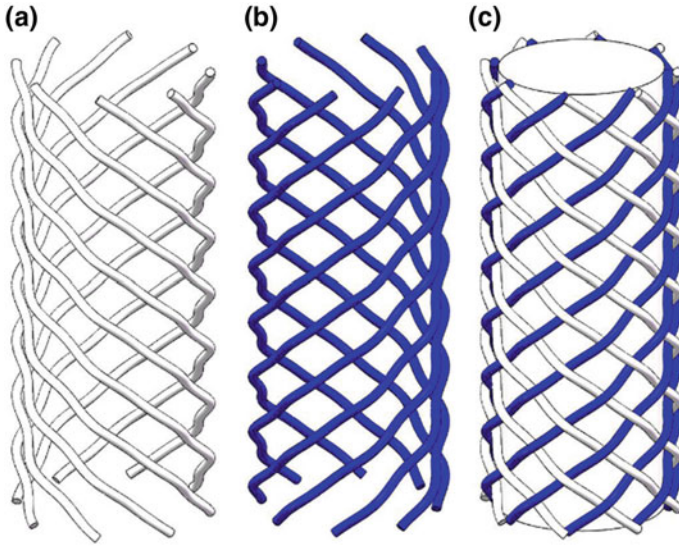


Fig. 5 Tubular braided structures **a** strands in anticlockwise, **b** strands in clockwise, and **c** diamond braid

The braiding curve is realized by the projection of secondary helix on the helical surface. The modeling method realizes the projection of a space curve onto a space surface, so this modeling method has universal practicality. From the stimulating effect, it could be observed that the modeling method based on the projective relationship between secondary helix and braiding curve could well reflect the interlacing features and the relative positions of strands.

5 Application and Discussion

Figure 6 shows the triaxial braids with different braiding angles. The parameters of braided structures simulated based on this modeling methods could be adjusted conveniently, such as the diameter, the braiding angle, etc. The braiding angles of Fig. 6a–c are 30° , 45° , and 60° , respectively.

Besides, if the primary helix is a kind of helix with variable pitch, it could obtain the braided structures with variable braiding angle as shown in Fig. 7. The braiding angle of braided structure in Fig. 7 is varied gradually from 60° to 80° .

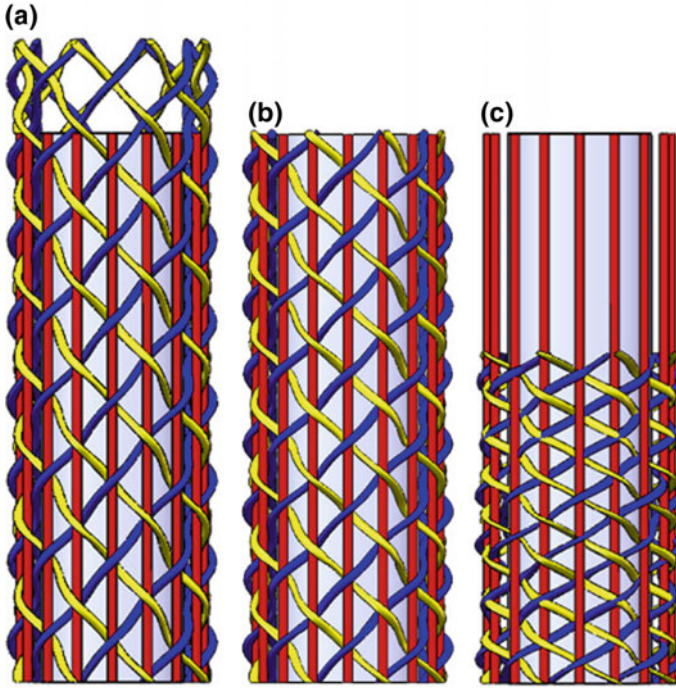
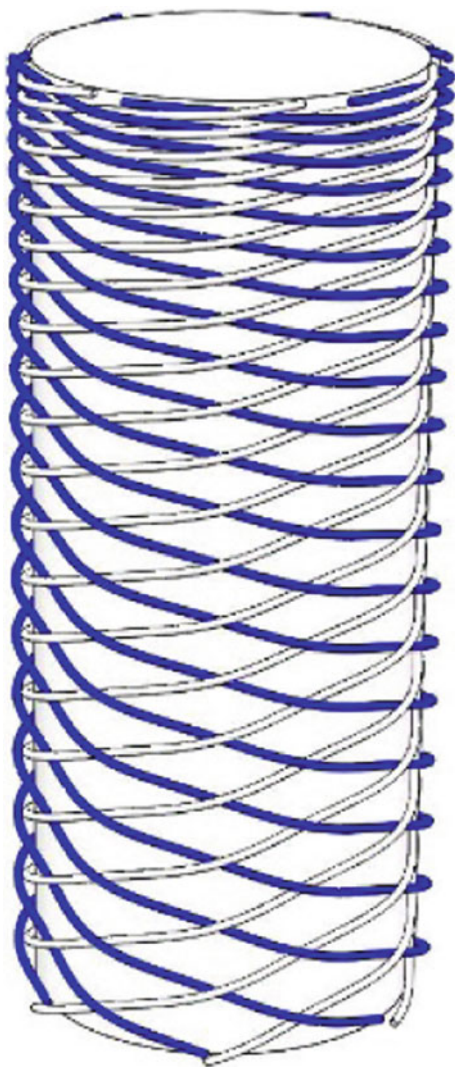


Fig. 6 Braids with different braiding angles **a** 30°; **b** 45°; and **c** 60°

This modeling method is also not confined by the cross section of strands. Figure 6 shows the structures with circular strands. While in practice, for the softness of strands, the strands could be flattened and the cross section of strand would be a kind of elliptical shape. In modeling process, this kind of structures could be obtained by sweeping the ellipse along the braiding curve, as shown in Fig. 8a. If the cross section is a hexagon cross section, the braided structures would be as shown in Fig. 8b.

In some cases, especially when the braided structures are used as covering or decoration, the braided elements are not strands with circle or ellipse but a very thin and wide fiber filaments or tapes. Under this case, it would be more reasonable to simulate the braids with tape structures. This kind of tape structures is the extreme case of elliptical structures and could be realized by replacing the ellipse by a segment, as shown in Fig. 8c.

Fig. 7 Braided structure with variable pitch



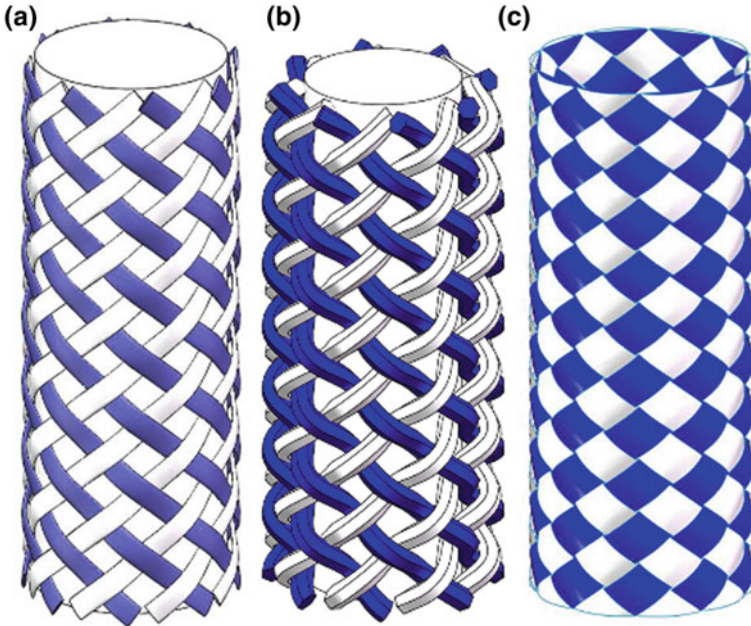


Fig. 8 Braided structures with different braiding elements **a** elliptical strands; **b** hexagon cross section; and **c** tape strands

6 Conclusion

This paper derived the mathematical models of braiding curve based on the projective relationship between secondary helix and braiding curve. Subsequently, the geometrical models are built by two kinds of different methods. One is the mathematical method which is realized based on the mathematical equations of braiding curve. In this process, the phase difference of strands in same direction and differences of projective curve of braiding strands on the cross section of braided structure are discussed in detail. Based on these equations, the whole braided structure would be simulated. The other is CAD method. During this process, the SolidWorks™ is employed. The projective relationship is realized by projective surface which is built based on the definition of projection. The braiding curve could be obtained by the intersection of projective surface and helical surface. The strands could be realized by sweeping the cross section of strands along the braiding curves. It could be observed that simulated models could reflect the interlacing characteristics of real braided structures.

Acknowledgements This work was supported by the China Scholarship Council [grant number 201200630034].

References

1. McKenna, H. A., Hearle, J. W. S., & Hear, N. O. (2004). *Handbook of fibre rope technology* (1st ed., p. 432). Cambridge CB1 6AH, England: Woodhead Publishing Limited.
2. Brunnschweiler, D. (1954). The structure and tensile properties of braids. *Journal of the Textile Institute Transactions*, 45(1), T55–T77.
3. Du, G. W., & Ko, F. K. (1993). Unit-cell geometry of 3-D braided structures. *Journal of Reinforced Plastics and Composites*, 12(7), 752–768.
4. Du, G. W., & Popper, P. (1994). Analysis of a circular braiding process for complex shapes. *Journal of the Textile Institute*, 85(3), 316–337.
5. Zhang, Q., et al. (1997). Structural analysis of a two-dimensional braided fabric. *Journal of the Textile Institute*, 88(1), 41–52.
6. Rawal, A., Potluri, P., & Steele, C. (2005). Geometrical modeling of the yarn paths in three-dimensional braided structures. *Journal of Industrial Textiles*, 35(2), 115–135.
7. Rawal, A., Potluri, P., & Steele, C. (2007). Prediction of yarn paths in braided structures formed on a square pyramid. *Journal of Industrial Textiles*, 36(3), 221–226.
8. Carey, J., Munro, M., & Fahim, A. (2003). Longitudinal elastic modulus prediction of a 2-D braided fiber composite. *Journal of Reinforced Plastics and Composites*, 22(9), 813–831.
9. Hristov, K., et al. (2004). Mechanical behavior of circular hybrid braids under tensile loads. *Textile Research Journal*, 74(1), 20–26.
10. Lomov, S. V., et al. (2001). Textile composites: modelling strategies. *Composites Part A Applied Science and Manufacturing*, 32(10), 1379–1394.
11. Tuba, A. (2012). 3D geometrical modelling of tubular braids. *Textile Research Journal*, 82(5), 443–453.
12. Rawal, A., et al. (2014). Geometrical modeling of near-net shape braided preforms. *Textile Research Journal*, 85, 1055–1064.
13. Liao, T., & Adanur, S. (2000). 3D structural simulation of tubular braided fabrics for net-shape composites. *Textile Research Journal*, 70(4), 297–303.
14. Wu, H. C., et al. (1995). Structural modeling of double-braided synthetic-fiber ropes. *Textile Research Journal*, 65(11), 619–631.
15. Adanur, S., & Liao, T. (1998). 3D modeling of textile composite preforms. *Composites Part B Engineering*, 29(6), 787–793.
16. Kyosev, Y. (2014). Machine configurator for braided composites profiles with arbitrary cross section. In *16th European Conference on Composite Materials*, Seville, Spain.
17. Kyosev, Y. (2015). Generalized geometric modeling of tubular and flat braided structures with arbitrary floating length and multiple filaments. *Textile Research Journal*.
18. Kyosev, Y. (2013). Computer aided colour and structural design of braided structures. In *Proceedings of the 1st International Conference on Digital Technologies for the Textile Industries*.
19. Vu, T. D., Durville, D., & Davies, P. (2015). Finite element simulation of the mechanical behavior of synthetic braided ropes and validation on a tensile test. *International Journal of Solids and Structures*, 58, 106–116.
20. Ning, F., & Yu, W. (2016). Computer-aided modeling of braided structures overbraiding non-cylindrical prisms based on surface transformation. *Advances in Engineering Software*, 98, 69–78.
21. Ning, F., et al. (2017). Geometrical modeling of tubular braided structures using generalized rose curve. *Textile Research Journal*, 87(4), 474–486.

Investigation of PET-Braided Vascular Stents Potential Compared with Commercial Metallic Stents

Hiba Jaziri, Sofiene Mokhtar, Khawla Aguir
and Saber Ben Abdessalem

Abstract Braided polymeric biomedical stents were developed as an alternative to replace commercial metallic ones presenting several failures caused especially by the used metals. Among those materials, the polyethylene terephthalate PET has been used to develop stents since it is suitable for several biomedical uses, such as vascular prosthesis. But in order to obtain the ideal PET-braided stent, its manufacturing parameters should be carefully chosen. For that, the current study aims at developing polymeric braided vascular stents made of PET monofilaments. According to a two-level fractional factorial design, stents are braided by varying most of their manufacturing and heat-setting parameters (monofilament diameter, stent diameter, braiding angle, heat-setting temperature and heat-setting time). Then, the structural (cover factor, porosity, unchanged bending diameter) and mechanical tests (radial compression, longitudinal compression, longitudinal elongation) are performed. Developed stents performances are compared to those of the Gore's Nitinol stents. Then, effects of manufacturing parameters on stents properties were investigated. After selecting the significant parameters for each performance, optimal values were determined. According to the experimental results, manufactured stents showed good performances comparing to Nitinol stents. According to the factorial analysis, considered factors have different effects from a response to another. The most common significant factors are monofilament diameter, stent diameter and braiding angle, whereas the least important factors are heat-setting temperature and heat-setting time. Also, models are adequate (p -value $< 0,05$ and $R^2 > 80\%$) at the 95% confidence level. Furthermore, the obtained optimum stent's manufacturing settings can lead to PET-braided stents as performant as Gore's Nitinol ones.

H. Jaziri (✉) · S. Mokhtar · S. Ben Abdessalem
Department of Textile Engineering, National Engineering School of Monastir,
University of Monastir, Monastir, Tunisia
e-mail: hiba.jaziri@yahoo.fr

H. Jaziri · S. Mokhtar · K. Aguir · S. Ben Abdessalem
Textile Materials and Processes Research Unit MPTex, National Engineering
School of Monastir, University of Monastir, Monastir, Tunisia

1 Introduction

Cardiovascular diseases such as coronary artery disease, vascular stenosis or aneurysm require the use of stents, which are tubular and perforated structures inserted in an organ (artery, intestine, trachea, etc.) in order to open its diameter and restore its primary function. Materials used to manufacture stents have steadily improved both in terms of technical performances and biological tolerance. Generally, metallic stents are the most common commercial stents but they present huge problems such as early thrombosis, intra-stent restenosis, infections, corrosion, etc. [1–3]. In order to avoid these complications, researchers have developed stents using biocompatible polymers such as polyethylene terephthalate (PET), polypropylene (PP), polyurethane (PUR), polydioxanone (PDS), polylactic acid (PLA), etc. The majority of the results showed that polymeric stents can help to minimize problems due to metallic ones and may replace them but investigation has to be continued in order to find their ideal manufacturing parameters [4–6]. PET monofilaments have been used to develop braided stents [3–5, 7]. Indeed, for biomedical uses (such as vascular prostheses), PET is well tolerated after implantation because it is reasonably chemically inert, biocompatible, flexible, elastic, and resistant to sterilization [8]. Furthermore, PET has a good tensile strength and rigidity, it is easy to handle and has a very low water retention that does not affect the mechanical properties or the Tg [4]. Moreover, for the development of stents, braiding seems to be the most suitable technique. In fact, braided stents could exhibit a good dimensional stability, excellent mechanical properties, high shape recovery, and good flexibility [3, 9]. For that, polymeric braid's design parameters and heat-setting conditions must be chosen correctly in order to obtain good structural and mechanical properties similar to those of metallic stents.

Unlike other studies, in this work, we investigate simultaneously most of the manufacturing and heat-setting parameters of PET vascular braided stents in order to identify the most significant factors on the stents main properties and determine their optimal values.

2 Materials and Methods

2.1 Stents Development

PET tubular braided structures were produced using a 16-head “LESMO” vertical braiding machine. Horn gears were set to braid “Regular” braid and it was necessary to use mandrels during manufacturing as a support for the braided tubular samples (Fig. 1). After fabrication, samples were heat-set in a “MATHIS” stenter.

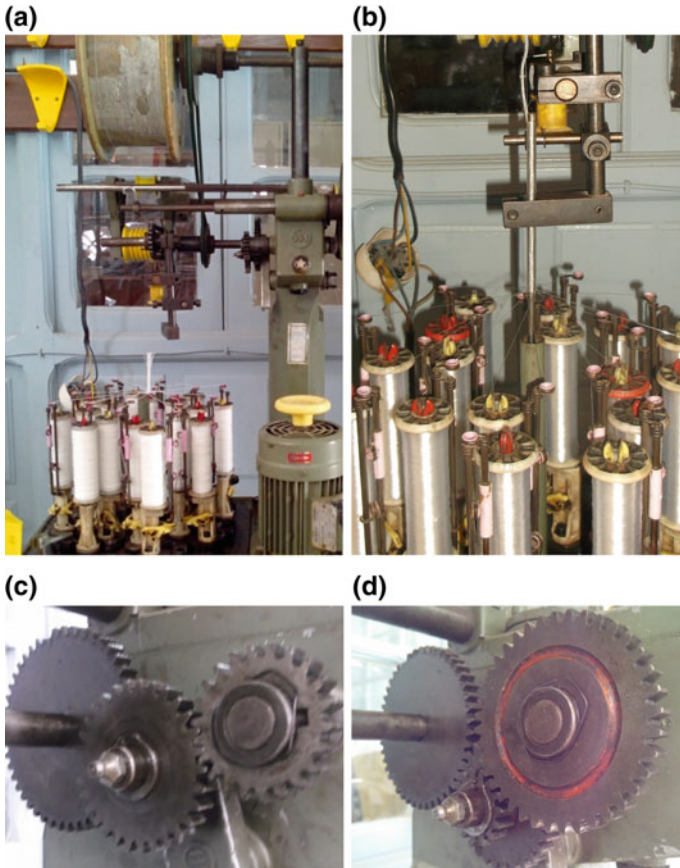


Fig. 1 Braiding machine. **a** General view **b** Braid formation and mandrel guidance **c** Gears setting for the higher braiding angle **d** Gears setting for the lower braiding angle

Five manufacturing parameters were simultaneously varied following a two-level fractional factorial design: PET monofilament diameter (ϕ_f : 0,3 and 0,5 mm), mandrel diameter (ϕ_s : 10 and 14 mm), braiding angle (α : 55° and 70°), heat-setting temperature (T : 170 and 190 $^\circ\text{C}$), and heat-setting time (t : 60 and 90 min).

The properties of the PET monofilaments are shown in Table 1:

Eight ($2^{(5-2)}$) different samples were manufactured (Table 2) and their structural and mechanical properties were measured.

Table 1 Tensile properties of raw materials

Diameter (mm)	Linear density (tex)	Tenacity (CN/ Tex)	Elongation (%)	Young's modulus (MPa)
0,3	86	53,61	34,34	4063,56
0,5	260	41,17	62,11	3099,4

Table 2 Sample's manufacturing parameters

Stent	\varnothing_f (mm)	\varnothing_s (mm)	α (°)	T (°C)	t (min)
S1	0,3	14	70	170	60
S2	0,3	10	70	190	60
S3	0,3	14	55	170	90
S4	0,3	10	55	190	90
S5	0,5	14	70	190	90
S6	0,5	10	70	170	90
S7	0,5	14	55	190	60
S8	0,5	10	55	170	60

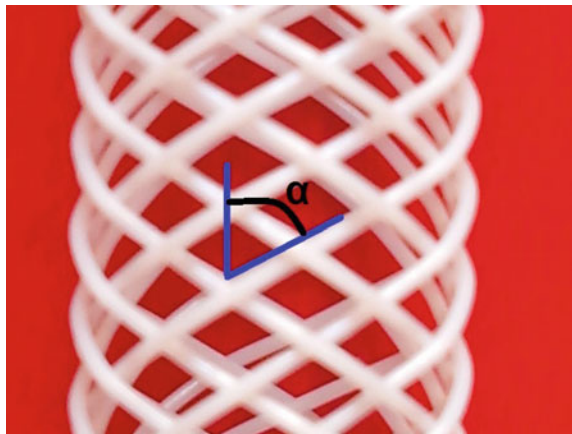
2.2 Stents Characterization

2.2.1 Structural Characteristics

Cover Factor

Tubular braid's cover factor ($CF_{\%}$) is defined as the ratio between the covered unit cell area and the total unit cell area, in other words, it is the percentage of the

Fig. 2 Manufactured tubular braided structure showing the braiding angle



mandrel surface covered by monofilaments [3, 10]. It is calculated using the following equation:

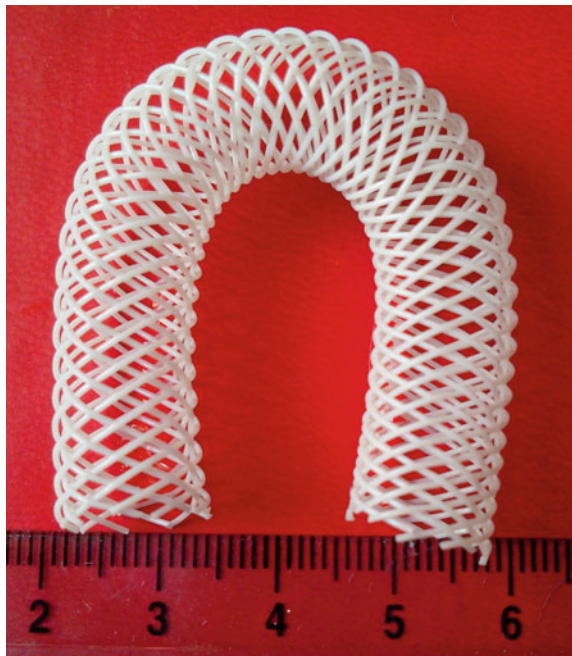
$$CF\% = \left[1 - \left(1 - \frac{\varnothing_f N}{2\pi \varnothing_s \cos \alpha} \right)^2 \right] \times 100, \quad (1)$$

Where N is the number of bobbins and α is the braiding angle ($^\circ$) (Fig. 2).

Porosity

Porosity ($P\%$) is an important characteristic for stents that expresses the blank area percentage not been covered by material occupying the whole stent surface area. A certain porosity provided space for cells to proliferate and the environment for gas exchange, nutrition access and metabolite eliminate. Without porous on stent, intima and blood flow were blocked, which would increase the risk of thrombosis and restenosis. However, with an oversize porous, there will not be enough area for cell proliferation, also a decrease on stent's mechanical properties [11].

Fig. 3 Bending test



In case of commercial vascular stents, and since they have as main function to keep the arteries open, these devices must present a high porosity, approximately, 70–80% [12, 13]. $P\%$ is given as follows:

$$P\% = 100 - CF\% \quad (2)$$

Unchanged Bending Diameter

Bent sections of implanted stents should maintain at least 75% of their original diameter, in order to avoid collapse [3]. Stent's specimens with 8 cm in length were

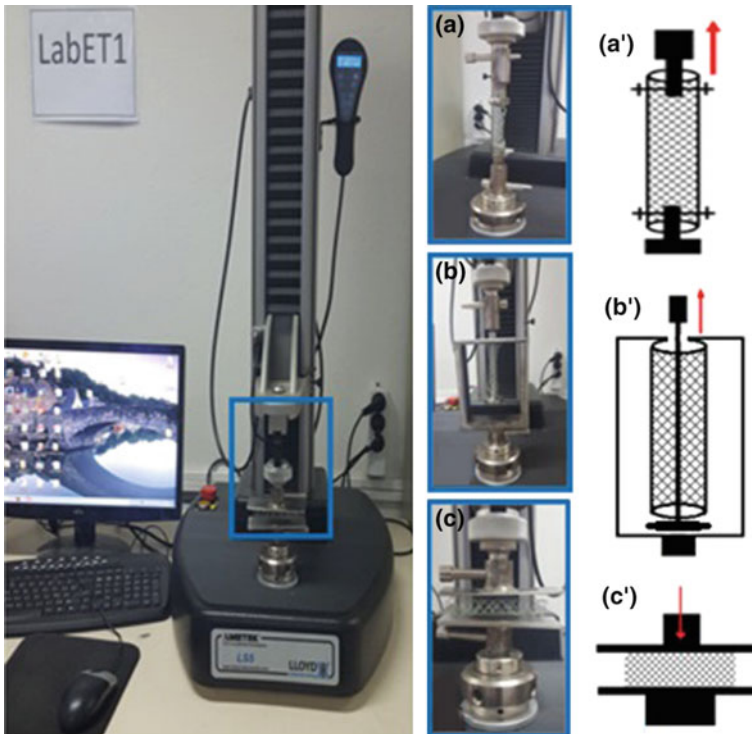


Fig. 4 Stent's Mechanical characterization: **a** Longitudinal elongation test, **b** Longitudinal compression test, **c** Radial compression test

bent until their ends were separated by 2 cm (Fig. 3). The diameter at the midpoint of the bent section (\varnothing_b (mm)) was measured and the average unchanged diameter ($\varnothing_{b\%}$ (%)) was calculated as follows:

$$\varnothing_{b\%} = \left(\frac{\varnothing_b}{\varnothing_s} \right) \times 100 \quad (3)$$

2.2.2 Mechanical Characteristics

Longitudinal Elongation Test

Stents must have a good potential to elongate during deployment [14]. In order to evaluate this potential, 10 specimens from each stent underwent an extension force of 70 g (0,69 N) at a speed of 100 mm/min with a distance of 6 cm between grips using a Lloyd tensile machine (Fig. 4a). The stent elongation All_1 (mm) and Young's modulus E_1 (MPa) were measured.

Longitudinal Compression Test

Stents must have good resistance to axial compression otherwise they will be easily compressed at their ends when inserted with catheters [3]. To mimic the potential of in vivo longitudinal compression forces, 10 specimens of 8 cm in length (from each manufactured stent) were compressed longitudinally by 15% at a speed of 100 mm/min using a Lloyd tensile machine (Fig. 4b). The average of longitudinal compression force F_{lc} (N) and Young's modulus E_{lc} (MPa) were determined.

Radial Compression Test

Radial compressive strength and stiffness must be enough to avoid stent recoil after implantation [15]. To measure and evaluate these properties, 10 samples from manufactured stents (8 cm in length) were compressed laterally by 25%, at a speed of 25 mm/min, between two flat plates in a Lloyd tensile machine (Fig. 4c). The average of radial compression force F_{rc} (N) and Young's modulus E_{rc} (MPa) were determined.

3 Results and Discussions

The responses corresponding to the eight manufactured stents are shown in Table 3.

Using MINITAB software (MINITAB Ltd, Coventry, UK), most significant factors for each response were identified from analysis of variance and main effects

Table 3 Performances of manufactured stents

Stents	Structural characteristics		Radial compression test		Longitudinal elongation test		Longitudinal compression test	
	P (%)	\varnothing_b (%)	F _{rc} (N)	E _{rc} (MPa)	All _l (mm)	E _l (MPa)	F _{lc} (N)	E _{lc} (MPa)
S1	70,85 ± 1,63	96,55 ± 0,35	12,58 ± 0,49	0,36 ± 0,01	88,42 ± 5,64	0,01 ± 0,001	0,05 ± 0,01	0,01 ± 0,001
S2	64,09 ± 1,08	98,09 ± 0,21	17,29 ± 2,67	1,69 ± 0,17	45,70 ± 3,83	0,02 ± 0,001	0,19 ± 0,01	0,02 ± 0,001
S3	79,47 ± 1,88	95,86 ± 0,32	1,99 ± 0,42	0,15 ± 0,03	38,39 ± 3,80	0,02 ± 0,001	0,11 ± 0,01	0,01 ± 0,001
S4	74,42 ± 2,01	97,14 ± 0,21	2,68 ± 0,34	0,48 ± 0,05	20,29 ± 2,36	0,04 ± 0,006	0,16 ± 0,01	0,02 ± 0,001
S5	53,06 ± 1,47	97,33 ± 0,33	49,09 ± 5,26	2,05 ± 0,22	22,54 ± 2,54	0,01 ± 0,002	0,61 ± 0,09	0,04 ± 0,005
S6	49,98 ± 1,30	96,36 ± 0,51	62,10 ± 6,21	4,88 ± 0,54	13,23 ± 1,46	0,06 ± 0,01	1,81 ± 0,48	0,07 ± 0,002
S7	70,78 ± 1,99	98,00 ± 0,21	14,58 ± 2,23	0,78 ± 0,11	7,02 ± 0,89	0,11 ± 0,04	0,40 ± 0,04	0,03 ± 0,001
S8	60,31 ± 0,77	95,45 ± 0,28	23,37 ± 3,03	2,36 ± 0,30	5,52 ± 0,64	0,17 ± 0,04	0,77 ± 0,02	0,05 ± 0,002

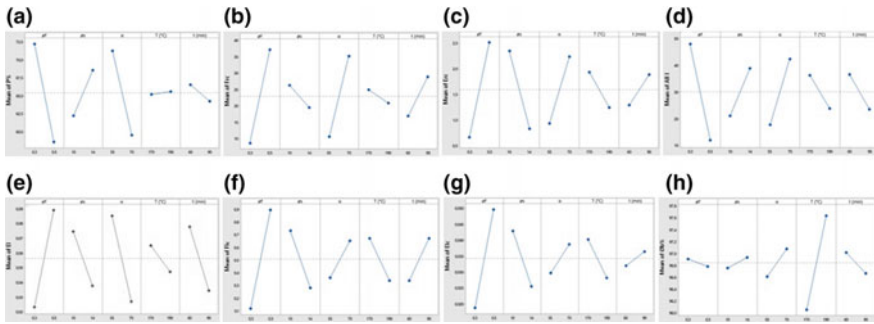


Fig. 5 Main effects plots for: **a** $P\%$, **b** F_{rc} , **c** E_{rc} , **d** All_I , **e** E_I , **f** F_{lc} , **g** E_{lc} , **h** $\varnothing_{b\%}$

Table 4 Linear final models

	R^2 (%)	R^2 (adj) (%)	S	Final models
$P\%$	96,71	94,25	2,49	$P\% = 73,79 - 68,38 \varnothing_f + 1,581 \varnothing_s - 5,888 \alpha$
\varnothing_b (%)	88,62	80,08	0,42	\varnothing_b (%) = $83,46 + 0,235 \alpha + 0,0793 T$ (°C) - $0,0117 t$ (min)
F_{rc} (N)	98,71	97,00	3,74	F_{rc} (N) = $-44,0 + 143,3 \varnothing_f - 1,700 \varnothing_s + 12,31 \alpha + 0,4003 t$ (min)
E_{rc} (MPa)	86,63	76,60	0,75	E_{rc} (MPa) = $2,45 + 9,24 \varnothing_f - 0,379 \varnothing_s + 0,651 \alpha$
All_I (mm)	84,49	72,86	14,31	All_I (mm) = $48,7 - 180,6 \varnothing_f + 4,48 \varnothing_s + 12,33 \alpha$
E_I (MPa)	96,92	92,80	0,015	E_I (MPa) = $0,1440 + 0,3300 \varnothing_f - 0,00925 \varnothing_s - 0,02900 \alpha - 0,001450 t$ (min)
F_{lc} (N)	92,68	74,38	0,29	F_{lc} (N) = $2,47 + 3,90 \varnothing_f - 0,1129 \varnothing_s + 0,146 \alpha - 0,0167 T$ (°C) + $0,01110 t$ (min)
E_{lc} (MPa)	98,06	95,48	0,004	E_{lc} (MPa) = $0,1328 + 0,1550 \varnothing_f - 0,004375 \varnothing_s + 0,00450 \alpha - 0,000600 T$ (°C)

R^2 is the coefficient of determination; R^2 (adj) is the coefficient of determination adjusted to the number of factors; S is the estimated standard deviation of the error term in the models

plots (Fig. 5). According to the p-value, which is the probability (within a 95% confidence interval) that the factor has a significant impact on the response, factorial analysis showed that the five studied factors exhibit different effects on each response.

Then, we developed linear models establishing relationship between each response and their significant factors. The prediction models for responses, given in Table 4, evaluate the effect of each variable to responses. The ANOVA indicates that regression models are adequate due to high coefficient of determination R^2 .

Cover factor and porosity

Only monofilament diameter, stent diameter, and braiding angle are important factors for porosity ($P\%$) (and cover factor ($CF\%$)). In fact, porosity increases with the increase of stent diameter. Stents with higher monofilament diameter and higher braiding angle show a lower porosity. The analysis of variance for the porosity ($P\%$)

has demonstrated that the model is adequate (p -value $< 0,05$) and explains the 96,71% of the variability in porosity at the 95% confidence level. Nitinol stents commonly used have porosity $>70\%$ [3] and by observing the porosity values of our developed stents, we find that only the stents S1, S3, S4, and S7 have $P_{\%}$ values between 70–80%.

Unchanged bending diameter

The percentage of unchanged bending diameter of PET-braided stents depends essentially on the braiding angle and the heat-setting conditions (temperature and duration). The most remarkable is that it increases when the heat-setting temperature increases.

In fact, heat-setting increased the handling of the stents during testing of the samples. Also, stents having a higher braiding angle have a greater flexural resistance resulting in a higher percentage of unchanged bending diameter. The advantage is that all our manufactured stents did not lose their initial diameters under bending, which is not the case for metallic stents. According to the obtained values, the percentages of unchanged bending diameters of the developed stents are all greater than 90% compared with 75% for Gore's Nitinol stents [3].

The analysis of variance for the response (\varnothing_b (%)) has demonstrated that the model is adequate (p -value $< 0,05$) and explains the 88,62% of the variability in unchanged diameter at the 95% confidence level.

Radial compression

The radial compression force of PET-braided stents depends essentially on the monofilament diameter, stent diameter, braiding angle, and heat-setting time. The Young's modulus of these stents depends essentially on the monofilament diameter, the stent diameter, and the braiding angle. Radial compression force and Young's modulus increase when the monofilament diameter, braiding angle, and heat-setting time increase and decrease when the stent diameter increases. Indeed, a larger monofilament diameter leads to a greater thickness of the stent, which results in a higher resistance to radial compression. In addition, a larger monofilament diameter improves the cover factor, hence improves the compactness of the stents. Also, the radial compression leads to the bending of the monofilaments. Those with a higher diameter are more resistant to bending, resulting in a greater resistance to radial compression.

Stents with a higher braiding angle are more resistant to radial compression. For higher braiding angles, the yarns are deposited more and more towards the transverse axis, resulting in greater resistance to transverse forces acting during radial compression. In addition, a higher braiding angle also improved the cover factor and compactness of the stent resulting in a higher resistance to radial forces. However, a too high braiding angle can also reduce the overlapping of the monofilaments (as they are arranged more parallel to one another), and increase the risk of slipping during compression.

By observing the values of the radial compression force F_{rc} and the Young's modulus E_{rc} of the samples, we find that S6 has the highest F_{rc} and E_{rc} values.

Comparison with Gore's Nitinol stents, having a radial compression force of 1,47 to 12,74 N [14], shows that S2, S5, S6, S7, and S8 have a very high F_{rc} .

The analysis of variance for the responses (F_{rc} (N)) and (E_{rc} (MPa)) has demonstrated that the models are adequate (p -value $< 0,05$) and explain the 98,71% and 86.63% of the variability in the radial compression force and Young's modulus at the 95% confidence level.

Longitudinal elongation

The longitudinal elongation of PET-braided stents depends essentially on the monofilament diameter, stent diameter, and braiding angle. Apart from these three parameters, the Young's modulus of these stents also depends on the duration of heat-setting. Elongation decreases significantly when the monofilament diameter increases, and increases when the stent diameter and braiding angle increase. We can also notice that the elongation is lower when the heat-setting conditions (temperature and duration) are higher. The longitudinal stiffness of the stents increases as the monofilament diameter increases and decreases as the stent diameter and heat-setting conditions increase. Also, the longitudinal stiffness increases as the braiding angle decreases because the stent has undergone a larger pull [7].

By observing the obtained values of samples elongation All_1 and Young's modulus E_1 , we find that stents with higher elongation have the lower rigidity. Comparing with Gore's Nitinol stents [14], having an elongation values between 4 and 49 mm, we find that all our stents (except S1) admit comparable values.

Longitudinal compression

The longitudinal compression force of PET-braided stents depends on the monofilament diameter, stent diameter, braiding angle, and heat-setting conditions. Indeed, the longitudinal compression force increases as the monofilament diameter, braiding angle, and heat-setting time increase and decrease as the stent diameter and heat-setting temperature increase.

The corresponding Young's modulus depends on the monofilament diameter, stent diameter, braiding angle, and heat-setting temperature. In fact, it increases when the monofilament diameter and the braiding angle increase, and decreases when the stent diameter and the heat-setting temperature increase.

According to Rebelo et al. [3], stents with larger monofilament diameter have a higher longitudinal compression force due to their high flexural rigidity, as in longitudinal compression stents are also subjected to flexion and buckling. An increase in the stent diameter led to a decrease in the longitudinal compression force. Stents with higher diameter have a lower cover factor, so a lower structural integrity, resulting in a lower resistance to axial compression forces.

An increase in the longitudinal compression force with the increase of braiding angle can be clearly observed. This was attributed to a better cover factor when the braiding angle is higher, which also results in better structural integrity and greater resistance to compression.

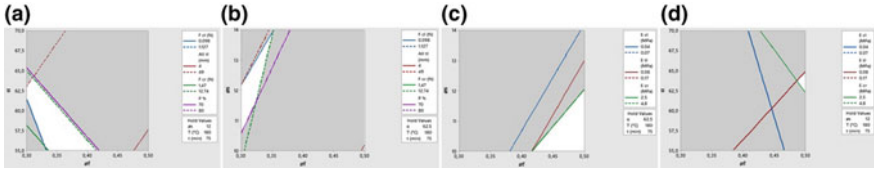


Fig. 6 Overlaid contour plots of: **a** F_{rc} , F_{lc} , All_l and $P\%$ when θ_f and α change while the other factors (θ_s , T and t) were set at medium levels, **b** F_{rc} , F_{lc} , All_l and $P\%$ when θ_f and θ_s change while the other factors (α , T and t) were set at medium levels, **c** E_{rc} , E_{lc} and E_l when θ_f and θ_s change while the other factors (α , T and t) were set at medium levels, **d** E_{rc} , E_{lc} and E_l when θ_f and α change while the other factors (θ_s , T and t) were set at medium levels

By observing the obtained values of the samples longitudinal compression force F_{lc} and Young's modulus E_{lc} , we find that stents having an important longitudinal compression force admit the higher stiffness. Comparing with Gore's Nitinol stents [14] having longitudinal compression force values between 0,098 and 1,127 N, we find that the stents S2, S3, S4, S5, S7, and S8 admit similar values.

Simultaneous optimization

We performed overlaid contour plots (Fig. 6) in order to determine optimum stent's manufacturing settings best satisfying the following requirements: radial compression force F_{rc} : 1,47–12,74 N, longitudinal compression force F_{lc} : 0,098–1,127 N, longitudinal elongation All_l : 4–49 mm [14], and porosity $P\%$: 70–80% (cover factor $CF_{\%}$: 20–30%).

Considering the most common significant factors for those responses (θ_f , θ_s and α), compromise regions were obtained only for F_{rc} , All_l , F_{lc} , and $P\%$ when θ_f and α change (Fig. 6a) and when θ_f and θ_s change (Fig. 6b).

Since there is no data showing the exact values of Young's modulus for radial compression, longitudinal compression or longitudinal elongation of stents, optimum stent's manufacturing settings are chosen in order to obtain the highest values of stiffness: E_{rc} : 2,5–4,8 MPa, E_{lc} : 0,04–0,07 MPa, and E_l : 0,08–0,17 MPa. In fact, stents must have the sufficient stiffness to expand the stenotic part and to prevent its collapsing [15–17]. Considering the most common significant factors for those responses (θ_f , θ_s and α), compromise regions were obtained only for E_{rc} , E_{lc} and E_l when θ_f and θ_s change (Fig. 6c) and when θ_f and α change (Fig. 6d).

The optimum values obtained by analyzing all the overlaid contour plots are: θ_f : 0,33–0,42 mm; θ_s : 10,5–12,5 mm and α : 61–65°.

4 Conclusions

In this study, the effects of five manufacturing parameters on main performances of PET-braided vascular stents were investigated in order to determine the most significant ones. Factorial analysis has shown that the entire considered factors are

significant but not for the same response. Indeed, the most common significant factors are monofilament diameter, stent diameter, and braiding angle, whereas the least important factors are heat-setting temperature and heat-setting time.

Comparing to the 6 mm Gore's Nitinol vascular stents, the developed PET stents showed an excellent unchanged bending diameter (all >75%) and generally good performances.

Furthermore, the obtained optimum stent's manufacturing settings can lead to PET-braided stents as performant as Gore's Nitinol ones. The optimum values obtained by analyzing all the overlaid contour plots are: ϕ_f : 0,33–0,42 mm; ϕ_s : 10,5–12,5 mm and α : 61–65°.

PET-braided stents show a huge potential to replace metallic commercial ones but work will continue in order to determine the most suitable braiding and heat-setting parameters which will lead to the ideal stent. For that, future work will concentrate on the evaluation of other stents performances, the determination of other braiding parameters and heat-setting conditions effects, and the study of the in vitro fatigue behavior of PET-braided vascular stents.

References

1. Sobocinski, J. (2013). *Fonctionnalisation de stents vasculaires par des matrices polymères contenant des molécules bioactives* (p. 2013). Médecine humaine et pathologie: Université du Droit et de la santé-Lille II.
2. Wang, Z., Li, N., Li, R., Li, Y., & Ruan, L. (2014). Biodegradable intestinal stents: A review. *Progress in Natural Science: Materials International*, 24, 423–432.
3. Rebelo, R., Vila, N., Figueiro, R., Carvalho, S., & Rana, S. (2015). Influence of design parameters on the mechanical behavior and porosity of braided fibrous stents. *Materials and Design*, 2015, 237–247.
4. Van der Giessen, W., Slager, J., Van Beusekom, H., Van Ingen Schenau, S., Huijts, A., Schuurbiens, C., et al. (1992). Development of polymer endovascular prosthesis and its implantation in porcine arteries. *Journal of Interventional Cardiology*, 5(3), 175–185.
5. Irsale, S., & Adanur, S. (2006). Design and characterization of polymeric stents. *Journal of Industrial Textiles*, 35(3), 189–200. (January 2006).
6. Saito, Y., Tanaka, T. & Andoh, A. (2007). Usefulness of biodegradable stents constructed of poly-L-lactic acid monofilaments in patients with benign esophageal stenosis. *World Journal of Gastroenterology*, 13, (29), 3977–3980. ISSN 1007-9327. (2007 August 7).
7. Yuksekkaya, E., & Adanur, S. (2009). Analysis of polymeric braided tubular structures intended for medical applications. *Textile Research Journal*, 79(2), 99–109.6.
8. Kannan, Y., Salacinski, J., Butler, E., Hamilton, G., Seifalian, M. (2004). Current status of prosthetic bypass grafts: A review. *Wiley InterScience, J Biomed Mater Res Part B: Appl Biomater*, 74B, 570–581.
9. Freitas, P., De Araujo, D., Zu, W., & Figueiro, R. (2010). Development of weft-knitted and braided polypropylene stents for arterial implant. *Journal of the Textile Institute*, 101(12), 1027–1034.
10. Kyosev, Y., & Aurich, M. (2016). Investigations about the braiding angle and the cover factor of the braided fabrics using Image Processing and Symbolic Math Toolbox of Matlab. In *Woodhead Publishing Series in Textiles* (Number 177, pp. 549–569). Advances in Braiding Technology, Specialized Techniques and Applications.

11. Wang, C., & Zhang, P. (2016). In vitro degradation behaviours of pdo monofilament and its intravascular stents with braided structure. *AUTEX Research Journal*, 16(2), 80–89.
12. Hoi, Y., Lonita, N., Tranquebar, V., Hoffmann, R., Woodward, H., Taulbee, B., et al. (2011). Flow modification in canine intracranial aneurysm model by an asymmetric stent: studies using digital subtraction angiography (DSA) and image-based computational fluid dynamics (CFD) analyses. *PubMed Central*.
13. Rebelo, R., Vila, N., Fangueiro, R., Carvalho, S., & Henriques, M. (2014). Development of braided fiber-based stents. *Innovation in Medicine and Healthcare*, 207, 135–144.
14. Goremedical (2011): Mechanical Properties of Nitinol Stents and Stent-Grafts: Comparison of 6 mm Diameter Devices, *L. Gore & Associates Inc.*
15. Schreiber, F., Schuster, P., Borinski, M., Vogt, F., Blindt, R., & Gries, T. (2010). Improving the mechanical properties of braided shape memory polymer stents by heat setting. *AUTEX Research Journal*, 10(3), 73–76.
16. Smewing, J. (2015). Testing the mechanical strength of coronary stents. <http://textureanalysisprofessionals.blogspot.com/2015/08/testing-mechanical-strength-of-coronary.html>, Tuesday, 4 August 2015.
17. Yoshino, D., & Sato, M. (2012). Design and evaluation of self-expanding stents suitable for diverse clinical manifestation based on mechanical engineering. *Mechanical Engineering*, pp. 182–208. ISBN: 978-953-51-0505-3.

Experimental and Numerical Investigation of Triaxial Braid Reinforcements

Boris Duchamp, Yordan Kyosev, Xavier Legrand and Damien Soulat

Abstract Triaxial braided reinforcements are extensively used as main constituent materials in various biomedical and composite applications. The material parameters, and the choice of process parameters during the braiding process, have a significant influence on the geometrical and mechanical properties of these reinforcements. In this study, the manufacturing on a braiding loom of triaxial braids with a large range of braiding angle is presented. On these samples geometrical properties, as bias yarn length, crimp, linear mass, are experimentally identified in function of the braiding angle. From uniaxial tests, the specific tensile behavior of these braided fabrics is characterized. These results are compared with analytical models described in the literature. Associated to this experimental approach, the geometry of these triaxial braids is numerically modeled thanks to TexMind Braider software dedicated for three-dimensional creation of braided structures. Comparison between characteristics experimentally identified and computed is analyzed.

1 Introduction

The internal geometry of textile reinforcement is an important factor in the reinforcement performance during composite manufacturing and in-service life of the composite material. For the manufacturer, impregnation of the reinforcement is governed by its porosity (size, distribution, and connectivity of pores). For mechanical requirements load transfer from the matrix to the reinforcement is governed by the fiber orientation, which plays a paramount role in the composite stiffness; Authors based on the description of the internal geometry of the textile on

B. Duchamp · X. Legrand · D. Soulat (✉)
GEMTEX, ENSAIT, Univ. Lille North of France, 2 allée Louise et Victor Champier,
59056 Roubaix, France
e-mail: damien.soulat@ensait.fr

Y. Kyosev
Hochschule Niederrhein—University of Applied Sciences, Krefeld, Germany

data obtained by optical or microscopical observations on dry textiles and on cross-sections of textile composites by tomography [1, 2]. These geometrical descriptions were then used to calculate the homogenized mechanical properties of the textile-based composites [3]. The major drawback of these models was their dependency on empirically obtained descriptions of the internal geometry of the textile. Realistic geometric representation of fabrics is essential for modeling of mechanical and physical properties of textiles and textile composites. For classical woven or 3D-woven structures, a lot of work were developed, for example, the development of softwares as Texgen or Wisetex [4, 5], few work concerns the comparison of geometrical models dedicated to braid reinforcement [6] with braids structures manufactured.

Braiding process deposits continuous, intertwined fiber tows to create a desired reinforcing braid architecture [7] and offers several advantages like control over the fiber deposition angle and fast fiber deposition rate [8–14]. The braiding angle, defined as the angle between the longitudinal direction of the braided preform and the deposited fibers, is a key parameter in the kinematic analysis [9, 15–19] of the process and of its influence on the mechanical behavior of braided composite [10–12, 19–27].

Contrary to the behavior of dry woven fabrics [28, 29] the behavior of braids reinforcement remains few studied. Potluri et al. [11] have focused on geometric modeling and micromechanical modeling of non-orthogonal structures, establishing the parallel between braided structures and sheared woven structures. Harte et al. [30] presents experimental results on the behavior of tensile of biaxial braids, and show the increasing of nominal axial strain in function of the braiding angle. Hristov et al. [31] and Dabiryan [32] describes the nonlinear responses under tensile loads in the axial direction of biaxial braids. DelRosso et al. [33] compare tensile behaviors of Dyneema®SK75 and Kevlar®49 biaxial micro braids. The understanding of tensile mechanics of braided materials is the subject of works of Rawal [34–37], and in a review [38] the key parameters that control the tensile properties of biaxial and triaxial braided reinforcements are described with models associated. Concerning triaxial braids some recent works [39–41] have shown that specific tensile behavior labeled “double peak”, can be decomposed to the behavior of axial yarns followed by the extension of bias yarns. This specific behavior depends on the braiding angle but also raw materials.

In this paper, production and characterization of triaxial braids are presented. Identification of structural characteristics, as braiding angle, linear density, and at mesoscopic scale, crimp, and yarn trajectory in function of braiding process are detailed. Tensile behavior of all braid samples produced is identified. Associated to this experimental approach, comparisons with models obtained with the TexMind Braider [42] software, dedicated for three-dimensional creations of braided structures, are presented.

2 Materials and Methods

For the production of braids, multifilament of high-density polyethylene, without twist, was used, characteristics are specified in Table 1.

From this polyethylene multifilament for axial (denoted 0° , on Fig. 1) and bias yarns, triaxial braids (schematized on Fig. 2) were produced in a horizontal braiding machine (Herzog GLH 1/97/96–100).

This loom (Fig. 1) has been previously described for the production of a complex shaped reinforced thermoplastic composite part made of commingled yarns with integrated sensor [43], or comingled (flax/PA66) braided reinforcement [44]. The maximum number of carriers is 96 for bias yarns and 48 for the axial yarns. For this study, two polyethylene multifilaments were used per bobbins. In a braiding machine, the gear train is typically circular, consisting of specialized gears called horn gears composed of a spur gear bottom and slotted gear top. These gears move two sets of bobbin carriers in opposite directions so that the yarns interlace to produce the braid. The motion of the bobbins is accomplished by horn gears and characterized by the number of horn gear (N_{HornGear}), the carrier rotational speed ($\omega_{\text{HornGears}}$), and the production speed (V_{braid}).

Bobbin carriers control the tension in the yarns, typically by interchangeable springs. These process parameters allow to control the braiding angle, denoted β and defined on Fig. 2, and can be used to compute it analytically [14, 19, 45], for example, by the relation (1):

Table 1 Properties of high-density polyethylene multifilament

Linear density (Tex)	169
Twist (tr/m)	0
Elongation (%)	3,9
Tensile strength (N)	517 (\pm 7)



Fig. 1 Braiding loom (back and side view)

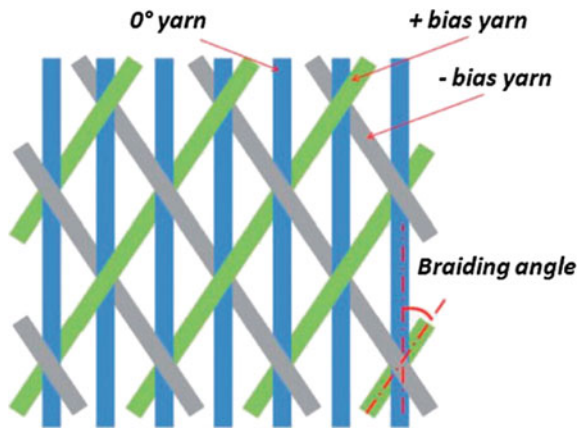


Fig. 2 Scheme of triaxial braid

$$\tan(\beta) = \frac{\omega_{\text{Horn gear}} D}{N_{\text{Horn gear}} V_{\text{braid}}} \quad (1)$$

Where $N_{\text{Horn gear}}$ is the number of horn gear on the machine, $\omega_{\text{Horn Gears}}$ the carrier rotational speed, D the diameter of the braid and V_{braid} the production speed. For this study, samples of triaxial braids have been manufactured with different values of these process parameters, presented in Table 2.

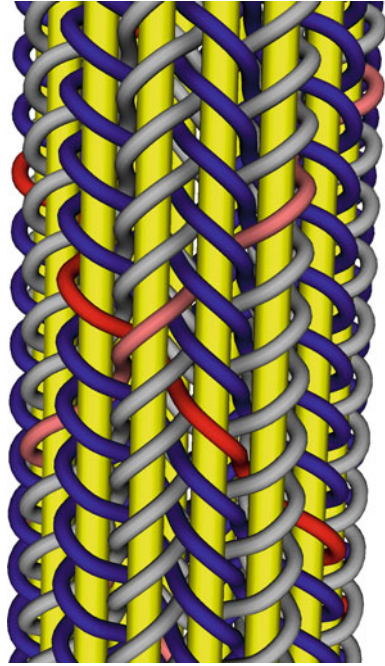
For each of these triaxial braids, different characteristics are experimentally measured. First, geometrical properties associated to bias yarn length, crimp but also linear mass and braiding angle. In a second step, mechanical properties are identified by uniaxial tensile tests.

The measure of the length of a bias yarns is done manually. From a braid, bias yarns (underlined on Fig. 3, as an example) are extracted, and their length is

Table 2 Triaxial Braids produced, process parameters values

Name of samples	Number of Bias yarns	Number of Axial yarns	V_{braid} (m/h)	$\omega_{\text{Horn Gears}}$ (Tr/min)
1	192	96	144	47,01
2	192	96	108	46,21
3	192	96	72	47,03
4	192	96	55	45,16
5	192	96	36	44,54
6	192	96	27	62,84
7	192	96	18	63,74

Fig. 3 Representation of braids and bias yarns



measured. Values are reported to 1m length of braid and represent the length of a bias yarn in the structure.

This bias yarn length can be computed, analytically, for 1 m braid, from the braiding angle, β , by the relation is given in Eq. (2), [46]:

$$L_{bias\ yarn} = \frac{1}{\cos(\beta)} \quad (2)$$

Due to the interlacing in a triaxial braid, and compared to biaxial braids, higher crimp for bias yarns is constated, as described by Endruweit and Long [47], and Kier et al. [27]. Crimp is not taken into account in Eq. 2. Consequently, at the microscopic scale, the crimp is experimentally measured. Braids are slightly (without pressure) impregnated of resin and cross-section can be cut to identify the crimp ratio, as illustrated on Fig. 4.

The braiding angles are measured during the braiding process and when braids are removed from the braiding machine. These measures are realized by optical techniques. Pictures of braids were taken and these pictures were analyzed using the IMAGEJ, a public domain image-processing software [48], to measure angle 10 times at different places along the width and the length of the sample (Fig. 5). An

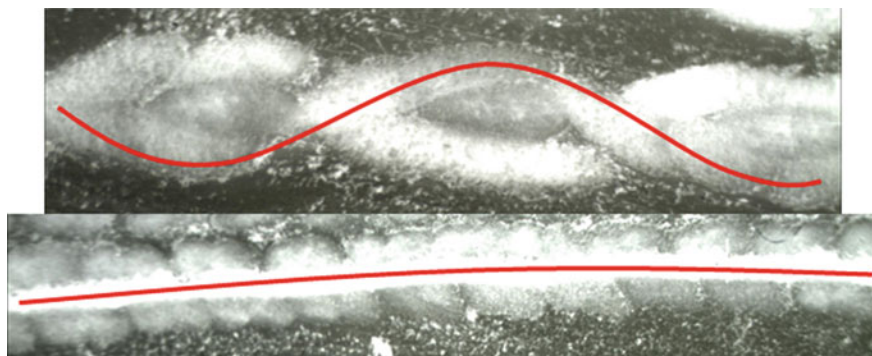


Fig. 4 Illustration of crimp of the bias yarn (up) and axial yarn (down)

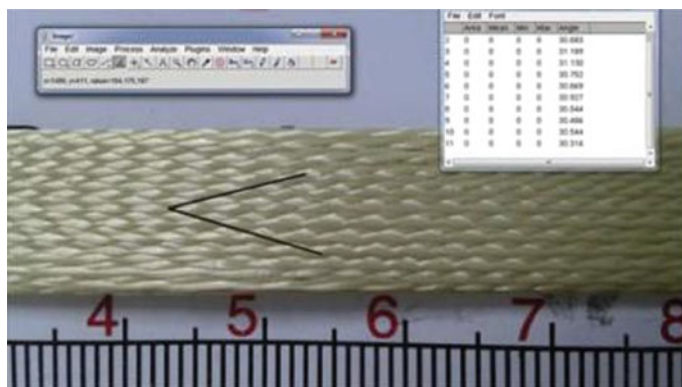


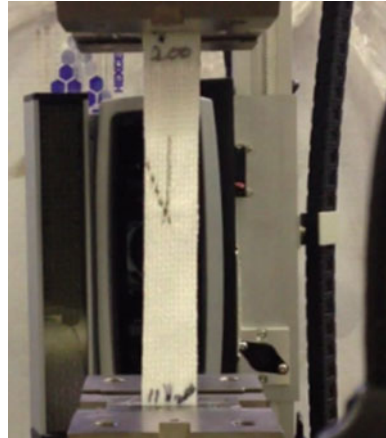
Fig. 5 Image J software to measure the braiding angle

average of these values is computed to obtain the braiding angle. The standard deviation of these measures is 0.5° .

Some studies [9] use the cover factor to characterize braids which are defined by the ratio of mandrel surface covered by the tows at the end of the braiding process. In this study, braids manufactured are characterized by their linear mass, in weighing 10 samples by configuration and assigned to their lengths. The precision of the balance is 0.001 g.

Additionally, to these geometrical properties (bias yarn length, crimp, braiding angles, linear mass) uniaxial tests on braids were conducted on an Instron tensile machine with a 250 kN load cell. According to the standard NF ISO 13 934, the test speed is equal to 50 mm/min. Ends of the sample are maintained by composites constituted by resin epoxy and UD glass, to avoid the sliding under the grips of the tensile machine. The results are obtained from the analysis of 10 samples tested for each configuration. All the tensile tests were realized in the axial direction, as illustrated in Fig. 6.

Fig. 6 Triaxial braid during uniaxial tensile test

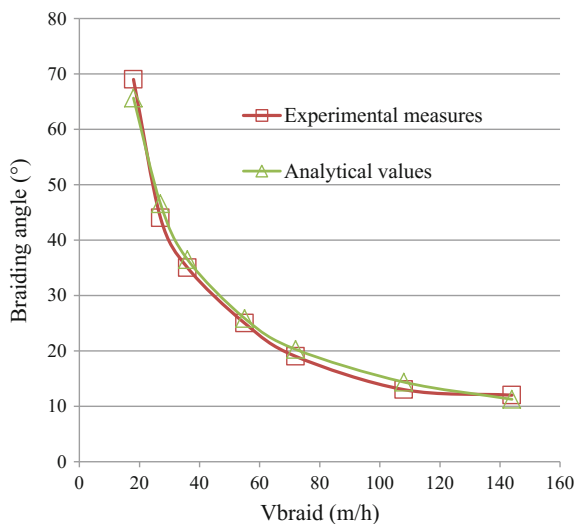


3 Geometrical and Tensile Properties of Triaxial Braids

For each sample of triaxial braids produced with braiding parameters, presented Table 2, braiding angles are measured experimentally, thanks to the protocol presented before. We report on Fig. 7 values of braiding angle in function of production speed (V_{braid}). Experimental values are compared to analytical values given by the Eq. 1.

These process parameter values were selected to have a wide range of braiding angles. The good adequacy, between values obtained experimentally and predicted by the analytical relation, demonstrates the good control of process parameters on the braiding loom.

Fig. 7 Braiding angles of triaxial braids versus production speed



Thanks to the protocol described before, crimp ratio is experimentally measured on triaxial braid samples. Table 3 reports values averaged on all configurations of braids manufactured, for the axial yarns and for the bias yarns.

Kier et al. [27] have shown, by micropictures of braids, the importance of crimp. The influence of the interlacing of the yarns creates a complex load path that reduces the effective stiffness of the composite in the longitudinal direction [49, 50], and the peak stresses occur at the undulating region and along the edges of the tow [26, 51]. Compared to biaxial or triaxial braids with a weaker braiding angle [52], we can underline that the crimp ratio is higher and especially for bias yarns.

In these braids samples, characterized by their braiding angles, bias yarn length and linear mass are measured. On the same Fig. 8, these two characteristics are superimposed with two scales of values (on y-axis, right, and left, respectively, for the linear mass and bias yarn length).

These two properties exhibit the same trend with the increase of the braiding angle. Concerning the bias yarn length, measured for all samples, on 1 m braid length, the increase of braiding angles involves a longer path for bias yarns and consequently a larger bias yarn length. These experimental values will be compared in Sect. 4, with those estimated by Texmind software. This augmentation in function of the braiding angle affects obviously the linear mass of braids, as shown in Fig. 8, which increases with the braiding angle.

If analytical relations predicting the cover factor in function of braiding parameters are given in literature [9, 15–19], models concerning the linear mass are

Table 3 Crimp ratio measured on triaxial braids

Parameter	Axial yarns	Bias yarns
Average crimp	4% (\pm 0.2%)	16% (\pm 1%)

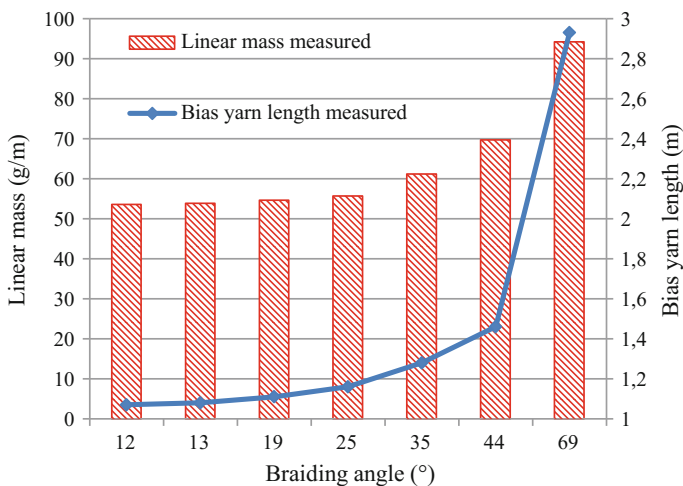
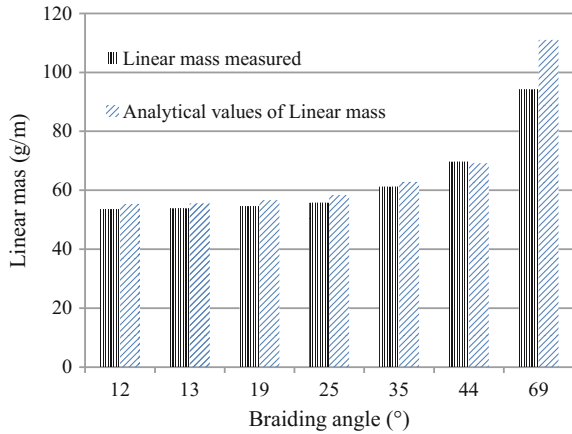


Fig. 8 Linear mass and bias yarn length of triaxial braids

Fig. 9 Linear mass of triaxial braids. Comparison between experimental and analytical values



unusual. In a previous study [52], the analytical relation has been proposed to compute the linear mass of braids (biaxial or triaxial) from the braiding angle, the linear density of the raw material and the number of yarns. For triaxial braids, this relation is given by the Eq. 3:

$$[M_{lin, triax} = \frac{N_{Bias}TC_{Bias}}{\cos(\beta)} + N_{Axial}TC_{Axial}] \tag{3}$$

N_{Bias} and N_{Axial} are, respectively, the number of bias (192) and axial (96) yarns, T the linear density of the yarn (value specified in Table 1), C_{Bias} and C_{Axial} are the crimp factor of bias and axial yarns (values measured in Table 3).

We report in Fig. 9, the comparison between values measured experimentally and those obtained by this analytical relation (Eq. 3). This figure shows a strong correlation between these results; The previous study [52] on biaxial and triaxial braids has proven the necessity to consider the crimp in the model predicting the linear mass. Let us denote that for a high braiding angle (Fig. 9) the difference between the analytical and the measured value is higher. For this triaxial braid, we can suppose that the crimp is higher that, the averaged value (specified in Table 3) and used in Eq. 3.

Tensile tests in axial direction have been conducted on triaxial braids. Tensile behavior of braid structures is illustrated by load-deformation curves, as presented in Fig. 10. The specific tensile behavior characterized by a “double peak” phenomena has been discussed and explained in previous studies [39–41, 52]. This behavior can be divided into two parts. First with the contribution of the axial yarns until their break (first peak) following to a load recovery from the bias yarns (second peak). In [39, 52] it was shown the dependence of the braiding angle on this type of behavior, for triaxial braids with a small braiding angle, or for biaxial braids (without axial yarns) the second peak is not present.

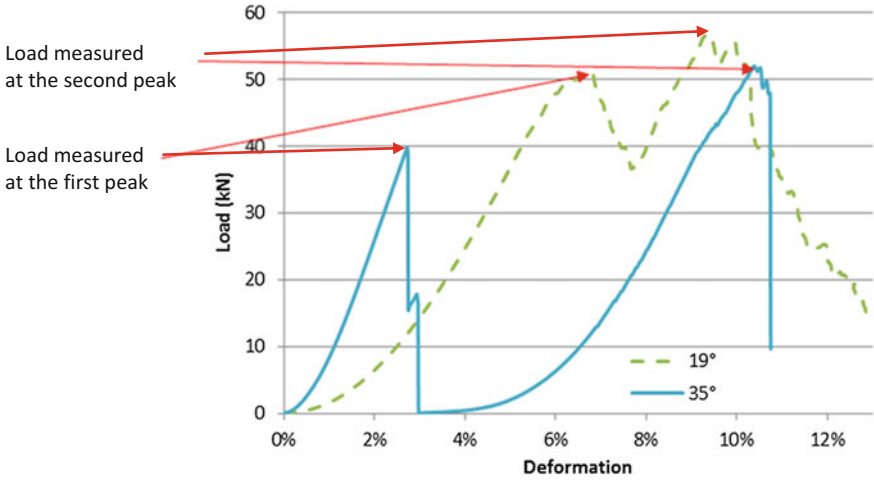


Fig. 10 Tensile behaviors in axial direction of triaxial braids of 19° and 35° braiding angles

For triaxial braids manufactured we report in Fig. 11, mechanical behaviors of two triaxial braids, (of respectively, 19° and 35° braiding angles) which present a “double peak” phenomena. The evolution of the load modulus (defined by slopes of linear parts of these tensile curves) in function of the braiding angle has been discussed, in a previous study [52]. In this paper from these tensile curves, maximum loads at each peak, as defined on the Fig. 10, are measured for each triaxial braid. Values of maximum load are specified on Fig. 11.

This figure shows that maximum loads decreases significantly when braiding angle increase. This evolution is constated for the first peak until a limit angle (35°,

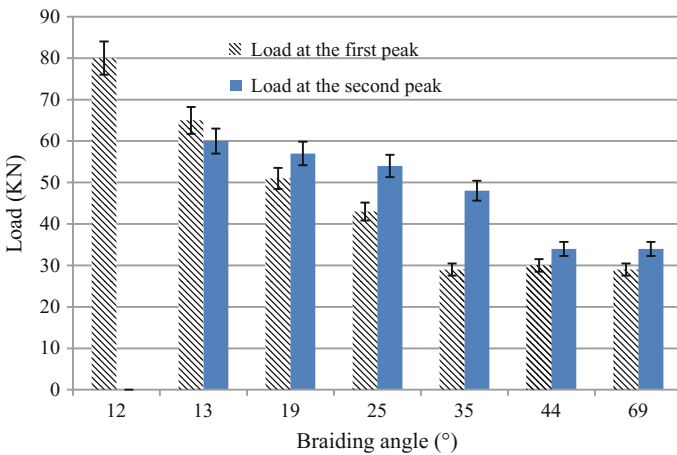


Fig. 11 Maximum loads measured for triaxial braids

for the triaxial braids considered in this study) from which the maximum load, at the first peak, remains constant. The evolution of the maximum load at the second peak follows the same trend, until a braiding angle of 44° where the maximum loads, at the second peak, become constant. Triaxial braid with the smaller braiding angle (12°) does not present a double peak. For the first part of the tensile behavior of triaxial braids, the evolution presented on the Fig. 11, shows that the maximum load does not depend only of the contribution of axial yarns (in the load direction) but the bias yarns contribute to the performance of the triaxial braids. Compared to the previous experimental study [52] conducted on the same raw material, but with just one yarn on bobbins for axial and bias position, and for which values of maximum load were weaker, we can conclude that the maximum load at the first peak depends on the following parameters: linear density of raw material, number of yarns in axial and bias position and the braiding angle. For the second part of the tensile behavior, called second peak, the measure of the evolution of the braiding angle during the tensile test [52, 53] has shown, especially for triaxial braids with an initial large braiding angle, a significant reduction of this angle, which can explain the decreasing of the maximum load value until an asymptotic level.

4 Geometrical Modeling of Triaxial Braids

Associated to the manufacturing of triaxial braids on the braiding loom and to the characterization of the geometrical and mechanical properties, described before, the computer-aided design (CAD) software for braiding TexMind Braider [42] has been used.

This software, based on the relations for interlacement of the yarns during the braiding process, is a generalized geometrical model able first to generate 2D and 3D geometries of braids by computation of the yarn axis coordinates from datas given by user (Numbers of yarns, section of yarns, diameter of the braids, type of braids, etc....). The description of this software can be found in [54–57] and has been extended to a generalized geometrical approach for modeling flat and tubular braided structures, with arbitrary floating length and filaments in the yarn based on the braiding machine [58].

The aim of this part is to compare measured properties presented before to those computed by the software on all the triaxial braids studied in this work.

For two triaxial braids with respectively a weak (19°) and a large braiding angle (69°), we represent Fig. 12 the comparison between the triaxial braids simulated by the software and those manufactured. Small windows are associated with the computation of the braiding angle obtained on the modeled geometry or from the measure by the Image J software.

Same process and raw material parameters have been given, as input datas, in the software, especially the choice to use, for this manufacturing, 2 yarns of each bobbins. The braiding angles computed on the modeled geometries are very close to the values measured.

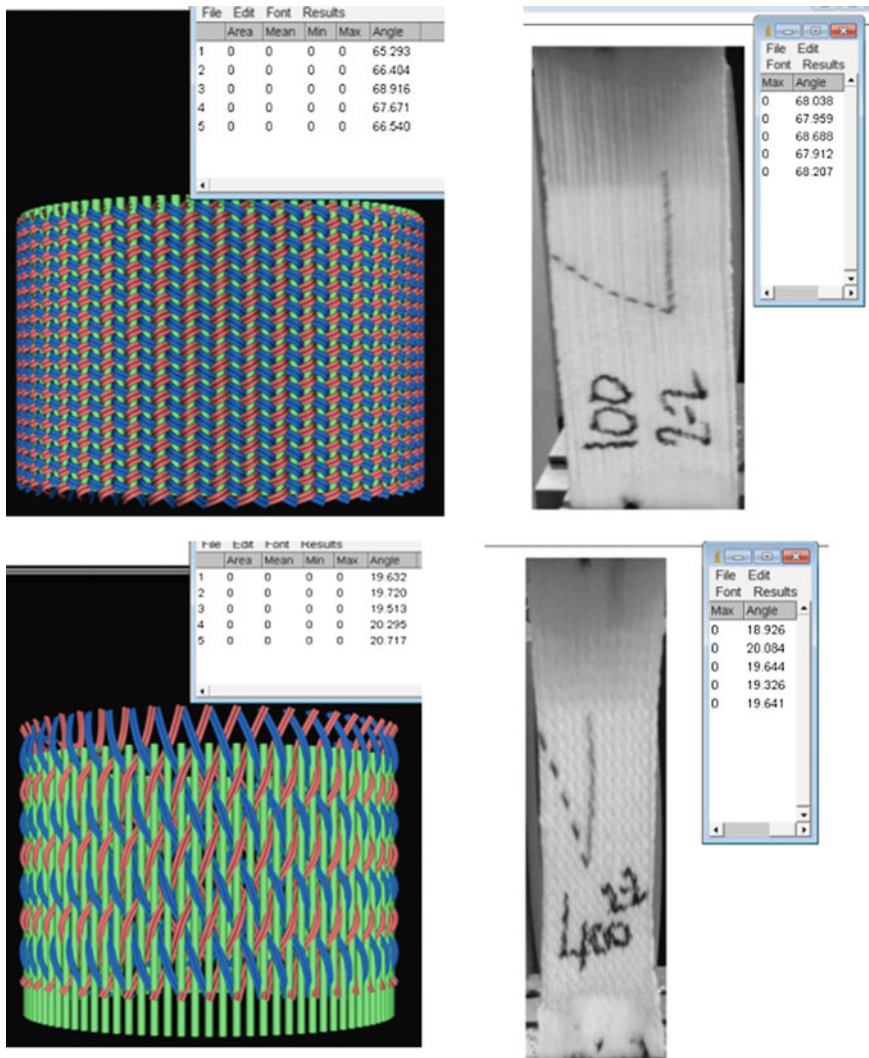


Fig. 12 Geometric model of triaxial braids. (Up : 69° braiding angle; down: 19° braiding angle). Comparison of the braiding angle computed (left) and measured (right)

Associate to the generation of braids models, TexMind Braider software is also able to compute braids properties as linear mass and the bias yarn length. We report in Table 4 values of these characteristics obtained by the simulation and identified experimentally, as described in previous sections, for all triaxial braids studied. All the results are given for one linear meter of the produced braid.

Comparisons on these quantities are illustrated on the Fig. 13, in function of the braiding angles.

Table 4 Linear mass and bias yarn length identified from models and measures

Samples	Computed (1 m of braid)		Measured (1 m of braid)	
	Linear mass (g/m)	Bias yarn length (m)	Linear mass (g/m)	Bias yarn length (m)
12	48,84	1,02	53,60	1,07
13	52,03	1,09	53,90	1,08
19	50,46	1,06	54,63	1,11
25	52,15	1,09	55,74	1,16
35	57,93	1,22	61,19	1,29
44	65,69	1,39	69,70	1,46
69	87,38	2,78	94,24	2,92

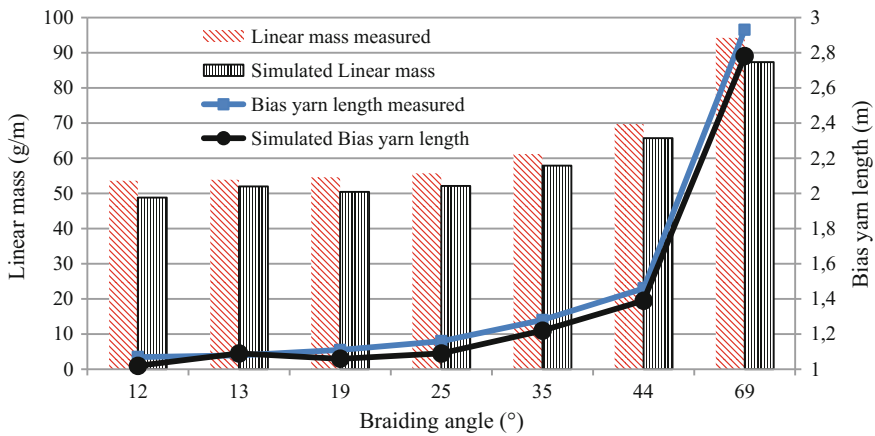


Fig. 13 Comparisons between geometrical properties of triaxial braids identified from models and measures

Concerning the evolution of the bias yarn length in function of the braiding angle, the Fig. 13 shows the same trend for experimental measures and values predicted by TexMind Braider Software. Experimental values are slightly different than those given by the software. Values computed by the software are based on analytical relation given in Eq. 2.

For the linear mass, values measured and computed by the software follow, also, the same trend with the increasing of the braiding angle, phenomenon which has been explained previously, and values are close. However, from the Fig. 13 we can show that computed values underestimate experimental values which were well-approximated (Fig. 9) by the analytical relation specified in Eq. 3 (except for higher braiding angle). Taking into account of the crimp for the prediction of linear mass can explain differences between measured and computed values.

Besides the computation of geometrical properties of braids, as presented before, the Texmind Braider software proposes to estimate maximum tensile strength, from

input data as the tensile load of yarns (specified in Table 1), the numbers of yarns and the braiding angle of the braid. We use this option, in fact, to compare with load values identified experimentally (presented Fig. 11) during tensile tests.

In Fig. 14 we report, in function of braiding angles of triaxial braids, experimental values of maximum tensile strengths measured at the first and the second peak, as discussed previously, numerical values computed by the software according to two models. The first model concerns the contribution of axial yarns to the maximum strength, denoted F_{axial} , computed from the number of axial yarns N_{axial} and the tensile load of yarns F_{yarns} . The second model is associated to the contribution of bias yarns, noted F_{bias} , computed from the number of bias yarns N_{bias} , the tensile load of yarns F_{yarns} and the braiding angle β . These models are given in Eq. 4.

$$\begin{aligned} F_{axial} &= N_{axial}F_{yarns} \\ F_{bias} &= N_{bias}F_{yarns} \cos(\beta) \end{aligned} \tag{4}$$

Comparisons with experimental values, expressed in Fig. 14, can conduct to the following analysis. The first part of the tensile behavior cannot be associated with the only contribution of the axial yarns, in the direction of the load applied. Compared to experimental values (at the first peak), for small braiding angles the strength from axial yarns is too weak, and for higher braiding angle (superior to 20°, in this case), this contribution overestimates the strength at the first peak. Concerning the second part of the tensile behavior, the contribution of bias yarns, computed from the initial braiding angle of triaxial braids leads to overestimate the strength at the second peak, especially for small braiding angles. This comparison, based on strength, allows to conclude that a triaxial braids cannot be considered as a simple superposition of axials yarns and bias yarns. Relatively to the first model used in this study, the development of significant models able to predict mechanical

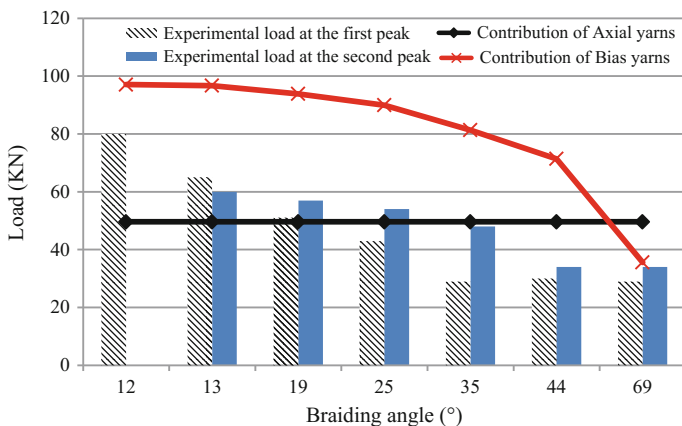


Fig. 14 Comparisons between experimental measures and computed values

properties (stiffness, strength, deformation) characterizing tensile behavior, requires to take into account two parameters. First, the crimp of yarns from the interlacing during the braiding process which modifies the alignment of yarns in the load direction and consequently decreases the contribution of these yarns to the strength. Second, the modification of the braiding angle during the tensile test. All of the models consider the initial braiding angle, but during the tensile test, bias yarns are free to rotate in the load direction, and consequently, the braiding angle decreases, as shown in previous works [52, 53].

5 Conclusions

Associated with the braiding technology, this paper presented a comparison between models able to describe braided fibrous materials and experimental measures from braids manufactured on a braiding machine. This study has been dedicated to triaxial braids with the contribution of axial and bias yarns to geometrical characteristics but also to mechanical parameters characterizing the mechanical behavior. Experimental measurement has been realized at different scales to identify crimp, linear mass, bias yarn length but also the braiding angle, main parameter of braids, which depending on the control of braiding parameters during manufacturing. Tensile behavior of triaxial braids produced with two yarns by bobbins and with a large range of braiding angle has been analyzed. Depending on the value of braiding angle a specific behavior with or without a double peak has been underlined. Associated to this experimental approach, comparisons with computation models from TexMind Braider software have been presented. This study has shown the importance to consider crimp for geometrical characteristics. Future works will concern the development of accurate models to predict the mechanical behavior.

Funding

A part of this work was financially supported by the French government and the “Hauts de France” land.

References

1. Desplentere, F., Lomov, S. V., Woerdeman, D. L., Verpoest, I., Wevers, M., & Bogdanovich, A. (2005). Micro-CT characterization of variability in 3D textile architecture. *Composites Science and Technology*, 65(13), 1920–1930.
2. Naouar, N., Vidal-Salle, E., Schneider, J., Maire, E., & Boisse, P. (2015). 3D composite reinforcement meso F.E. analyses based on X-ray computed tomography. *Composite Structures*, 132, 1094–1104.
3. Rahali, Y., Assidi, M., Goda, I., Zghal, A., & Ganghoffer, J.F. (2016). Computation of the effective mechanical properties including nonclassical moduli of 2.5D and 3D interlocks by micromechanical approaches. *Composites Part B*, 98,194–212.

4. Lomov, S. (2011). Modelling the geometry of textile reinforcements for composites: Wisetex. In P. Boisse (Ed.), *Composite Reinforcements for Optimum Performance*. Woodhead Publishing Series in Composites Science and Engineering; Woodhead Publishing. ISBN: 978-1-84569-965-9.
5. Long, A., & Brown, L. (2011). Modelling the geometry of textile reinforcements for composites: Texgen. In P. Boisse (Ed.), *Composite Reinforcements for Optimum Performance*. Woodhead Publishing Series in Composites Science and Engineering; Woodhead Publishing. ISBN: 978-1-84569-965-9.
6. Ning, F., Potluri, P., Yu, W., & Hearle, J. (2016). Geometrical modeling of tubular braided structures using generalized rose curve. *Textile Research Journal*, 0040517516632471, first published on February 18, 2016.
7. Brunnschweiler, D. (1953). Braids and braiding. *The Journal of the Textile Institute*, 44, 666–686.
8. Mouritz, A. P., Bannister, M. K., Falzon, P. J., et al. (1999). Review of applications for advanced three-dimensional fibre textile composites. *Composites Part A*, 30, 1445–1461.
9. Potluri, P., Rawal, A., Rivaldi, M., et al. (2003). Geometrical modelling and control of a triaxial braiding machine for producing 3D preforms. *Composites Part A*, 34, 481–492.
10. Potluri, P., Manan, A., Francke, M., et al. (2006). Flexural and torsional behaviour of biaxial and triaxial braided composite structures. *Composite Structures*, 75, 377–386.
11. Potluri, P., & Manan, A. (2007). Mechanics of non-orthogonally interlaced textile composites. *Composites Part A*, 38, 1216–1226.
12. Ayranci, A., & Carey, J. (2010). Predicting the longitudinal elastic modulus of braided tubular composites using a curved unit-cell geometry. *Composites Part B*, 41, 229–235.
13. Bilisik, K. (2013). Three-dimensional braiding for composites: A review. *Textile Research Journal*, 83, 1414–1436.
14. Branscomb, D., Beale, D., & Broughton, R. (2013). New directions in braiding. *Journal of Engineered Fibers and Fabrics*, 8, 11–24.
15. Potluri, P. (2012). Braiding. In L. Nicolais, & A. Borzacchiello (Eds.), *Wiley encyclopedia of composites* (2nd edn.) New York: Wiley.
16. Kessels, J. F. A., & Akkerman, R. (2002). Prediction of the yarn trajectories on complex braided preforms. *Composites Part A*, 33, 1073–1081.
17. Van Ravenhorst, J. H., & Akkerman, R. (2014). Circular braiding take-up speed generation using inverse kinematics. *Composites Part A*, 64, 147–158.
18. Lyons, J., & Pastore, C. M. (2004). Effect of braid structure on yarn cross-sectional shape. *Fibers and Polymers*, 5, 182–186.
19. Du, G. W., & Popper, P. (1994). Analysis of a circular braiding process for complex shapes. *Journal of the Textile Institute*, 85, 316–337.
20. Ayranci, C., & Carey, J. (2008). 2D braided composites: A review for stiffness critical applications. *Composite Structures*, 85, 43–58.
21. Laberge-Lebel, L., & Van Hoa, S. (2007). Manufacturing of braided thermoplastic composites with carbon/nylon commingled fibers. *Journal of Composite Materials*, 41, 1101–1120.
22. Birkefeld, K., Roder, M., von Reden, T., et al. (2012). Characterization of biaxial and triaxial braids: Fiber architecture and mechanical properties. *Applied Composite Materials*, 19, 259–273.
23. Castejon, L., Miravete, A., & Cuartero, J. (2001). Analytical formulation of (0° , $+\alpha^\circ$) braided composites and its application in crashworthiness simulations. *Mechanics of Composite Materials and Structures*, 8, 219–229.
24. Aggarwal, A., Ramakrishna, S., & Ganesh, V. K. (2002). Predicting the strength of diamond braided composites. *Journal of Composite Materials*, 36, 625–643.
25. Quek, S. C., Waas, A. M., Shahwanb, K. W., et al. (2003). Analysis of 2D triaxial flat braided textile composites. *International Journal of Mechanical Sciences*, 45, 1077–1096.
26. Goyal, D., & Whitcomb, J. D. (2006). Analysis of stress concentrations in 2*2 braided composites. *Journal of Composite Materials*, 40, 533–546.

27. Kier, Z. T., Salvi, A., Theis, G., et al. (2015). Estimating mechanical properties of 2D triaxially braided textile composites based on microstructure properties. *Composites Part B*, 68, 288–299.
28. Hivet, G., & Boisse, P. (2008). Consistent mesoscopic mechanical behaviour model for woven composite reinforcements in biaxial tension. *Composites Part B*, 39, 345–361.
29. Hivet, G. (2013). Vidal-Salle´ E and Boisse P. Analysis of the stress components in a textile composite reinforcement. *Journal of Composite Materials*, 47, 269–285.
30. Harte, A. M., & Fleck, N. A. (2000). On the mechanics of braided composites in tension. *European Journal of Mechanics A/Solids*, 19, 259–275.
31. Hristov, K., Carroll, E. A., Dunn, M., et al. (2004). Mechanical behaviour of circular braids under tensile loads. *Textile Research Journal*, 74, 20–26.
32. Dabiryan, H., & Johari, M. S. (2016). Analysis of the tensile behaviour of tubular braids using energy method, part I: Theoretical analysis. *Journal of Textile Institute*, 107.
33. Del Rosso, S., Lannucci, L., & Curtis, P. T. (2015). Experimental investigation of the mechanical properties of dry microbraids and microbraid reinforced polymer composites. *Composite Structures*, 125, 509–519.
34. Rawal, A., Kumar, R., & Saraswat, H. (2012). Tensile mechanics of braided structures. *Textile Research Journal*, 82, 1703–1710.
35. Rawal, A., Potluri, P., & Steele, C. (2005). Geometrical modeling of the yarn paths in three dimensional braided structures. *Journal of Industrial Textiles*, 35, 115–135.
36. Rawal, A., Saraswat, H., & Kumar, R. (2013). Tensile response of tubular braids with an elastic core. *Composites Part A*, 47, 150–155.
37. Rawal, A., Sibal, A., & Saraswat, H. (2013). Tensile behaviour of regular triaxial braided structures. *Mechanics of Materials*, 91, 277–289.
38. Rawal, A., Saraswat, H., & Sibal, A. (2015). Tensile response of braided structures: A review. *Textile Research Journal*, 85, 2083–2096.
39. Duchamp, B., Legrand, X., & Soulat, D. (2016). Structural and tensile behaviors of braided reinforcements: Characterization and model. In Y. Kyosev (Ed.), *Advances in Braiding Technology Specialized Techniques and Applications*, Woodhead Publishing. ISBN: 9780081009260.
40. Magalhaes, R., Subramani, P., Lisner, T., Rana, S., Ghiassi, B., Fangueiro, R., et al. (2016). Development, characterization and analysis of auxetic structures from braided composites and study the influence of material and structural parameters. *Composites Part A*, 87, 86–97.
41. Subramani, P., Rana, S., Ghiassi, B., Fangueiro, R., Oliveira, D. V., Lourenco, P. B., et al. (2016). Development and characterization of novel auxetic structures based on re-entrant hexagon design produced from braided composites. *Composites Part B*, 93, 132–142.
42. Kyosev, Y. (2012). TexMind Braider, Monchengladbach www.texmind.com.
43. Riscicato, J. V., Kelly, F., Soulat, D., et al. (2015). A complex shaped reinforced thermoplastic composite part made of commingled yarns with integrated sensor. *Applied Composite Materials*, 22, 81–98.
44. Jacquot, P. B., Wang, P., Soulat, D., & Legrand, X. (2016). Analysis of the preforming behaviour of the braided and woven flax/polyamide fabrics. *Journal of Industrial Textiles*, 46 (3), 698–718.
45. Kostar, T. D., & Chou, T. W. (2002). A methodology for Cartesian braiding of three-dimensional shapes and special structures. *Journal Materials Science*, 37, 2811–2824.
46. Kyosev, Y. (2015). Productivity calculations in braiding. In Y. Kiosev (Ed.), *Braiding Technology for Textiles*. Woodhead Publishing Series in Textiles.
47. Endruweit, A., & Long, A. C. (2011). A model for the in-plane permeability of triaxially braided reinforcements. *Composites Part A*, 42, 165–172.
48. Image J: An open Platform for Scientific image analysis. Retrieved from August 24, 2016, from <http://imagej.net/Welcome>.
49. Byun, J. H., Whitney, T. J., Du, G. W., et al. (1991). Analytical characterization of two-step braided composites. *Journal of Composite Materials*, 25, 1599–1618.

50. Buyn, J. H. (2000). The analytical characterization of 2-D braided textile composites. *Composite Science Technology*, 60, 705–716.
51. Ishikawa, T., & Chou, T.-W. (1982). Elastic behaviour of woven hybrid composites. *Journal of Composite Materials*, 16, 2–19.
52. Duchamp, B., Legrand, X., & Soulat, D. (2016). The tensile behavior of biaxial and triaxial braided fabrics. *Journal of Industrial Textiles*. Retrieved June 16, 2016, from DOI [10.1177/1528083716654469](https://doi.org/10.1177/1528083716654469).
53. Duchamp, B. (2016). Contribution à l'élaboration de préformes textiles pour le renforcement de réservoir souples. Ph.D. thesis, Université Lille. (to be published, in French).
54. Kyosev, Y. (2013). Some computational and modelling aspects about the multifilament modeling of braided preforms. In: S. Lomov (Ed.), *Proceedings of Composites Week@Leuven and TexComp-11 conference*. Leuven.
55. Kyosev, Y. (2015). Computer assisted design (CAD) software for the design of braided structures. In Y. Kyosev (Ed.), *Braiding Technology for Textiles*. Woodhead Publishing Series in Textiles.
56. Kyosev, Y., & Cordes, A. (2016). Geometrical modelling of tubular and flat braids within the jamming limits—verification and limitations. In Y. Kyosev (Ed.), *Recent Developments in Braiding and Narrow Weaving*.
57. Kyosev, Y. (2016). Geometrical modeling and computational mechanics tools for braided structures. In Y. Kyosev (Ed.), *Advances in Braiding Technology Specialized Techniques and Applications*, Woodhead Publishing Series in Textiles.
58. Kyosev, Y. (2016). Generalized geometric modeling of tubular and flat braided structures with arbitrary floating length and multiple filaments. *Textile Research Journal*, 86(12), 1270–1279.

Fibre-Rope-Driven Parallel Handling Device

Christoph Müller, Markus Helbig and David Holschemacher

Abstract A concept of a rope-driven handling device was developed. The scope of the work was to achieve a significant noise reduction by the utilisation of high-performance fibre ropes actuated by motor winch devices. A two-dimensional demonstrational was implemented and analysed. Furthermore, a concept for the compensation of the weak axis was set up. In comparison to conventionally built axles, a significant lowering of the emitted sound pressure level was achieved.

1 Introduction

The performance of current order picking systems, which determines the average time to deposit and withdraw goods, is limited by the predominant mechanical systems that use conventional serial kinematics. Furthermore, the noise emission by conventional axis set-ups proves to be quite problematic. In contrast, rope-driven parallel kinematics and handling devices are known as highly flexible dynamic as well as low-noise emitting structures. This is related to their low mass motion and guiding element, the fibre rope. The general positioning operation is carried out simultaneously by the ropes, which refers to the definition of parallel actuators. Established applications are camera guiding systems, rehabilitation training devices and particular conveying systems mainly used in the commissioning process. Advantages of cable robots (Fig. 1) in general can be described as follows: (i) highly efficient in terms of material and energy consumption, (ii) scalable workspaces due to marginal mass gathering by longer actuators, (iii) superior relation of actuator mass versus payload enables higher dynamics and (iv) in addition, fibre ropes come with extremely smooth running characteristics, which are not comparable with conventional axis set-up.

C. Müller (✉) · M. Helbig · D. Holschemacher
Faculty of Mechanical Engineering, Professorship of Materials Handling and Conveying
Engineering, University of Technology Chemnitz, Chemnitz, Germany
e-mail: christoph.mueller@mb.tu-chemnitz.de

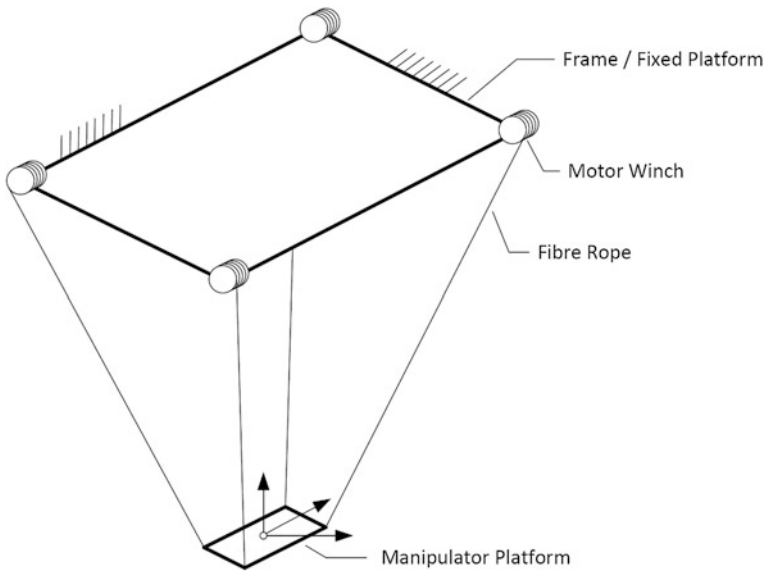


Fig. 1 The fibre-rope-driven manipulator platform is maintained under a stable position due to the action of gravity. In accordance with [1]

In the present study, a prototypical rope-driven handling system was developed. The positioning of a traverse moving in between shelf units is realised through two propelled rope slings (Fig. 4). This enables the traverse to be positioned planar and simultaneously maintaining tension in all rope sections by synchronous operation of all drives. The main objective was to substitute commonly used serial kinematic systems with a parallel rope kinematic system. Motion assemblies in serial kinematics such as drivebelts or gear rods are highly responsible for the noise emission in conveying systems due to their gear contacts. In contrast, rope-driven kinematics is nearly noiseless due to missing gear contacts. Another aspect in terms of noise emission is the general power input. A comparison of completely different chain conveying systems (the conveying velocity as a measure of power input) shows major influence on the emitted sound pressure level (SPL) (Fig. 2).

Concept of a CRPM cable robot with weak axis compensation.

Cable-driven robots with non-redundant axis set-up (Table 1, CRPM) are kept stable only under the action of gravity. Thus, the axes can be described as ‘weak’, because only the force of gravity leads to restoring forces in the ropes. However, the authors prefer the concept of weak axis as a matter of cost efficiency. Redundancy in the axis has major effects on the number of independent motion assemblies, because every optional motor winch increases the resulting costs (Fig. 3). When it comes to substitution of serial kinematic robots, a 2d planar motion only needs two separate motion assemblies. Furthermore, a parallel rope robot should contain only two separate motor winches, which lead to the described set-up.

Fig. 2 SPL versus conveying speed of five different chain conveying systems, low speed and high speed measure for each system

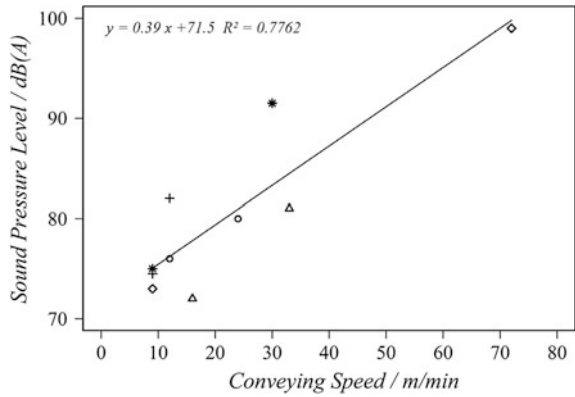
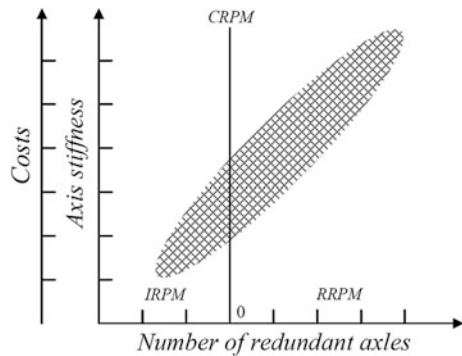


Table 1 Level of redundancy. In accordance with [2]

Abbrev.	Condition ^a	Meaning
IRPM	$m \leq n$	Incompletely Restrained Positioning Mechanism
CRPM	$m = n + 1$	Completely Restrained Positioning Mechanism
RRPM	$m > n + 1$	Redundantly Restrained Positioning Mechanism

^a m = Number of separate motion assemblies, n = Degrees of Freedom (DOFs)

Fig. 3 Costs and axis stiffness versus level of redundancy qualitative plot



Therefore, the concept of a cascade of compensatory strategies for the weak axes was developed to achieve acceptable dynamic stability and positioning accuracy. In stage I, the known ideal stiff consideration of the fibre rope without regard to the ropes mechanical behaviour is replaced by a visco-elastic model. This model takes into account the time dependency of stiffness and damping phenomena which are mandatory for the modelling of oscillating rope deformation. In Stage II, the model is utilised to calculate the manipulator center point (MCP) by realistic rope lengths. Furthermore, the rope loads can be estimated by the model. Therefore, a new access to the positioning process (acceleration, const. axis velocity, braking)

is possible. In Stage III, dynamic parameters within the axis drive control are set to the estimated limits of the fibre rope. In Stage IV, the axis stiffness is increased by active phase opposite position control, e.g. compensation of overshooting or inertia adapted breaking ramps.

2 Implementation

A space-related model of an order picking system was implemented (Fig. 4). A planar motion (x/y) of the central beam (1) is initiated by two separate motor rope winches (2). The two winches drive the upper so-called ‘master’ rope slings. The lower two rope slings so-called ‘slaves’ were strained by a static load applied through a rope reservoir (3). The both free ends of one master rope sling are driven by one motor winch. The both free ends of one slave rope sling are driven by one rope reservoir. This is necessary in order to move both ends of the traverse parallel. At the one side, a position measurement system (draw wire sensors) was attached. In a preliminary test set-up, the motor winches were set up and parameterised in the motion control. The rope drives were implemented as linear axles in the motion control unit. Therefore, the mechanical parameters, e.g. gear ratio and winch drum diameter were parametrised.

In a direct forward approach, an algorithm for computing the axis coordinates (A1 and A2) from the MCP coordinates (x and y) was implemented. Since the given parallel kinematic is non-redundant, in terms of a completely restrained positioning mechanism (CRPM), the algorithm is only geometrical determined for the static case. The coordinate transformation was derived from Fig. 5. Thus, the motion control could be set up. Two different operating methods were implemented (i) manual movement via a joystick and (ii) a cyclic positioning process with

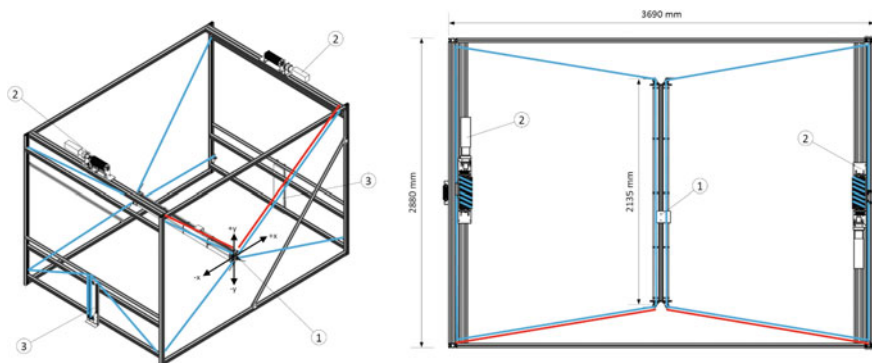


Fig. 4 Functional structure of the demonstrational with parallel axes; representation of rope slings (blue) and position measurement (red)

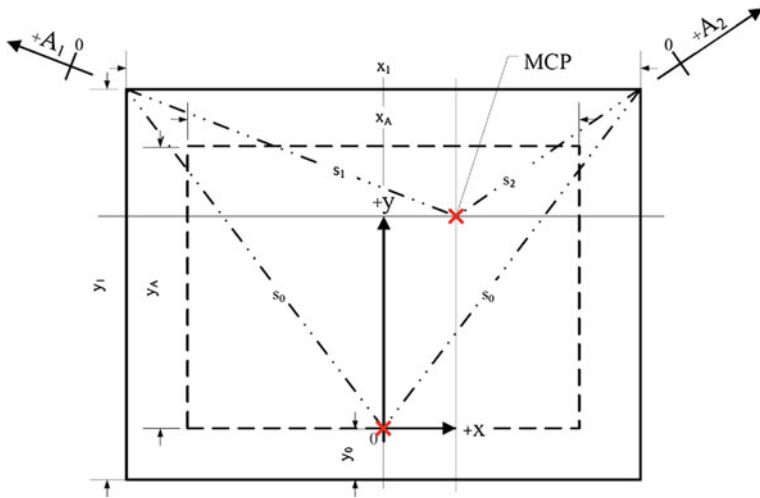


Fig. 5 Coordinate transformation

randomly sampled endpoints. In all cases, the motor moment was limited in order to the estimated limit of 10% of the breaking load of the ropes (Table 2).

Further, the mechanical components of the (i) motor winch, (ii) rope reservoir and (iii) traverse were designed and built (Fig. 6). The PA 6 G winch drum is driven by a Siemens integrated drive and a 10/1 planetary gear. So, the maximum winch momentum is 45 Nm at maximum 450 rpm. The drum has an effective diameter of 100 mm which leads to a maximum of 900 N rope force. The rope reservoir was mass loaded. The lower sheaves were vertically displaceable in order to apply the load on the rope slings. The traverse was equipped with four independent rotatory mounted sheaves on each side. So, there was no rigid connection in between the rope and the traverse.

Table 2 Rope design

Core		Cote		Rope	
Design	12 strand, $d_{nom} = 2.5$ mm	Design	16 strand	Breaking force F_B	2.85 kN
Material	Technora T221	Material	Polyester	Rope load limit	$<0.1 \times F_B$
Braid angle	35°	Yarn/strand	1		
Twist	11°	Twist	0°		
Lin. density	5 kTex				
Braid length	10 mm				

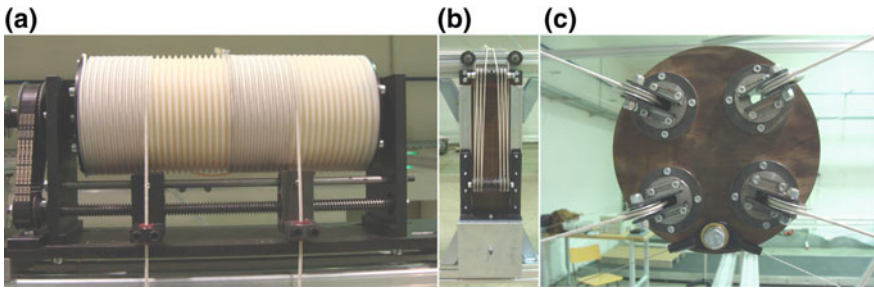


Fig. 6 Components of the demonstrational; **a** Winch drum, **b** Rope reservoir and **c** Central beam (traverse)

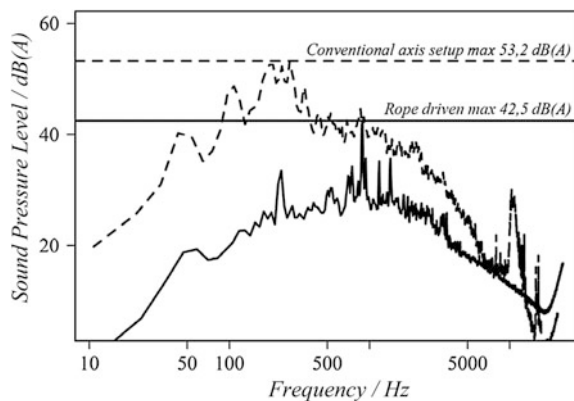
3 Rope Design

A stiff rope design is reasonable for precise positioning and repeating accuracy. In combination with a highly damping structure, overshooting can be minimised. In terms of durability, the bending over sheave cycles is the most significant mechanical property. Therefore, a D/d ratio of 25 was achieved with a 4 mm rope design (Table 2). Static tension tests as well as dynamic strain step response tests delivered time parameters for the motion control.

4 Results

A demonstrational has been built as a space-related model of a real picking system. The main objective was to proof the practical functionality of handling a traverse in two axes via a fibre-rope-driven parallel actuator. Furthermore, the emitted noise had to be reduced by a significant amount. Both requirements were met by the

Fig. 7 Comparison of the emitted sound pressure level (A-weighted) of a conventional build axis (drivebelt) versus the rope-driven handling system



developed system. The actuator showed stable motion characteristics, e.g. minor overshooting at the driven dynamic parameters occurred (1.5 m/s travel speed and 5 m/s² acceleration while testing). The system provides good adaptivity, since the axis length is variable to a certain extent and the driving power is less compared to conventional systems. It comes with enhanced acoustic properties in comparison to conventionally built axles (lowering of the sound pressure level > 6 dB(A), Fig. 7).

Acknowledgements The study was granted by the BMWi via the ZIM program. Financial support is gratefully acknowledged.

References

1. Bruckmann, T., & Pott, A. (2013) *Cable-driven parallel robots, mechanisms and machine science* (Vol. 12). Springer. ISBN 978-3-642-31987-7
2. Verhoeven, R. (2004) *Analysis of the workspace of tendon-based Stewart platforms*. Doctoral Thesis.

Pattern Design with the Variation Braider VF of Company Herzog GmbH

Peter Gleßner and Yordan Kyosev

Abstract This paper presents an overview about the patterning possibilities of the new variational braider of the company Herzog GmbH. Presented are two practical examples with the sequences of their programming and some issues about the programming with the user interface. Some configurations for production of flat braids are checked using simulation software TexMind Braiding Machine Configurator. It is found that regular flat braids with three carriers and irregular flat braids with four carriers can be produced with the machine as well.

1 Introduction

The Herzog variation braider type “VF 1/(4-32)-140” is a 3D braiding machine with switchable, pneumatic controlled crossings which permit the change of the track plate during the braiding process.

Concerning to the horn gear setup of a variation braider with 16 horn gears on a 4×4 grid, the first idea of usage is the 3D-braid sector with its characteristic diagonal tracks for building three- or four-track braids with a square cross section. In this regard, 3D braids are defined by fibers which are orientated in through-thickness direction [1].

The left 2×2 grid in Fig. 1 is a setup used to produce square braids (in fact tubular) with eight carriers which is, for example, practiced by the industrial production of round candle wicks [2]. This implies that it is possible to produce four square braids with eight carriers each in one process on one machine. Compared to four separated 2×2 grid braiders, the flexibility of the 4×4 variation braider is a huge advantage.

Furthermore, the machine can produce a two-layer braid in once process, if the inner four horn gears built a 2×2 grid with an eight-carrier round braid, and the

P. Gleßner · Y. Kyosev (✉)
Hochschule Niederrhein, Mönchengladbach, Germany
e-mail: yordan.kyosev@hs-niederrhein.de

outer horn gears are running with a 24-carrier round setup using a 1 full 1 empty arrangement [3] (Fig. 2).

The Herzog VF braider is also mounted with a part length control which gives the possibility to change the braid properties during the braiding process in defined intervals. These properties are individual lay length, horn gear speed, creating non-braided parts by moving the take-off without turning the horn gears or

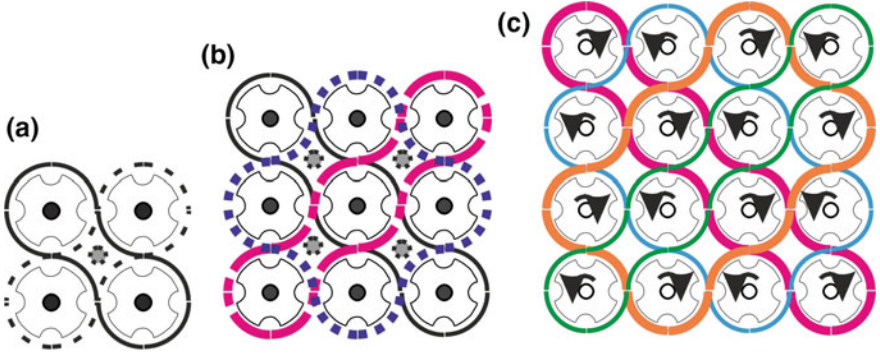


Fig. 1 Tracks for two-, three-, and four-diagonal braids (packing braids) on the variation braider

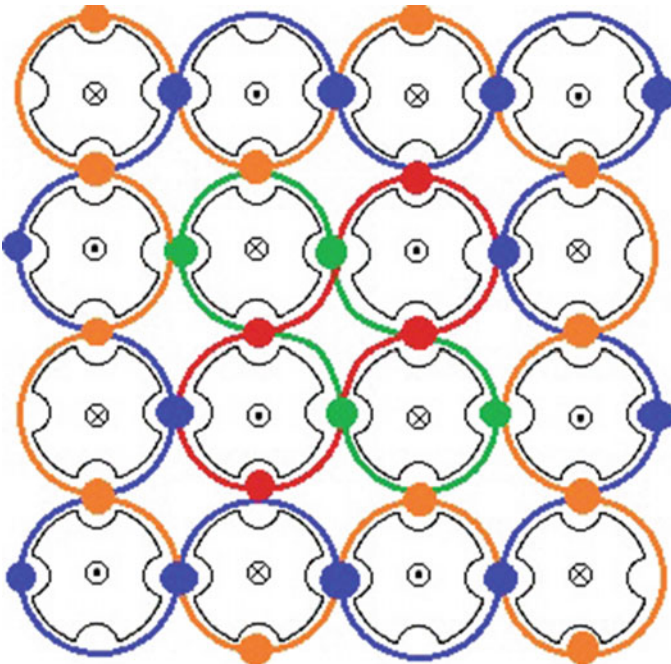


Fig. 2 Track sketch for a two-layer braid on the VF machine

changing the geometry by using the crossing control. If the machine is equipped with a horn gear revolution counter, it is possible to set a part length for a defined number of horn gear revolutions.

The following sections will give an overview of pattern possibilities by using the part length and crossing control.

2 Overview of Some Patterning Options on the VF Braider

Besides the already mentioned possibility of producing three- and four-track or two-layer braids, the computer and pneumatic controlled crossings allow to choose a setup for braiding of different tubular patterns like for instance 4-, 8-, 12- 16-, 24-, or 32-carrier braids with a 1 full 1 empty, 1 full—3 empty and most of them as well with 2 full—2 empty carrier arrangement [2].

However, the option of switching the crossings without using a tool during the process brings the opportunity to change the geometry of the braid by programming loops in the variation braider mode. The following pattern is an example for a sixteen-carrier braid which splits into two eight-carrier braids for a defined part length until it joins back together. For this loop, there are eight steps necessary which are shown in Fig. 3.

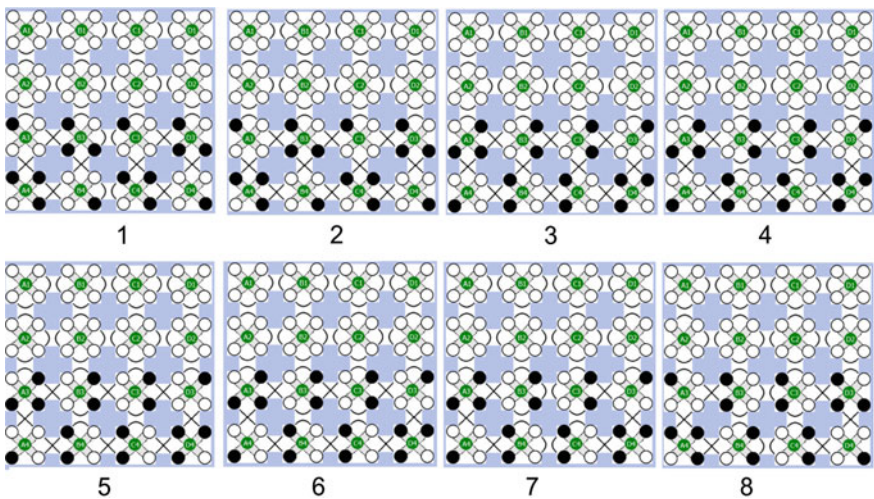


Fig. 3 Pattern 1—Crossing loop for 1×16 to 2×8 to 1×16 geometry. Steps: 1—start position; 2—change crossings, 3—move forward, 4—change crossings: end position; 5—start position, 6—change crossings, 7—move forward; 8—change crossings: end position



Fig. 4 Pattern 1—Crossing loop for 1×16 to 2×8 to 1×16 geometry

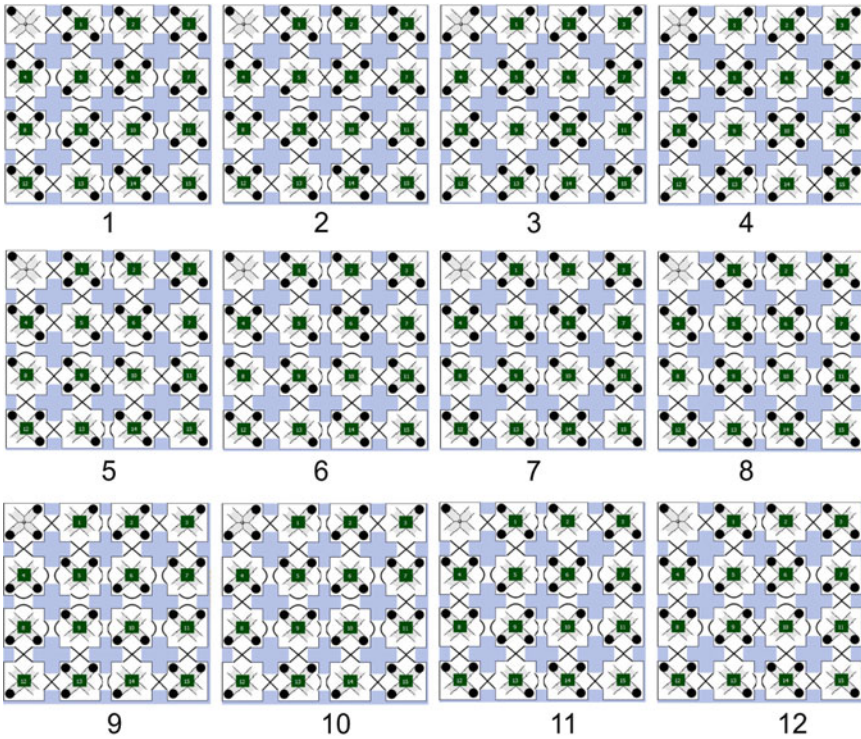


Fig. 5 Steps: 1—start position, 2—change crossings; 3—move forward; 4—change crossings; 5—move forward; 6—change crossings, end position; 7—start position; 8—change crossings; 9—move forward; 10—change crossings; 11—move forward, 12—change crossings, end position

According to the complexity of the bifurcation, there are more steps necessary, however, there are a lot of mistake sources relevant to the evenness of the braid. The following pattern shows a 32-carrier tubular braid which splits into four 8-carrier tubular braids and comes back together in a 12-step crossing loop (Fig. 4 produced sample and Fig. 5 sequence).

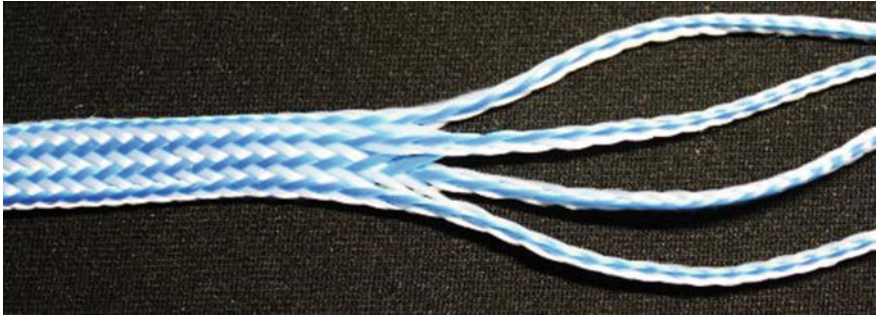


Fig. 6 Pattern two with four splits

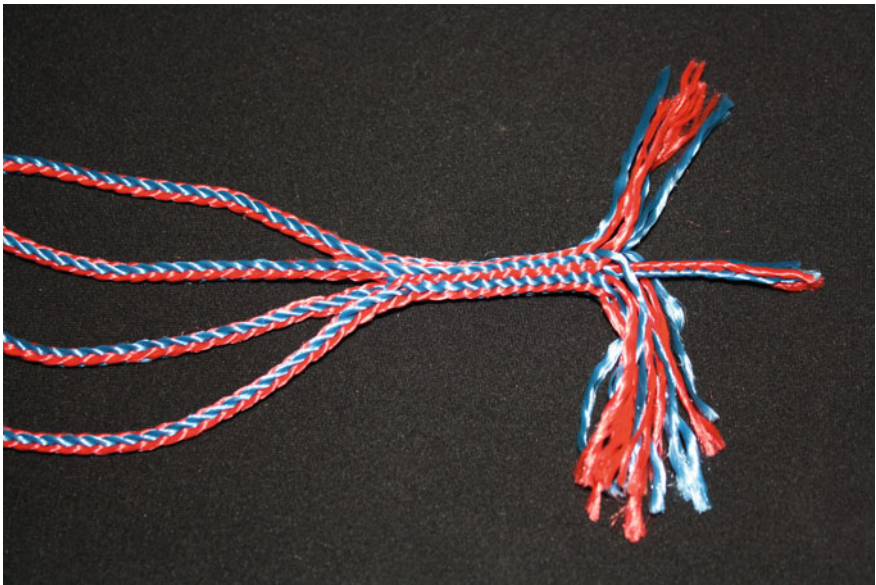


Fig. 7 Two-layer braid with bifurcations

It is also possible to build a two-layer braid as shown in Fig. 2, which splits into four eight-carrier braids (Fig. 6) and unifies to a two-layer braid back again (Fig. 7).

3 Control Software

Like described in the introduction, the VF braider gives the possibility to change parameters like lay length, horn gear speed, or height correction for a defined number of horn gear rotations or braided length. The operator can program all steps in a part length editor on the touchscreen (Fig. 8).

Step:	1	of	0	next step:	0
Partlength setp.	+0.0	act.	+0.0		m
Horn gear speed			0		RPM
Laylength:			+0.000		mm
TO height correction	+0.0	mm			Off
quarterstep act.:	0	act.	0		Off
partlength stop					Off
final stop					Off
change setup	Off			change sequence: present step	0
				startstep:	0
				stopstep:	0
Home screen	read step	save step	edit	clear cnt	reset control

Fig. 8 Part length control

In the yellow field, it can be found an interface to the crossing control which gives the opportunity to reserve one or more part length steps for a track change. The crossings must be programmed in a separate surface called variation braiding (Fig. 9).

The variation braiding interface is a live-teach-in program. The crossing change must be saved step by step whereby one step can be changing one or more crossings, moving forward or moving backward.

You can change crossings only if the machine is stopped and the horn gears are in 45° position which is detected by a sensor and a blue lever. There are also sensors which detect the carrier position so the operator can see the current set of carriers on the display. If the machine is equipped with a Version 3.7.11 or higher, there is a new setup check and sequence editor with the following properties [4]:

- Compare the actual setup with the aimed setup in the sequence's recipe
- Playback simulation of the whole transition step by step or automatically
- Edit carrier, crossing, and control information in every step without reprogramming the whole sequence
- Create empty recipes

Once a crossing sequence is programmed and stored, it must be linked in the part length editor. When the part length step is achieved, the carries will move to the programmed start position to begin the crossing change sequence.

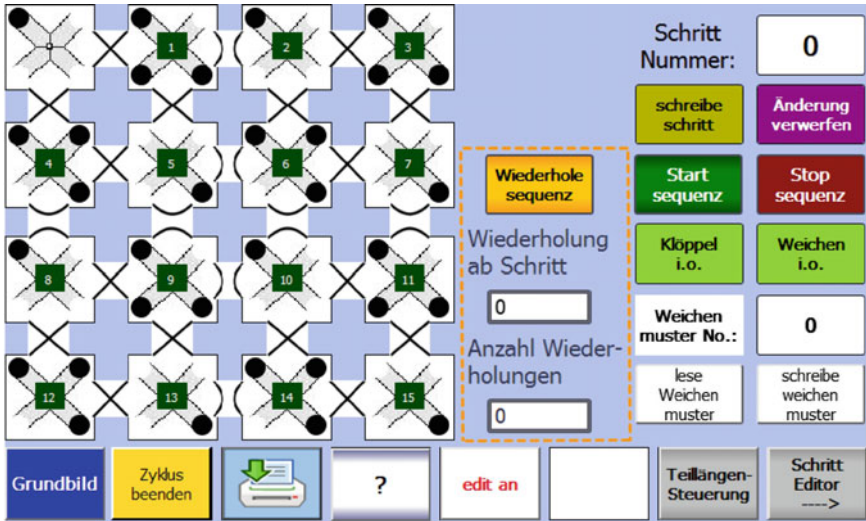


Fig. 9 Crossing control

4 Flat Braids on Variation Braider

The variation braider allows as well production of **some** flat-braided structures. With the Software TexMind Braiding Machine Configurator [5, 6] is possible the simulation of different arrangements of gears and carriers and their motion, including the check if the carriers are crashing. With the current configuration of the variation braider of the company Herzog, it has horn gears with four slots each. The production of regular flat braids with larger number of carriers is not possible. For production of flat braids, gears with at one more (five) or less (three) slots have to be placed at the edges (Fig. 10b). This additional slot shifts the phase of the motion of the carrier and places it after turning its direction in an empty slot of the next gear. If the turning slot has four slots as all other gears (Fig. 9a), its carriers will have to be placed at occupied sots after changing their direction.

The problem with the crash actually can be avoided for some configurations and not all, but some flat small braids can be produced on the variation braider too.

Figure 11 demonstrates a configuration with two horn gears, both with four slots, where configuration with three and four carriers is possible. Structurally, both braids are identical, the second one (Fig. 11d, machine Fig. 11b) has two yarns which are building a group. If three gears are used in the machine, again four carriers can be arranged and used for production of similar to flat braids (Fig. 12).

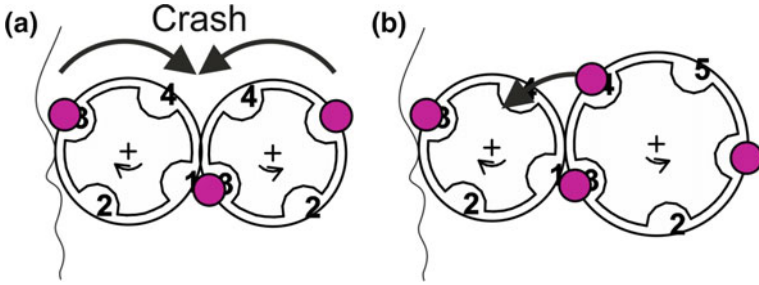


Fig. 10 Tuning problematic **a** after turning its direction the carrier crashes because its future slot is still occupied. **b** in the normal case, the turning gear has one more slot and shifts the need for new empty slot in the time at one cycle

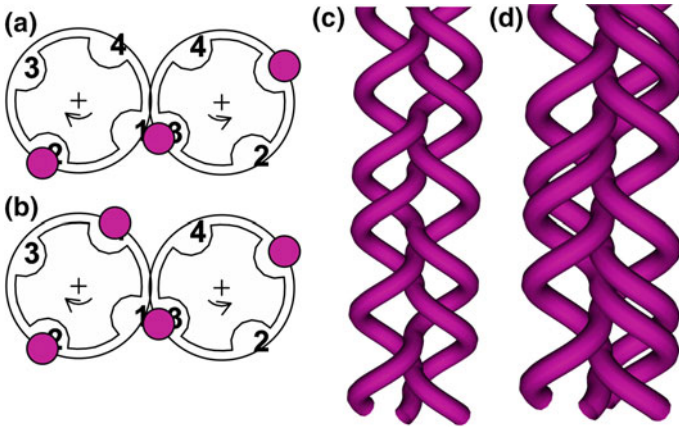


Fig. 11 Production of flat braids (soutache) with three yarns and irregular braid with four yarns. Configuration (a) leads to braid (c); configuration (b) lead to braid (d)

In this case, the structure becomes more irregular—some yarns float over two another yarns at one place and over one at different place.

The Configurator can simulate diagonal braids and any of the adjustment of the variation braiding machine (Fig. 13) in very convenient way. It allows simulation of the carrier motion which helps in the search of reasons for collisions between the carriers. Its current version actually does not support dynamical change of the state of the switches. If this option becomes available, it would significantly simplify the design of the complex braids.

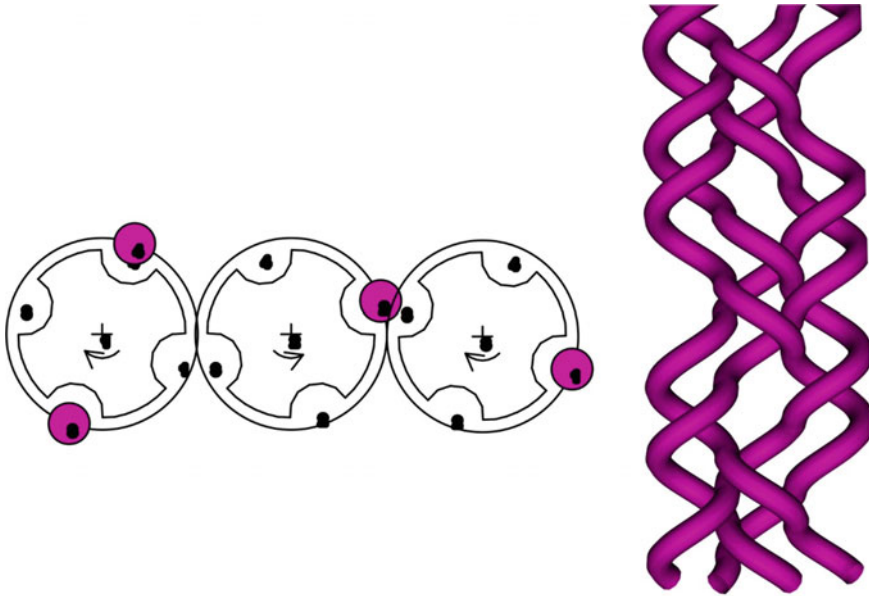


Fig. 12 Irregular flat braid with four carriers over three gears

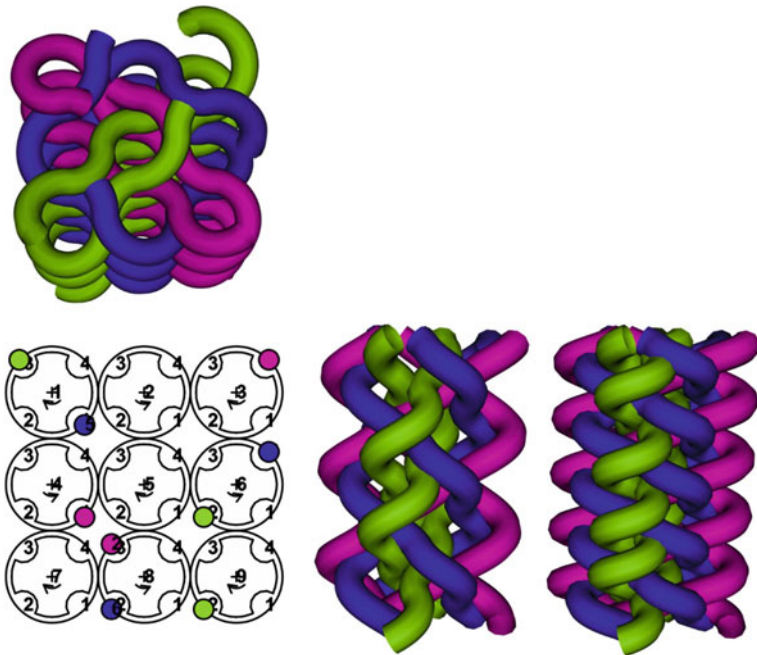


Fig. 13 Carrier arrangement and top view of a setup of the variation braider for production of three diagonal (packing) braids. The side views are with different braiding angle

5 Conclusions

Compared to classic braiding machines, the VF braider and its switchable crossings take braiding to another level. The pattern opportunities and possible applications are diverse and incomparable to other braiding machines.

However, the programming of loops can bring some problems. When carriers are moving forward or backward inside of a crossing loop, they release additional yarn length and thus cause longer visible floating yarns or unequal lay length. Moreover, when the carriers move to a start position for a cross change loop, the same effect might happen. Furthermore, the used yarn count can influence the braid structure if there are different yarns or yarn numbers on carriers in the same track. This problem may especially be bad for braids with bifurcations like shown in Fig. 5 or 6 because the carriers can be mixed. For a smooth braid structure, it is also important to think about the take-off inside crossing loops. When moving the carriers in a loop, the take-off system should be stopped to prevent lay length mistakes. From other point of view, using the software TexMind Braiding Machine Configurator, several arrangements of the machine can be simulated. This reduces the design time of the braids and can help in the preparation of the braiding programs.

References

1. Carey, J. (Ed.) (2016). *Handbook of advances in braided composite materials: Theory, production, testing and applications*. Amsterdam: Woodhead Publishing.
2. Kyosev, Y. (2014). *Braiding technology for textiles*. Amsterdam: Woodhead Publishing.
3. Kyosev, Yordan (Ed.). (2016). *Advances in braiding technology: Specialized techniques and applications*. Amsterdam: Woodhead Publishing.
4. Kastner, T. (2014). Operating manual: Electronic laylength control of braiding machines. Custom designed features for variation braider., Version 3.5.0., Oldenburg: Herzog GmbH.
5. Kyosev, Y. (2014). Machine configurator for braided composite profiles with arbitrary cross section. In *16th European Conference on Composite Materials ECCM 16*. Seville-Spain.
6. Kyosev, Y. (2016). TexMind braiding machine configurator. User's guide, TexMind, Mönchengladbach. www.texmind.com.

Ultrasonic Dip Coating of Fibre Ropes with Large Diameters

David Häser, Klaus Nendel, Christoph Müller and Markus Helbig

Abstract Conveyor-technical and winch-based applications like elements in cranes or shipbuilding with required payloads of 5 tons and above put enormous requests on high-strength fibre ropes. The application of wear-reducing coatings is therefore essential. In case of the structural design of fibre ropes with large diameters, a complete penetration with coatings is not achievable with conventional coating techniques. Therefore, the coating with the help of ultrasonic is a new way to improve the penetration of fibre ropes with higher diameters.

1 Introduction of Fibre Ropes with Large Diameters in Conveyor-Technical Applications

Textile machine elements such like braided ropes made out of high-strength polymer fibres offer significant advantages compared to steel-wire ropes with the same diameter. In addition to their low mass combined with high tensile strength, good bending properties and corrosive resistance characterize them. Particularly in extremely demanding conveyor-technical applications like winches, cranes but also high-dynamical uses like shuttle systems and fast operating load elevators, considerable mass and thus energy savings are obtainable.

Due to the required minimum safety factor of 8 or more for the traction means in crane and winch-based applications, breaking loads of up to 400 kN result for the rope construction. As a result, fibre rope diameters of 20 mm and above are required despite the use of high modulus-high tensile materials. Due to the demanding load settings, the application of wear protection plays an important role of stretching the operational capability of fibre ropes as far as possible. The standard methods for applying wear protection agents for fibre ropes with small diameters up to 12 mm like dip coating are not suitable for greater diameters. A full penetration

D. Häser (✉) · K. Nendel · C. Müller · M. Helbig
Institute for Materials Handling Conveying and Plastics Engineering,
Technical University of Chemnitz, Chemnitz, Germany
e-mail: david.haeser@mb.tu-chemnitz.de

with wear protection cannot be guaranteed. Instead, a complex wet finishing of the individual yarns or rather braids is necessary, which afterwards braided to finished ropes. This additional time- and money-consuming manufacturing step should be avoided with the application of ultrasonic in the wet finishing of fibre ropes with large diameters.

2 Problems with the Coating of Fibre Ropes with Large Diameters

The complete penetration of the rope with the coating is an absolute necessity since it not only meets wear protection but also fulfils other tasks such as hydrophobing and UV protection. During the coating of fibre ropes with a large diameter with conventional coating methods, only the outer regions of the cross-section can be coated, but the core of the rope experiences only inadequate coating penetration. This uncoated area is only inadequately protected against wear and tear in operation. At the inner section of the rope, more fibre-to-fibre friction is generated. The resulting heat superimposes itself with other tribological effects and leads to an accelerated degradation of the yarns and strands in the core of the rope. The deposit of the rope is achieved earlier than it would be the case with an optimum application of coating materials.

The reasons for the insufficient penetration of fibre ropes of large diameters are due, among other things, to the viscosity of the coatings. By adapting the coating formulas, the viscosity can be adjusted (use of Silica/Teflon oils). The structural design of fibre ropes is also causing problems. If the cross-section gets larger, the number of braids also climbs and with it the number of interspaces between these braids. These only one hundred of a millimetre large structures work against coatings with great surface tensions. At conventional water-based coatings, the high surface tension of the water counteracts the complete penetration of the rope structure. An additional effect encounters at the standard application for coating of fibre ropes with large diameters, the continuous dip coating process. For this purpose, fibre ropes are endlessly guided through the coating bath with high throughput speeds to maintain high productivity. However, this causes the formation of flow effects on the surface of the rope, which cause an indirect proportionality between the speed of penetration and the depth of penetration of the coating solution.

These mentioned effects counteract the optimal penetration of fibre ropes with large diameters (cf. Fig. 1).

Avoiding those effects can be achieved through opening the rope structure. Therefore, the mechanical impact of ultrasonic waves on the rope material can be used. The use of ultrasonic waves has different effects considering frequency and other parameters, like acoustic pressure and the position of the acoustic maxima. For example, causes the use of the typical frequency range for ultrasonic in



Fig. 1 Insufficient coating input into PES-rope (white core), diameter 20 mm

mechanical applications (30–35 kHz) a cleaning effect on surfaces. The cleaning effect on surfaces through ultrasonic waves should be used for the coating of fibre ropes. Therefore, a higher range of frequency is used (40–140 kHz) to offset the boundary surface effects and allow the coating even of the inner layers of the rope cross-section.

2.1 State-of-the-Art for the Coating of Fibre Ropes with Large Diameters

All efforts for the coating of fibre ropes with large diameters are facing the same issue, as depicted in Sect. 2. In addition to the conventional dip coating process, with its known compromise between optimal penetration and productivity, there are some more approaches. The coating of the entire rope cross-section by means of an annular slot nozzle or a suction beam is to be estimated as insufficient in the case of the mentioned rope diameters. Both methods work with the buildup of a defined excess pressure or vacuum right at the rope material. At diameters of 20 mm and above, the surface condition causes variabilities from 1, 5 mm and more over the whole cross-section. The sealing and therefore setup of the defined pressure milieu cannot be guaranteed. In summary, it can be stated that, according to the current state-of-the-art, there is no reliable method or technique by which an optimum coating of fibre ropes of large diameters can be ensured. The common approach comprises, in additional working steps, the coating of the individual strands before they are intertwined into a rope. Even here, an optimum result is not guaranteed, because the coating is rubbed off at the deflection points and the twisting passages. This leads to local interruptions of the coating and subsequent potential wear in the

finished rope. Moreover, this way of production leads to an increased process time. This creates the problem that each strand (twisted strands in S- and Z-direction) must be coated individually. Since technical ropes are usually braided from 8 to 12 strands, then two strands must be coated with 4–6 times the length of the final rope. In addition, there is the considerable cleaning effort on the braiding machines with a necessary change of parts (Figs. 2 and 3).

In summary, it can be announced that the known methods for the coating of fibre ropes with large diameters do not offer sufficient potential in regard to the quality of the coating, the productivity or rather cost-efficiency. With the use of ultrasonic, integrated into the coating process of already produced ropes, these target conflicts are to be avoided.

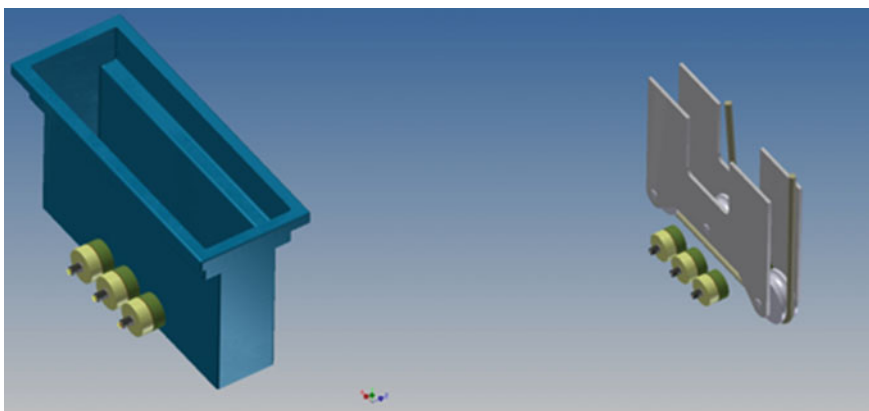


Fig. 2 Left side CAD-design for the ultrasonic dip coating bath, right side rope guiding system, dip coating pan faded out



Fig. 3 Left side mixed rope made from PES-PP, right side pure PES-rope

2.2 Ultrasonic Dip Coating

The aim of the research project is to establish the coating of fibre ropes with a large diameter as an in-line process. This means that already processed ropes can be coated with high productivity thus omitting additional processes such as the coating of individual strands.

A conventional coating device, the immersion bath, was equipped with ultrasonic transducers as an approach to solving the problem of optimizing the coating while simultaneously achieving the highest possible throughput or productivity. For this purpose, a variant study was carried out in advance and finally, the variant was selected with ultrasonic converters mounted outside on the pan on the sides. The goal was to be able to utilize the existing MAGEBA RopeLiner thermosetting system as much as possible while at the same time enabling a simple changeover between the conventional and the ultrasonic immersion bath.

In essence, the system used consists of a generator unit (1000 W) considering the bath volume, a stainless steel tank (35 l capacity) and the opposing ultrasonic converters placed on the outside of the pan. These “banks” are connected in the same way so that a standing wave can emerge in the immersion bath. The arrangement of the oscillators is selected in such a way that the entire pan is used as an oscillating body, and thus, the rope passed through interacts with the forming ultrasonic waves during the duration of the immersion bath. An optimal effect of the ultrasonic on the rope material is therefore achieved. The generator power can be altered fully variable from 0 to 100%. For the first preliminary tests, the ultrasonic transducers were operated with a fixed frequency of 40 kHz. With the help of further fine-tuning and supplementation of a new generator unit, four additional frequencies can be controlled (81/94/100/140 kHz).

3 Experimental Investigations

At the time of the experimental investigations carried out, the system was only capable of mapping a frequency of 40 kHz. Nevertheless, this is to be regarded as sufficient since the effect of ultrasound on fibre ropes is to be investigated. Subsequent adjustments of the frequency are then to be evaluated for the optimization of the coating performance. For the tests, the speed at the MAGEBA RopeLiner plant was selected as high as possible for each experiment. This is oriented close to the maximum speed of the plant in order to depict real operating conditions with short dwell times of the rope material in the coating bath. The tank was filled with the same water-based coating for each experiment and the temperature of the solution and the level were continuously monitored during the tests. The power of the generator was continuously increased by 20% steps per rope section in order to be able to compare the different feed rates of the coating between the different power levels.

The feeding rate was determined by weighing the respective rope sections in comparison with the zero sample, which means that the rope was coated without the use of ultrasound (0% ultrasonic power) as well as the alignment with the uncoated rope section.

Two different fibre strand constructions were examined for the investigations. These are ropes with a diameter of 20 mm, a 12-stranded, twisted polyester rope and a rope with a polyester core and polypropylene jacket in a 13×9 wire-lay design. Particularly interesting is the PES/PP mixed rope. Due to its properties, polypropylene has almost no water absorption and is therefore a particularly difficult case for coating with water-based dispersions.

4 Results of the Investigations

After the coating of the PES/PP mixing rope and the subsequent drying, the rope sections were measured several times using a fine balance. In particular, the effects, as already explained in Sect. 2, were observed for the coating results. The coating input shows without the use of ultrasonic the expected minimum result. However, with the use of ultrasonic, an improvement of the feeding rate is detectable.

The results for the mixed rope made from a polyester core and a polypropylene jacket in a 13×9 wire-lay-design are shown in Table 1.

The manufacturer of the coating specifies a feeding rate of 6–10% in addition to the weight of the polyester fibre. By comparing the results with the uncoated rope section, no further improvement can be seen in comparison with the expected coating input despite the use of the ultrasonic dip coating. Nevertheless, a mixed rope with a polypropylene core is depicted here. This material tends to take on almost no water and thus coating. Hence, an improvement in the coating take-up is only possible in the 13-strand polyester jacket of the mixing rope. The core of the rope, which only makes up about 60% of the mass of the complete rope mass, could be coated close to the expected optimum, despite the parameters (large rope

Table 1 Results coating test with the PES-PP mixed rope

Power ultrasonic [%]	Mass rope sample [g]	Variation facing sample zero [%]	Changes facing mass of the uncoated rope [%]
Sample zero	782.5	–	6.02
20	808.6	3.23	9.05
40	796.6	1.77	7.68
60	812.1	3.64	9.44
80	799.1	2.08	7.97
100	797.9	1.93	7.83

Mass of the uncoated rope: 735,4 g

diameter, high throughput speed) were not ideally held. Furthermore, it can be seen that the best results in the coating performance apparently do not correlate with the power input into the ultrasonic bath. The best results were achieved at 20 and 60% ultrasonic performance, while the rest of the performance levels were similar for the coating input. The temperature measurements carried out continuously during the coating tests in the dip coating bath also indicate a temperature rise of the coating solution, which, however, occurs to a lesser degree with regard to the power levels 20 and 60%. This means that in the case of the best coating results, also the smallest amount of ultrasonic power in the form of heat has been released into the immersion bath. Subsequently, the tests were carried out with the pure, twisted polyester rope. Analogous to the manufacturer’s data, coating amounts of 6–10% are to be expected in addition to the fibre weight. The results are shown in Table 2.

The tests with the pure polyester rope show a differentiated behaviour compared to the experiments with the mixed rope. The expected coating input is slightly below the conventional immersion bath. This is a proof to the difficult conditions for the coating input with large rope diameters in combination with a high throughput speed.

Furthermore, it can be seen that the use of ultrasonic provides only a small part for improving the feeding rate as long as the power of the ultrasonic system is down-regulated. The best results are shown here at 60 and 100% ultrasonic performance, with a significant improvement only after the full power input in the immersion bath. The improvement of the feeding rate versus the zero sample is about 4.6%, which is a significant improvement in the coating results despite the given system limits (ultrasonic frequency fixed at 40 kHz) and the difficult conditions within the immersion bath.

The slight differences in the feeding rates are noticeable in the lower power stages. The strong increase in the feeding rate at 100% ultrasonic power indicates that the boundary surface effects which counteract the coating input can only be overcome with this. The results of the feeding rate in the rope also coincide with the temperature measurements of the immersion bath during the test run. An overview of the temperature measurements taken during the test series is shown in Table 3.

Table 2 Results coating test pure PES-rope

Power ultrasonic [%]	Mass rope sample [g]	Variation facing sample zero [%]	Changes facing mass of the uncoated rope [%]
Null probe	1490.6	–	5.89
20	1492.5	0.13	6.01
40	1494.5	0.26	6.14
60	1504.5	0.92	6.76
80	1498.2	0.51	6.37
100	1562.2	4.58	10.20

Mass of the uncoated rope: 1402,8 g

Table 3 Temperature of the ultrasonic dip coating bath while the tests

Power ultrasonic [%]	Measured temperature dip coating bath PES/PP mixed rope [°C]	Measured temperature dip coating bath PES-rope [°C]
0	22.5	22.7
20	23.0	23.6
40	23.3	23.6
60	23.0	23.4
80	23.4	23.6
100	23.4	23.3

Highest feeding rate achieved

5 Conclusion

The tests carried out have proven the effectiveness of ultrasonic on the coating input in fibre ropes. Despite the system limits, the test setup used for this purpose is already capable of improving the feeding rate in fibre ropes of large diameters by almost 5%. With an expansion of the frequency band further improvements can be expected in the future. The aim is to achieve an optimized coating input for various fibre strand constructions of large diameters with the aid of extensive series of tests and thus to provide a future in-line capable system for cable coating systems.

Overlay Finishes and Coatings for Improving Abrasion Resistance in Braided Polyarylate Fiber Ropes

Loet Hoppe, Koen van Goethem, Hans-Gunter Kluczik, Forrest Sloan, Jens Mammitzsch and Markus Michael

Abstract Polyarylate fibers are commonly used in rope making, in lightweight structures, textile reinforced composites, and textile-based mechanical components for technical applications. Due to higher demands on abrasion resistance of fiber ropes in technical applications, such as hoisting and lifting applications, investigations have been carried out to improve the abrasion resistance of braided fiber ropes, made from polyarylate fibers Vectran™. Overlay finishes and coatings have been applied on braided fiber ropes to investigate the influence of fiber finishes and to investigate the influence of coatings and overlay finishes on the ropes' properties. Further, in a part of the rope samples, the fiber finish has been removed before coating, in order to investigate the interactions between fiber finish and applied coatings.

1 Introduction

Polyarylate fibers Vectran™¹ are offering a unique property profile, including high strength, high stiffness, good thermal resistance, low moisture absorption, and minimal creep. Therefore, these fibers are applied in running and static fiber ropes, such as mooring lines, lifting ropes in deep-water lifting, utility ropes, and robotic

¹Vectran™ is a registered trademark of Kuraray Co., Ltd., Tokyo, Japan.

L. Hoppe · K. van Goethem
I-Coats N.V, Berchem, Belgium

H. -G. Kluczik
Kuraray Europe GmbH, Business Unit Industrial Fibers, Hattersheim, Germany

F. Sloan
Kuraray America Inc., Vectran Division, Chesterfield, VA, USA

J. Mammitzsch (✉) · M. Michael
Intelligent Fiber Reinforced Structures, University of Applied Sciences Mittweida,
Mittweida, Germany
e-mail: mammitzs@hs-mittweida.de

tethers. Due to the good thermal resistance, it is also applied in aircraft and aeronautic applications.

Over the years, there have been higher demands on strength and abrasion resistance of fiber ropes, not only meaning the resistance to external abrasion but also the resistance to internal fiber-fiber abrasion processes. In return, there is a high interest in not increasing the diameters of the ropes, to keep the advances of using thin and lightweight fiber ropes in technical applications. For the reasons mentioned above, the fiber manufacturers invented several fiber types with different fiber finishes, providing additional functional properties.

Still, for many applications, e.g., winch applications and other hoisting applications, the available fiber finishes still do not fully cover the customers' demand for more and more increasing lifetime of fiber ropes. This demand can also not be fully covered by improving the textile structure, because there is a balance to be found between optimal strength, optimal flexibility, optimal dimensional stability, and optimal fatigue resistance, always considering the requirements of the intended final application.

One approach for solving this is, to apply overlay finishes and coatings for further reducing abrasive processes and thereby improving lifetime of Vectran™ ropes in technical applications with abrasive influences.

This paper is showing the influences of lubricating overlay finishes and polyurethane-based coatings on a type of Vectran™ fibers, already containing a lubricating fiber finish. Fiber ropes have been braided from these Vectran™ fibers, coated with overlay finishes and mixtures of overlay finishes and coatings. Tensile tests and hex bar abrasion tests have been performed to investigate the influence of coatings and overlay finishes on the rope performance. For a part of the rope samples, the fiber finish has been removed before applying overlay finishes and coatings, to investigate the influence of the fiber finish and maybe occurring interactions between fiber finish and additionally applied materials.

2 Materials Selection and Description of Samples

As a basis for the intended investigations and tests, a fiber type with lubricating fiber finish was needed which is state of the art, easily available on the market and commonly used in rope making. The fiber Vectran™ T97 has been chosen because it is fulfilling all requirements. Table 1 is displaying basic tensile properties of Vectran™ yarns.

The polyarylate fiber Vectran™ T97 is containing a fiber finish, based on silicone oils. This fiber finish is, besides protecting the yarns during textile manufacturing (twisting, spooling, braiding), providing additional lubricating properties for inhibiting internal abrasion in textile structures, and has been optimized for being used in braided and laid fiber ropes.

Table 1 Properties of the polyarylate yarns according to [1]

	GPa	g/den
Break strength	3.2	25.9
Initial modulus	75	600
Elongation at break [%]	3.8	—

The fibers have been provided as yarns with a linear density of 1670 dtex (1500 den).² For twisting strands, three of these yarns have been pre-twisted with a twist rate of 20.2 TPM. For making the rope, six strands in S-twist and six strands in Z-twist have been braided on 12-strand braiding machinery as a 1-on-2 braid with a pitch length of 27 mm.

Since the braiding machinery does not contain a back twist device, the S-twisted yarns have been placed on the S-bobbins, the Z-twisted yarns on the Z-bobbins, to make sure that the strands are further up-twisted, not untwisted. This creates an effective twist rate in the strands of approx. 57.24 TPM.

The final rope diameter is approx. 3.3 mm.

Following overlay finishes and coatings have been considered for the coating tests:

ICO-LUBE 10

This overlay finish is based on waxes and silicone and is meant to be applied on the fibers. It has been developed to prevent damage, caused by textile processing, and is additionally improving the abrasion resistance of polyester, polyamide, polyarylate, and high-modulus polyethylene fibers.

ICO-THANE 10

This coating is an aqueous polyester-based aliphatic polyurethane, providing medium hard and flexible coating layers on polymer fibers. The polyurethane is providing a low coefficient of friction compared to other polyurethanes and is optimized for being applied to polyester, polyamide, polyarylate, and high-modulus polyethylene fibers. Besides, with suitable additives, polyurethane layers are providing certain protection against UV radiation.

LAGO 45

This coating is a special synthetic binder with a polyurethane resin for the impregnation of textile ropes, twines, and fishing nets made from HMPE. It is providing a strong adhesive, self-repairing coating layer with high flexibility. It showing a relatively high coefficient of friction.

For coating the ropes, following overlay finishes and coating mixtures have been applied to the rope samples:

²Linear density without fiber finish T97.

- ICO-LUBE 10, undiluted
- ICO-LUBE 10, diluted with water; 1 part ICO-LUBE 10 to 5 parts water (dilution 1:5)
- ICO-LUBE 10 (dilution 1:5) after which a coating of ICO-THANE 10 (dilution 1:2) was applied
- ICO-LUBE 10 (dilution 1:5) after which a coating of LAGO 45 (dilution 1:2) was applied

One set of rope samples were washed before coating, to remove the fiber finish.

After removing the fiber finish, the ropes of this set of samples were coated with ICO-LUBE 10 (dilution 1:5) + ICO-THANE 10 (dilution 1:2).

All coatings have been applied to the fiber ropes by dipping in an emersion bath.

3 Abrasion Tests

For determining the improvements in abrasion resistance, an abrasion test has been performed. In this test setup, the rope sample is abraded over a hexagon steel bar, made from stainless steel, with a width across flats of 6.05 mm, as can be seen in the setup, displayed in Fig. 1. The outer diameter of the deflection sheaves is 80 mm, the diameter on the groove's ground is 60 mm, the groove width is 5 mm. The abrasion setup is based on ASTM D 6611, while the bottom deflection sheave has been replaced by a hex bar.

The rope samples have been tensioned with a relative load of 0.15 cN/dtex. The stroke length is 200 mm and the samples have been abraded over the hex bar at 66 cycles per minute. Four samples have been tested per parameter/coating setup. All tests have been performed as dry tests (without influence of water) under standard climate conditions.

The results of the abrasion tests are shown in Fig. 2. Data analysis and interpretation has also been performed following ASTM D 6611.

As can be noticed in Fig. 2, the fiber finish of Vectran™ T97 is already providing an improved abrasion resistance and is increasing the lifetime in the abrasion test by about 10%, compared to the fiber without finish.

When additionally adding the overlay finish ICO-LUBE 10, the abrasion resistance is not further improved. In opposite, when adding the finish in undiluted conditions, the abrasion resistance is decreasing, while diluting the finish in water at a mixture of 1:5 and applying this dilution to the ropes, the abrasion resistance is almost the same. Looking to this more detailed, it is found that the average of the ICO-LUBE 10 is a little lower, but the variation is higher. This probably is an indication for the fact that applying ICO-LUBE 10 by dipping is less consistent than the method used by Kuraray. With a more consistent application method (e.g., kiss-roll), it is expected that the variation decreases and the average values go up. Thus, the performance of the T97 finish is comparable to that of the ICO-LUBE 10. When the ICO-LUBE 10 is applied undiluted, then the abrasion performance is



Fig. 1 Setup for abrasion tests

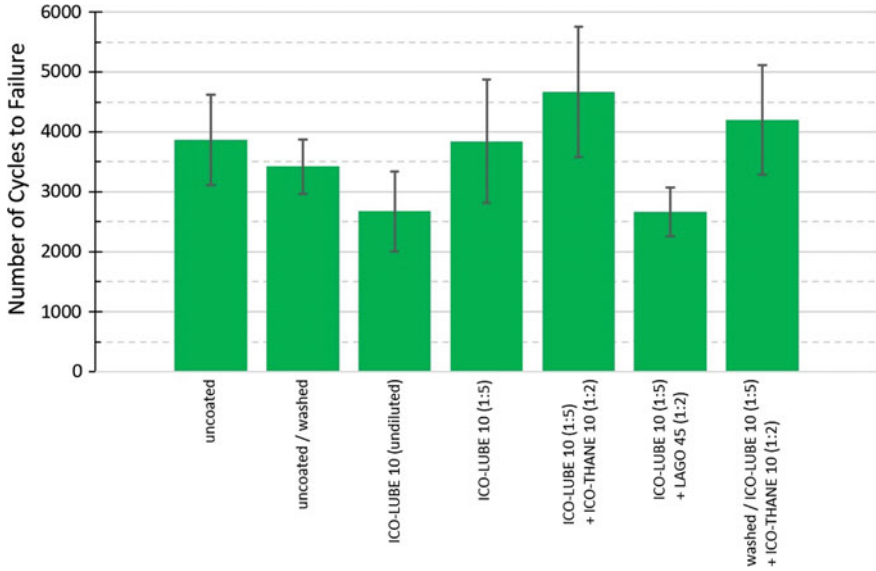


Fig. 2 Results of abrasion tests

lower. This is probably because the film is too thick and is scraped off in the abrasion causing uneven running and tension variations. Especially the higher tension will cause the abrasion to accelerate. From this point of view, it can be stated that applying an overlay finish on top of an existing fiber finish will not automatically significantly improve performance. Second, it should always be verified what the optimum amount of overlay finish is for a given design and conditions of use.

After applying the overlay finish ICO-LUBE 10 and adding the polyurethane coating ICO-THANE 10, the abrasion resistance is improved by 20%, for both, washed and non-washed rope samples. The improved abrasion resistance of the mixture, compared to the pure or diluted overlay finish, is due to the fact that the lubricating overlay finish is creating a lubricating layer on top of the abrasion resistant polyurethane coating layer on the fibers.

Analyzing the results of the rope coated with ICO-LUBE 10 and LAGO 45, shows that LAGO 45 is also creating a decrease in abrasions resistance. This is probably caused by the higher coefficient of friction of the rope coated with LAGO 45. Because of the higher friction, the abrasion is also higher for the same loading conditions.

4 Summary

As a conclusion, it can be stated that the abrasion resistance of braided fiber ropes can be improved by applying overlay finishes and coatings.

For optimal performance, a mixture of additional overlay finishes and hard-flexible coatings with a low coefficient of friction seems to be the most effective way of coating a Vectran™ fiber rope. In this case, it must be made sure that the combination of overlay finish and coating is working effectively with the selected fiber type and its fiber finish.

The fiber type Vectran™ T97 contains fiber finish at an amount of 5% per weight of fiber. So, using a fiber type with a lower amount of applied fiber finish (e.g., Vectran™ T150 or Vectran™ T117) could even further improve the abrasion resistance after applying additional overlay finishes and coatings.

These topics need to be investigated and evaluated by application-oriented testing of the intended final product (fiber type, rope design) under consideration of the loads occurring in the real application and environmental influences, such as temperature, humidity, and exposure to sunlight.

Reference

1. Kuraray Co. Ltd., Japan. www.vectranfiber.com/properties/tensile-properties/.

Part III
Smart Textiles

Metal-Textile Hybrid Carrier Modules with Integrated Functions Based on Textile Sensors

Enrico Putzke, Andreas Müller and André Riedel

Abstract Based on the results of a research project it is described how material selection and user friendly design improves the properties of metal-textile hybrid carrier modules, in comparison to conventional carriers, and thus generate new marketing approaches. By textile means processed nets and straps with metal reinforcement structures form the starting point for these new variants of carrier constructions. The textile inner layer has integrated sensors and application-oriented coating. To prevent harmful environmental influences on the structure of the textile construction, an additional outer layer can be installed. For the textile sensors, it was necessary to capture the current state of the art, to transfer a preferred version in a practical application.

1 Motivation and Overview of the Proposed Technological Development

The project resulted from the demands to increase the efficiency and flexibility of bulk storage and transport. Approximately 15% of all raw materials are bulk goods and transported on road-based systems like trucks. On pages of the finished goods, the value reduces to 3%. Therefore, on average, 9% of the total transport volume arises to be bulk material [1]. A variety of analyzed textile silos, for bulk solid applications, indicated the technical limit of conventionally used textile structures. These must be overcome by new intelligent hoist or hybrid constructions. The research work represents a novelty, in the construction of bulk handling silos, with

E. Putzke (✉) · A. Müller · A. Riedel
Chemnitz University of Technology, Reichenhainer Straße 70, 09126 Chemnitz, Germany
e-mail: enrico.putzke@mb.tu-chemnitz.de

A. Müller
e-mail: andreas.mueller@mb.tu-chemnitz.de

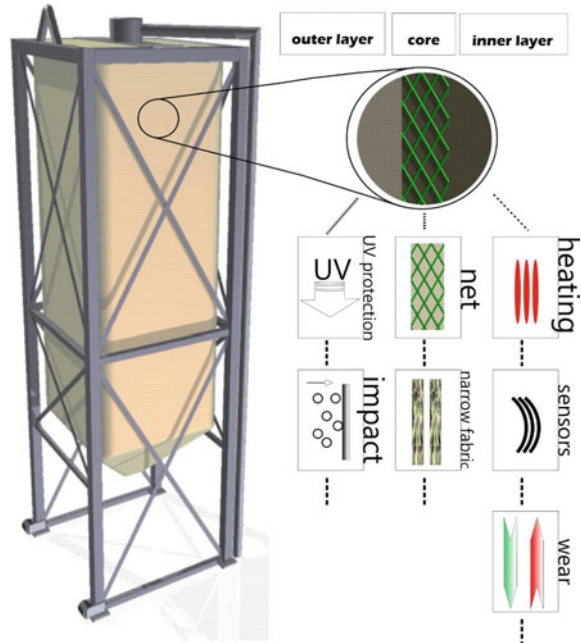
A. Riedel
e-mail: andre.riedel@mb.tu-chemnitz.de

the intended functional separation of the textile silo wall. By the separation of the wall in a supportive, bulk receiving textile silo wall and a load-bearing, high-strength belt structure, much larger bulk quantities can be stored in a textile silo. For the outdoor use, a moisture-absorbing and UV-resistant shell should be realized, preferably by a corresponding coating. Using modified textiles has been taken into account by other projects as well: e.g., to develop a textile integrated, intelligent sensor system for the detection of seat occupancy and seating position in vehicles [2]. In the corresponding case, to achieve the implementation, different concepts based on textile technology, have to be transferred on textile silos. This includes, in addition to the type and design of sensor elements, the study of placement opportunities within the textile structure (dots, linear ...) during the production process. The South Korean LG has recently presented a textile pressure sensor that is flexible. The company is yet to commercialize the technology but said that the sensor is superior to the present inflexible and stiff pressure sensors. According to the company, the new pressure sensor is made from a flexible and elastic polyurethane material that enables it to be integrated into other products seamlessly. Furthermore, it is said that the sensor detects pressure across the whole of its exterior rather than just specific points [3]. In early 2015, Teijin Limited announced the development of a PLA and carbon-fiber-based piezoelectric fabric. The fabric comprises a piezoelectric poly-L-lactic acid and carbon fiber electrode. Plain, twill and satin weave versions were produced for different applications, e.g., plain weave detects bending, satin weave detects twisting, and twill weave detects shear and three-dimensional motion. Whereas, the sensing function can detect uninformed displacement or directional changes. So the function allows fabric to be applied to the actuator or sensor to detect complicated movements [4]. According to the present project approach, intelligent, connected sensors should be used. Important parameters such as loading level, humidity, and temperature are measured. The sensors in the inner or outer hull structure and the structure of power supply must be implemented depending on the parameters to be collected. Figure 1 shows a collectively simplified Schematic of the research approaches.

2 Research on Textile Load-Bearing Webbing

Different seam structures were developed, for the selected materials for load-bearing net structure and the silo wall, which were suitable for the partial or complete connection of respective elements. The refinement and implementation of the sewing thread material ultimately determine the seam effectiveness, as well as the type and the cross section of the needle does so. In addition, the joints of the load-absorbing webbing nets were investigated on tensile strength and elongation. Depending on the design and optimization of different belts, the seam edge or the seam itself tend to be the breaking point. A further focus was set in the testing and evaluation of coating functionality to resist abrasive stress, by the testing of surface-coated textiles. In the project, this aspect was especially important to

Fig. 1 Abstractive model of a mobile, textile greater bulk solids silos



identify a suitable range of materials whose performance, in the flexible system, stays long enough to be later discharged on regular reversion cycles. It was assessed to maintain the compatibility with existing logistics systems. Therefore, for the overall concept, it was noted that the outer dimensions of conventional carriers will have to be maintained anyway. In addition to standard rupture and cycle tests, it was necessary to identify a test scenario closer to that of the strain in the demonstrator applications, which is displayed in Fig. 2. The results of the tensile tests show that with straight-vertical force, the breaking load of the network structure can be scaled linearly with the number of belts used. A deviation of the strength resulted in only 10%. It should be noted that the cross straps and its seams have only minor impact on the breaking strength. In addition, the resistance of the materials was tested by Xenon and long-term climate tests. These tests showed that the strength decreases rapidly, due to the weathering, which must be considered as a factor in the interpretation of the tensile strength of used net structures.

Later on “close to end” applications, preliminary attempts were carried out, to test the properties of the rather complex textile structure. This was done by using a $1.5 \times 1.5 \times 2$ m bag filled with sand and exposed to a set of everyday driving situations on a truck (comp. Fig. 3). The road test was recorded from four different camera angles and analyzed later. It turned out that at normal speed (city, highway) the hybrid bag and textile unit quietly behaved as predicted. Only in extreme situations, it comes to more significant movements, e.g., when a sudden stop from 40 km/h was carried out. The bag waved off considerably (comp. Fig. 4). This



Fig. 2 Tensile tests on two network segments

situation describes a borderline case, which should not occur in the industrial application by the planned crosswise fixation of the textile structure. The brake test rather served a first validation of the seam and belt strength in dynamic user environments.

The driving tests lead to a better understanding of the behavior, of the bulk, during the transport process. For the material wear conception, the available test benches at the research facility have been taken into account and evaluated for suitability. Only unsatisfactory results were obtained for the determination of the application-oriented wear of textiles, by using common methods. Based on DIN 295-3 [5] (“stoneware pipe systems part 3: test methods for sewers and channels”) a modified test bench got developed, which now allows testing of (textile) semi-finished products with different abrasive materials (comp. Fig. 5). In the described test, different textiles with and without coatings have been tested on their abrasion resistance. In initial trials, different bulk materials like wheat, plastic scratch, screws, and cutting pieces of steel were used. For wheat, the abrasive effect is quite low and the test periods must be long until a visible effect can be recognized. The tilting angle during the tests was 32° in both directions and 10 cycles per minute. Within a cycle, the bulk material laid back 1.9 m. The tensile strength of the textiles, in consequence of the stress in the test setup with metal scrap lead to a reduction to 15% of the tensile strength of the output value. Wheat drops the value



Fig. 3 Preparation test drive with camera technology



Fig. 4 Sample silo during test drive, sudden breaking of the truck



Fig. 5 Test bench with enclosure

to only 65%. Both numbers refer to 100.000 cycles. The number of 100.000 cycles is taken from the DIN of 295-3 and is considered a first clue for the testing of textile with the novel tipping gutter tester.

3 Review of Production Sequences, as Well as the Metallic Construction

The design of application-specific systems resulted in several solutions or variants. A first demonstrator, a Multicar container (according to DIN 30735 [6]) (comp. Figs. 6 and 7), was used for this verification. As one result, the hybrid construction allowed a reduction of Tara weight to 190 kg, which is equivalent to a weight saving of 20%. This demonstrator was designed specifically for the garden care or public service. The mesh of the textile webbing has a lower breaking load, the structure is close-meshed, a third outer layer was not necessary and the inner bag has a highly resistant PU coating. Moreover, a roll-off container according to DIN 30722 [7] with three single hanging sacks, including frame, was designed and implemented too. With this system, it is possible to carry three different conveying goods, which increases the utilization and productivity in logistics. Different textiles can be implemented to respond to the respective bulk goods. Also, these containers can be extended by sensors.

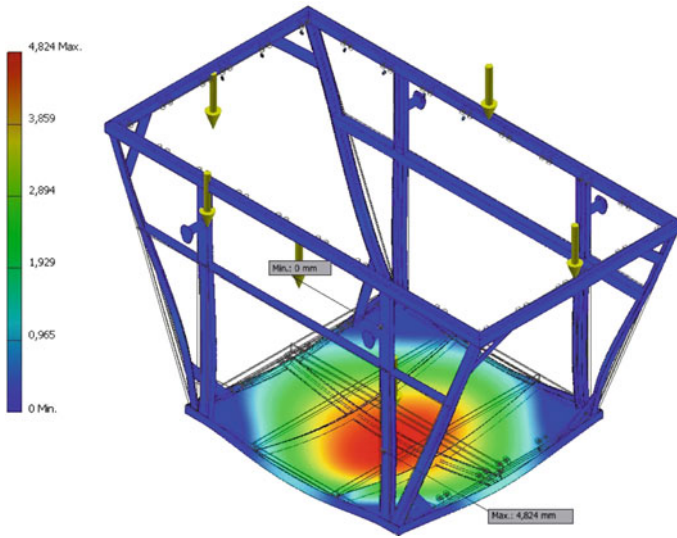


Fig. 6 FEM calculation—shift

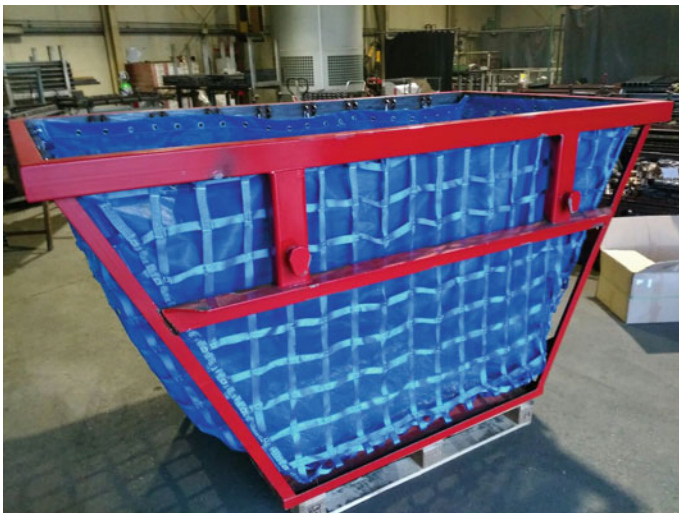


Fig. 7 Hybrid multicar container

4 Development of Measuring and Data Transmission Concept

In this section, the electronic wise material and component selection was the main part. Right from the beginning, it can already be stated that hardly any real components as textile sensors were available at that time. This was not clear at the

beginning of the project from the information of the state of the art. Anyway, first smaller segments, of the larger textile construction, were equipped with chip-based sensors and fitted to the textile by embroidery technology, including data and energy supply. In this way, it was possible to demonstrate the basic functions like temperature, humidity, and load detection (comp. Fig. 8). The determined textile/measurement configurations can be used for the demonstration, of the project approach, e.g., in the field of agriculture and recycling.

In the course of the project, different types of sensors were taken into account. The need oriented assessment revealed a limited selection of important products by parameters and from user point of view, thus sensor types for the measurement concept were selected. These included pressure, temperature, humidity, air pressure, GPS, and motion sensors. For operating and reading the sensors data microcontrollers have been used, because of the small energy they require, the space-saving and the low-costs. As unit controller served, on the one hand, the Linux-based Raspberry Pi and on the other hand Arduino-based microcontrollers. Arduino is a physical computing platform consisting of soft- and hardware and it is open source. The hardware consists of a simple Board with a microcontroller and analog and digital inputs and outputs. It is programmed in C or C++. By connecting the microcontroller with the individual sensors, the data can be read and can be processed further. The sensors and data transmission technology was attached to the mobile and stationary new silos. When speaking of the mobile type, a sufficient supply of power posed a problem. The required energy increases with shorter reading and transmission intervals. To counter the problem, photovoltaic modules have been installed together with a battery pack. Displaying media and measuring graphs on the stationary silo application were done by using a 3.5" LCD screen. The mobile version was equipped with a GSM module to transfer data over the cellular network to a server. From there on, they were stored and available via an Internet site (comp. Fig. 9). An advantage of this Internet-based method is that



Fig. 8 Textile segments with integrated sensors and PC system

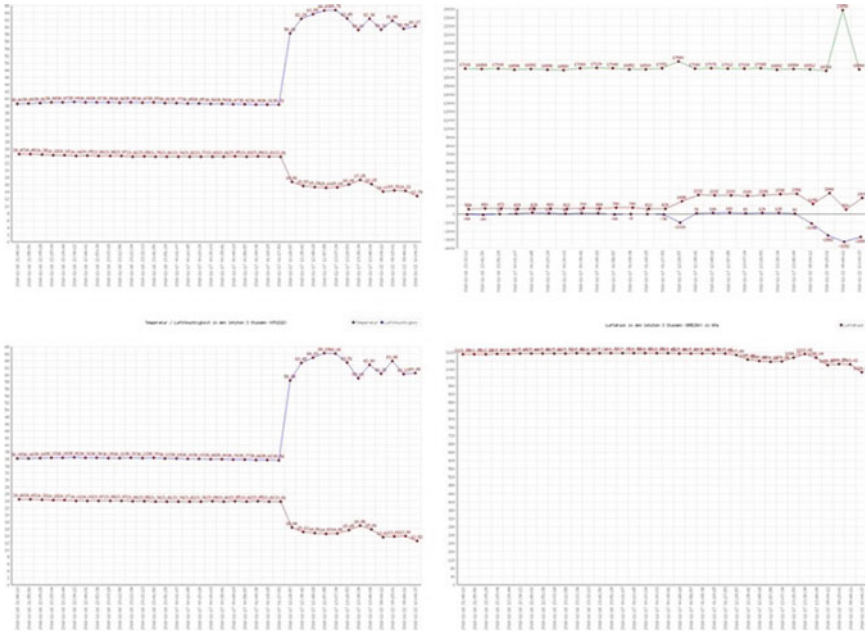


Fig. 9 Screenshot website live stats

unlike an app-based application, users do not dependent on Android or OS devices. In Fig. 10 the used sensors, microcontroller and other components for both, static and mobile, silo units are shown.

5 Continuous Testing Under Practical Conditions

Together with the project partners, the stationary silo variant got tested on functionality and durability. In a trial, the prototype got filled and charged for weeks with the bulk material, as a static test. Then the elongation of the silo got measured, which amounted to almost zero. Due to the high-strength belt structure, the system can absorb very high forces. The same demonstrator got equipped with a conveyor system and sensor technology (comp. Fig. 11). A spiral pump was used, which continuously transported the goods (wheat). The tests showed an undisturbed operation of the conveyor. A further advantaged could be proved due to the close-meshed structures, which lead to no bulges, stretching, or wrinkling (comp. Fig. 12). These things regularly occur when using conventional textile silos and big bags. The integrated sensor technologies also worked trouble-free and via a special Web address the current temperature, humidity, and fill

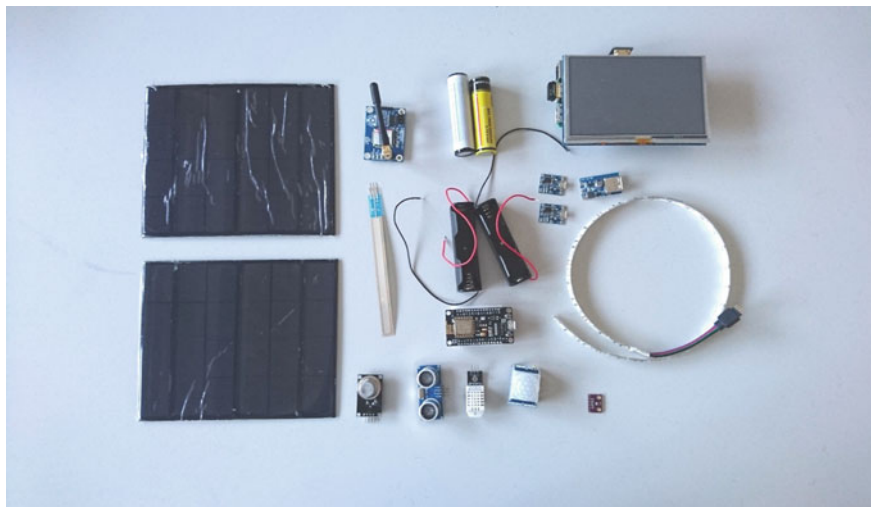


Fig. 10 Used sensors and microcontrollers

level was always available. In detail, the used sensors were the following: DHT22 temperature and humidity sensor, HC-SR04 ultrasonic sensors for determining the filling level and pressure sensors SF9375. The pressure sensors served as additional level points. When the pressure, caused by the bulk material, reached a certain level a signal is created and thus indicated whether the silo is empty (lower pressure sensor) or filled (upper-pressure sensor). In the operative phase, performance limits were determined. At the bottom of the silo, a metal outlet had to be installed to ensure the connection of the spiral conveyor. For bigger structures and silos it is advisable to form the lower part completely of steel sheets. The sensor system has been particularly discharged when attempting to measure in circulation mode. Through the above-mentioned core flow of loose material, the free-hanging temperature and pressure sensor got torn off by the bulk material. The forces were too large for the reinforced signal cable. In the future, the signal cable should be supported through appropriate food chains (plastic/stainless steel) or moved to the periphery of the silo.

6 Conclusion and Prediction

Until the end of the project, several prototypes were used for field tests, which were designed differently and examined during the test procedure regarding functionality and optimization for the application. These applications included hybrid silo constructions for driving tests under load, skip container for multicar vehicles, roll-off container for trucks (comp. Fig. 13), and stationary silos as well. The evaluations of the tests lead to no striking findings in the filling and emptying operations in the

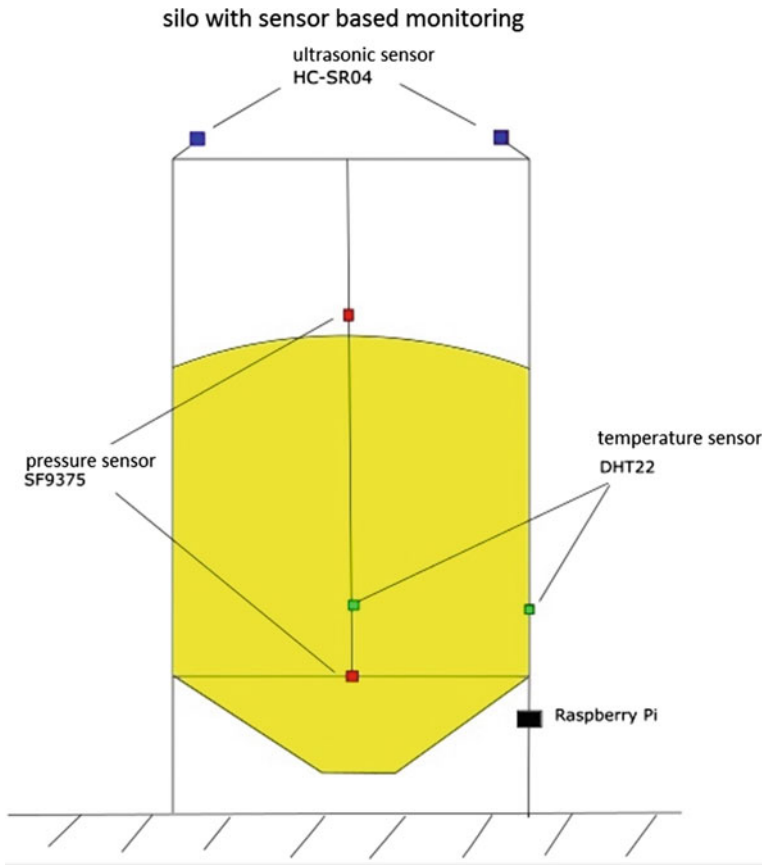


Fig. 11 Schematic setup

textile system. When emptying the textile silo it behaves analogous to conventional silos. The construction of intermediate bulk containers is focused on the modularity and compatibility with existing systems. Particularly in the area of handling smaller batches, a benefit can be achieved with such a scalable system. Concerning transport capacities, it can be used to store the bulk material in the same transport rack and connected it to the internal material logistics. By marketing activities of the project partners, the exact needs of the targeted market segments must now be examined more closely. In case of agriculture, it can be stated that the trend toward more specific methods of cultivation and seldom types of grains has become a topic. The rather unsatisfying integration of real textile sensors will be addressed with further development with the mobile version of the silo. With new collaborations, which emerged in first successfully, in-belt load sensors will be tested (comp. Fig. 14).



Fig. 12 Experimental setup onsite mill



Fig. 13 Modular, mobile silos on truck

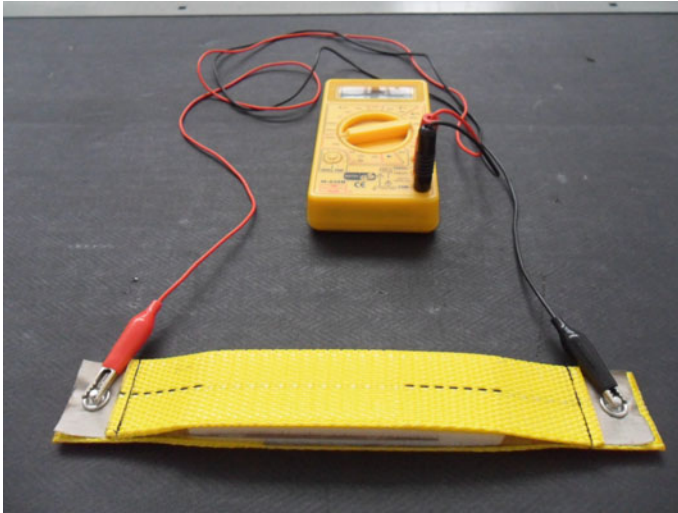


Fig. 14 Capacity sensor made by textile means only

Acknowledgements Thanks to the Federal Ministry of economy and energy for the project grant.



References

1. Chr, P. (Hrsg.). (2003). *Güterverkehr—Eine Integrationsaufgabe für die Logistik*. Berlin, Deutschland: Erich Schmidt Verlag GmbH & Co.
2. Textilforschungsinstitute Thüringen-Vogtland e.V. et.al. (2011). Entwicklung eines textilintegrierten MST-Sensor-Systems zur Erkennung von Sitzbelegung und Sitzposition in Kraftfahrzeugen—SeatSen, BMBF 16SV3457, Greiz. www.tib.eu.
3. T.EVO. (2016). LG develops flexible pressure sensing fabric, T.EVO Sep/Oct 2016, no. 3, p. 15.
4. Corporate Communications Teijin Limited, NEWS RELEASE. (2015). Teijin Develop World's First Piezoelectric Fabrics for Wearable Devices. Tokyo, Japan: Kansai Univ.
5. DIN EN 295-3:2012-03. (2012). Steinzeugrohrsysteme für Abwasserleitungen und -kanäle— Teil 3: Prüfverfahren; Deutsche Fassung EN 295-3:2012, Beuth Verlag.
6. DIN 30735:2016-02. (2016). Normbehälter mit einer maximalen Breite von 1520 mm für Absetzkipperfahrzeuge - Maße, Werkstoff, Ausführung, Beuth Verlag.
7. DIN 30722-1:2015-12. (2015). Abrollkipperfahrzeuge, Abrollbehälter—Teil 1: Abrollkipperfahrzeuge bis 26 t, Abrollbehälter System 1570 aus Stahl, Beuth Verlag.

4D Textiles: Hybrid Textile Structures that Can Change Structural Form with Time by 3D Printing

David Schmelzeisen, Hannah Koch, Chris Pastore and Thomas Gries

Abstract Additive manufacturing combined with highly elastic, extensible textile materials provides the opportunity to explore a new range of materials: 4D textiles. The name is derived from “4D Printing”, a combination of 3D printing and a time change element, providing the fourth dimension. In the case of 4D textiles, the time response is necessary, but also the textile material provides a crucial role in responding to external stimuli. Whereas 4D printing is currently limited to very small deformations and very slow changes in time, 4D textiles offer the opportunity to increase deformation and response time. This paper covers the concepts of 4D printing, achievements in 3D printing, and the concept of 4D textiles. The role of materials, critical process parameters, critical textile processes, and potential application areas are presented. Strengths and weaknesses of 4D textiles are discussed.

1 Introduction

There has been rapid growth in research regarding 3D printing in recent years driven by the low cost and material efficiency of the technology. Combining 3D printing and textile materials is still a relatively new research area [1–3]. It is a growth area that offers the promise of “4D Textiles”—hybrid textile/3D-printed structures that can change structural form with time [4]. There is a need to develop a deeper understanding of the textile–polymer interface in this process.

D. Schmelzeisen (✉) · H. Koch · T. Gries
RWTH Aachen University, ITA, Aachen, Germany
e-mail: David.Schmelzeisen@ita.rwth-aachen.de

H. Koch
e-mail: Hannah.Koch@ita.rwth-aachen.de

T. Gries
e-mail: thomas.gries@ita.rwth-aachen.de

C. Pastore
Thomas Jefferson University, Philadelphia, PA, USA
e-mail: PastoreC@philau.edu

4D printing has been described by Ge et al. [5] as

...active materials, such as shape memory polymers, can be printed to create an active microstructure within a solid. These active materials can subsequently be activated in a controlled manner to change the shape or configuration of the solid in response to an environmental stimulus. This has been termed 4D printing, with the 4th dimension being the time-dependent shape change after the printing.

This concept has been extended to 4D textiles [4]. Utilizing pre-stretched hyperelastic textiles as energy storage, the effect of 4D printed objects can be multiplied.

Work in the areas of 4D printing and 4D textiles has led to an investigation of methods to combine the concepts. 4D printing has been typified by the use of shape memory polymers (SMP) [5–7] for example. While printing, the polymer “remembers” the shape in which it was deposited. It can later be plastically deformed to a different shape. When exposed to heat above its transition temperature, the polymer attempts to return to the learned shape.

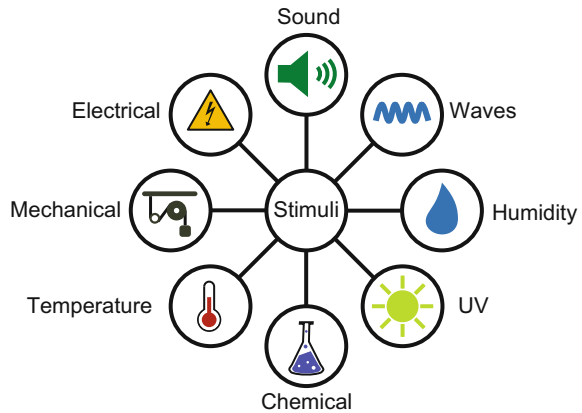
4D textiles explore the interaction of elastic textiles and 3D printing, wherein the textile is pre-stretched prior to printing, and after the printing is complete, the fabric strain causes curvature in the assembly [3, 8, 9] for example.

The underlying concept behind these hybrid material systems is to store energy in the textile material prior to printing and then release that energy to affected form and function of the hybrid system. Typically, knitted fabrics that contain elastic material are used due to the high elastic strain available and sufficient recovery force. The material should be highly deformable but still maintain a reasonable tensile modulus. After printing, the stored energy is released which leads to a structural change in the system, generally changing form from a 2D-printed structure to a 3D-curved structure. When properly designed, it is possible to make a 3D structure that is metastable, and thus able to assume two or more different stable structural forms that can be switched back and forth with nominal energy applied.

The behavior of this system depends, amongst other things, on the adhesion between the textile and the printed polymer. Not only does this dictate the static strength of the system but is also key to future studies around durability and reliability as the structure undergoes multiple transitions from one metastable state to another.

There is some existing work on the adhesion strength between the fabric and the printed polymer. Studies have explored the effect of polymer temperature and print speed on the adhesion [2, 10]. However, a detailed exploration of the adhesion between the textile and polymer has not been achieved to date.

Fig. 1 Stimuli that can activate the change over time



2 4D Technology

In 2013, Skylar Tibbits defined 4D printing as 3D printing with time as an added fourth dimension [11]. According to Pei in 2014 [12], “4D printing is a process that creates multi-material prints with the ability to transform over time or special material systems that can change shape. Today, due to the constant development of the technology, 4D printing is defined as a targeted modification of 3D printed structures with regard to form, properties, or functionality.”

Some of the properties that can be considered as changing with time (the 4th dimension) are stiffness, permeability, color, and degree of water absorbency [13]. Over time, changes may take place in the other dimensions, e.g., color or space. These changes are caused by stimuli [7, 13, 14] as illustrated in Fig. 1. Moisture, light, and warmth, as well as combinations of all three, can be considered stimuli. Sound, UV radiation, and microwaves, in addition to chemical, electrical, and mechanical forces, are further stimuli that may activate a system [7]. The resulting structure is able to achieve self-assembly, multifunctionality, and self-repair [13].

3 3D Printing on Textile

Textile materials can be integrated into 3D printing with various forms and functions as illustrated schematically in Fig. 2. As functional fibers, they are integrated into composite print materials which can achieve shape memory effects [15, 16]. They can be used as a textile surface or to reinforce a thin layer of plastic. Conversely, instead of a fully printed plastic surface, an expansion of the structure can be made possible in the layer [2]. As a functional textile material, the fabric can be used to store or transmit energy to the printed polymer.

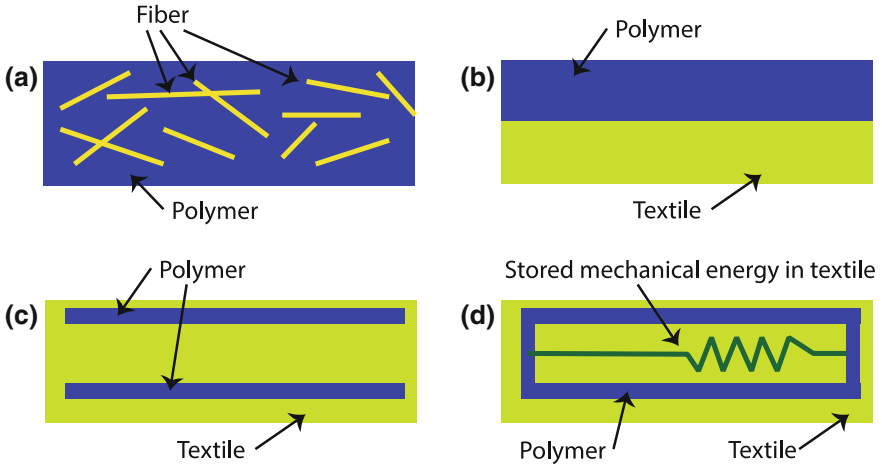


Fig. 2 Schematic illustration of uses of textile (yellow) and 3D printing (blue): **a** composite print material, fibers in the polymer filament, **b** layered reinforcement, **c** polymer partially printed on textile, and **d** Polymer partially printed on textile. Textile used as a spring to store or transmit energy

With respect to 3D printing using textiles, the setup and procedure do not differ from traditional 3D printing procedures. The literature only describes the fused deposition modeling (FDM) method for 3D printing on textiles. Possible reasons for this are the UV sensitivity of the textile, which is relevant for multi-jet modeling, the variety of materials that can be used in the FDM method, and the lack of possibility to incorporate the textile in other processes in a targeted manner [2].

Pei et al., Rivera et al., and Grimmelsmann et al. conducted and described 3D printing experiments on textiles [2, 17, 18]. Some examples of successful printed textiles are shown in Fig. 3.

Within the scope of our experiments, we have integrated the spatial expansion dimension into 3D printing on textile process. The change in the spatial extent takes place once after the manufacturing process. The structures are printed two-dimensionally on a pre-stressed textile. Upon completion of the printing process and the removal of the pre-stress, the hybrid structure changes its extent in the



Fig. 3 Published examples of 3D printing on textiles: **a** auxetic print [18], **b** braille print [2], and **c** grommets [17]

x, y, and z directions. This makes it possible to produce complex three-dimensional structures in one manufacturing step. The structures were developed following the concepts from architecture, metamaterials and bionics. Some of these structures are shown in Fig. 4. In Fig. 4, the textile is a polyester/Lycra jersey knit (yellow color). The filament is a thermoplastic elastomer (TPU) (blue color, in Fig. 4a, c) or a polylactic (PLA) (white color, in Fig. 4b).

3.1 Materials

To realize successful 3D printing on textile, a variety of thermoplastics suitable for 3D printing can be used. The materials to be used depend on the printer and the textile substrate. The molten polymer must not be so hot as it damages the textile. Pei et al. described the use of PLA, nylon, and acrylonitrile butadiene styrene (ABS) [2] as print materials. The best adhesion reported was with PLA. When combined with a textile made of PLA yarn, the level of adhesion increased further.

Textiles, such as knitted fabrics, woven fabrics braided fabrics, and nonwovens, can be used as the substrate. For adhesion between fabric and polymer, it is necessary to have sufficient porosity—too little and the polymer simply forms a film on

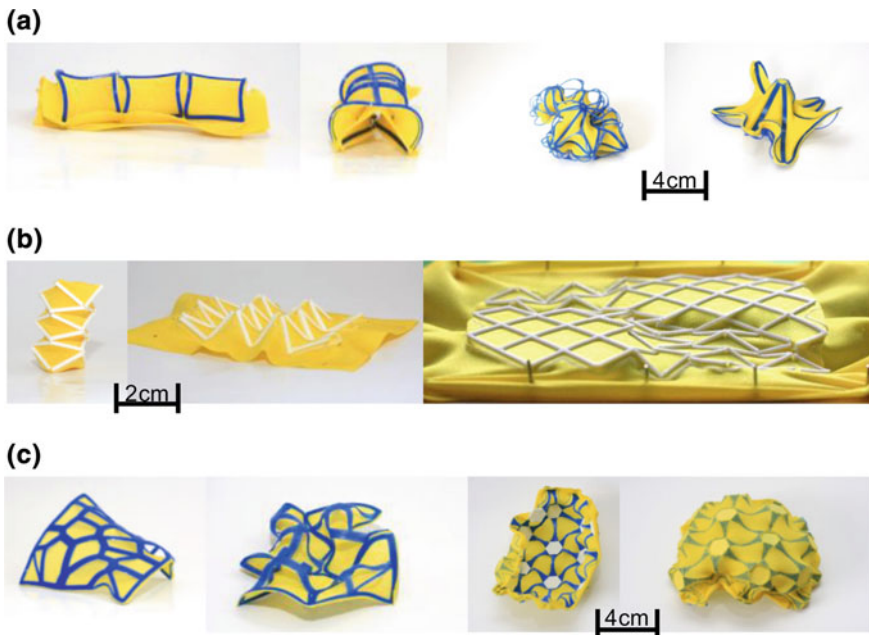


Fig. 4 3D-printed textile hybrid structures: **a** models based on bionics, **b** models based on the concept of metamaterials, and **c** models based on architecture

the surface—too much, and there is little textile in the final product. Fabric with variable porosity which can be controlled through pre-tensioning, such as knits, make them quite suitable for use.

3.2 Procedure

When 3D printing on textiles using the FDM method, the plastic is extruded onto and into the textile through the printer nozzle as shown both schematically and photographically in Fig. 5. The mechanical connection between the printed plastic and the textile to be printed on is created by the infiltration of the molten polymer around the fabric threads and the subsequent hardening of the plastic when it cools [2, 3]. A photomicrograph showing the infiltration of polymer through a knitted fabric is presented in Fig. 6.

There may also be a chemical bond between the textile fiber and the printed polymer, depending on the particular materials used and the surface treatments on the fabric. Because of the relatively high viscosity of the molten thermoplastic and the surface tension, a sufficiently high porosity of the textile is necessary [9]. High porosity can be either a fundamental textile characteristic or achieved by pre-straining the textile. According to Riviera et al., the textile can be treated as a further layer in the FDM process [17]. Two important factors in 3D printing on textiles are as follows: first, the adhesion of the plastic to the textile and second, the stability of the textile during the process.

According to Riviera et al., the first can be ensured by selecting suitable materials. Nevertheless, the adhesion between thermoplastic printed material and textile fabric need deeper understanding. Especially, the influence of textile parameters on micro- and meso-scale (such as surface tension, roughness, shape of the fiber, twist, hairiness of yarn, pore geometry, elasticity, and topography of the fabric) has to be questioned in detail. Furthermore, the influence of the process parameters of FDM printing (temperature of heatbed and nozzle, flow rate,

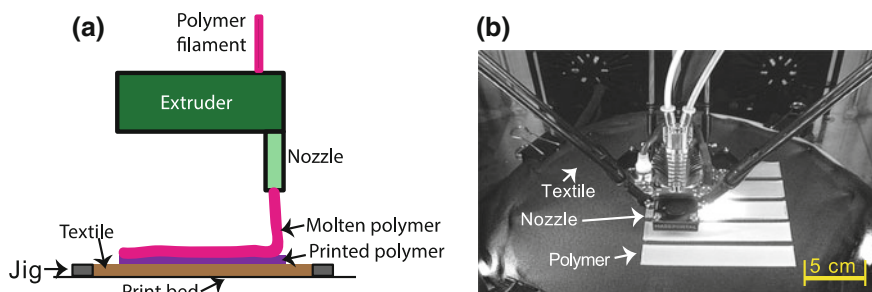
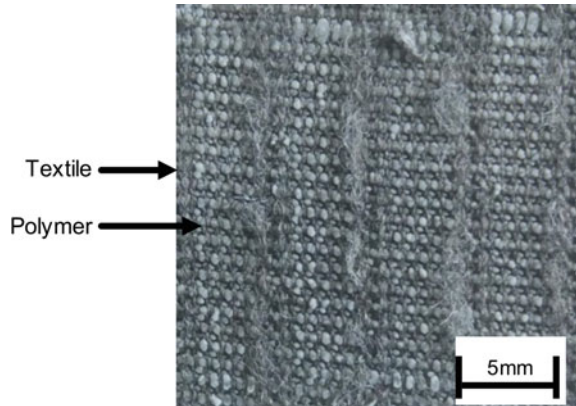


Fig. 5 3D printing on textile process: **a** Schematic sketch of 3D printing on textile process and **b** 3D print on textile

Fig. 6 Polymer infiltrated knitted textile after 3D printing process. This shows the back of fabric where the polymer can be seen having penetrated the pores of the knit structure



production speed and distance between nozzle and textile, etc.) has to be analyzed. To ensure comparable data, standardized testing procedures have to be developed. Based on experimental data, models can be derived leading to a better understanding of the influence of textile and process parameters on adhesion and mechanical properties of the hybrid material 4D textile.

4 4D Textile

Based on the definition of 4D structures, the term 4D textiles comprises textiles that change shape and functions over time [2]. 4D textiles can be realized using various approaches. One approach that has become increasingly popular in the last few years is the use of shape memory materials in textiles. In this context, the shape change of textile structures due to an external stimulus has already shown great potential [19]. For example, shape memory materials can be incorporated via weaving, stitching, or braiding. In the past, various studies have been conducted on this topic [19].

Another approach to creating textiles with form and function change is 3d printing onto pre-strained textiles, wherein the textile acts as an energy storage device. These 4D textiles are hybrid materials of fabric and printed polymer.

The group of Schmelzeisen et al. at the Institut für Textiltechnik (ITA) of RTWH Aachen University focus on the approach to utilize 3D printing on textile to develop microstructures that change mechanical properties over time. This approach combines the flexibility of the 3D printing process in regard to materials, process, and size with pre-stretched hyperelastic textiles as energy storage. The effect of 4D-printed objects can be multiplied. Some examples are shown in Fig. 7.



Fig. 7 4D textile; stimulus: heat [20]

4.1 Materials

The material requirements for 4D textiles are very similar to those for any hybrid textile/3d printing process, as described in Sect. 3 above. There is benefit to making the distinction between basic and functional materials in this context. Basic materials cannot, by themselves, effect an autonomous change over time. Functional materials can effect an autonomous change over time due to their properties.

We have discussed the use of shape memory materials in 4D structures, and these can be functional materials as the printed polymer or incorporated into the textile itself.

The fabric can be a functional material as well, especially if the goal is mechanical energy storage and release. In this regard, knitted fabrics are attractive because of the high strain to failure, allowing the ability to store significant strain energy, and also providing a desirable pore geometry. Knits are usually anisotropic, and this anisotropy can be precisely adjusted during the textile manufacturing processes. This enables us to set up the change over time partially in the textile itself.

Due to their structure, knits also exhibit extensibility and elastic recovery. The expansion behavior depends on the structure and the material. The material dependency of the expansion is identical in the course and wale directions. The structural expansion depends on the bond. By using material combinations, highly extensible knits with a high level of restoring force can be manufactured. Most commonly some elastic element is used in the knit, such as Spandex to provide the recovery force. Such knits are very suitable for use as substrates for 4D textiles.

4.2 Stimuli

In general, the stimuli can be used that also effect change over time in traditional 4D printing. However, the interactions with the textile must be considered separately.

4.3 Applications

4D structures have great potential in the field of medical products, soft robotics, architecture, automotive, sports and clothing, and more. The advantages are the high customization and functional adjustment.

4D textiles are used in size-changing objects, pressure-sensitive components [17], sound-absorbing textiles [21], and adaptive footwear [22] as shown in Fig. 8. 3D printing on textile is used, for example, to produce jewelry [17] handbags and clothing with integrated Braille [2] as shown in Fig. 3.

4.4 Design Approach

The development of 4D structures is material-driven. To fit the customers' needs, its design should be user-centric. It is therefore practical to combine user-centered design methods with the classical design methodology, according to Pahl and Beitz [23].

The proposed method is divided into three phases, which are taken from the methodology Design Thinking: the **Understand**, **Create**, and **Deliver** phase. During the Understand phase, the 4D potential for an application is determined and the task is formulated. In the Create phase, material-based and practical solution (prototyping) for the problem is searched. In the Deliver phase, a selection of the material and the definition of the descriptive quantities are chosen. The design

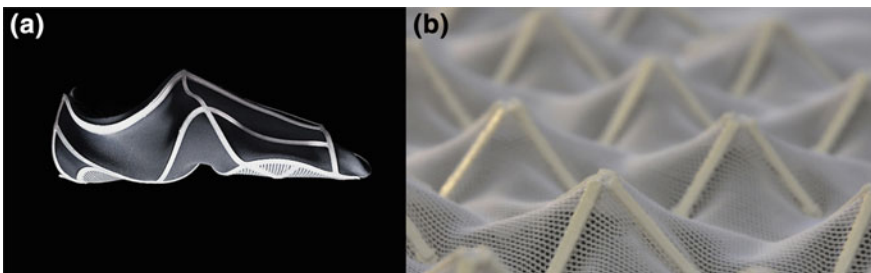


Fig. 8 4D applications: **a** Adaptive Shoe [22] and **b** Sound-absorbing Panel [21]

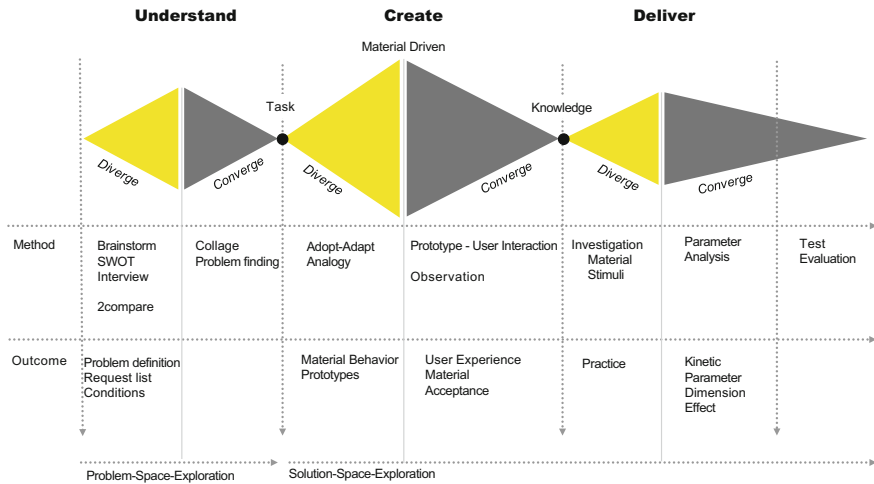


Fig. 9 Design approach by Schmelzeisen et al.

process is characterized by diverging the space of possibilities and converging to a decision point (Fig. 9).

Understand: By applying methods such as SWOT, interviews, collages, and problem definition, the actual needs and/or parameters of the situation that will be designed for can be identified in the understand phase and merged into a task to be solved. In order to meet the specific development of 4D textiles, the change of properties over time should be addressed. For this reason, methods are developed that are specifically designed for the application in the 4D textile sector.

Create: The foundations for the development of products are the four building blocks: function, material, process, and form. In the material-based product development, the limits of the achievable functionality lie in the properties of the material. During the development process, an attempt is made to make full use of the properties of the material and to realize the combination with known material [24]. The Create phase, which follows the Understand phase, is therefore characterized by a material exploration. In particular, the analogy technique is helpful. The material can be understood from many material prototypes. Using the prototype–user interaction, the interaction of material and users can be observed and conclusions can be drawn for further development.

Deliver: In the third phase, the Deliver phase, a parameter analysis follows in order to bring the developed material and its application to the stage of product maturity. Particular consideration must be given to the following parameters: dimension, kinetic, effective area, effect, and effect height. The final product is created with the help of optimal material selection. Further tests and an evaluation phase follow.

5 Conclusions

As discussed above, textiles have favorable properties that make them attractive for use in combination with 3D printing. Textiles can be folded, twisted, deformed, and cut. Many textiles can be stretched. The necessary properties can be precisely adjusted during production of the textile. Textiles can be trimmed, which has no effect on their previous properties. The combination makes it possible to manufacture stiff structures with embedded flexible structures or flexible structures with additional functions [17]. Their extensibility and flexibility differentiate textiles from paper as a surface material. Therefore, textiles can be used to store and transmit energy. According to Riviera et al., the expansion of the printable area is seen as an advantage of the use of textiles as a basis in the 3D printing process. After one printing section has been completed, the textile substrate can be moved and printed on again in another area. In this way, the otherwise limiting size of the printer's build area can be circumvented. Using textiles, large blank spaces can be bridged during printing [17].

Savings in printing time and material are advantages of 3D printing on textiles. Surfaces otherwise created with printed plastic can be replaced by textiles. In this case, the textile has been manufactured in the previous step.

There are known methods for precisely stiffening specific parts of textiles. These methods typically require a great deal of work for alignment and location. Using 3D printing on textiles, the level of stiffening can be customized and realized with less effort [17].

For apparel applications, textiles have the advantages of high comfort and wearability. These factors can be adjusted via the surface characteristics of the textile.

However, the benefits of textiles can also lead to negative effects and particular difficulties in 3D printing on textiles as summarized in Tables 1 and 2. Tensions and displacements in the stitch structure can be caused by the relative movement of the printer nozzle and textile on the build plate [17]. High-viscosity polymers require additional pressure to penetrate the textile [2]. These printing parameters have already been discussed in the previous publications. The selection of suitable parameters for the textile, for example, with regard to stitch width and fiber fineness, has not been sufficiently discussed to date.

Table 1 Potentials and deficits of 4D printing

Potentials	Deficiencies
+ Design freedom	- Low productivity
+ Functional adjustment	- Limited print area
+ Saving of production steps	- Material understanding
+ Simplified logistics	- Effect height
+ Material savings	- Choice of production method

Table 2 Potentials and deficits of 3D print on textile and 4D textiles

Potentials	Deficiencies
+ Textile material properties	- Additional material needed
+ Enlarge the print area	- Connection of materials
+ Material saving	- Additional limitations
+ Time saving	
+ Human comfort	
+ Use for energy storage and power transmission	

References

1. Brinks, G. J., Warmöskerken, M. M. C., Akkerman, R., et al. (2013). The added value of 3D polymer deposition on textiles. Dresden.
2. Pei, E., Shen, J., & Watling, J. (2015). Direct 3D printing of polymers onto textiles: Experimental studies and applications. *Rapid Prototyping Journal*, *21*, 556–571.
3. Sabantina, L., Kinzel, F., Ehrmann, A., et al. (2015). Combining 3D printed forms with textile structures—mechanical and geometrical properties of multi-material systems. *IOP Conference Series: Materials Science and Engineering*, *87*, 1–5.
4. Simonis, K., Schmelzeisen, D., Gesché, V., et al. (2017). 4D textiles: application in sports industry. *Future Textiles*, *2*, 38–39.
5. Ge, Q., Qi, H. J., & Dunn, M. L. (2013). Active materials by four-dimension printing. *Applied Physics Letters*, *103*. Epub ahead of print. doi:10.1063/1.4819837.
6. Bahr, R., Tehrani, B., Hester, J., et al. (2016). Additive manufacturing techniques for origami inspired 4D printed RF components and modules. (pp. 1–4). IEEE.
7. Choi, J., Kwon, O-C., Jo, W., et al. (2015). 4D Printing Technology: A Review. *3D Printing and Additive Manufacturing*; *2*, 159–167.
8. Korger, M., Bergschneider, J., Lutz, M., et al. (2016). Possible applications of 3D printing technology on textile substrates. *IOP Conference Series: Materials Science and Engineering*, *141*, 012011.
9. Melnikova, R., Ehrmann, A., & Finsterbusch, K. (2014). 3D printing of textile-based structures by Fused Deposition Modelling (FDM) with different polymer materials. *IOP Conference Series: Materials Science and Engineering*, *62*, 012018.
10. Sanatgar, H. R., Campagne, C., & Nierstrasz, V. (2017). Investigation of the adhesion properties of direct 3D printing of polymers and nanocomposites on textiles: Effect of FDM printing process parameters. *Applied Surface Science*, *403*, 551–563.
11. Tibbits S. The emergence of ‘4D printing’.
12. Pei, E. (2014). 4D Printing: Dawn of an emerging technology cycle. *Assembly Automation*, *34*, 310–314.
13. Momeni, F., Mehdi Hassani, M. N. S., Liu, X., et al. (2017). A review of 4D printing. *Materials and Design*, *122*, 42–79.
14. Chae, M. P., Hunter-Smith, D. J., De-Silva, I., et al. (2015). Four-Dimensional (4D) printing: A new evolution in computed tomography-guided stereolithographic modeling. principles and application. *Journal of Reconstructive Microsurgery*, *31*, 458–463.
15. Truby, R. L., & Lewis, J. A. (2016). Printing soft matter in three dimensions. *Nature*, *540*, 371–378.
16. Bodaghi, M., Damanpack, A. R., & Liao, W. H. (2016). Self-expanding/shrinking structures by 4D printing. *Smart Materials and Structures*, *25*, 1–15.

17. Rivera, M. L., Moukperian, M., Ashbrook D., et al. (2017). Stretching the bounds of 3D printing with embedded textiles. In G. Mark, S. Fussell, C. Lampe, et al. (Eds.), *Proceedings of the 2017 CHI Conference on Human Factors in Computing Systems—CHI'17* (pp. 497–508). New York: ACM Press.
18. Grimmelsmann, N., Martens, Y., Schäl, P., et al. (2016). Mechanical and electrical contacting of electronic components on textiles by 3D printing. *Procedia Technology*, 26, 66–71.
19. Cabral, I., Souto, A. P., Carvalho, H., et al. (2015). Exploring geometric morphology in shape memory textiles: Design of dynamic light filters. *Textile Research Journal*, 85, 1919–1933.
20. Neuß, J., Kreuziger, M., Grimmelsmann N., et al. (2017). Interaction between 3D deformation of textile fabrics and imprinted lamellae.
21. Clasen, D., Wallasch, M., Köneke, O., et al. (2017). Sonogrid <http://sonogrid.de/konzept/>.
22. Guberan, C., Clopath, C., & Tibbits, S. Active Shoes <http://www.selfassemblylab.net/ActiveShoes.php>.
23. Pahl, G., & Beitz, W. (1978). *Konstruktionslehre: Handbuch für Studium und Praxis*. Berlin: Springer.
24. Ashby, M, F. (1999). *Materials selection in mechanical design* (2nd ed.,) Oxford, OX ; Boston, MA: Butterworth-Heinemann.

Functional Nanofiber Mats for Medical and Biotechnological Applications

Robin Böttjer, Timo Grothe and Andrea Ehrmann

Abstract Nanofiber mats from different polymers, possibly blended with other organic or inorganic components, can be created by the electrospinning technology. Such nanofiber mats possess large surface–volume ratios in comparison with other textile fabrics, such as common nonwovens. This property enables enhanced interactions with their environment, making them suitable for applications in wound dressing, drug delivery, biotechnological filter technology, etc., especially if prepared from biopolymers with intrinsically antimicrobial or other qualities. In a recent project, we investigate the possibilities to create such nanofiber mats from diverse (bio-) polymers by “green” electrospinning, i.e., electrospinning from aqueous solutions or other nontoxic solvents. The article gives an overview of the latest results from needleless electrospinning pure polymers and polymer blends as well as typical physical and chemical properties of the created nanofiber mats, especially for medical and biotechnological purposes, and shows diverse possibilities to crosslink water-soluble biopolymer nanofiber mats.

1 Introduction

Electrospinning belongs to the primary spinning processes, resulting in fibers with diameters usually in the range between 100 nm and 1 μm . It can be performed using a syringe through which polymer melt or solution is pressed and afterward dragged by a high electric field to a substrate. Alternatively, in the so-called needleless electrospinning, the polymer melt or solution is coated on a rotating drum or on a wire on which a high voltage is applied, so that the polymer is drawn to the counter electrode and thus placed in form of a nanofiber mat on the substrate between both electrodes.

In this way, continuous nanofibers or nanofiber mats can be created with relatively small equipment, opposite to common primary spinning technologies [1–5].

R. Böttjer · T. Grothe · A. Ehrmann (✉)
Bielefeld University of Applied Sciences, Bielefeld, Germany
e-mail: andrea.ehrmann@fh-bielefeld.de

Their large inner surfaces allow for using them as medical wound dressings [6], catalyzers [7], filter materials [8–10], cell growth [11–13], etc.

Nanofiber mats can be spun from diverse polymers. On the one hand, water-insoluble materials, such as PA6 (polyamide 6) or PAN (poly(acrylonitrile)), can be dissolved for spinning them solely or blended with other materials [14, 15]. On the other hand, diverse biopolymers are spinnable from aqueous solutions. Several biopolymers show special intrinsic properties making them suitable for diverse applications. Chitosan, e.g., is hemostatic and thus often used for medical purposes [16]. Its ability to remove heavy metals or organo-chemical components from watery solutions makes it also suitable as a bioactive filter material [17]. Aloe vera nanofiber mats also support wound healing [18, 19] and show antiseptic properties [20]. Alginate, on the other hand, can absorb large amounts of wound fluid and thus supports drying of bleeding wounds [21]. Hyaluronic acid is also used for wound dressing of deep second-degree burns [22] and in combination with poly(lactic-co-glycolic acid) as a scaffold for skin regeneration [23].

Keratin, e.g., was electrospun with gelatin for the application in skin wound repair [24]. Pure keratin nanofibers electrospun on titanium surfaces were shown to support fibroblast alignment without increasing the adhesion of bacteria [25]. Co-spun with PEG (poly(ethylene glycol)), keratin was tested for application in air filtration [26].

Denatured whole-chain marine collagen was electrospun with different equipments to upscale this process to commercial scale [27]. Collagen hydrolysate was electrospun using different methods and found suitable for medicine and health applications [28]. Blends of collagen with poly(lactic acid) were even tested for mimicking the fascicles of a human tendon [29].

While these materials have been investigated deeply by several research groups, reports about the morphologies of nanofiber mats electrospun from some other biopolymers as well as crosslinking such water-soluble materials are still scarce in the literature. Dextran, e.g., was co-electrospun with PVP for drug delivery applications [30]. Combined with poly(2-vinyl-N-pyrrolidone)/octadecyl amine-montmorillonite, dextran was investigated for biomedical and electrochemical applications [31]. Co-spun with polyurethane, dextran can also be used for drug delivery [32].

Ploxamer, formerly known as Lutrol (poly(oxyethylene-b-oxypropylene-b-oxyethylene)), was also used for drug delivery in combination with poly(epsilon-caprolactone) [33]. Co-spun with poly(epsilon-caprolactone-co-lactide), ploxamer was examined for skin tissue engineering [34] and wound healing [35].

For most applications, the challenge of stabilizing these water-soluble materials after electrospinning remains. This is why this article shows not only results of electrospinning some pure and blended biopolymers but also tests to increase water stability of the resulting nanofiber mats.

2 Experimental

Electrospinning was performed using the needleless electrospinning machine Nanospider Lab from Elmarco (Czech Republic).

The following chemicals were used for electrospinning:

- Dextran 500 for biochemistry, 500,000 kDa (Carl Roth GmbH + Co. KG, Karlsruhe/Germany);
- Poloxamer “lutrol F 68”, 7680-9510 Da, $2 \times 40\%$ hydrophilic parts (BASF, Germany);
- Keratin 2000 Da (alexmo cosmetics, Weyhe/Germany), 30% in aqueous solution;
- Collagen (alexmo cosmetics, Weyhe/Germany), 1% in aqueous solution;
- Polyacrylonitrile;
- Poly(ethylene glycol), 600 kDa (S3 Chemicals, Bad Oeynhausen, Germany), 8% in aqueous solution; and
- Pentaerythritol tetraacrylate (PETRA) (Carl Roth GmbH + Co. KG, Karlsruhe/Germany).

For investigation of the nanofiber mat morphologies, a confocal laser scanning microscope (CLSM) VK-9000 (Keyence) with a nominal magnification of $2000 \times$ was used.

3 Results and Discussion

In the first test series, keratin was co-spun with PEG in different ratios (the numbers specify the ratio of the aqueous solutions, as described in the Experimental section). Figure 1 depicts the results. While for a ratio of 50:50, a membrane is built rather than nanofibers, increasing the keratin content results in more and more fibers being created. However, even for a ratio of 90% keratin and 10% PEG, no single nanofibers are visible. Instead, a matrix from relatively thick, connected fibers with irregular holes between them is formed. This behavior is opposite to other blends with PEG—usually, PEG strongly supports fiber formation, and relatively high PEG contents can be blended with several biopolymers without significant changes of the mat morphologies. For pure keratin, however, no electrospinning occurred at all.

Although this result shows that blending keratin with PEG does not lead to nanofiber mats, the resulting structures are nevertheless interesting as a different morphology for cell growth examinations or filter applications and will be examined more in detail in the near future.

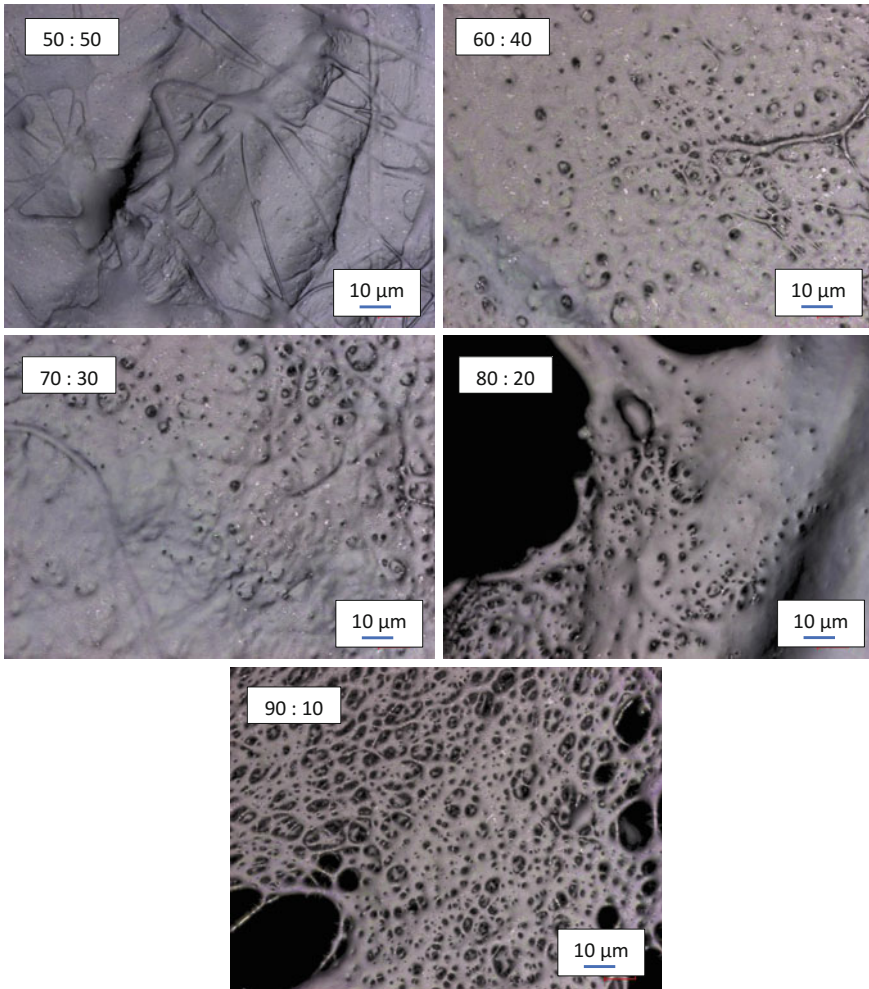


Fig. 1 CLSM images of keratin co-spun with PEG in different ratios keratin:PEG

In Fig. 2, the equivalent test series mixing collagen and PEG is depicted. Here, for a ratio of 50:50 or 60:40, the mat morphology is approximately identical with typical PEG nanofiber mats. Increasing the collagen content results in some membrane-like areas, until for a ratio of 90:10, large holes in the nanofiber mat become visible.

In the next experiments, different possibilities of crosslinking several water-soluble biopolymers were investigated. First, PEG nanofiber mats were treated with PETRA and UV irradiation to increase crosslinking, a method which is known from PEG hydrogels [36].

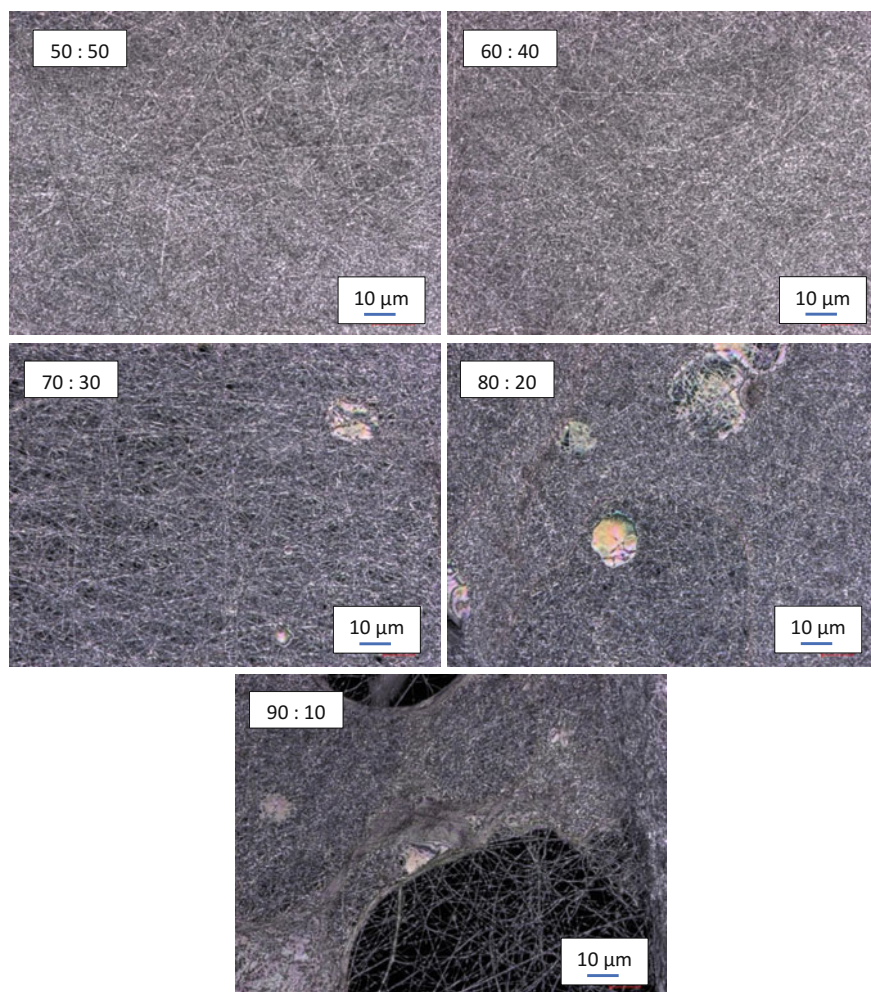


Fig. 2 CLSM images of collagen co-spun with PEG in different ratios collagen:PEG

The results are depicted in Fig. 3. Starting with pure chemical crosslinking without UV irradiation, a significant modification of the nanofiber mat is already visible. Large areas seem to be connected. Nevertheless, after 1 min in water, the nanofibers are completely dissolved, and only a membrane is left where the dissolved material was apparently accumulated during drying.

Using additional UV radiation for increasing time, the membrane-like parts which seem to be crosslinked increase until large areas are completely covered by membranes. Nevertheless, after 1 min in water, only re-accumulations are visible on the thicker substrate fibers.

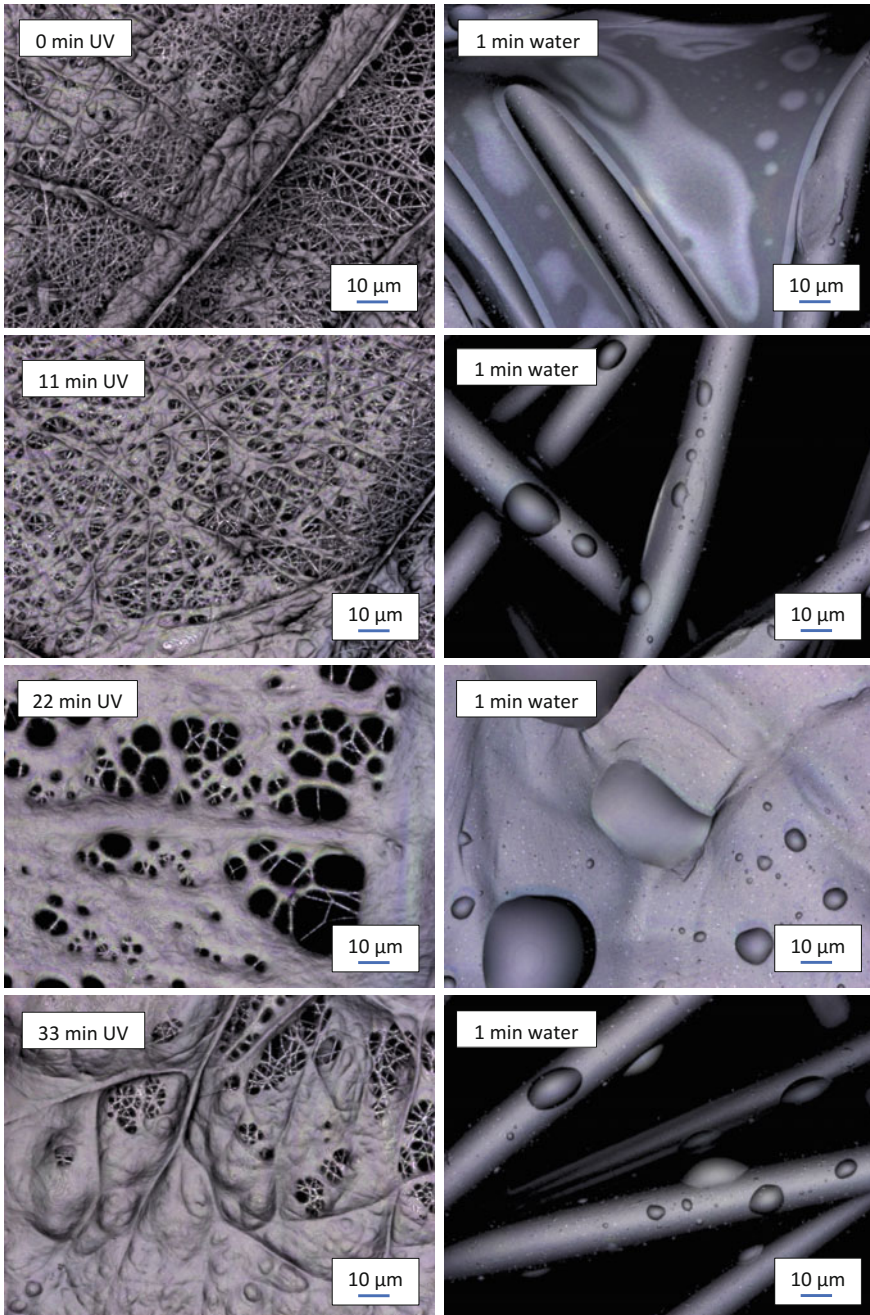
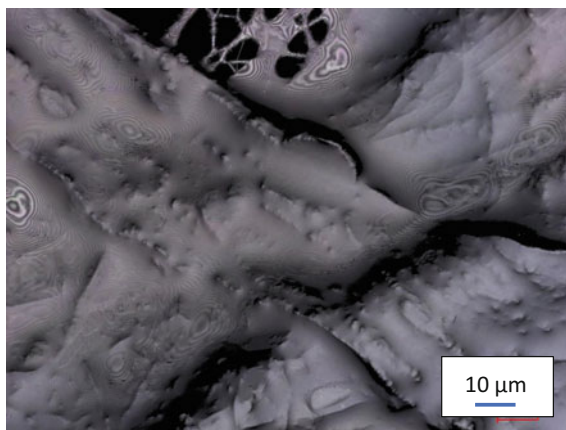


Fig. 3 PEG after crosslinking with PETRA and UV irradiation for the time given in the inset (left panels) and after inserting the UV-PETRA treated PEG fabric in water for 1 min (right panels)

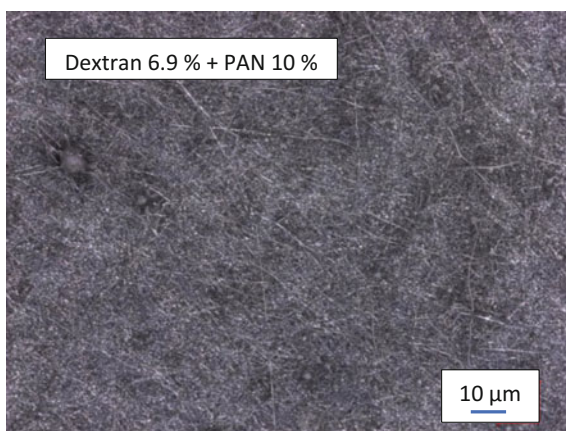
Fig. 4 PEG co-spun with PETRA after UV irradiation



Since this method does not seem to work with nanofiber mats, in the next experiment, PEG and PETRA were co-spun. The resulting mat mostly contained a relatively thick coating, significantly thicker than the usual membranes which occur on several nanofiber mats (Fig. 4). Only some areas showed networks of fibers with varying thickness. While the fabric was indeed waterproof for 1 min, the surface remained sticky and thus unusable for most applications. Apparently, more tests are necessary to transfer the idea of UV crosslinking PEG supported by PETRA from hydrogels to nanofiber mats.

Another idea to make biopolymers more water-resistant is co-spinning them with a waterproof polymer, such as PAN. PAN can be dissolved in DMSO (dimethyl sulfoxide) which has to be handled with care, but is nontoxic, so that it can also be used to create nanofiber mats for medical or biotechnological applications.

Fig. 5 Dextran co-spun with PAN



One of the biopolymers which were tested with PAN is dextran. Here, the solution contained 6% dextran and 10% PAN. The resulting nanofiber mat is depicted in Fig. 5. Besides some beads which are typical for spinning PAN in relatively low concentrations, fine, straight nanofibers are visible without any holes that are strong morphology deviations in the created mat.

Results of co-spinning poloxamer and PAN are depicted in Fig. 6 for two different concentration combinations. Both solutions were slightly modified by adding a few grains of NaCl to increase their conductivity. First, higher concentrations of poloxamer result in significantly increased fiber diameters. Future tests modifying both concentrations separately will show the influence of both parameters.

Second, adding NaCl to the solution with lower poloxamer content also increases the fiber diameter. Apparently, this is an easy way to influence the fiber morphology without reducing the spinning output significantly due to a strongly increased viscosity.

Now, these partly water-stable nanofiber mats were immersed in water for 1 min and for 3 days as well as in saltwater for 3 days. Figure 7 depicts the results of tests on the dextran/PAN nanofibers mat shown in Fig. 5.

Immersing the nanofiber mat in water for 1 min already resulted in a significantly changed mat morphology. The large fibers are nearly vanished; only a rough, partly fibrous underground remains visible. After 3 days in water, this effect is still increased.

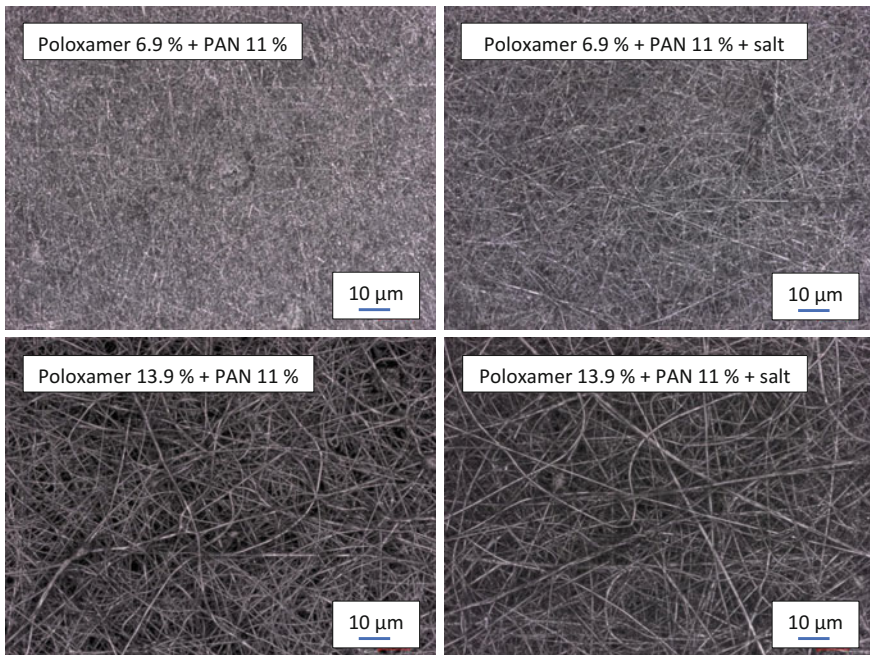


Fig. 6 Poloxamer co-spun with PAN with different concentrations

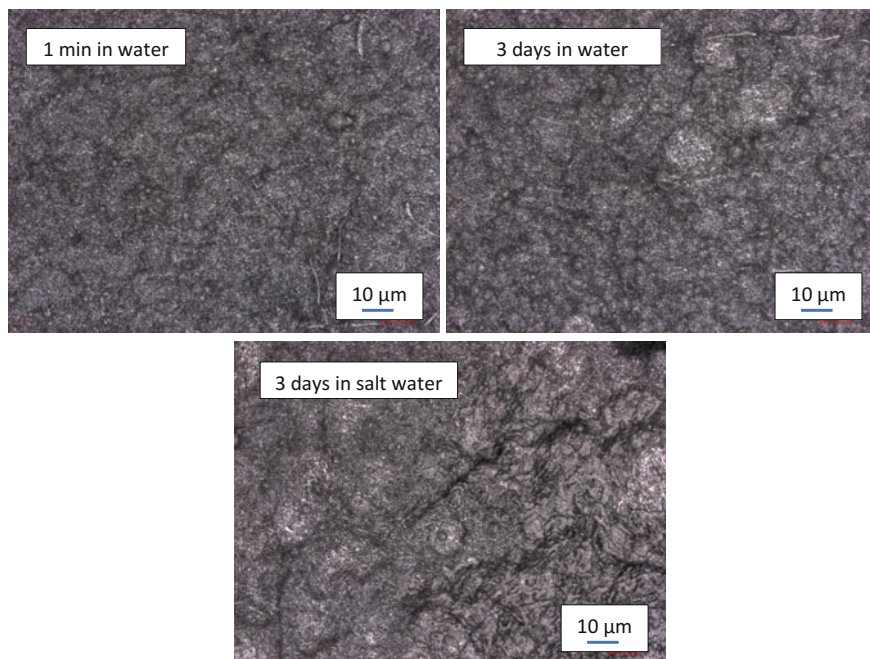


Fig. 7 PAN 10%/dextran 6.9% nanofiber mat after inserting in water for 1 min, in water or saltwater for 3 days

Nevertheless, there are still fiber compounds visible. An additional effect occurs when introducing the nanofiber mat in saltwater. Unexpectedly, some areas of the nanofiber mat seem to be crosslinked; an effect which is neither visible in the original nanofiber mat nor after introducing the mat into pure water for 3 days. This behavior will be investigated in more detail in the near future.

The equivalent experiment was performed on the poloxamer/PAN nanofiber mats with 6.9% poloxamer (Fig. 8). After 1 min in water, the nanofibers are still well visible, although the mat seems to have a higher density now, compared to the original one (cf. Fig. 6). After 3 days in water, however, large “beads” on top of the fiber mat are visible, probably stemming from dissolved and re-accumulated poloxamer. This effect, however, does not occur after 3 days in saltwater; there, the complete nanofiber mat is maintained. Apparently, salt does not only influence the spinning process but also the effect of water on the respective nanofiber mats.

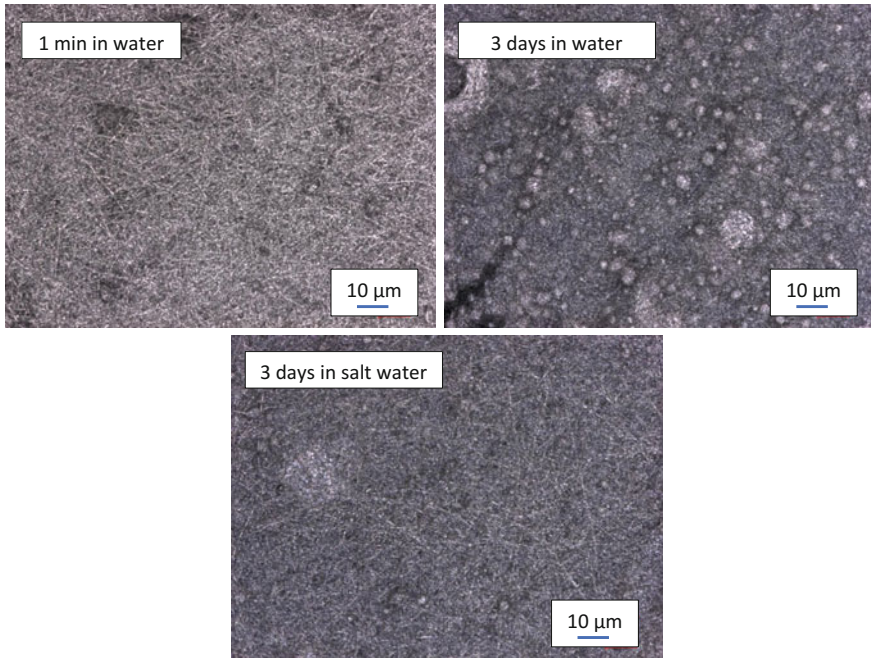


Fig. 8 PAN/poloxamer nanofiber mat after inserting in water for 1 min, in water or saltwater for 3 days

4 Conclusion

Different (bio)polymers, such as keratin, collagen, dextran, and poloxamer, were co-electrospun with PEG or PAN to create nanofiber mats. Depending on the spinning solutions, fabric morphologies varied between nanofiber mats and membranes or even thicker coatings.

Approaches to make the nanofiber mats water-resistant included photo-crosslinking PEG with PETRA which did not work sufficiently and co-spinning water-soluble biopolymers with the water-stable PAN, partly leading to positive results. Additionally, a small amount of NaCl was shown to strongly influence spinning and wetting processes.

Future experiments are necessary to investigate some of the unexpected effects found here more in detail and especially to increase water stability of biopolymer blends for medical and biotechnological applications.

Acknowledgements The authors acknowledge gratefully the program FH basis of the German federal country North Rhine-Westphalia for funding the “Nanospider Lab”. This investigation was partly funded by the HiF fund of Bielefeld University of Applied Sciences.

References

1. Subbiah, T., Bhat, G. S., Tock, R. W., Parameswaran, S., & Ramkumar, S. S. (2005). Electrospinning of Nanofibers. *Journal of Applied Polymer Science*, *96*, 557–569.
2. Greiner, A., & Wendorff, J. H. (2007). Electrospinning: A fascinating method for the preparation of ultrathin fibers. *Angewandte Chemie International Edition*, *46*, 5670–5703.
3. Li, D., & Xia, Y. (2004). Electrospinning of nanofibers: Reinventing the wheel? *Advanced Materials*, *16*, 1151–1170.
4. Teo, W. E., Inai, R., & Ramakrishna, S. (2011). Technological advances in electrospinning of nanofibers. *Science Technology Advances Materials*, *12*, 013002.
5. Agarwal, S., Greiner, A., & Wendorff, J. H. (2013). Functional materials by electrospinning of polymers. *Progress in Polymer Science*, *38*, 963–991.
6. Ashammakhi, N., Ndreu, A., Yang, Y., Ylikauppila, H., & Nikkola, L. (2012). Nanofiber-based scaffolds for tissue engineering. *European Journal of Plastic Surgery*, *35*, 135–149.
7. Wang, X., Kim, Y. G., Drew, C., Ku, B. C., Kumar, J., & Samuelson, L. A. (2004). Electrostatic Assembly of Conjugated Polymer Thin Layers on Electrospun Nanofibrous Membranes for Biosensors. *Nano Letters*, *4*, 331–334.
8. Lackowski, M., Krupa, A., & Jaworek, A. (2011). Nonwoven filtration mat production by electrospinning method. *Journal of Physics: Conference Series*, *301*, 012013.
9. Filatov, Y., Budyka, A., & Kirichenko, V. (2007). *Electrospinning of Micro- and Nanofibers: Fundamentals and Applications in Separation and Filtration Processes*. Moscow: Begell House Inc.
10. Lemma, S. M., Esposito, A., Mason, M., Brusetti, L., Cesco, S., & Scampicchio, M. (2015). Removal of bacteria and yeast in water and beer by nylon nanofibrous membranes. *Journal of Food Engineering*, *157*, 1–6.
11. Schnell, E., Klinkhammer, K., Balzer, S., Brook, G., Klee, D., Dalton, P., et al. (2007). Guidance of glial cell migration and axonal growth on electrospun nanofibers of poly-epsilon-caprolactone and a collagen/polyepsilon-caprolactone blend. *Biomaterials*, *28*, 3012–3025.
12. Klinkhammer, K., Seiler, N., Grafahrend, D., Gerardo-Nava, J., Mey, J., Brook, G. A., et al. (2009). Deposition of electrospun fibers on reactive substrates for in vitro investigations. *Tissue Engineering Part C*, *15*, 77–85.
13. Großerhode, C., Wehlage, D., Grothe, T., Grimmelsmann, N., Fuchs, S., Hartmann, J., et al. (2017). Investigation of microalgae growth on electrospun nanofiber mats. *AIMS Bioengineering*, *4*, 376–385.
14. Wang, J. N., Zhao, W. W., Wang, B., Pei, G., & Li, C. (2017). Multilevel-layer-structured polyamide 6/poly(trimethylene terephthalate) nanofibrous membranes for low-pressure air filtration. *Journal of Applied Polymer Science*, *134*, 44716.
15. Mao, Z. P., Xie, R. Y., Fu, D. W., Zhang, L., Xu, H., Zhong, Y., et al. (2017). PAN supported Ag-AgBr@Bi₂₀TiO₃₂ electrospun fiber mats with efficient visible light photocatalytic activity and antibacterial capability. *Separation and Purification Technology*, *176*, 277–286.
16. Porett, F., Rosen, T., Körner, B., & Vorwerk, D. (2005). Chitosan pads versus manual compression to control bleeding sites after transbrachial arterial catheterization in a randomized trial. *Fortschr Röntgenstr*, *177*, 1260–1266.
17. Tayel, A. A., El-Tras, W. F., & Elguindy, N. M. (2016). The potentiality of cross-linked fungal chitosan to control water contamination through bioactive filtration. *International Journal of Biological Macromolecules*, *88*, 59–65.
18. Fulton, J. E. (1990). The Stimulation of Postdermabrasion Wound Healing with Stabilized Aloe Vera Gel-Polyethylene Oxide Dressing. *The Journal of Dermatologic Surgery and Oncology*, *16*, 460–467.

19. Chithra, P., Sajithlal, G. B., & Chandrakasan, G. (1998). Influence of Aloe vera on collagen characteristics in healing dermal wounds in rats. *Molecular and Cellular Biochemistry*, *181*, 71–76.
20. Surjushe, A., Vasani, R., & Saple, D. G. (2008). Aloe vera: A short review. *Indian Journal of Dermatology*, *53*, 163–166.
21. Seymour, J. (1997). Alginate dressings in wound care management. *Nursing Times*, *93*, 49–52.
22. Ebrahimi-Hosseinzadeh, B., Pedram, M., Hatamian-Zarmi, A., Salahshour-Kordestani, S., Rasti, M., Mokhtari-Hosseini, Z. B., et al. (2016). In vivo evaluation of gelatin/hyaluronic acid nanofiber as Burn-wound healing and its comparison with ChitoHeal gel. *Fibers and Polymers*, *17*, 820–826.
23. Lee, E. J., Lee, J. H., Jin, L., Jin, O. S., Shin, Y. C., & Oh, S. J. (2014). Lee, Hyon S H, Han D W. Hyaluronic Acid/Poly(lactic-co-glycolic acid) Core/Shell Fiber Meshes Loaded with Epigallocatechin-3-O-Gallate as Skin Tissue Engineering Scaffolds. *Journal of Nanoscience Nanotechnology*, *11*, 8458–8463.
24. Yao, C. H., Lee, C. Y., Huang, C. H., Chen, Y. S., & Chen, K. Y. (2017). Novel bilayer wound dressing based on electrospun gelatin/keratin nanofibrous mats for skin wound repair. *Materials Science and Engineering C*, *79*, 533–540.
25. Ferraris, S., Giachet, F. T., Miola, M., Bertone, E., Varesano, A., Vineis, C., et al. (2017). Nanogrooves and keratin nanofibers on titanium surfaces aimed at driving gingival fibroblasts alignment and proliferation without increasing bacterial adhesion. *Materials Science and Engineering C*, *76*, 1–12.
26. Li, B., Huang, C., & Yang, X. (2017). Preparation and Characterization of Electrospun Wool Keratin/Polyethylene Oxide Nanofibers for Air Filtration Applications. *Digest Journal of Nanomaterials and Biostructures*, *12*, 293–301.
27. LeCorre, Bordes D. S., Jaksons, P., & Hofman, K. (2017). Mind the gap: Ensuring laboratory-scale testing of an electrospinning product meets commercial-scale needs. *Journal of Applied Polymer Science*, *134*, 44836.
28. Kovalenko, G. M., Bokova, E. S., Filatov, I. Y., & Mironseva, V. V. (2017). Electrospun Fibrous Materials Made of Collagen and Chitin Derivatives. *Fibre Chemistry*, *48*, 466–469.
29. Sensini, A., Gualandi, C., Cristofolini, L., Tozzi, G., Dicarolo, M., Teti, G., et al. (2017). Biofabrication of bundles of poly(lactic acid)-collagen blends mimicking the fascicles of the human Achille tendon. *Biofabrication*, *9*, 015025.
30. Maslakci, N. N., Ulusoy, S., Uygun, E., Cevikbas, H., Oksuz, L., Can, H. K., et al. (2017). Ibuprofen and acetylsalicylic acid loaded electrospun PVP-dextran nanofiber mats for biomedical applications. *Polymer Bulletin*, *74*, 3283–3299.
31. Rzayev, Z. M. O., Bunyatova, U., & Simsek, M. (2017). Multifunctional colloidal nanofiber composites including dextran and folic acid as electro-active platforms. *Carbohydrate Polymers*, *166*, 83–92.
32. Kumar, Y. S., Unnithan, A. R., Sen, D., Kim, C. S., & Lee, Y. S. (2015). Microgravity biosynthesized penicillin loaded electrospun polyurethane-dextran nanofibrous mats for biomedical applications. *Colloids and Surfaces A—Physicochemical and Engineering Aspects*, *477*, 77–83.
33. Natu, M. V., de Sousa, H. C., & Gil, M. H. (2011). Electrospun Drug-Eluting Fibers for Biomedical Applications. *Active Implants and Scaffolds for Tissue Engineering*, *8*, 57–85.
34. Pan, J. F., Liu, N. H., Sun, H., & Xu, F. (2014). Preparation and Characterization of Electrospun PLCL/Poloxamer Nanofibers and Dextran/Gelatin Hydrogels for Skin Tissue Engineering. *PLoS ONE*, *9*, e112885.
35. Gu, J. Y., Liu, N. H., Yang, X. R., Feng, Z. H., & Qi, F. Z. (2014). Adipose-derived stem cells seeded on PLCL/P123 electrospun nanofibrous scaffold enhance wound healing. *Biomedical Materials*, *9*, 035012.
36. Wong, R. S. H., Ashton, M., & Dodou, K. (2015). Effect of crosslinking agent concentration on the properties of unmedicated hydrogels. *Pharmaceutics*, *7*, 305–319.

Sensorized Woven Tapes and Their Testing

W. Scheibner, A. Neudeck, K. Ullrich, A. Krahmer, H. Oschatz,
M. Weiser and U. Möhring

Abstract Sensorizing of woven tapes is the starting point for many innovations when physical properties like force, pressure, temperature, shape change, or moisture have to be supervised in medical textiles, wellness requisites, load bearing belts, buildings, and sporting goods. In order to produce textile-based sensors, fibers or bundles of fibers, ribbons and other textile substrates are furnished with coatings which can advantageously be tailored to any desired sensing capability. Hereby, the textile material remains nearly unchanged and keeps up its textile typical behavior. The sensorized area is free from nontextile components. The presented chapter deals with textile sensors for the measurement of contact pressure, temperature, and moisture. For this reason, sensorized threads are interwoven into tapes and connected with wires for the transmission of signals. Further on, woven tapes with sensing coatings and their applications are presented. A second part of this chapter is dedicated to questions regarding the accessibility to evaluation units, the minimization of cross-sensitivities and environmental influences as well as the reproducibility of sensor characteristics. Finally, a testing method for smart textiles is introduced based on simultaneously applying mechanical stress and monitoring the change in electrical resistance.

1 Introduction

Sensors are a basic requirement and the main initiator when textiles have to be equipped with intelligent functions. Especially 3-D textiles, such as knitted spacer fabrics or pile woven fabrics, offer empty space for the integration of sensors and possess an elastic resilience force which can advantageously be used for many sensory applications. On the basis of a current analysis of the smart textiles market,

W. Scheibner · A. Neudeck · K. Ullrich (✉) · A. Krahmer · H. Oschatz · M. Weiser
U. Möhring
Textilforschungsinstitut Thüringen-Vogtland E. V, Zeulenrodaer Str. 42,
07973 Greiz, Germany
e-mail: k.ullrich@titv-greiz.de

the focus was placed on measurements of the contact pressure with emphasis on prospective applications in medicine and wellness requisites. In addition, textile-based temperature and moisture sensors were included in the investigations since they comprise a suitable completion for many adjacent uses [1].

The variables to be measured were converted via a resistance measurement into an electrical signal. In order to generate a spatially resolved sensor signal, a network of electrically conductive threads was incorporated into the textile. The sensorized area remains free from nontextile materials. Force and pressure measurements were carried out using piezo-resistive signal converters, moisture was measured via resistance changes caused by hygroscopicity or swelling, and the thermo-electric effect was used for temperature measurements with woven thermocouples.

A further part of the R&D activities aimed at the connection between sensors and evaluation units, at the minimization of influences caused by environmental conditions and cross-sensitivities as well as at the reproducibility of the sensor characteristics. Textile typical connection techniques such as tailoring, embroidery [2], snap buttons, and rivets were applied to transmit electrical signals and for contacting with evaluation units.

The textile sensors were finished with partially applied coatings made of polymer pastes. Typical exposures of textile sensors to mechanical and thermal load were simulated in accelerated tests on laboratory scale in order to derive some reliability-enhancing measures. Textile-based sensors provide many opportunities to develop new products with functionalities exceeding the capabilities of conventional sensors with respect to both technical parameters (size, flexibility, and response time) and manufacturing costs.

The high integration depth of sensor devices and textile opens up new application fields and increases the acceptance of early adopters especially when sensors have to be worn proximal to the body. First applications were put into practice in the form of woven and braided sensors for the two-dimensional supervision of load and moisture in buildings.

2 Experimental

Two approaches were chosen to equip textiles with sensing capabilities: First, the sensory behavior arises from yarns which were varnished with sensory coatings, interwoven into the textile, and finally connected to lead-in wires. Second, a sensory coating was applied onto a woven fabric which was previously structured with a network of conductors for the signal transfer.

Polyurethane and acrylate were used as appropriate film-forming polymeric materials to produce sensory layers on the textile substrate acting as resistive signal converters. For this reason, the aqueous polymer solutions were mixed up with carbon black or lithium chloride (LiCl) to produce sensors responding to changes of mechanical load and humidity, respectively. After applying the coatings, they were dried in a conveyor-type furnace at approximately 150 °C.

The sensory formulation was transferred from a supply tank onto the yarn using a transfer roll, whereas an air-squeegee was used to apply pastes or foams on fabrics. In particular, the last-mentioned method was used to apply a piezo-resistive foam in manufacturing a sensor mat for the measurement of the contact pressure for medical purposes and the like. Elongation sensing fibers with diameters ranging from 0.5 to 2.0 mm were made of a silicone rubber (polydimethylsiloxane) from Rehau AG filled with carbon black. These fibers were incorporated in elastic tapes which can be utilized to measure elongations up to 200%.

The textile sensors were finished with partially applied coatings made of polymer pastes (e.g., polyurethane) to protect them against environmental attack. The coatings were cured in a laboratory hot air oven with coating device type Labdryer LTE (Werner Mathis AG).

Electrical resistance measurements were performed with a Keysight 34972A Data Acquisition/Data Logger Switch Unit with a 6 ½ Digit Digital Multimeter and plug-in modules for data acquisition from the sensors. In all cases, the resistances to be measured were at least three orders of magnitude higher than those of the measuring cables. So measurements were carried out using a two-wire connection.

Textile temperature sensors in the form of woven thermocouples (type T) were built from copper and constantan wires with a diameter of 80 and 100 μm , respectively. The metal wires were woven into the fabric together with the textile threads and connected with compensating cables to a precision-second-thermometer GMH 3210 (Greisinger electronic GmbH).

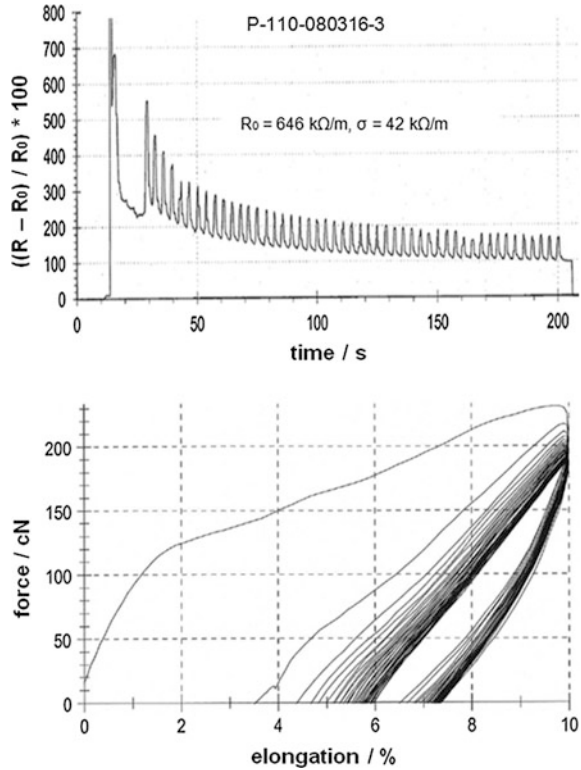
The completed textile-based sensors were manufactured using production techniques like weaving, knitting, embroidery, and braiding.

3 Force, Pressure, and Elongation Sensors

In manufacturing sensors to detect mechanical load, piezo-resistive layers were applied on polyester yarns. For this purpose, various yarns were coated with the polyurethane-based compound Tubicoat EHL (CHT R. Beitlich GmbH) which is filled with carbon black. So the polyurethane coating became electrically conductive and changes its electrical resistance upon stretching or compression. Figure 1 shows the results of a stretching test at room temperature. To investigate the effect of mechanical deformation on the sensory behavior of the yarn, it was subjected to stretch-relaxation cycles with a velocity of 20 mm/s up to an elongation of 10%, while its electrical resistance was recorded simultaneously.

From Fig. 1, it becomes obvious that an initial transient response is followed by a steady-state mechanical and electrical behavior of the sensor threads.

Fig. 1 Graph of the relative change in resistance versus time for a cyclic stretching test performed with a sensor thread (PES 110 dtex coated with Tubicoat EHL) (above) and corresponding force-elongation curve (below)



In order to produce planar pressure sensors, which can be utilized to determine the contact pressure, the polyurethane dispersion was foamed up to a volume weight of about 200 g/l and spread on a woven fabric which was equipped with electrodes for signal tapping.

Figure 2 shows the arrangement of the interwoven electrodes and the external wiring for signal generation schematically. It should be emphasized that the wires in the x- and y-columns were not in electrical contact with each other.

An implementation example of a sensor matrix is shown in Fig. 3. Peripheral contacts were accomplished using textile typical connection techniques (e.g., push buttons).

The resistance-pressure characteristic of piezo-resistive sensor cells was determined using a penetrometer PNR 10 (Petrotest Instruments) to exert pressure on the sensor. Figure 4 shows the electrical resistance of a sensor cell with a 10 mm

Fig. 2 Schematic view of a sensor mat for contact pressure measurements with the arrangement of measuring electrodes, external wiring, and piezo-resistive foam (1—multilayer woven fabric, 2—electrically conductive threads, 3—insulated intersection point, 4—layer of piezo-resistive foam, 5—resistance metre)

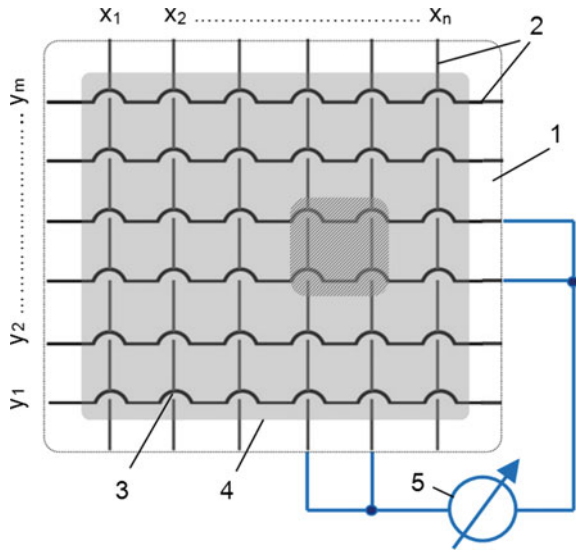
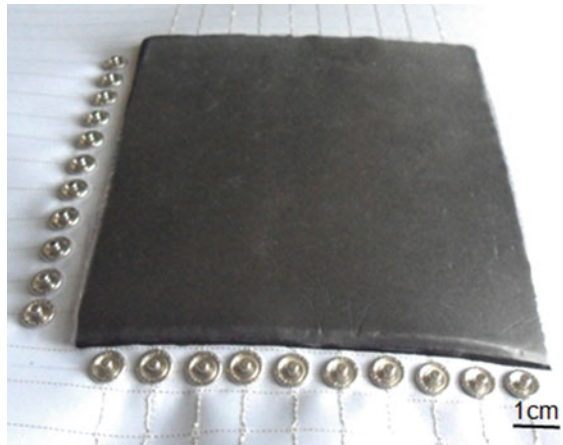


Fig. 3 Implementation example of a sensor mat for contact pressure measurements



x 10 mm grid plotted against the applied pressure for both the burden and the relief cycle. The observed hysteresis seems to be characteristic of piezo-resistive polymer sensors since it was also found for other such materials [3, 4].

Fig. 4 Graph of the electrical resistance of a 10 mm × 10 mm sensor cell versus the applied pressure for burden and relief of the piezo-resistive foam

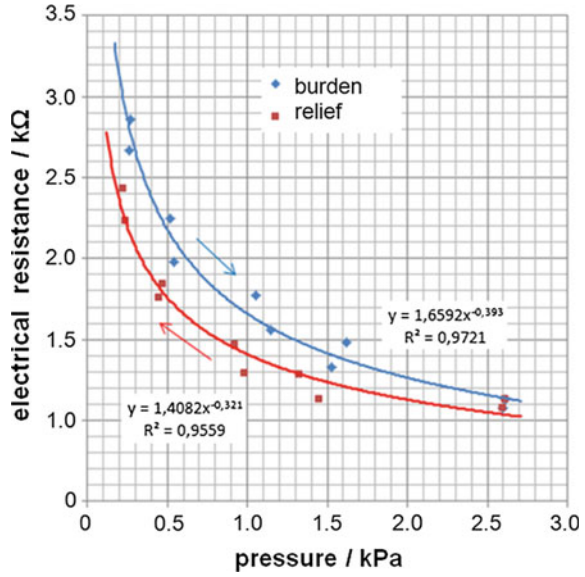
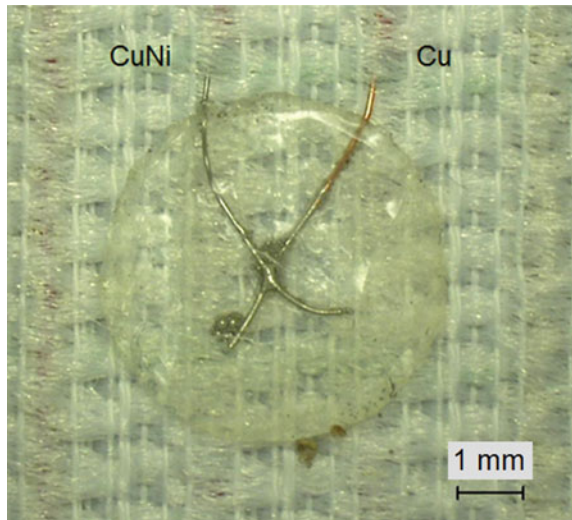


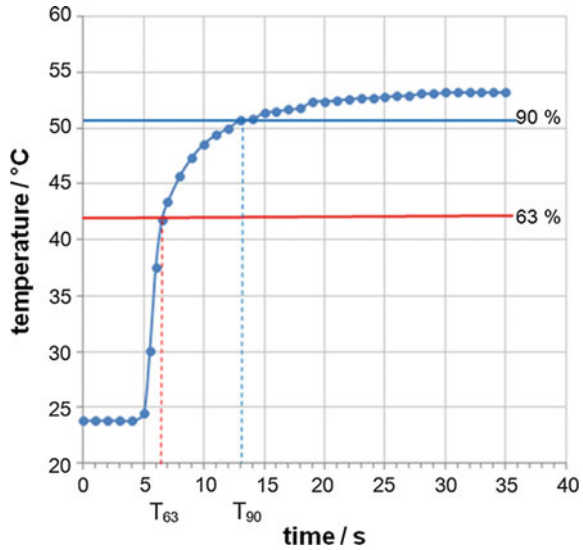
Fig. 5 Woven thermocouple with encapsulation of polyurethane varnish



4 Temperature Sensors

Woven thermocouples represent a convenient method to place punctual temperature test points in a fabric. Figure 5 shows a woven thermocouple made of copper and constantan wires encapsulated with a dot of polyurethane varnish.

Fig. 6 Step response of a woven thermocouple



Woven thermocouples can advantageously be manufactured in a large number using the leno weaving method [5]. Their simple construction and fast response to temperature changes make them a feasible means for smart textile applications. The step response of a woven thermocouple to an abrupt temperature rise of about 30 K is depicted in Fig. 6.

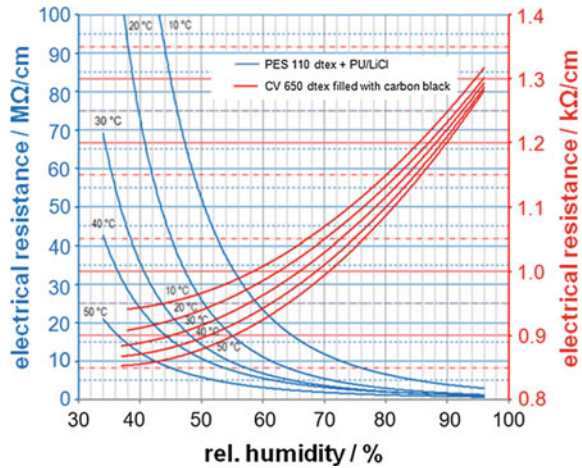
5 Humidity Sensors

Two different effects were used to prepare sensors threads which respond to varying humidity with typical resistance changes: Swelling of a viscose yarn filled with carbon black and hygroscopicity of polyurethane coatings due to admixtures of lithium chloride.

Figure 7 shows a family of characteristics which can be used to determine the relative humidity via a measurement of the electric resistance of sensor threads. The curves for the two thread types made from viscose (CV) and polyester (PES) are denoted by the red and blue color, respectively.

Intermediate values for various temperatures can be determined with the help of interpolation techniques.

Fig. 7 Family of resistance-humidity characteristics for a 650 dtex viscose yarn filled with carbon black (Thüringisches Institut für Textil- und Kunststoffforschung e. V.) (red) and for a 110 dtex polyester yarn coated with a polyurethane mixed up with 5 mass% lithium chloride (blue)



5.1 Why Testing Is Necessary

The tested conductive yarns used in woven sensor fabrics are in a wide range of specific conductivities made from a wide variety of materials. The spectrum ranges from metal fibers (e.g., Bekinox) to yarn constructions made of wires and partly highly elastic core filaments, metallized synthetic fibers (usually polyamide), and spun yarns filled with carbon modifications (e.g., graphite, fullerenes, carbon nanotubes, and graphene) and conductive yarns produced by electrospinning polymers. These yarns are the prerequisite for smart textiles with electronic functions.

Many of the woven samples with those fibers have proved to be particularly durable and robust due to the basic textile structure. The reliability of the new products depends less on the polymer thread than on the partly highly conductive yarns for which there are currently no standardized tests for quality assessment, process control during production and characterization of long-term stability and aging.

5.2 Requirements for Quality Control—New Simultaneous Testing Methods

Except for the spun metal fibers and the yarns made from conductive polymers in the electrospinning, all other combinations are materials of various physical properties, such as thermal expansion, thermal shrinkage, modulus of elasticity, and tensile strength. The different physical properties alone do not have a negative effect on the final property of the hybrid yarn.

Frequently, the required properties, e.g., the conductivity or extreme tensile strengths or elongation properties can only be achieved in the appropriate

combination. If the focus is too much on a physical property such as the conductivity, other effects are neglected, leading to degradation and ultimately to early aging phenomena. Therefore, for a comprehensive characterization of conductive yarns, it is not sufficient to accurately characterize the resistances, the current carrying capacity, the corrosion resistance (exchange current density from the panel plot, cyclic voltametric characterization of the oxidation resistance, and electrochemical impedance spectroscopy) of the yarns. If materials are used in clothing, mechanical, thermal stresses must not be neglected. For this purpose, only the textile properties (such as strength, elongation, elasticity, and frictional behavior) are currently being tested and the electrical properties are checked again only after the load tests.

The practice shows, however, that high-quality fluctuations, especially on metallized yarns, are difficult to master in this way, and materials which are subject to the individual tests fail in practice.

Only combined test methods make it possible to understand the failure mechanisms and to make reliable statements about the reliability of the new textile materials. The electrical parameters must be recorded under mechanical and thermal stress and must be correlated with practical experience.

5.3 Simultaneous Tests of Electrical and Mechanical Properties—RFs Characteristic

Only the simultaneous detection of resistance R and force F (RFs characteristic) over a strain cycle (path s) provides important information about the number of defect sites on filaments as the resistance decreases briefly with the strain as a result of the contact between the filaments and the bridging of the defect sites is caused (see Fig. 8).

A sharp rise following the resistance drop and the distinct hysteresis of the resistance course during the stretching versus the subsequent expansion characterize the adhesion of the metal layer in the case of metallized yarns. This resistance-strain pattern typical of metallized yarns can be described as a series of defect and parallel-connected contact resistances between the filaments, connected in series with the equivalent circuit diagram shown in Fig. 9, across the filament resistor when both the number of defect sites and the contact points grow exponentially (Fig. 10).

The equivalent circuit diagram qualitatively describes the resistance drop, the sudden rise and the renewed decrease in strain as well as the course during the relaxation. The strong increase in resistance is caused by the exponentially growing number of defect sites which are compensated for by the increasingly stronger thread closure and the increasing number of contact points. Thus, the resistance tip is a measure of the defect sites forming, which also manifests itself in multicyclic strain tests.

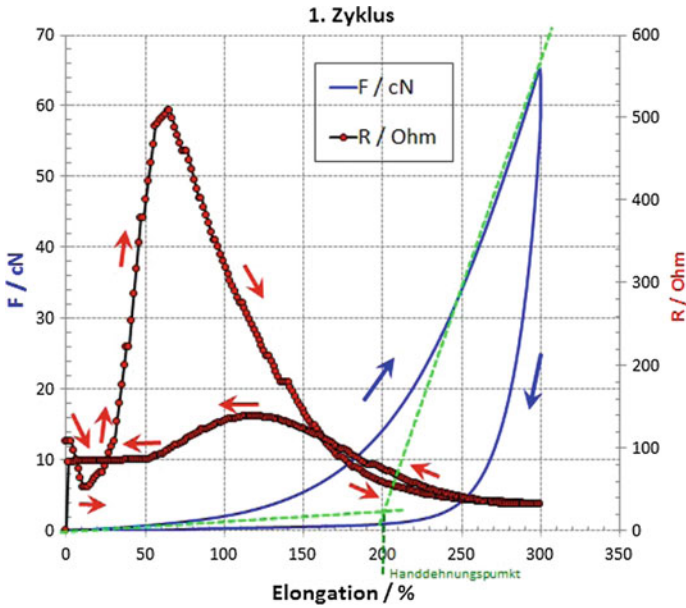
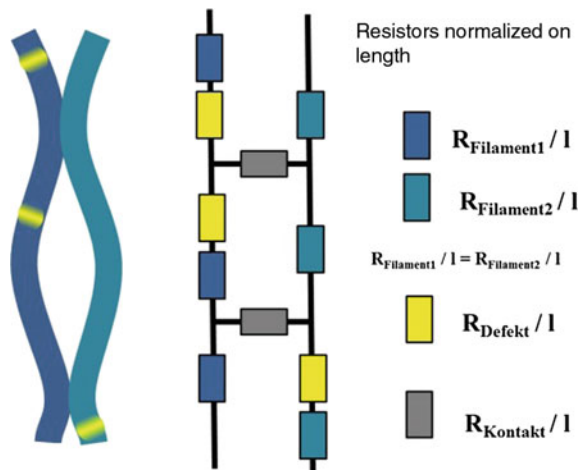


Fig. 8 Typical resistance-strain dependency of a highly metallized yarn with good adhesion of the metal layer and including the synchronously measured force

If the resistance tip is significantly larger when stretched, the resistance peaks will increase sharply during the cycle-to-cycle stretching until the conductivity of the thread completely tears after a few further cycles. The resistance increases spontaneously and only briefly into the mega-ohm range until the conductivity is completely interrupted.

Fig. 9 Equivalent circuit diagram with the example of two filaments in contact with each other



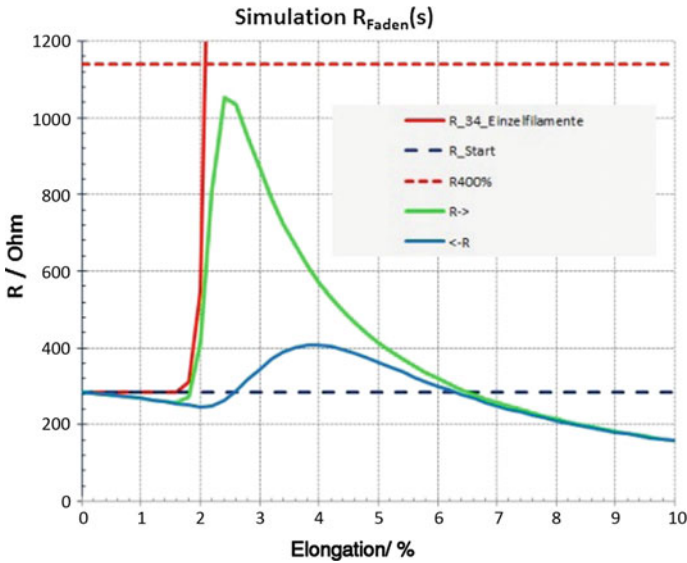


Fig. 10 The simulated resistance-strain curves (red) simulated with the equivalent circuit diagram for a filament with 34 filaments for noncontacting filaments for filaments (green) contacting filaments (green) during stretching and (turquoise) during relaxation

The relative resistance maximum is shown in Fig. 11 during the elongation of the filament of $(508 \text{ } \Omega - 109 \text{ } \Omega) / 109 \text{ } \Omega * 100\% = 366\%$ represents a typical value for silver-plated yarns with good silver adhesion. With a relative resistance increase of 400% and more, the typical behavior described above is observed for yarns with poor adhesion of the metal layers.

If the metal layer is galvanically strengthened on such yarns, adhesion problems and the corresponding aging phenomena are intensified. If the simultaneous RFs characteristic is recorded again on galvanically amplified yarns, the relative resistance peaks $(R_{\text{Peak}} - R_0) / R_0 * 100\%$ increase significantly in the strain cycle from cycle to cycle. Already after less than 10 cycles, the conductivity of the thread tears off briefly. While the total failure in the case of premetallized yarns in the boundary region is often not observed within 50 cycles, in the case of metallized yarns with a high metal layer and inadequate adhesion, this occurs as a rule after 20 cycles or earlier (see Figs. 11 and 12).

6 Conclusion

With the detection of the RFs characteristic, the electrical properties under the load are checked as in later use. The cyclic load changes and the simultaneously detected thread resistance can be used to simulate aging in use.

Fig. 11 RFs characteristic of a metallized filament with good adhesion of the metal layer

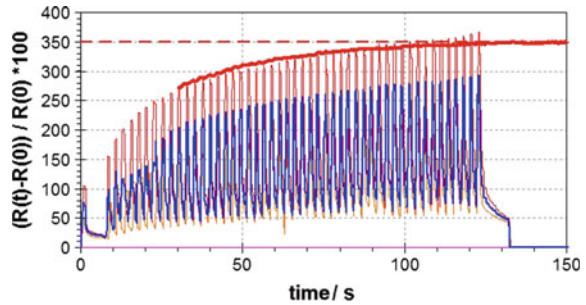
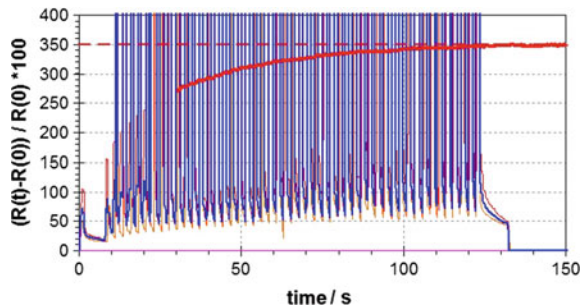


Fig. 12 RFs characteristic of a metallized filament with poor adhesion of the metal layer



In order to limit the test time, the strains can be slightly above those in later use. A correlation between the amplitude of the strain used in the test and the number of cycles up to the total failure is indicated and is currently being worked out in more detail. With the aid of the RFs characteristic, however, already preassembled yarns with insufficient adhesion can already be detected and sorted out before the galvanic reinforcement.

The example of the test of the RFs characteristic clearly shows that simultaneous measurements make it possible to predict the aging of conductive yarns and thus their reliability. In addition, RFs examinations can also be applied to conductive textile structures (e.g., sensorized narrow fabrics) so that not only statements about the reliability of the yarns but also of the conductive textile structures in the smart or electronic textiles are possible based on their subsequent use.

In addition to the mechanical stress, the yarns are still subject to the thermal stress caused by the different heat coefficients of their conductive and nonconductive components and to chemical stress depending on their application. For this reason, these influences are to be recorded during the test for the ever more complex material combinations, which are no longer concerned solely with the conductivity of the yarns, but also with their use under cyclic mechanical, thermal, and chemical stresses, and new simultaneous test methods are to be developed.

Acknowledgements



The IGF project 18435 BR of the Research Association Forschungskuratorium Textil was funded via the AiF as part of the program to support Industrial Collective Research (IGF) by the Federal Ministry for Economic Affairs and Energy on the basis of a decision by the German Bundestag.



The European Project “1D Neon” (H2020-NMP-22-2015 GA No. 685758) was funded by the EC as part of the Horizon2020 framework program with funds from the European Union.

References

1. Castano, L. M., & Flatau, A. B. (2014). Smart fabric sensors and e-textile technologies: a review. *Smart Materials and Structures*, 23, 053001–053027. doi:[10.1088/0964-1726/23/5/053001](https://doi.org/10.1088/0964-1726/23/5/053001).
2. Gimpel, S., Thurner, F., Zschenderlein, D., & Möhring, U. (2007). Ersetzt das Sticken bald das Löten? *Eurostitch*, 15, 32–35.
3. Melnykowycz, M., Koll, B., Scharf, D., & Clemens, F. (2014). Comparison of piezoresistive monofilament polymer sensors. *Sensors*, 14, 1278–1294. doi:[10.3390/s140101278](https://doi.org/10.3390/s140101278).
4. Mattmann, C., Clemens, F., & Tröster, G. (2008). Sensor for measuring strain in textile. *Sensors*, 8, 3719–3732. doi:[10.3390/s8063719](https://doi.org/10.3390/s8063719).
5. M. Kienbaum, *Bindungstechnik der Gewebe*, Bd.3: Drehergewebe, Faltengewebe, Florgewebe und Jacquardgewebe, Fachverlag Schiele & Schön, Berlin 1996, ISBN 978-3-794-90607-9

Integration of Solar Cells and Other Electronic Components into Clothes

Susanna Fafenrot, Paul Silbermann, Nils Grimmelsmann,
Johannes Assig and Andrea Ehrmann

Abstract Wearables and smart textiles are a growing field in the fashion trade. Primarily, the textile industry can thereby expand and become again more local in Germany. The interest in clothes and textiles with new functions rises continuously, resulting in the fact that functionality and design should be well joined to convince the end-consumer. In an interdisciplinary project of designers and engineers, a flexible solar module was integrated into clothes that it is not visible at first sight. It was hidden behind a laser-cut to provide a good integration of technology in clothes and to enrich the design. The influence of the laser-cut was analyzed in various measurements and was optimized so that the solar cells can still provide enough power to control a sound module for MP3 files. With textile buttons, which contain conductive textiles and threads, it is possible to operate the music. The results are two androgynous outfits with electronic components. The intention was to develop garments for both genders, to give them a function for increasing the value and to put forward the sustainability.

1 Introduction

Smart textiles often contain electronic parts which are either integrated to avoid standing out, or which are planned to attract attention by showing them openly. Away from the catwalk, in both cases, embedding electronic parts must meet some criteria which are necessary to fulfill the users' requirements: The nontextile objects must not restrict the wearability, i.e., the wearer should be able to use a smart garment like a common one, without limitations due to hard, protruding parts [1–4]. Additionally, whether nearly invisible or being used as a design element, electronics should not reduce the aesthetic quality of a garment.

The wearability of smart textiles is addressed in several publications, especially related to the wearing comfort of tight-fitting garments. A typical example is

S. Fafenrot (✉) · P. Silbermann · N. Grimmelsmann · J. Assig · A. Ehrmann
Bielefeld University of Applied Sciences, Bielefeld, Germany
e-mail: susanna.fafenrot@fh-bielefeld.de

textile-based ECG sensors which were developed in different research groups to increase the comfort level during long-term monitoring, as opposed to common pregelled glue electrodes [5, 6]. This task is of special importance if babies are planned to be monitored with such wearable sensors [7].

Electronics for posture monitoring in neurological rehabilitation are placed in a wearable system aiming at wearability and ease of use [8]. Similarly, electronics integrated into an insole for gait monitoring also aim at being lightweight, thin, and comfortable to wear [9].

Conduction lines between the different electronic elements are also under investigation, trying to find solutions which are not only washable and abrasion resistant but also stretchable and comfortable for the wearer of such a garment [10].

Design aspects, however, are related to technical requirements in most scientific publications, while design in the meaning of “making a garment look attractive for possible wearers” is often neglected. Only few scientific publications address the need to combine (electronic) functions with an aesthetic design [11–17], some of them, on the other hand, ignore the more technical requirements such as washability and wearing comfort.

Our chapter shows the possibilities and challenges occurring for the integration of different electronic parts and conduction lines into garments for both genders and shows possible solutions to combine aesthetics with new functionalities without losing the wearing comfort.

2 Experimental

The complete garments include electronic parts, leading to respective technical requirements, as well as design aspects. All these parts are described in the following subsections.

3 Electronic Devices

Due to the desire to create sustainable smart textiles, a solar module is included to provide power for a sound module. For this, a flexible solar module with nominal voltage 5 V, open-circuit voltage 6.7 V, nominal current 340 mA, short-circuit current 400 mA, and power 1.5 W (purchased from Lemo-Solar GmbH, Ilsfeld/Germany). The solar module is bendable, weatherproof, break-proof, lightweight, and thus suited for integration in garments.

The included sound module GPD2856C for MP3 files is an MP3 decoder board with a 3 W amplifier for Arduino and microcontroller, purchased from LV Verkauf (Ostfildern/Germany). It can use 3.6–5.5 V, has an AUX connection for headphones (stereo 3.5 mm) and a 16 GB microSD card slot which can find the MP3

files automatically. Furthermore, there are buttons for *Prev*, *Next*, *P/P*, *Repeat*, *V-*, *V+*, and *Mode* on the board. These buttons are connected with textile buttons afterward.

To enable listening to music without being in the sun, a lithium polymer accumulator with nominal voltage 3.7 V, end-of-charge voltage 4.2 V, end-of-discharge voltage 3.0 V, deep discharge limit 2.3 V, and a capacity of 1700 mAh was bought from KT-Elektronik (Königs Wusterhausen/Germany).

A charge controller (based on a TP4056 Micro USB 5 V, purchased from maxsuperdeal, Freilassing/Germany) connects all elements and fits the solar module power to the accumulator as well as to the sound module.

Switches (purchased from alpha electronic—Ing. A. Berger GmbH Bielefeld/Germany) allow for directing the power from the solar module completely to the MP3 player or the accumulator, respectively, as well as for switching off the whole circuit.

Conductive textiles (purchased from Less EMF Inc.) are used in the textile push buttons. A conductive thread (purchased from Statex Bremen/Germany) was combined with a laser-cut circuit board to make a bridge between the flexible conductive thread and the stiff wires (purchased from alpha electronic—Ing. A. Berger GmbH, Bielefeld/Germany).

4 Textile Fabrics and Garment Construction

Diverse textile fabrics were chosen for the final garments. Since a collection of two outfits for women and men was planned, colors and different material combinations were used to play with stereotypes, such as pink silk for “typical female” and dark sports fabrics as “typical male.”

Push buttons for controlling the sound module were realized as textile versions with the help of a laser cutter according to Ref. [18]. All electronic parts can be taken out of the garments to enable washing and to allow changeableness.

5 Laser Cutting

To integrate the solar cells into the garments instead of simply gluing them on top of the textile parts and to get the effect of a print, they are partly hidden under a laser-cut pattern. For this, an Epilog Zing 24 laser (60 W, 608 × 304 mm) was used in the FabLab DEZENTRALE Dortmund. There were also laser-cut details (jackets, trousers, bags, and further processed headphones) to promote the aesthetics and raise the value of the garments using new technologies. The details are frayed sportive stripes, cut seams, the form of the handbags, mesh out of pink silk and the above-mentioned laser-cut for the solar cell.

Vector graphics for laser cutting were prepared using Adobe Illustrator CS6. For the pattern for the solar module, the help of different layers was necessary. The first

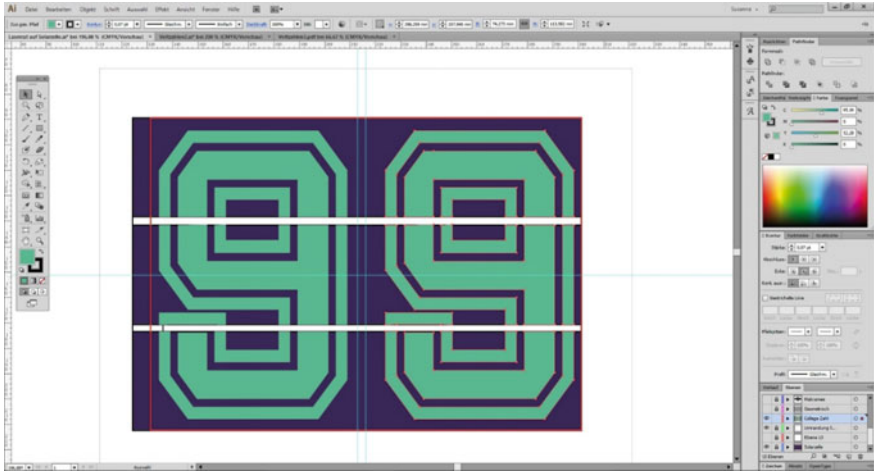


Fig. 1 Vector graphics were prepared with different layers in Adobe Illustrator CS6 for the laser cutter, used font: Emilio 20 by Adien Gunarta available at <https://www.dafont.com/emilio-20.font>

layer is a re-creation of the solar module and in the layers above, different designs can be tried out. It is important to make sure that the white border of the solar module is hidden while the white horizontal lines were made consciously visible to support the sporty look. Figure 1 depicts the use of different layers. The three blue stripes and the red mark represent the solar module, while the green areas show one of the tested cuts (this is the visible part of the solar module).

The open area of the cuts was calculated by means of the Adobe script “GetShapeArea” to evaluate the power of the solar module in reference to the whole circuit.

6 Results and Discussion

The electronic elements and their interdependencies were first tested without any integration into a textile fabric. First tests showed that 22 mA is necessary to operate the sound module and the whole circuit. In the diffuse light of the laboratory lamps, only 18 mA was generated by the solar cell, i.e., 4 mA had to be added by the accumulator. Changing to concentrated light from a desk light, a current of 34 mA could be achieved. Both values are significantly smaller than the specified nominal current of 340 mA of the solar module. While the idea of using an accumulator in combination with a solar cell works in principle, the power gained from the solar cell from the usual light inside a building is apparently insufficient to operate even a small consumer such as a sound module.

Nevertheless, the next tests of the dependence of voltage and current of the solar panel on the shaded solar cell area was tested with a desk light to avoid undesired

changes of the light intensity. Figure 2 depicts the results. While the voltage reaches the maximum values already for approx. 30% open area, the current increases continuously with increasing illuminated area. It should be mentioned that these tests were performed using laser-cut patterns in order to measure as realistic as possible with respect to the planned application.

The next experiments, however, were performed in daylight. Figure 3 depicts the currents measured outside with partial shadowing of the solar module. While the measurements in the shadow still show quite low currents, even smaller than in previous inside tests, the currents gained in the sun are sufficient to operate the sound module (with 22 mA) and charge the accumulator at the same time. Nevertheless, it should be mentioned that the specified nominal current of 340 mA is still not reached.

Further long-term tests in the full sun with different laser-cut patterns, all shadowing approx. 50% of the solar module, resulted in a broad spectrum of time-dependent current values, ranging between 50 mA and 130 mA. In spite of

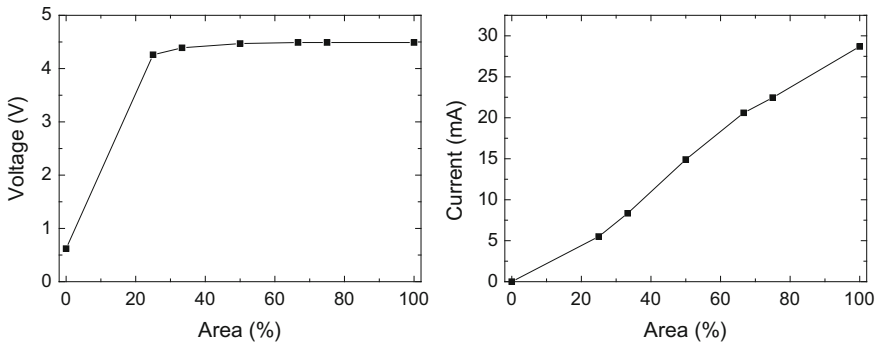
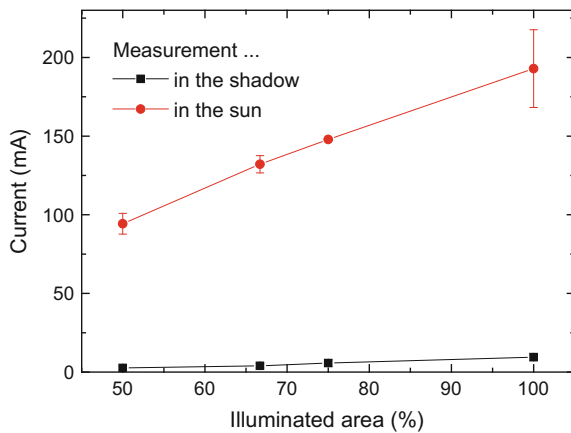


Fig. 2 Current and voltage as functions of the illuminated area of the solar panel

Fig. 3 Currents measured in the shadow and in the sunlight, respectively, for the partly illuminated solar module



these large deviations, the minimum value of 50 mA is still sufficient to operate the sound module. The speed of loading the accumulator, however, will vary strongly.

Different laser-cut patterns were examined with respect to the illuminated area. To make the functionality of the solar cell visible, this pattern should refer to its electronic properties. Since the currents were found to vary strongly, the voltage values measured for the solar panel were chosen.

Figure 4 shows some ideas of which pattern 2 was finally chosen, with a slight modification. This pattern has an open area of 49% which can be related to an expected average current of 94 mA, extrapolated from the values in Fig. 3.

This choice of the laser-cut pattern led to a new problem: The inner corners of the pattern had to be fixed to avoid fluttering in the wind. For this, the laser-cut textile was planned to be fixed on a net-lace fabric, using Vliesofix gluing interlining (purchased from Nähzentrum Eilers, Bielefeld/Germany). This means that the effect of the net-lace fabric has to be tested in addition to the influence of the large-area shadowing due to the laser-cut.

Figure 5 depicts the laser-cut pattern on one of the three possible net-lace fabrics, covering the solar module. To investigate the influence of these net-lace fabrics, Fig. 6 shows the results of long-term measurements under equal light conditions (indoor at the window without direct sunlight) .

Apparently, the solar module performance is nearly uninfluenced by the different net-lace fabrics. Thus, this fabric was chosen due to design aspects.

For the textile push buttons, all parts were laser-cut (Fig. 7(1)) except the conductive textile. Inside, two conductive layers are separated by compressible sandwich mesh (knitted fabric) with several open areas, working as a spacer—the conductive layers only get into contact when a pressure is applied. The buttons have

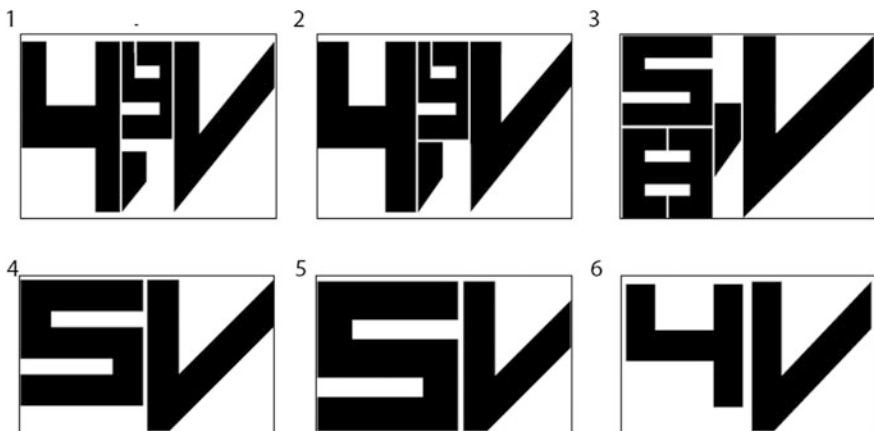
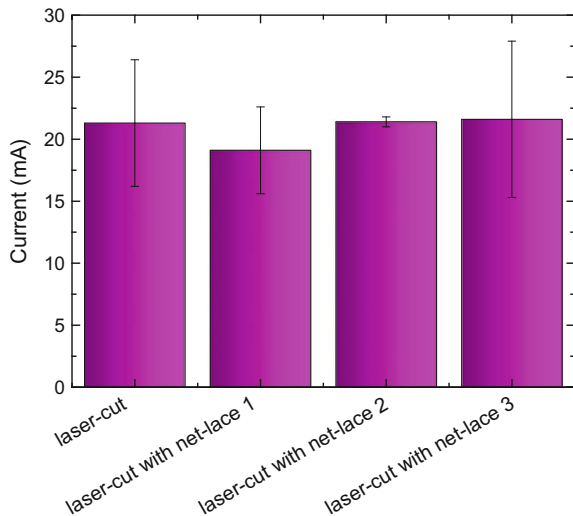


Fig. 4 Possible laser-cut patterns with open areas between 35% (#6) and 55% (#5) related to the whole area of the solar module, used font: Vermin Vibes by Andrew McCluskey (NALGames) available at <https://www.dafont.com/de/vermin-vibes.font>



Fig. 5 Laser-cut pattern placed on the solar module, fixed on a net-lace fabric

Fig. 6 Influence of net-lace fabrics on the current produced by the solar module



laser-cut symbols to depict their functions. After this preparation, all parts were sewn together and the conductive threads were sewn on the conductive textile (Fig. 7(2)), as suggested by Bohne [18].

These buttons were placed on the front of the circuit bags which have laser-cut marks and open areas for the conductive threads and switches. On the back, the laser-cut circuit boards are visible which have the aim to build a bridge between the flexible conductive thread and the stiff wires (Fig. 7(3), (4)). Then, the wires can be soldered on the circuit board and the front bag can be sewn together with the back (Fig. 7(5), (6)).



Fig. 7 Shows the process of preparing the textile buttons and the circuit bag

The wires are now the positive and negative terminals of the textile buttons and should be connected with the primary buttons on the board of the sound module. After soldering, the textile buttons can operate the sound module. The electronics can be stashed in the bag and the switches can be put through the cuts to the outside (Fig. 7(7), (8)). For the switches separating the sound module and the accumulator from the charge controller, conventional parts were used.

As described above, these parts are placed together with the other electronic objects and conductive thread in a small bag which can be taken out of the garments for washing. The solar module and all wires are fixed in integrated bags, closed with hook-and-loop fasteners.



Fig. 8 Jackets with integrated solar cells, other electronic parts and laser-cut details

Figure 8 depicts the final smart jackets with the electronic parts as described above, combined with trousers, pullovers, and a bag belonging to the same collection. The technical parameters stay unaltered during integration of the electronic elements in the jackets. The jackets are thus capable of receiving enough solar energy in the sunlight to power a sound module and at the same time load an accumulator to save energy for using the MP3 player inside a building.

7 Conclusion

In a recent project, smart jackets were developed, including solar cells, a sound module, an accumulator, and a charge controller together with switches to control whether the power gained by the solar cell should be stored in the battery, operate the MP3 player, or both. The design was used to combine androgynous aesthetics with references to the included technical system, using the laser-cut pattern “4.9 V” which was one of the highest measured voltage values gained from the solar module. In this way, combining reliable technique and appealing design can pave the way to a more natural utilization of smart textiles and electronics with diverse functionalities. All clothes are interchangeable because they are intended for both genders. Inspiration for this was gender fluidity and androgyny. Garments are

changeable and dimensions adjustable. This is an important aspect concerning the sustainability because a couple could share the garments, for example. Furthermore, it is mentionable that the clothes increase in value because of the electronics and smart of textiles. This affects the esteem of the clothes.

Acknowledgements The authors acknowledge gratefully the possibility to use the laser cutter in the FabLab DEZENTRALE Dortmund, particularly Julia Krayer and Uwe Heuer. During the process, a second laser cutter of the FabLab Paderborn e. V. was used for some samples. The authors wish to express their gratitude to the photographer Lianna Hecht, the models Marvin Geronimo Wieser-Kloß and Joyce Gosemann, and the assistant of the photo shooting Caroline Eckert.

References

1. Andreoni, G., Standoli, C. E., & Perego, P. (2016). Defining requirements and related methods for designing sensorized garments. *Sensors, 16*, 769.
2. Stoppa, M., & Chiolerio, A. (2014). Wearable electronics and smart textiles: A critical review. *Sensors, 14*, 11957–11992.
3. Luprano, J. (2009). Bio-sensing textile for medical monitoring applications. *Advances in Science and Technology, 57*, 257–265.
4. Shim, B. S., Chen, W., Doty, C., Xu, C. L., & Kotov, N. A. (2008). Smart electronic yarns and wearable fabrics for human biomonitoring made by carbon nanotube coating with polyelectrolytes. *Nano Letters, 8*, 4151–4157.
5. Yapici, M. K., & Alkhidir, T. E. (2017). Intelligent medical garments with graphene-functionalized smart-cloth ECG sensors. *Sensors, 17*, 875.
6. Aumann, S., Trummer, S., Brücken, A., Ehrmann, A., & Büsgen, A. (2014). Conceptual design of a sensory shirt for fire-fighters. *Textile Research Journal, 84*, 1661–1665.
7. Bouwstra, S., Chen, W., Feijs, L., & Oetomo, S. B. (2009). Smart jacket design for neonatal monitoring with wearable sensors. In *Proceedings of 6th International Workshop on Wearable and Implantable Body Sensor Networks* (p. 162).
8. Wang, Q., Chen, W., Timmermans, A. A. A., Karachristos, C., Martens, J. B., & Markopoulos, P. (2015). Smart rehabilitation garment for posture monitoring. *IEEE Engineering in Medicine and Biology Society Conference Proceeding, 37*, 5736–5739.
9. Lin, F., Wang, A. S., Zhuang, Y., Tomita, M. R., & Xu, W. Y. (2016). Smart insole: A wearable sensor device for unobtrusive gait monitoring in daily life. *IEEE Transactions on Industrial Informatics, 12*, 2281–2291.
10. Yokus, M. A., Foote, R., & Jur, J. S. (2016). Printed stretchable interconnects for smart garments: design, fabrication, and characterization. *IEEE Sensors Journal, 16*, 7967–7976.
11. Stead, L., Goulev, P., Evans, C., & Mamdani, E. (2004). The emotional wardrobe. *Personal and Ubiquitous Computing, 8*, 282–290.
12. Stylios, G. K., & Wan, T. Y. (2007). Shape memory training for smart fabrics. *Transactions of the Institute of Measurement and Control, 29*, 321–336.
13. Vili, Y. Y. F. C. (2007). Investigating smart textiles based on shape memory materials. *Textile Research Journal, 77*, 290–300.
14. McCann, J. (2009). Design for ageing well: Improving the quality of life for the ageing population using a technology enabled garment system. *Smart Textiles, Advances in Science and Technology, 60*, 154–163.
15. Chen, W., Oetomo, S. B., Feijs, L., Bouwstra, S., Ayoola, I., & Dols, S. (2010). Design of an integrated sensor platform for vital sign monitoring of newborn infants at neonatal intensive care units. *Journal of Healthcare Engineering, 1*, 535–553.

16. Wang, Q., Chen, W., & Markopoulos, P. (2015). Smart garment design for rehabilitation. *Communications in Computer and Information Science*, 515, 260–269.
17. McCann, J. (2016). Sportswear design for the active ageing. fashion practice. *The Journal of Design Creative Process & the Fashion Industry*, 8, 234–256.
18. Bohne, R. (2012). *Making things wearable—Intelligente Kleidung selber schneiden*. KG: O'Reilly Verlag & Co.

Washing and Abrasion Resistance of Conductive Coatings for Vital Sensors

Patricia Schäl, Irén Juhász Junger, Nils Grimmelsmann,
Hubert Meissner and Andrea Ehrmann

Abstract In the area of medical textiles, several applications necessitate conductive sensors, such as ECG or pulse measurements, breathing sensors, etc. Additionally, connections between electronic elements, data transfer units, and other parts of sensor networks need conductive paths. The resistance of conductive yarns or coatings against mechanical and chemical influences, however, is often low. Silver particles in coatings or on yarns, e.g., can oxidize during washing. Thin coatings can easily be abraded and offer only a low conductivity due to low layer height, while thicker coatings can be stiff and break during bending. In a recent project, we evaluate different coatings with respect to their resistance against mechanical stress due to abrasion against diverse materials, as a typical demand of sensory shirts or other medical textiles. Conductive silicone rubber, as well as graphite-polyurethane dispersions with different graphite concentrations, were coated on diverse textile fabrics in a defined height. Abrasion tests were performed on these samples using a linear abrasion tester. The electrical resistance of the conductive coatings was measured after each test cycle. Additionally, confocal laser scanning microscopy was used to detect micro-cracks or modifications of the coating surface. The article gives an overview of the results and depicts the advantages and challenges of the conductive coatings under examination.

1 Introduction

Conductive yarns or textile coatings have diverse applications in the area of smart textiles [1]. They are necessary to measure vital signs, e.g., ECG or pulse [2–13], pressure [14, 15] or elongation [16–22]. Besides these sensory applications, they are also used to transfer energy or data through conductive transmission lines [23–25] or through textile antennas to an external receiver [26].

P. Schäl · I. Juhász Junger · N. Grimmelsmann · H. Meissner · A. Ehrmann (✉)
Bielefeld University of Applied Sciences, Bielefeld, Germany
e-mail: andrea.ehrmann@fh-bielefeld.de

The main issue in using conductive yarns or textile coatings is their resistivity against mechanical and chemical impacts, i.e., abrasion and washing. This is why novel conductive textile coatings are investigated in many research groups, e.g., consisting of carbon nanofibers [27], reduced graphene oxide, and silver nanoparticles [28], or graphene/poly(vinyl alcohol) [29]. For reduced graphene, another examination found satisfying washing resistance [30]. Nevertheless, it should be mentioned that sodium hydrosulfite, a noxious chemical which can explode, is needed for converting graphene oxide into reduced graphene. Less dangerous coatings, such as Poly(3, 4-ethylenedioxythiophene)-poly(styrenesulfonate) (PEDOT:PSS), are known to not withstand UV radiation [31–33].

An alternative to expensive conductive materials, such as noble metals, oxidizing, or other instable materials, such as other metals, or dangerous materials is carbon in the forms of carbon black or graphite. Nevertheless, only little research is published on the influence of mechanical or chemical impact on carbon-based conductive coatings [34, 35].

This is why graphite-polyurethane coatings were prepared on diverse textile materials in a recent project and tested with respect to their abrasion fastness. As a comparison, a commercially available conductive silicone rubber is used which has to be polymerized at high temperatures and is thus not usable on each textile fabric.

2 Experimental

For the graphite-polyurethane (PUR) coatings, dispersion were prepared using *bredderpoX®R15 GB-Flex* PUR resin, *bredderpoX®R15 GB-Flex* PUR hardener and diluting agent *Verdünnern XA* (Breddermann Kunstharze, Schapen/Germany). Graphite particles with diameters 3–5 μm (Algin, Neustadt Glewe/Germany) were added in concentrations of 25% and 29%, respectively, since lower graphite concentrations resulted in significantly increased electrical resistances, while higher graphite concentrations led to brittle coatings. In all coatings, 10% silicone oil was added to increase the flexibility of the final layer.

Additionally, the conductive silicone rubber *Powersil 466 A + B* (Wacker Chemie AG, Munich, Germany) was tested after curing in an oven at 200 °C for 2 h.

All coatings were applied using a doctor's knife. The coating dimensions of 10 mm width and 150 mm length, as well as the coating layer height, were defined by adhesive tape glued on the textile fabrics.

Two samples were prepared per coating and base fabric on which three different ranges of 100 mm length each were marked so that each result was averaged over six measurements.

Table 1 shows the four woven fabrics used in this investigation. Material, thickness and areal weight are varied.

Abrasion tests were performed by a sliding block test according to DIN EN ISO 13427. The standard abrasive material, sandpaper with grain size 100, was exchanged by a sandpaper grain size 400 as well as the jeans and the viscose fabrics

Table 1 Thickness and areal weight of textile fabrics used for coating

Name	Material	Thickness/ mm	Areal weight/(g/m ²)	Warp threads/cm	Weft threads/cm
CO	Cotton	0.32	94	30	22
VI	Viscose	0.17	67	24	40
LI	Linen	0.34	141	26	24
Jeans	Cotton	0.90	371	3.5	2.5

defined in Table 1 to investigate more realistic situations. Additionally, each coating was abraded against itself.

Resistance measurements were performed using a *Mastech PM334* digital multimeter with a maximum measurable resistance of 30 M Ω . All resistances are measured between two points in a distance of 100 mm.

A confocal laser scanning microscope (CLSM) VK-9700 by Keyence was used for microscopic examination of the coatings before and after rubbing fastness tests. All CLSM images depicted in this article have the same nominal magnification of 2000 x.

3 Results and Discussion

One of the biggest challenges in the examination of conductive textile coatings is the measurement of the electrical resistance. Opposite to hard, flat surfaces, such as plastics or metals, measurements on textile surfaces usually depend strongly on the contact area, contact pressure, and also on a possible movement or bending of the conductive fabric. This is why in a first test series three different contacting methods were tested: small (crocodile) clamps with “teeth” pressed into the conductive coatings; large clamps with broad, flat contact areas pressed on the conductive coatings; and conductive Cu-Zn bands which were glued onto a table in the desired measurement distance and on which the sliding block with the fabric under examination below was placed.

Figure 1 depicts the results of these measurements, performed on the three different coatings described above. Comparing all results, it is obvious that the Powersil coating gives relatively high resistances and standard deviations, as expressed by the error bars. For the PUR coating with 29% graphite, all measurements show significantly reduced standard deviations, with the smallest values being measured using the Cu-Zn band. Only for the measurement of the coatings with 25% graphite included, a significant difference between the contacting methods is visible. Here, the measurements with the Cu-Zn band show very small error bars, while measurements with both clamps result in visibly larger standard deviations.

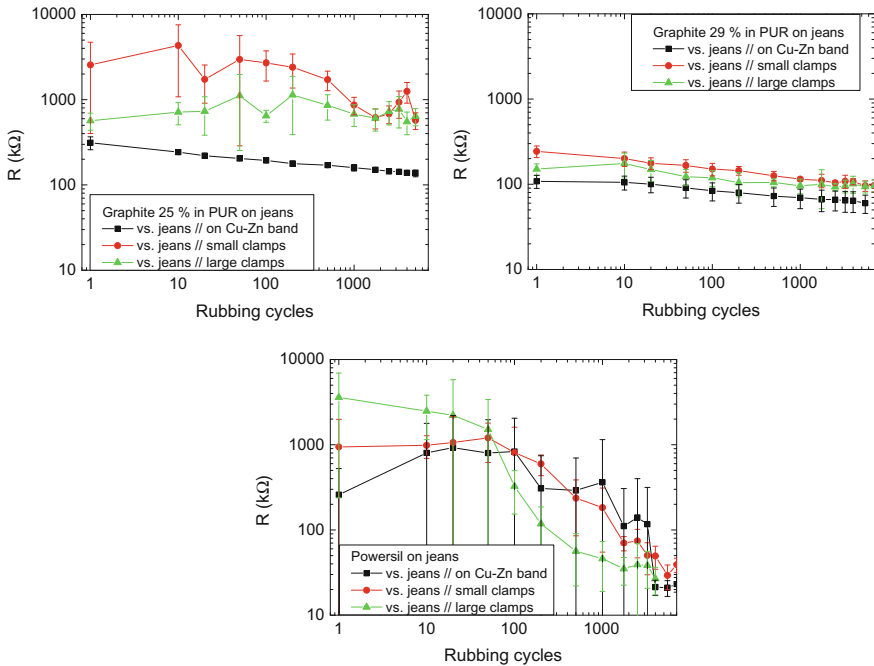


Fig. 1 Comparison of different electrical connection methods for measurements, tested for graphite/PUR and Powersil coatings on jeans, abraded against jeans. All graphs are depicted with double-logarithmic axes, meaning that apparently linear correlations are in reality exponential

This is why the following tests were performed using the Cu-Zn band.

Next, different rubbing partners were tested: the jeans fabric and the viscose fabric (cf. Table 1) as well as a sandpaper grain size 400. Figure 2 shows the results of these experiments. Again, the coatings with 29% graphite showed the most stable measurements. In all three cases, a slight decrease of the resistance is visible with increasing numbers of rubbing cycles.

For 25% graphite content in the PUR coating, rubbing against jeans or viscose resulted in a resistance decrease again, while rubbing against sandpaper resulted in increased error bars and approximately constant resistance values. Apparently, for this coating, the sandpaper is too harsh.

In the case of the Powersil coating, rubbing against all three materials of choice supported the decrease of the electrical resistance. Only for jeans as rubbing partner, however, the error bars became acceptable after 5000 rubbing cycles. Since this material also showed good results in the tests of the graphite-PUR coatings, it was chosen as rubbing partner for the examination of the conductive coatings on different textile substrates.

In Fig. 3, the results of these experiments are shown. All three coatings were tested on the four textile substrates, rubbed against jeans and measured using the Cu-Zn band.

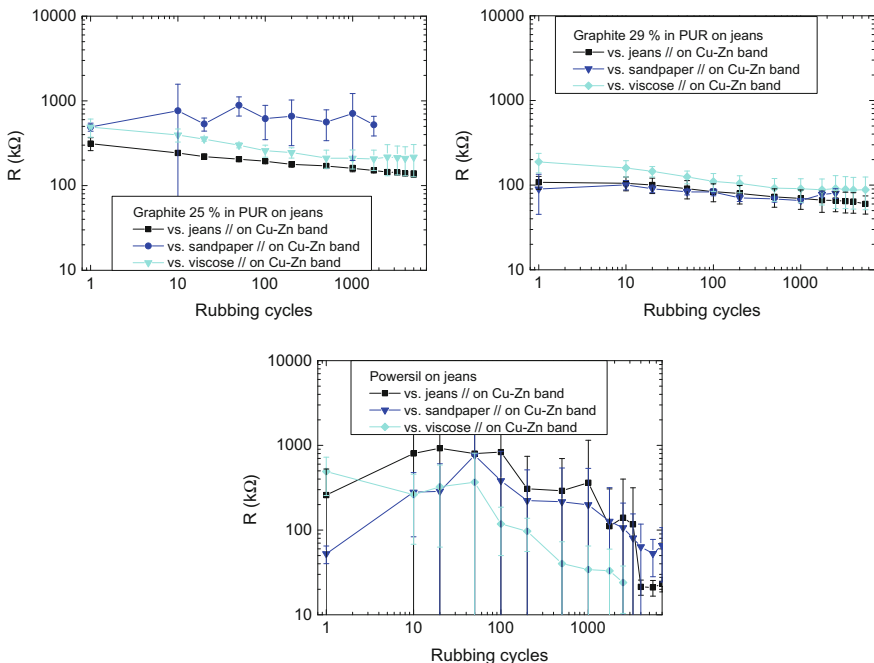


Fig. 2 Comparison of different abrasion partners, tested for graphite/PUR and Powersil coatings on jeans, measured on Cu-Zn band

Again, the Powersil coatings showed the highest standard deviations, with this coating on viscose giving the best and most stable results. For large numbers of rubbing cycles, however, both the resistances and their standard deviations decrease significantly.

For the more stable measurements on the graphite coatings, it becomes obvious that the resistances on jeans are higher than on the other (thinner and finer) textile substrates. Apparently, not only the coating but also the chosen substrate strongly influences the resulting resistance values. Comparing the three finer fabrics, however, does not reveal significant differences. All of them show an approximately exponential decrease, in the double-logarithmic plots used here visible as apparently linear correlations.

Finally, all three coatings on fine cotton were tested using the respective identical samples as rubbing partners, modeling a situation where such conductive coatings are used as switches, etc. The results are shown in Fig. 4. For both graphite coatings, the resistance is now approximately constant, with a slight increase toward larger numbers of rubbing cycles. For the Powersil coating, the situation is worse—the resistances, as well as their standard deviations, remain high, until after approx. 200 rubbing cycles, the cotton fabrics were partly destroyed, and the experiment had to be stopped.

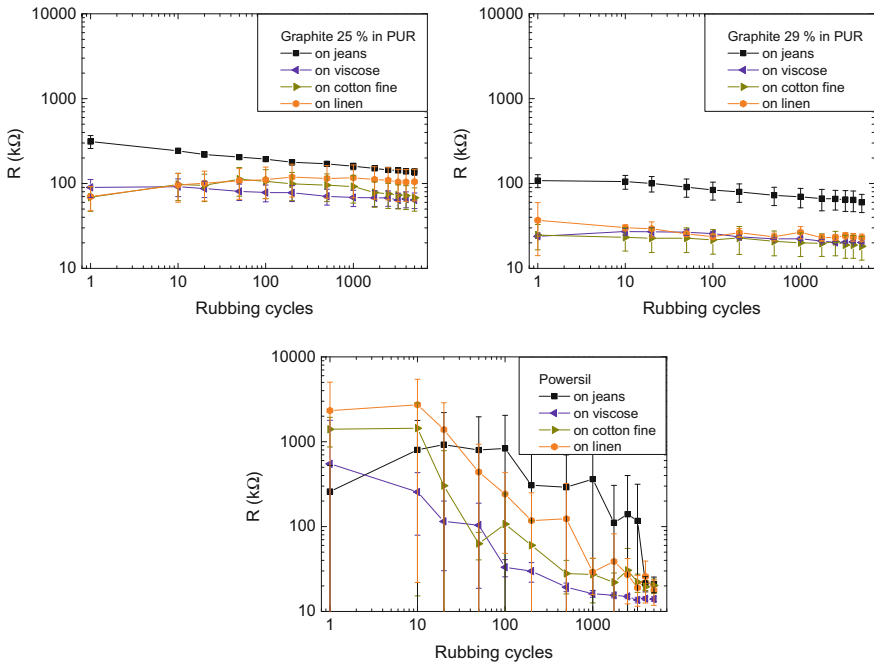
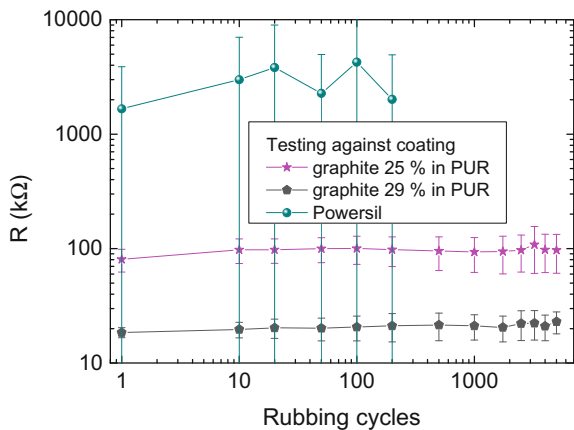


Fig. 3 Comparison of different textile substrates, tested for graphite/PUR and Powersil coatings abraded against jeans, measured on Cu-Zn band

Fig. 4 Comparison of the coatings under examination on fine cotton, abraded against themselves, measured on Cu-Zn band



Destroying of this fabric was due to the high friction between both Powersil layers—this resulted in the fabrics being moved with respect to the rough surfaces of the sliding and the rubbing block, leading to destroying them from the backsides.

To understand the influences of these rubbing processes better, Figs. 5, 6 and 7 depict the coating surfaces before the abrasion processes and after 5000 rubbing

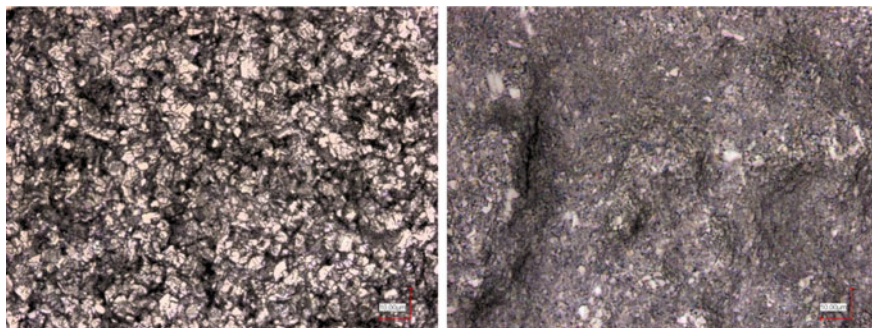


Fig. 5 Graphite 25% in PUR before abrasion (left panel) and after 5000 rubbing cycles against jeans

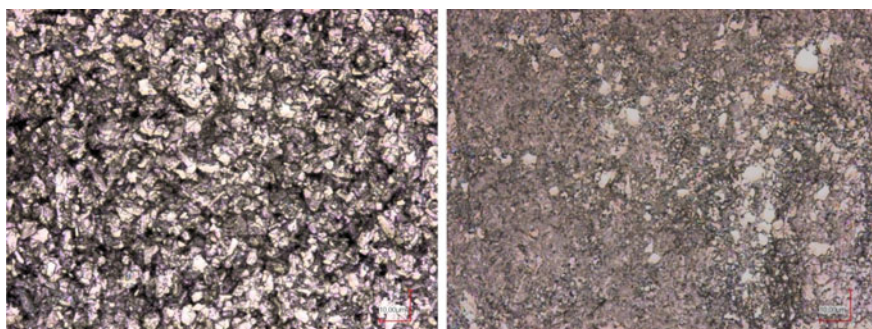


Fig. 6 Graphite 29% in PUR before abrasion (left panel) and after 5000 rubbing cycles against jeans

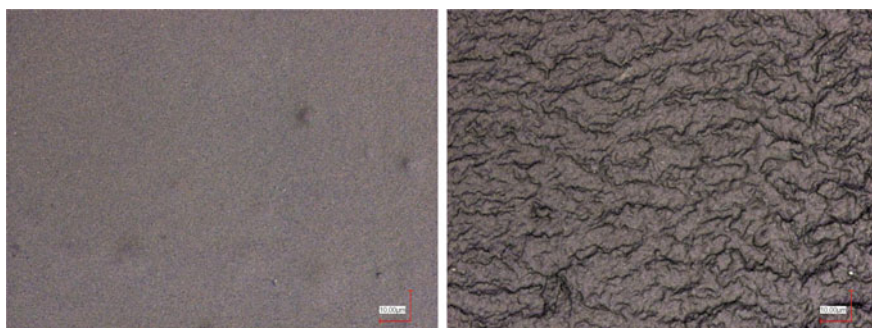


Fig. 7 Powersil before abrasion (left panel) and after 5000 rubbing cycles against jeans

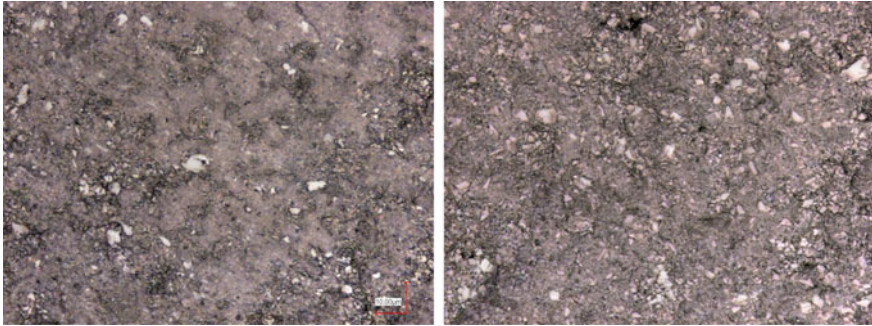


Fig. 8 Graphite 25% (left panel) and graphite 29% (right panel) in PUR after 5000 rubbing cycles against the identical coatings

cycles against jeans. Both graphite coatings show typical graphite flakes on the surfaces before the abrasion tests which are nearly vanished after the 5000 test cycles.

Apparently, the abrasion cycles rub off all loose material, i.e., especially the graphite flakes laying on the surface. While this seems to be counterproductive at first glance, we assume that it helps contacting the graphite which is really fixed in the conductive layer and has contact to the percolation paths inside the coating, while the original outer layer seems to consist of pure graphite with less contact to the actual conductive bulk material.

For Powersil, another surface modification takes place. Here, rubbing results in a riffle structure which may be attributed to a stick-slip friction effect between the Powersil surface and the textile rubbing partner. We assume that, opposite to the graphite coatings, the positive effect of rubbing can be attributed to opening the surface toward the more conductive bulk material.

Finally, Fig. 8 depicts images of the graphite coatings rubbed against themselves. Apparently, instead of removing all non-fixed material, here mostly small parts of graphite flakes are exchanged between both rubbing partners, prohibiting the advantageous “cleaning” of the conductive surface.

4 Conclusion

In a recent project, rubbing tests were performed on three different conductive materials, coated on four textile fabrics each. Tests revealed that measurements gave most reliable results when performed with the coating under examination being placed on conductive Cu-Zn bands in a defined distance under a defined pressure. Both graphite-PUR coatings showed more stable results than the commercially available, flexible Powersil coating. Additionally, our experiments showed that rubbing the conductive coatings against a suitable partner material supports the absolute values as well as the stability of the conductivity.

References

1. Schwarz-Pfeiffer, A., Obermann, M., Weber, M. O., & Ehrmann, A. (2016). Smarten up garments through knitting. In *IOP Conference Series: Materials Science and Engineering* (Vol. 141, p. 012008).
2. Hertleer, C., Grabowska, M., van Langenhove, L., Catrysse, M., Hermans, B., Puers, R., Kalmar, A., van Egmond, H., & Matthys, D. (2004). The use of electroconductive textile material for the development of a smart suit. In *4th AUTEX Conference, Roubaix 2004*.
3. Mühlsteff, J., Such, O., Schmidt, R., Perkuhn, M., Reiter, H., Lauter, J., Thijs, J., Musch, G., & Harris, M. (2004). Wearable approach for continuous ECG and activity patient-monitoring. In *Proceedings of the 26th Annual International IEEE EMBS Conference 2004* (pp. 2184–2187).
4. Coosemans, J., Hermans, B., & Puers, R. (2006). Integrating wireless ECG monitoring in textiles. *Sensors and Actuators A*, 130–131, 48–53.
5. Pacelli, M., Loriga, G., Taccini, N., & Paradiso, R. (2006). Sensing fabrics for monitoring physiological and biomechanical variables: E-textile solutions. In *Proceedings of the 3rd IEEE-EMBS International Summer School Symposium Medical Devices and Biosens* (pp. 1–4).
6. Habetha, J. (2006). The MyHeart project—Fighting cardiovascular diseases by prevention and early diagnosis. In *Proceedings of the 28th Annual International IEEE EMBS Conference 2006* (pp. 6746–6749).
7. Luprano, J., Sola, J., Dasen, S., Koller, J. M., & Chetelat, O. (2006). Combination of body sensor networks and on-body signal processing algorithms: The practical case of MyHeart project. In *Proceedings of the International Workshop Wearable Implantable Body Sensor Networks 2006* (pp. 76–79).
8. Luprano, J. (2006). European projects on smart fabrics, interactive textiles: Sharing opportunities and challenges. In *Workshop Wearable Technology Intelligent Textiles, Helsinki/Finland 2006*.
9. Weber, J. L., & Porotte, F. (2006). Medical remote monitoring with clothes. In *International Workshop on PHealth, Luzern/Switzerland 2006*.
10. Kim, S., Leonhardt, S., Zimmermann, N., Kranen, P., Kensche, D., Müller, E., & Quix, C. (2008). Influence of contact pressure and moisture on the signal quality of a newly developed textile ECG sensors shirt. In *Proceedings of the 5th International Workshop on Wearable and Implantable Body Sensor Networks, Hong Kong/China 2008*.
11. Xu, P. J., Zhang, H., & Tao, X. M. (2008). Textile-structured electrodes for electrocardiogram. *Textile Progress*, 40, 183–213.
12. Silva, M., Catarino, A., Carvalho, H., Rocha, A., Monteiro, J., & Montagna, G. (2009). Textile sensors for ECG and respiratory frequency on swimsuits. In *Intelligent Textiles and Mass customization International Conference, Casablanca/Morocco* (pp. 301–310).
13. Aumann, A., Trummer, S., Brücken, A., Ehrmann, A., & Büsgen, A. (2014). Conceptual design of a sensory shirt for fire-fighters. *Textile Research Journal*, 84, 1661–1665.
14. Tillmanns, A., Heimlich, F., Brücken, A., & Weber, M. O. (2009). Weft knitted spacer fabrics as pressure sensors. *Technical Textiles*, 52, E207.
15. Meyer, J., Arnrich, B., Schumm, J., & Tröster, G. (2010). Design and modeling of a textile pressure sensor for sitting posture classification. *IEEE Sensors Journal*, 10, 1391–1398.
16. Farrington, J., Moore, A. J., Tilbury, N., Church, J., & Biemond, P. D. (1999). Wearable sensor badge and sensor jacket for context awareness. In *The Third International Symposium on Wearable Computers 1999* (pp. 107–113).
17. Catrysse, M., Puers, R., Hertleer, C., van Langenhove, L., van Egmond, H., & Matthys, D. (2004). Towards the integration of textile sensors in a wireless monitoring suit. *Sensors and Actuators A*, 114, 302–311.
18. Zhang, H., Tao, X., Yu, T., & Wang, S. (2006). Conductive knitted fabric as large-strain gauge under high temperature. *Sensors and Actuators, A: Physical*, 126, 129–140.

19. Zieba, J., & Frydrysiak, M. (2006). Textronics—Electrical and electronic textiles. Sensors for breathing frequency measurement. *Fibers and Textiles in Eastern Europe*, 14, 43–48.
20. Ehrmann, A., Heimlich, F., Brücken, A., Weber, M. O., & Haug, R. (2014). Suitability of knitted fabrics as elongation sensors subject to structure, stitch dimension and elongation direction. *Textile Research Journal*, 84, 2006–2012.
21. Atalay, O., & Kennon, W. R. (2014). Knitted strain sensors: Impact of design parameters on sensing properties. *Sensors*, 14, 4712–4730.
22. Atalay, O., Atalay, A., Gafford, J., Wang, H., Wood, R., & Walsh, C. (2017). A highly stretchable capacitive-based strain sensor based on metal deposition and laser rastering. *Advanced Materials Technologies*, 1700081.
23. Kuhn, H. H., & Child, A. D. (1998). Electrically conducting textiles. In T. A. Skotheim, R. L. Elsenbauer, & J. R. Reynolds (Eds.), *Handbook of Conducting Polymers* (pp. 993–1013). New York: Marcel Dekker.
24. Kirstein, T., Cottet, D., Grzyb, J., & Tröster, G. (2002). Textiles for signal transmission in wearables. In *Proceedings of ACM of First Workshop on Electronic Textiles, San Jose/California 2002*.
25. Lesnikowski, J. (2011). Textile transmission lines in the modern textronic clothes. *Fibres and Textiles in Eastern Europe*, 19, 89–93.
26. Locher, I., Klemm, M., Kirstein, T., & Tröster, G. (2006). Design and characterization of purely textile patch antennas. *IEEE Transactions on Advanced Packaging*, 29, 777–788.
27. Shi, M. J., Yang, C., Song, X. F., Liu, J., Zhao, L. P., Zhang, P., et al. (2017). Stretchable wire-shaped supercapacitors with high energy density for size-adjustable wearable electronics. *Chemical Engineering Journal*, 322, 538–545.
28. Babaahmadi, V., Montazer, M., & Gao, W. (2017). Low temperature welding of graphene on PET with silver nanoparticles producing higher durable electro-conductive fabric. *Carbon*, 118, 443–451.
29. Li, X. T., Hua, T., & Xu, B. G. (2017). Electromechanical properties of a yarn strain sensor with graphene-sheath/polyurethane-core. *Carbon*, 118, 686–698.
30. Cao, J. L., & Wang, C. X. (2017). Multifunctional surface modification of silk fabric via graphene oxide repeatedly coating and chemical reduction method. *Applied Surface Science*, 405, 380–388.
31. Choi, C. M., Kwon, S. N., & Na, S. I. (2017). Conductive PEDOT:PSS-coated poly-paraphenylene terephthalamide thread for highly durable electronic textiles. *Journal of Industrial and Engineering Chemistry*, 50, 155–161.
32. Tadesse, M. G., Loghin, C., Chen, Y., Wang, L. C., Catalin, D., & Nierstrasz, V. (2017). Effect of liquid immersion of PEDOT: PSS-coated polyester fabric on surface resistance and wettability. *Smart Materials and Structures*, 26, 065016.
33. Alamer, F. A. (2017). A simple method for fabricating highly electrically conductive cotton fabric without metals or nanoparticles, using PEDOT:PSS. *Journal of Alloys and Compounds*, 702, 266–273.
34. de Oliveira, C. R. S., Batistella, M. A., de Souza, S. M. A. G. U., & de Souza, A. A. U. (2017). Development of flexible sensors using knit fabrics with conductive polyaniline coating and graphite electrodes. *Journal of Applied Polymer Science*, 134, 44785.
35. Topp, K., Haase, H., Degen, C., Illing, G., & Mahltig, B. (2014). Coatings with metallic effect pigments for antimicrobial and conductive coating of textiles with electromagnetic shielding properties. *Journal of Coatings Technology and Research*, 11, 943–957.

Resource-Efficient Production of a Smart Textile UV Sensor Using Photochromic Dyes: Characterization and Optimization

Sina Seipel, Junchun Yu, Aravin P. Periyasamy, Martina Viková, Michal Vik and Vincent A. Nierstrasz

Abstract Niche products like smart textiles and other technical high-end products require resource-efficient processes and small batches contrary to conventional textile processes that require larger batches and are water-, chemical- and energy-intensive. This study focuses on digital inkjet printing and UV light curing as a flexible and resource-efficient and therewith economic production process of a smart textile UV sensor. The UV sensor is based on a UV-curable inkjet ink and a commercial photochromic dye. The inkjet ink is cured via free radical polymerization initiated by a UV-LED lamp. This system contains two photoactive compounds for which UV light both cures and activates the prints. An important challenge is therefore polymer crosslinking of the resin and UV-sensing performance of the photochromic dye. In this paper, we present performance as a function of belt speed and lamp intensity during curing. Via wash tests, we investigate the durability of the photochromic prints. The UV-sensing textile is characterized by colour measurements, differential scanning calorimetry (DSC) and dynamic mechanical analysis (DMA).

S. Seipel (✉) · J. Yu · V. A. Nierstrasz
Faculty of Textiles, Engineering and Business, Department of Textile Technology,
Textile Materials Technology Group, University of Borås, 501 90 Borås, Sweden
e-mail: sina.seipel@hb.se

J. Yu
e-mail: junchun.yu@hb.se

V. A. Nierstrasz
e-mail: vincent.nierstrasz@hb.se

A. P. Periyasamy · M. Viková · M. Vik
Faculty of Textile Engineering, Department of Material Engineering,
Technical University of Liberec, Studentská 2, 461 17 Liberec, Czech Republic
e-mail: aravinprince@gmail.com

M. Viková
e-mail: martina.vikova@tul.cz

M. Vik
e-mail: michal.vik@tul.cz

1 Introduction

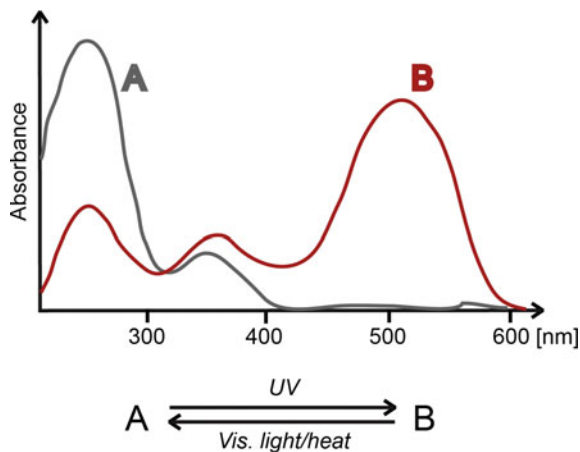
Today, smart textile UV sensors can typically be produced using screen printing [1–3], conventional dyeing [4, 5] and compounding and melt spinning [3, 6]. Successful UV-sensing textiles have been produced using these conventional technologies. However, due to the large production scale of these conventional processes and the fact that photochromic dyes are costly chemicals, this did not lead to an economically industrial-viable process. This paper therefore focuses on the potential of both digital inkjet printing and UV light curing in the production of a smart textile UV sensor using photochromic dyes. UV radiation triggers a reversible colour change in photochromic dyes as a result of a change in absorption spectra as shown in Fig. 1. The colour change is caused by ring-opening isomerization initiated by high photoelectric energy. Depending on the type of photochromic dye, the reverse reaction to the dye's uncoloured state is triggered by visible light (P-type) or by temperature (T-type) [7, 8].

Both digital inkjet printing and UV-curing are resource-efficient technologies, which conserve unnecessary amounts of chemicals and energy, as well as waste that is produced. Furthermore, the combination of these technologies introduces process flexibility in regards to produced run lengths, change in pattern and ink [9–11].

Digital inkjet printing puts high physical requirements on the development of the printing ink to guarantee ink jet ability and storage. Properties like the ink's stability, particle size, surface tension and viscosity have to be compatible with the chosen print head.

In this paper, ink has been developed containing a commercial photochromic dye, mixture of acrylate monomer and oligomer and a UV-LED photo-initiator. The role of UV light as curing initiator and activator of the photochromic colour change and its influence on the performance of the UV-sensing prints is explored. The production of the textile UV sensor using digital inkjet printing and UV-curing

Fig. 1 Scheme of change in absorption spectra between the colourless, ring-closed isomer A and the coloured, ring-opened isomer B initiated by UV light and reversed by either visible light or temperature



is optimized using different UV light intensities; 1, 25 and 80% of the maximum dosage, and two different conveyor belt speeds; 50 and 300 mm/s, during curing. The smart textile UV sensor is characterized and evaluated in terms of colour yield, colouration and decolouration rates and degree of polymer crosslinking of the ink on the textile surface. The mechanical properties of the UV-sensing textile are influenced by the different curing intensities. The change in stiffness of the photochromic prints is determined via DMA measurements.

2 Experimental Part

As described previously [12], a photochromic inkjet ink, which consists of a UV-curable carrier and a commercial photochromic dye Reversacol Ruby Red (Vivimed Labs, UK), was used to produce photochromic prints on plain-woven polyester fabric of 147 g/m² (FOV Fabrics, Sweden). The UV-curable carrier consists of dipropylene glycole diacrylate monomers (DPGDA), amine modified polyetheracrylate oligomers Ebecryl 81 (Allnex, Belgium) and a UV-LED photo-initiator Genocure TPO-L (Rahn AG, Switzerland). A digital inkjet printing system featuring a piezoelectric drop-on-demand print head Sapphire QS-256/10 AAA (Fujifilm Dimatix, USA) was used to produce prints in multi-pass mode with 3, 5 and 10 layers of photochromic ink (Fig. 2a). To cure the prints, a FireJet UV-LED lamp (Phoseon Technology, USA) with emission wavelengths of 380 to 420 nm was used (Fig. 2b).

Ink characterization is done to ensure jetting of the ink formulation and desired drop placement on the textile. Essential ink properties and specifications according to the print head requirements are the fluid's surface tension, viscosity, overall stability of the ink and the particle size. The surface tension of the ink is measured using a tensiometer One Attention (Biolin Scientific, Sweden) as pendant drop. The ink viscosity is measured at a shear rate of 10,000 s⁻¹ at 20 °C using a rheometer

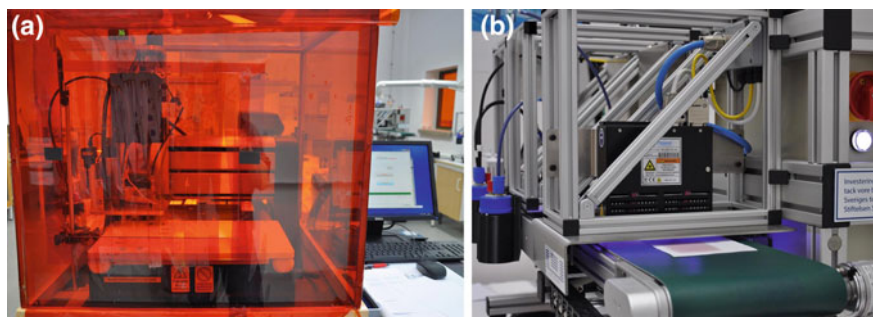


Fig. 2 a Digital inkjet printing system featuring a piezoelectric print head for UV-curable ink and b curing of photochromic ink using a UV-LED lamp with emission wavelengths of 380–420 nm on plain-woven polyester fabric

Physica MCR 500 (Anton Paar, Austria). Particle size assessment is done via filtration and ink stability is tested via storage tests.

For process and sensor optimization, curing parameters were varied by (i) change in transportation speed of the print passing the UV source, i.e. conveyer belt speed, and (ii) intensity of the maximum UV-LED lamp power, i.e. lamp intensity. Conveyer belt speeds varied among 50 or 300 mm/s and were combined with 1, 25 or 80% of the maximum lamp intensity as the production process scheme shows in Fig. 3.

The inkjet-printed and UV-cured photochromic ink on polyester fabric is heated from 25 to 290 °C at a scanning rate of 10 °C per min using a Q1000 DSC (TA Instruments, USA). The shift of the melting peak of polyester is used to analyse the degree of crosslinking of the ink for each curing setting; respective belt speed and lamp intensity. The photochromic print's colour properties were measured using a custom-made LCAM Photochrome spectrophotometer (Technical University of Liberec, Czech Republic), which enables continuous colour measurements upon various cycles of UV activation and reversion [13]. The textile UV sensor's performance is characterized by the achieved colour yield $\Delta K/S$, colouration rate $k_{\text{colouration}}$ and decolouration rate $k_{\text{decolouration}}$ upon isomerization between the uncoloured and coloured state of the photochromic dye. The influence of the different curing settings on the mechanical properties of the photochromic prints on the polyester fabric is measured using a Q800 DMA (TA Instruments, USA). The stiffness of the textile UV sensors is determined via the storage modulus as a function of frequency. The storage modulus was measured at a frequency sweep between 1 and 12 Hz with a preload force of 0.01 N.

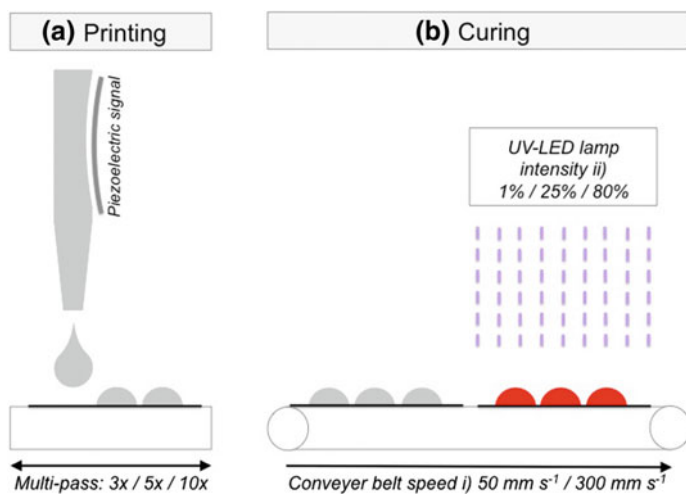


Fig. 3 Production process scheme of **a** printing and **b** curing of photochromic prints on polyester fabric

3 Results and Discussion

The developed UV-curable photochromic ink fulfils the requirements of the Sapphire QS-256/10 AAA print head with the following specifications:

- Surface tension: ca. 35 mN/m
- Viscosity: 10–14 mPa s
- Particle size: <0.1 μm
- Ink stability.

The different curing settings; combinations of 50 mm/s and 300 mm/s belt speeds and 1, 25 and 80% of maximum lamp intensity influence the crosslinking densities of the printed polyester fabrics and alter achievable colouration yields, as well as colouration and decolouration rates. High colour yields $\Delta K/S$ and fast reaction rates $k_{\text{colouration}}$ and $k_{\text{decolouration}}$ of the photochromic dye in the UV-curable matrix between the uncoloured and coloured states are favoured by high belt speed and low lamp intensity.

As shown in Fig. 4a, the storage modulus of the inkjet-printed and UV-cured polyester fabric obtained higher storage modulus than the nonprinted polyester sample. The crosslinking of the UV-curable ink increased the hardness of the overall textile sensor. Furthermore, the sample cured at higher UV dosage, i.e. at 50 mm/s belt speed with 80% lamp intensity, had a higher storage modulus. At a frequency of 12 Hz, the polyester fabric without print has a storage modulus of 300 MPa. A photochromic print cured at low intensity, i.e. conveyor belt speed of 300 mm/s and lamp power of 1%, increases the storage modulus to ca. 1000 MPa. For prints, which undergo strong curing, i.e. 50 mm/s belt speed and 80% lamp intensity, the storage modulus reaches 1400 MPa. This suggests that there are more

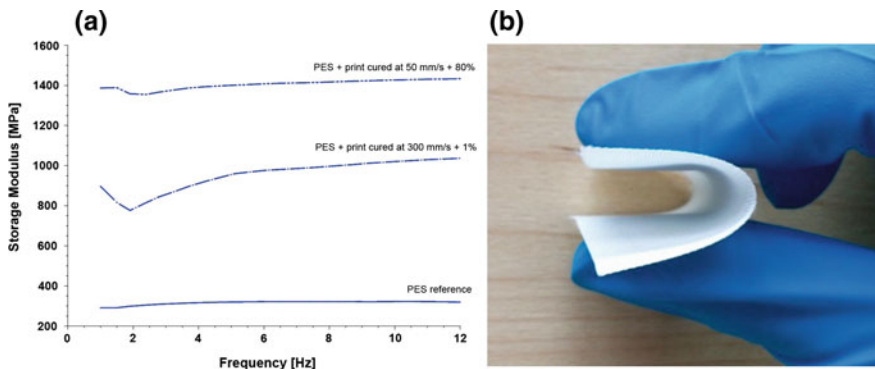


Fig. 4 **a** Increased storage modulus of photochromic prints on polyester in comparison to the polyester fabric reference. Print cured at highest intensity, i.e. belt speed of 50 mm/s and lamp intensity of 80% has highest stiffness throughout a frequency sweep of 1–12 Hz. **b** Bendability demonstrates suitable flexibility of the textile UV sensor cured at 50 mm/s belt speed with 80% lamp intensity in use

crosslinks of the sample cured under higher dosage of UV exposure. The same trend is confirmed by DSC measurements, which present an increase in melting peak as a function of curing intensity. However, the textile sensor is still bendable and rather flexible for the sample cured at 50 mm/s belt speed with 80% lamp intensity (Fig. 4b).

4 Challenges and Conclusion

This paper demonstrates the potential of combined digital inkjet printing and UV-LED curing in a resource- and cost-efficient textile production process. We conclude that changes in UV light intensity and belt speed during the curing process achieve distinct results in terms of colouration yields and kinetics of the colouration and decolouration reaction of the photochromic dye. These changes also affect the degree of polymer crosslinking, which influences the durability of the smart textile UV sensor in use. The degree of polymer crosslinking also influences the stiffness of the UV-sensing textiles. The stronger the curing intensity, the higher is the storage modulus of the printed fabrics as a result of higher degree of polymer crosslinking. However, in use, the flexibility of the photochromic prints, irrespective of curing intensity, is suitable for wearable applications, such as smart textile sensors.

In addition, we explore the effect of washing on the colour performance and switching reactions of the textile UV sensor. High belt speed and lower UV-LED light intensity enables faster colour changing and higher colour yield. The same effect is seen after washing despite a lower degree of polymer crosslinking.

Acknowledgements The authors gratefully acknowledge the support of Borås Stad, Sparbankstifelsen Sjuhärad, TEKO (The Swedish Textile and Clothing Industries Association) and SST (Stiftelsen Svensk Textilforskning) for enabling this research.

References

1. Little, A. F., & Christie, R. M. (2010). Textile applications of photochromic dyes. Part 2: Factors affecting the photocolouration of textiles screen-printed with commercial photochromic dyes. *Coloration Technology*, 126, 164–170.
2. Feczko, T., Samu, K., Wenzel, K., et al. (2013). Textiles screen-printed with photochromic ethyl cellulose–spirooxazine composite nanoparticles. *Coloration Technology*, 129, 18–23.
3. Víková, M. (2011). *Photochromic Textiles*. Edinburgh: Heriot-Watt University.
4. Billah, S. M. R., Christie, R. M., & Shamey, R. (2012). Direct coloration of textiles with photochromic dyes. Part 3: dyeing of wool with photochromic acid dyes. *Coloration Technology*, 128, 488–492.
5. Aldib, M., & Christie, R. M. (2011). Textile applications of photochromic dyes. Part 4: application of commercial photochromic dyes as disperse dyes to polyester by exhaust dyeing. *Coloration Technology*, 127, 282–287.

6. Viková, M., Periyasamy, A. P., Vik, M., et al. (2016). Effect of drawing ratio on difference in optical density and mechanical properties of mass colored photochromic polypropylene filaments. *Journal of The Textile Institute*, 1, 1–6.
7. Bouas-Laurent, H., & Dürr, H. (2001). Organic photochromism (IUPAC Technical Report). *Pure and Applied Chemistry*, 73, 639.
8. Bamfield, P., & Hutchings, M. G. (2010). *Chromic phenomena: Technological applications of colour chemistry*. Place: Royal Society of Chemistry.
9. Hudd, A. (2011). Inkjet printing technologies. In S. Magdassi (Ed.), *The chemistry of inkjet inks* (pp. 3–18). Singapore: World Scientific.
10. Singh, M., Haverinen, H. M., Dhagat, P., et al. (2010). Inkjet Printing—Process and Its Applications. *Advanced Materials*, 22, 673–685.
11. Lin, A. H. L. (2004). Challenges of UV curable ink-jet printing inks—A formulator’s perspective. *Pigment & Resin Technology*, 33, 280–286.
12. Seipel, S., Yu, J., Nierstrasz, V., et al. (2017). Characterization and optimization of an inkjet-printed smart textile UV-sensor cured with UV-LED light. In *AUTEX World Textile Conference*.
13. Viková, M., Christie, R. M., & Vik, M. (2014). A unique device for measurement of photochromic textiles. *Research Journal of Textile and Apparel*, 18, 6–14.

Direct Printing of Light-Emitting Devices on Textile Substrates

Inge Verboven and Wim Deferme

Abstract Smart textiles are a rapidly expanding field in the world of textiles, announcing a new and intriguing era. Different functionalities can be added to the textile to make the textile smart and intelligent. One of these functionalities is the addition of light-emitting layers or devices that can be incorporated into the textiles. These light-emitting textiles find a broad application in the field of interior and exterior design and wearable applications. Depending on the application, two light-emitting devices, the alternating current powder electroluminescent (ACPEL) device and the organic light emitting diode (OLED), both consisting out of a stack of thin layers, can be directly printed on top of the textile substrates. With its relatively high AC voltage of 50–200 V, the ACPEL device is more suited for interior and exterior applications while the OLED with a low DC voltage of 3–5 V is a perfect candidate for wearable applications. To maintain typical textile properties such as flexibility, breathability and drapability, different smart designs of the ACPEL devices are suggested, screen printed and analysed. More challenging is to apply the OLEDs on textile substrates. The very thin nanometre range layers make a planarizing layer to smoothen the textile surface indispensable. Different techniques such as spin coating, ultrasonic spray coating, inkjet printing and thermal evaporation are used to apply the complete OLED stack.

1 Introduction

Textiles with an enhanced functionality by integrating electronics, also named smart textiles, gained a lot of interest and significance during the last years. This emerging technology is pushing the boundaries of sciences forward and finds its

I. Verboven · W. Deferme (✉)
Hasselt University, Institute for Materials Research (IMO-IMOMECE), Wetenschapspark 1,
3590 Diepenbeek, Belgium
e-mail: wim.deferme@uhasselt.be

I. Verboven · W. Deferme
Imec vzw, Division IMOMECE, Wetenschapspark 1, 3590 Diepenbeek, Belgium

application in numerous fields. One approach of functionalizing textiles is to incorporate light-emitting layers or devices. These luminous textiles show promise in the field of interior and exterior design and wearable applications such as protective clothing and even healthcare in the form of light therapy.

For this purpose, two light-emitting devices, the alternating current powder electroluminescent (ACPEL) device and the organic light-emitting diode (OLED), are selected, manufactured and investigated. Both devices consist of thin flexible layers, making it possible to be coated or deposited directly onto the textile surface and therefore maintaining typical textile properties such as flexibility, drapability and breathability. ACPEL devices operate with an AC voltage of 50–200 V, making them too hazardous for wearable applications, but highly suited for interior and exterior applications such as flags, banners and wallpaper. Layer thicknesses are in the micrometre range and applied using the screen printing technique followed by an annealing step. OLEDs, on the other hand, only need a DC voltage of 3–5 V to emit light and are therefore a perfect candidate for lighting wearables. They have much thinner nanometre layer thicknesses that are deposited using vacuum deposition techniques or solution processing techniques such as spin coating, ultrasonic spray coating and inkjet printing. When exposed to oxygen and water vapour, OLEDs degrade much faster than the ACPEL devices and are therefore in need of a high-barrier encapsulation.

Years of research have gone into the development and insight in the working principles of the light-emitting devices. It all started in 1907 when the phenomenon electroluminescence was observed for the first time by Henry Round when he let a current pass through a silicon carbide detector [1]. In 1936, George Destriau was the first to name the phenomenon during his experiments with powder phosphors suspended in oil [2]. By exposing phosphor materials to a high electric field, non-thermal generation of light, or electroluminescence (EL) occurs. The introduction of transparent conducting electrodes based on tin oxide (SnO_2) in the late 1940s gave a boost to the research of scientists and raised the interest of the industry [3]. This led to the development of the first practical EL device in 1952. Engineers at Sylvania Electrical Products Inc. produced and presented an inorganic powder EL panel [4]. During the 1950s, research into the EL device and electroluminescence was conducted worldwide. The new light source was very popular due to its characteristics such as a low power dissipation, a multicolour emission, its flatness and the lack of catastrophic failure. The first developed devices consisted out of a doped ZnS powder suspended in a dielectric and sandwiched between two (transparent) electrodes and the structure of the devices nowadays has not changed much since then. In the decades that followed, the devices lost interest due to their low brightness, lifetime and efficiency. However, in the 1980s, the research was revived to tackle these shortcomings and the devices were commercialized to be used in advertisement and displays [1, 2, 4].

In 1987, the first small molecules OLED (SM-OLED), presented by Tang and Van Slyke, announced the upcoming of organic electroluminescence [5]. The most basic OLED stack consists out of two electrodes between an emissive layer.

Small molecules, however, are usually deposited using expensive and non-roll-to-roll compatible vacuum evaporating techniques, but their material properties can be adapted relatively easy. Polymers, on the other hand, can be applied using low-cost solution processing techniques and possess a better chemical stability. Therefore, in 1990, Burroughs and his group from the University of Cambridge manufactured the first polymer OLED (P-OLED) with a conjugated polymer poly(phenylenevinylene) (PPV) as emissive layer [6]. Gustafsson et al. revealed the first flexible OLED on polyethylene terephthalate (PET) in 1992 [7].

The past years, numerous attempts into incorporating light-emitting devices on textile substrates have been made. In case of the ACPEL device, these attempts were very successful. de Vos et al. presented a smart fabric EL lamp directly screen printed onto woven fabric [8]. Subsequently, they obtained similar performances with flexible ACPEL lamps deposited by using a novel dispenser printing technique. ACPEL devices were fabricated onto PET mesh fabrics by Bin Hu et al. [9]. As a transparent electrode, the conductive polymer PEDOT:PSS was inkjet printed onto the textile. To complete the stack, a phosphor powder was mixed with an epoxy resin and dispensed onto an aluminium (Al) foil. All these devices, however, have a light-emitting surface that completely covers the textile, maintaining only the flexible properties of the substrate. To also preserve other typical textile properties such as drapability and breathability, this work addresses diverse smart ACPEL designs that are screen printed and characterized on their crease recovery, air permeability and light output.

Incorporating OLEDs into textile substrates is, however, not so straightforward due to their very thin nanometre layer thicknesses, often causing short circuits. Mostly the devices are deposited onto other non-textile substrates and subsequently attached to the textile surface. At the Fraunhofer Insitute in Germany, a research group integrated miniaturized OLEDs on plastic foils onto textiles by using conductive adhesives (TexOLED project) [10]. In other research, the same group developed a fibre-based OLED, similar to other research groups [11–13]. The light output of those fibre OLEDs is nevertheless very limited due to the 360° scattering of light. Woohyun Kim et al. presented an OLED on soft fabrics for wearable display purposes [14]. They used a lamination and spin coating process to apply polyurethane (PU) and poly(vinyl alcohol) (PVA) layers onto the fabric to planarize the relatively rough surface. In this work, OLEDs are directly deposited onto the textile substrates to preserve the previously named properties of the textiles. It is more challenging to apply the OLEDs directly onto the textiles as they are in need of a high barrier encapsulation and planarizing layers to overcome the roughness of the textiles.

2 Working Mechanism and Device Manufacturing

2.1 ACPEL Device

2.1.1 Working Mechanism

Figure 1 shows the typical layer stack of an ACPEL device in its standard and reversed structure. The following layers can be distinguished: a substrate (a), a transparent electrode (b), a phosphor layer (c), a dielectric layer (d) and another electrode (e). The phosphor layer consists of doped zinc sulphide (ZnS) powders with a particle size of 5–20 μm . The total thickness of the device is around 40 μm .

Extensive research into the working mechanism has been conducted, leading to several theories, but the bipolar field-emission model or Fisher model has been pushed forward as the most generally accepted theory [15–17].

When he applied a certain threshold voltage, Fisher observed a line-shaped light emission that looked like two comets fleeing each other, covering almost the entire diameter of a phosphor particle (Fig. 2). To explain this occurrence, he started by looking at the manufacturing process of the ZnS powder particles. These are produced by a high temperature (1100–1200 $^{\circ}\text{C}$) firing process. During the cooling down, a phase transition of the hexagonal phase (wurtzite) to the cubic phase (zinc blende) takes place and due to their similar lattice energies, many imperfections and screw dislocations are formed. Excessive copper (Cu), that is added as a dopant before the firing process, participates on those defects and forms high conductive copper sulphide (Cu_{2-x}S) needles.

Within the conductive needles, electrons can freely move around, which is not the case for the semiconductor ZnS where a bandgap has to be overcome (Fig. 3).

When an electric field is applied, the conductive needles, with a component parallel to that field, relax so they remain at equal potential. This results in a field intensification from the centre to the tips of the needle that causes an alteration of

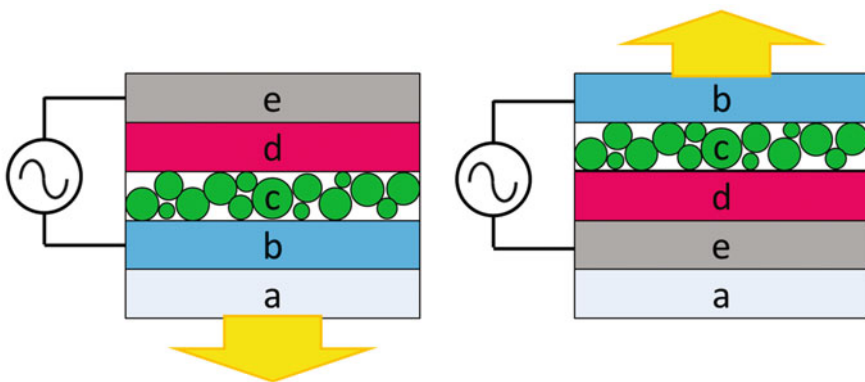


Fig. 1 Standard and reversed structure ACPEL device

Fig. 2 Observed EL lines [18]

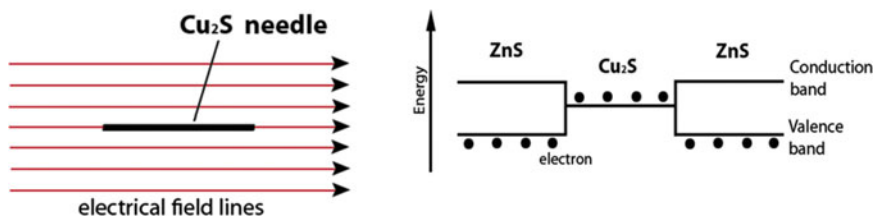
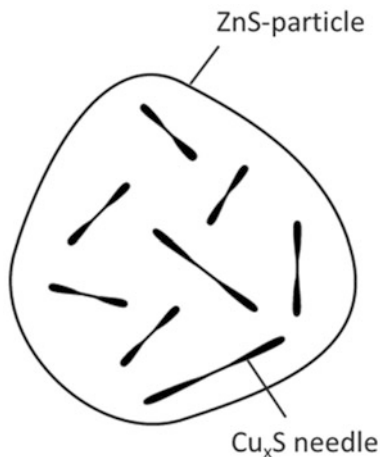


Fig. 3 Electric field lines and band model before applying an external electric field [18]

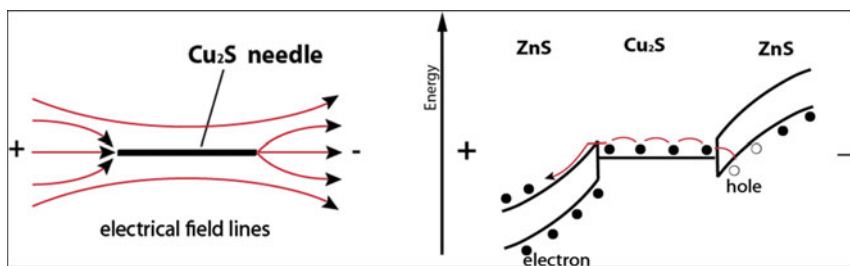


Fig. 4 Electric field lines and band model after applying an external electric field [18]

the energy bands and makes tunnelling of holes and electrons from the needle to the ZnS possible (Fig. 4).

The injected electrons possess a relatively high mobility compared to the injected holes. The latter is quickly captured by deeper lying levels and form a positive space charge around the needle. The holes trapped in front of the positive end of the needle create a polarization field that prevents further hole emission and electron emission

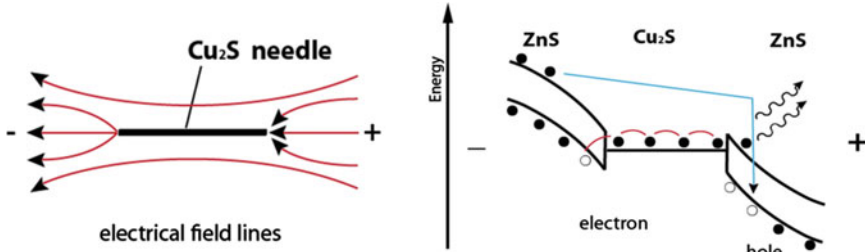


Fig. 5 Electric field lines and band model at field reversal [18]

from the negative end of the needle. When the electric field is reversed, injected electrons from the negative end of the needle recombine with the trapped holes at the positive end of the needle and recombination radiation or primary light emission takes place (Fig. 5). A secondary light emission may occur due to electrons, returning from the opposite end, recombining with the trapped holes.

2.1.2 Device Manufacturing

The layers of the ACPEL devices are applied using the screen printing technique [19]. This technique deploys a screen or a woven mesh of synthetic fabric or metal wire to transfer a paste or ink onto a substrate. The substrate is positioned on the substrate holder and the screen is placed directly above it. A paste or ink, which has been deposited onto the screen, is pushed through the open areas of the screen by a moving fill blade or squeegee. When the blade reverses, it removes the excessive paste or ink. Screen printing is a roll-to-roll compatible and low-cost technique.

The complete layer stack (Fig. 6) is screen printed on a polyester fabric with a roughness lower than $1 \mu\text{m}$. After the deposition of every layer, a thermal annealing step is required at $130 \text{ }^\circ\text{C}$ for 10 min to obtain uniform layers of $10 \mu\text{m}$ thickness. First, an Ag bottom electrode (Gwent) is applied on top of the substrate. This layer is also used to planarize the roughness of the substrate. Subsequently, a barium titanate (BaTiO_3) dielectric layer (Gwent), a light-emitting Cu-doped ZnS layer (Gwent) and a transparent PEDOT: PSS EL-P 3145 top electrode (Orgacon) are screen printed. Light is generated by applying an AC voltage of 80 V at a frequency of 400 Hz.

2.2 OLED

2.2.1 Working Mechanism

OLEDs are semiconductor devices which, in their most basic form, consist of an organic emissive layer (EL) sandwiched between two inorganic (transparent)

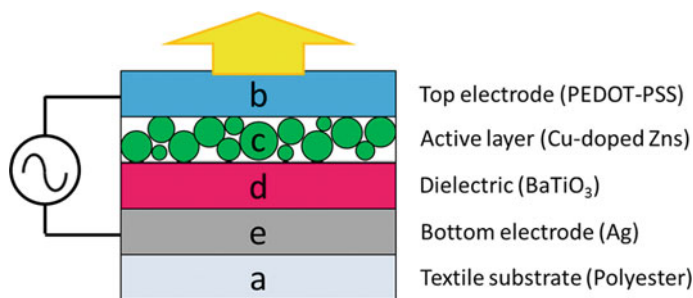


Fig. 6 Screen-printed stack ACPEL device

electrodes (Fig. 7). To increase the performance of an OLED, several layers, electron and hole injection, transport and blocking layers (EIL, ETL, EBL, HIL, HTL and HBL), can be added to the OLED stack. The latter has a total thickness around 1 μm with layers thicknesses varying between 1 and 200 nm. By applying a DC voltage of only 3 to 5 V, the OLED will emit light through the bottom (BEOLED) or the top (TEOLED).

Research into the working mechanisms of an OLED has been thoroughly conducted and numerous papers and other publications give a detailed description of the mechanism [20–22]. For an OLED to emit light, following processes take place sequentially: charge injections at the anode and cathode, charge transportation through the layers, recombination and exciton formation in the emissive layer and the emission of light (Fig. 8).

An important property of the electrodes is the minimum energy required to extract an electron, also called the work function. At the cathode, it is easy to remove an electron as it has a low work function, and at the anode, the opposite is true, hence it has a high work function. For the OLED to work properly, this built-in potential is absolutely critical.

Charge injection into the Fermi level of the electrodes takes place when a DC voltage is applied across the OLED. Electrons are injected into the cathode and holes into the anode. When a certain threshold voltage is reached, the electrons translocate into the lowest unoccupied molecular orbital (LUMO) and the holes into the highest occupied molecular orbital (HOMO) of the adjacent layer. The charges are then transported through the LUMO and HOMO level of the other layers towards the emissive layer. During their travel, they have to overcome energy barriers at the layers interfaces, increasing the driving voltage. According to the Langevin theory, electrons and holes will recombine and form excitons when the distance between them is so small that their mutual binding Coulomb energy is greater than the thermal energy. These excitons return to their ground state by releasing energy in the form of photons, also called recombination radiation.

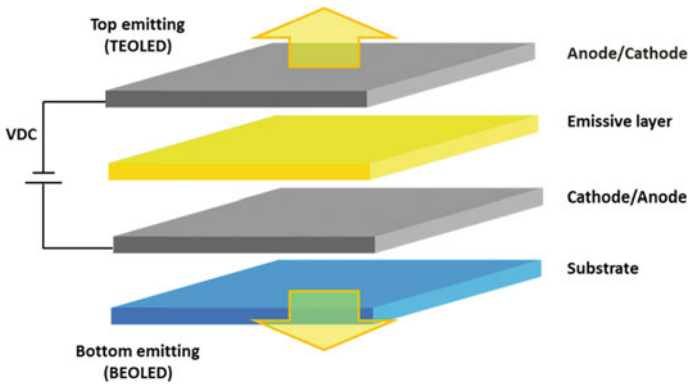


Fig. 7 Basic OLED stack

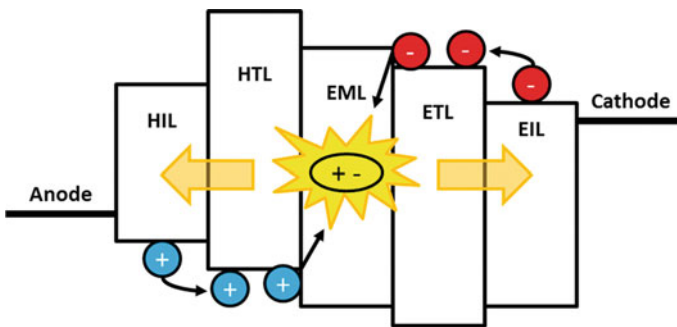


Fig. 8 Working mechanism OLED

2.3 Device Manufacturing

The TEOLEDs (Fig. 9) are manufactured on glass, PET and textile substrates by applying various deposition techniques. The textile substrates are fairly rough compared to the nanometre layers of the OLED and to avoid short circuits a planarizing layer is added. For this purpose, polyurethane (PU) or acrylate is laminated onto the textile substrate. To prevent the OLEDs from fast degradation, a high barrier encapsulation of alternating organic and inorganic layers is applied using plasma techniques [23]. On top of the barrier layer, a 200 nm Ag anode is thermally evaporated at a base pressure of 10^{-7} mbar. Thermal evaporation is a vacuum deposition technique where a current is sent through intermetallic boats containing the deposition material [24, 25]. Due to the current, the boats are heated and the deposition material is melted and evaporated onto the above lying samples. Subsequently, a 35 nm hole injection/transport layer of the conductive polymer PEDOT:PSS Clevios™ P AI 4083 (Heraeus) is spin coated under a fume hood. Spin coating is a lab-scaled thin film deposition technique [26]. The deposition

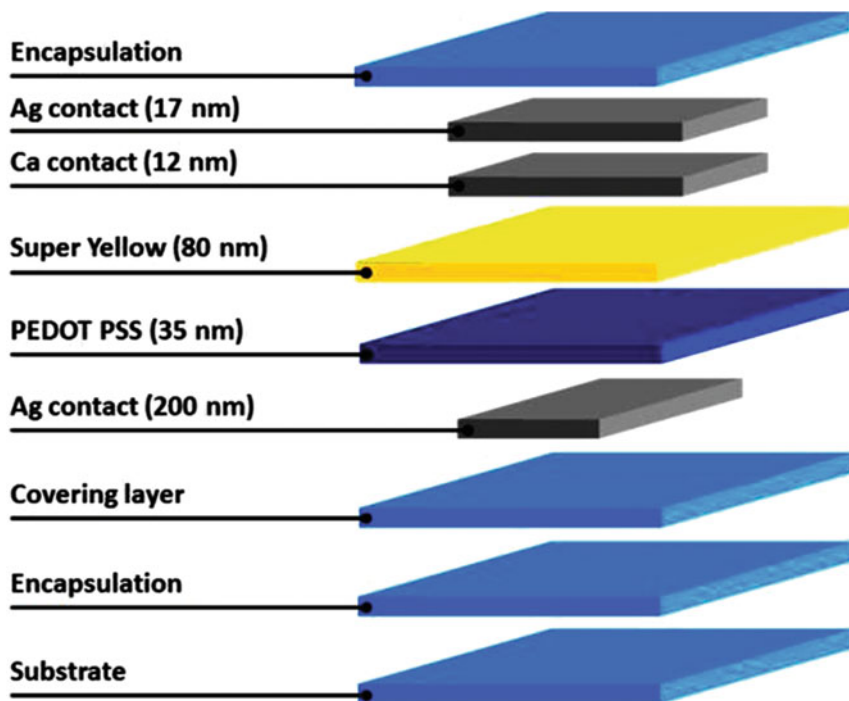


Fig. 9 TEOLED stack

material is dispensed in the centre of the sample which is rotated at a high speed and acceleration and a thin uniform film is obtained. An active emissive layer of 80 nm is deposited using the same spin coating technique, but in an inert atmosphere glovebox system (O_2/H_2O ppm < 0.1). This layer contains the PPV-polymer Super Yellow PDY-132 (Merck) which is dissolved in chlorobenzene with a mass concentration of 5 mg/ml and stirred overnight at 50 °C. As a transparent top cathode Ca/Ag of, respectively, 12 and 17 nm is thermally evaporated at a base pressure of 10^{-7} mbar. To finish the OLED stack, another barrier layer is added using plasma techniques.

3 Results and Discussion

3.1 ACPEL Device

Smart Designs

Most ACPEL devices have a light-emitting area that (almost) completely covers the entire surface of the substrate. If such a device is manufactured on textile substrates,

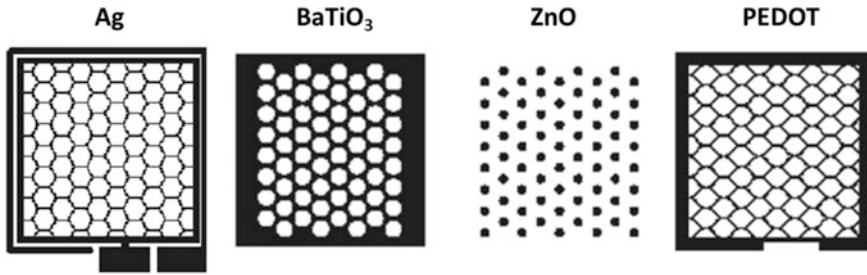


Fig. 10 Screen design of hexagonal structure

it seriously limits the air permeability and the drapability of the used fabric. To maintain these typical textiles properties, several smart designs based on a hexagonal cell structure of the ACPEL device were screen printed. An example of such a screen design can be seen in Fig. 10.

Both the electrodes, the Ag bottom layer and the transparent PEDOT:PSS layer, have a honeycomb structure with a line width of 0.5 mm. The dielectric and phosphor layer consist only of dots on the cross points of that structure. The amount of dots is alternated between three dots per hexagon, referred to as the single pixel design, and six dots per hexagon or the dual pixel design. The diameter of the dots is varied between 1.5 and 2.5 mm (Fig. 11).

Scanning electron microscopy (SEM) is a technique to obtain magnified and detailed images of the different designs of the ACPEL devices. This technique scans the surface of a sample with a focused beam of electrons. Information on the sample's surface morphology and composition is obtained due to the interaction of the electrons and the atoms of the sample. Figure 12 demonstrates the light-emitting ACPEL devices with the different designs and the corresponding SEM images.

Air Permeability and Crease Recovery Angle

The air permeability indicates how easily air can pass through the ACPEL devices. For this purpose, a FX3300 LabAir IV Air Permeability tester is used [27]. By means of a vacuum pump, the device sends air through the sample that is clamped in a circular sample holder. When stable conditions are reached, the air flow is measured multiple times and on different spots of the sample to obtain accurate results. Alternating the amount of dots and their size obviously changes the air permeability and crease recovery angle of the ACPEL devices. These properties are measured for each design and compared with each other to determine the most promising and optimal design.

Figure 13 shows that when the diameter of the dots is decreased, more air can pass through, hence a higher air permeability is measured. It can be noticed that the air permeability of the single pixel design does not differ a lot when the diameter of the dots is alternated. This is, however, the case for the dual pixel design where the air permeability of the dots with a diameter of 2.5 mm is almost a third of that of the

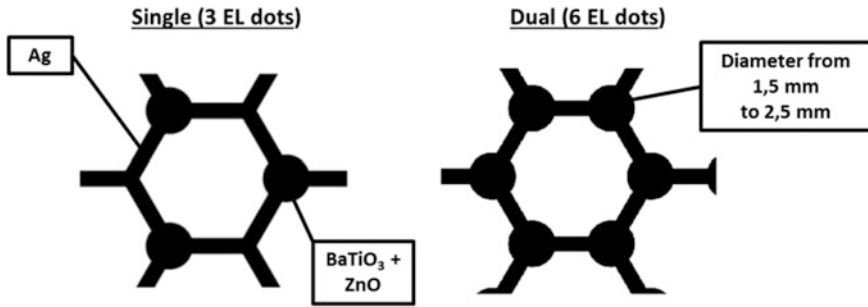


Fig. 11 Single and dual pixel design

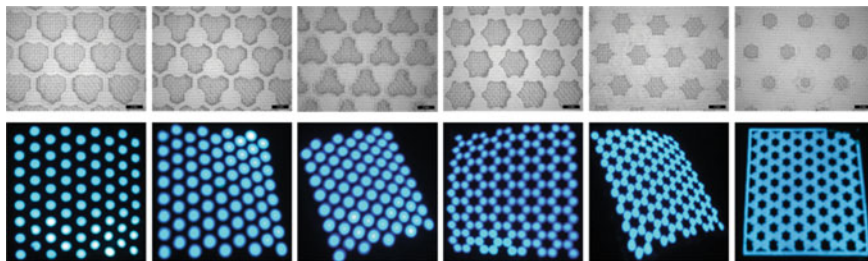
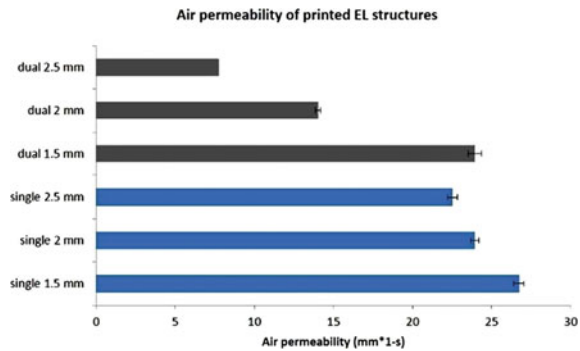


Fig. 12 Light-emitting ACPEL devices and corresponding SEM images

Fig. 13 Air permeability of ACPEL devices



dots with a diameter of 1.5 mm. Furthermore, the graph also indicates that the air permeability is comparable for the dual pixel design with 1.5 mm diameter dots and the single pixel design with 2 mm diameter dots.

The crease recovery shows the ability of the ACPEL devices to return to their original state after creasing. The textile is folded for 180° by applying a weight of 1 kg on top and kept folded for 5 min and for 30 min. When the weight is removed, the textile tries to return to its initial state and the crease recovery angle or the angle of the textile's return is measured. It is to be expected that the more the surface of

Fig. 14 Crease recovery angle of ACEPEL devices

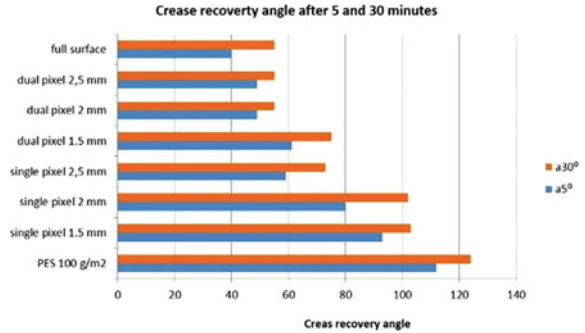
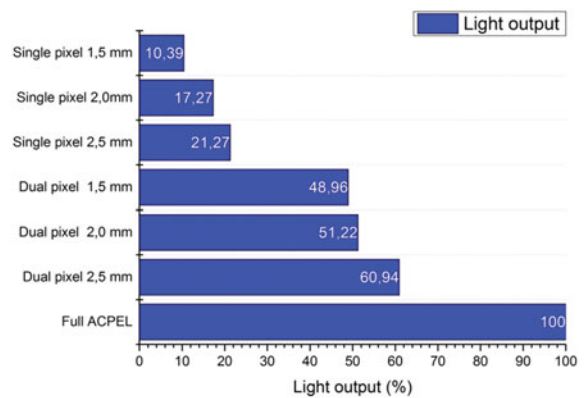


Fig. 15 Light output ACEPEL devices



the fabric is covered by a coating, the less the crease recovery angle will be. This is confirmed by the measurements and is indicated in Fig. 14. A fabric with a fully covered surface has the lowest crease recovery angle and a non-coated fabric has the highest. The samples with the dual pixel design with diameter 2.5 and 2 mm do not demonstrate a better recovery after bending. Better results are noted for the fabrics with a single pixel design.

Light Measurements

The light output performances of the ACEPEL devices are measured using a Keithley 2401 source metre to obtain the current and voltage characteristics and using an absolute calibrated integrating sphere spectrometer from Avantes to acquire the irradiance for every wavelength. The electrical power was obtained by calculating the integral of the irradiance–wavelength graph. The light output was acquired by comparing the electrical power to the coated area. Figure 15 shows the results of the light output measurements and calculations. In this graph, the designs are compared to a fully covered ACEPEL device. The dual pixel designs demonstrate half of the light output of that of the fully covered ACEPEL device. The light output of the single pixel designs is even less than half of that.

Optimal Design

Based on the application, different designs can be optimal. If it is important that the textile substrate preserves as much as possible its textile properties such as flexibility, drapability and air permeability and the light output is less important, then the single pixel design with a diameter of 2 mm is the best option. If, however, the light output is more essential, the dual pixel design with a diameter of 1.5 mm is optimal.

3.2 OLED

Challenges and Advantages

More challenging than the screen-printed ACPEL devices is the application of OLEDs on textile substrates. The roughness profile of the polyester sample (Fig. 16) measured with a Dektak profilometer indicates that the roughness can be found in the micrometre range, while the total thickness of the OLED stack amounts to only 0.5 μm and therefore the required surface roughness has to be below 5 nm.

So a planarizing or smoothing layer is an absolute necessity in order to prevent short circuits for the OLED. Due to their fast degradation when exposed to oxygen and water vapour, a high barrier encapsulation is also necessary, but to find and apply such a layer is not so straight forward. The requirements for an OLED encapsulation are very high, water vapour transmission rates (WVTR) and oxygen transmission rates (OTR) must be lower than respectively 10^{-6} g m⁻² per day and 10^{-3} cm³ m⁻² per day [28]. Another challenge lies in the applied deposition techniques, which can be quite expensive and are not necessarily roll-to-roll compatible. Promising is, however, the rise of printing techniques, which are far less expensive and roll-to-roll compatible.

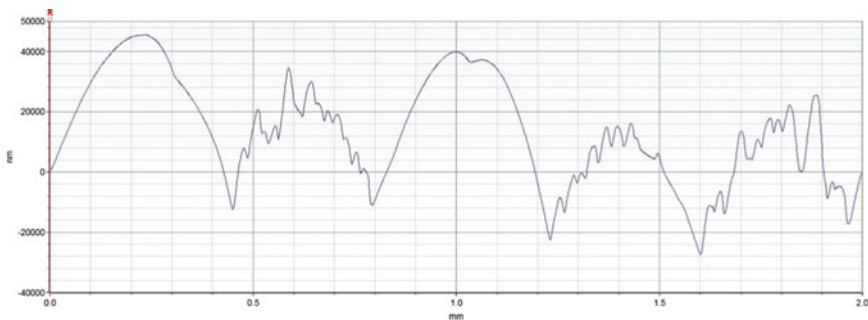


Fig. 16 Roughness profile polyester

Device Built-up

As means of experiment, the OLED stack is first completed on glass and PET substrates, before tackling textile substrates.

To planarize or smoothen the surface of the textile substrate, printable PU or acrylate is laminated onto that surface (Fig. 17).

To protect the OLEDs from degradation under influence of ambient conditions, a high barrier encapsulation system is applied using plasma techniques as shown in Fig. 18 [29]. The encapsulation consists of an oxygen-free silicon nitride (SiN) layer followed by an alternation between high barrier inorganic materials, for example, silicon oxide (SiO_x), and softer low barrier organic materials. The first layer protects the OLED against the deposition of the latter alternating barrier system. The alternation of organic and inorganic material stops the formation of defects leading to an increase in the diffusion length and good barrier properties.

After the encapsulation, a bottom Ag electrode of 200 nm is thermally evaporated and both the 35 nm PEDOT:PSS HIL/HTL and the 80 nm SY EL are spin coated, the first under a fume hood, the second in an inert glovebox system. The applied deposition techniques are not roll-to-roll compatible; furthermore, thermal evaporation is very expensive. As alternatives for both techniques, the materials can be applied using inkjet printing or ultrasonic spray coating. The inkjet printing technique is well known for its multiple uses in households and industries. This contactless printing technique recreates a digital image on a substrate by ejecting ink droplets. Ultrasonic spray coating is a large-area deposition technique where a continuous flow of micro-sized spherical droplets is created by atomizing the ink at the nozzle of the spray head. The ultrasonic spray coating process does not affect the polymer side chain nor the backbone of the PPV polymer, as stated in next work [30].

The top electrode has to be transparent since the light has to pass through the top of the OLED. In recent years, extensive research has been conducted on innovative materials for transparent electrodes [31]. Here, two different approaches to acquire a transparent top cathode were followed, inkjet-printed metal grids and thermally evaporated very thin metal layers as shown in Fig. 19 [32]. Ag grids with hexagonal and triangular structures with a thickness of 150–250 nm were inkjet printed

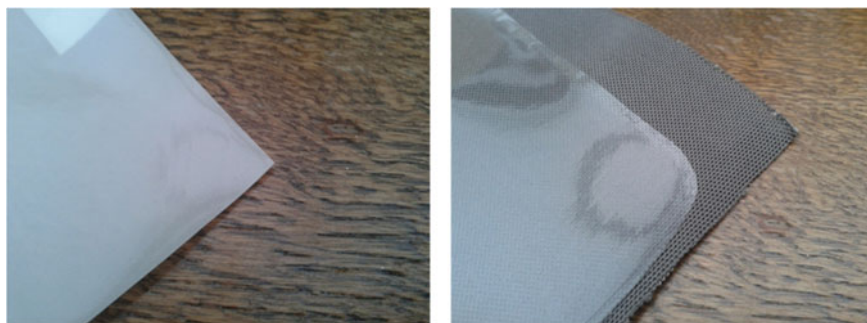


Fig. 17 Printable PU and acrylate laminated on textile substrates

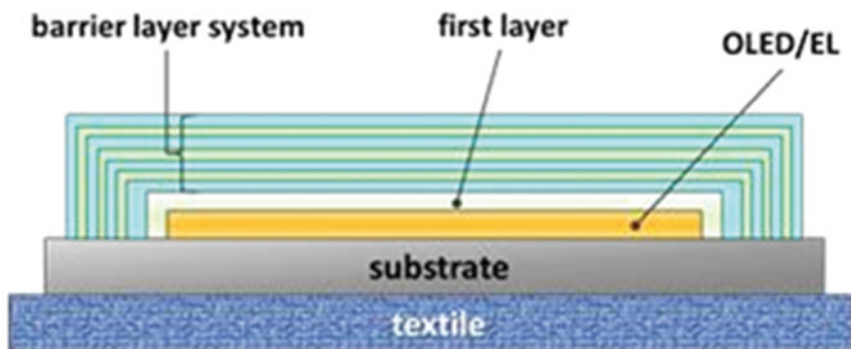


Fig. 18 High barrier encapsulation system

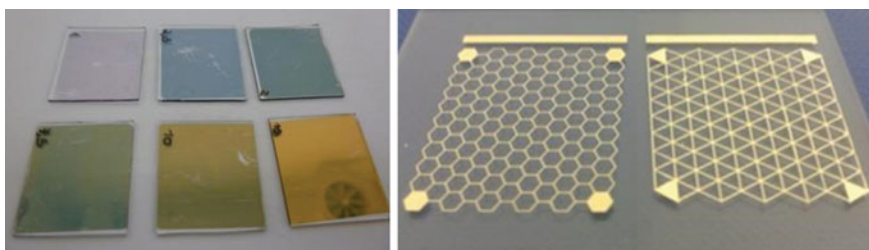


Fig. 19 Thermally evaporated Au layers and inkjet-printed structures on glass substrates

on glass substrates and sintered at 200 °C. To obtain a very thin and transparent cathode, gold (Au) layers were thermally evaporated onto glass samples with a varying thickness of 1–15 nm.

Both the grids and the thin layers were examined for their sheet resistance and their transparency. Figure 20 demonstrates the transparency of both the grids and the thin layers. It is clearly shown that the Ag grids show a much higher transparency (70–90%) than the Au layers (25–70%). The hexagonal structured grids have the highest transparency.

Table 1 Sheet resistance of Au layers and Ag grids lists the results from the sheet resistance measured with the Van der Pauw set up [33]. The grids showed a lower sheet resistance of 0.82–2.7 Ω/\square than the thin metal layers which obtained 3.2–123.7 Ω/\square .

If one only looks at these two characteristics, the Ag grids are clearly pushed forward as the winner. There is, however, a deal breaker, the used commercially available ink has to be sintered at 200 °C, a temperature that will terminate the underlying layers. A solution for this could be the usage of new commercially available Ag inks, based on precursors instead of Ag nanoparticles, which can be sintered at a much lower temperature [33].

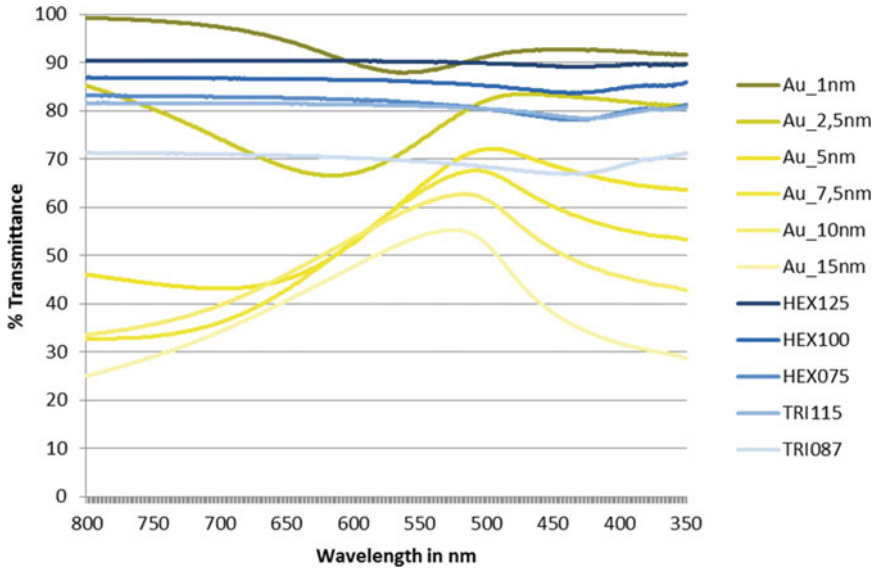


Fig. 20 Transmittance of Au layers and Ag grids

Table 1 Sheet resistance of Au layers and Ag grids

	Rs (Ω/\square)
HEX125	2.7
HEX100	1.5
HEX075	1.5
TRI115	1.2
TRI087	0.82
Au 1 nm	>20 M
Au 2.5 nm	>20 M
Au 5 nm	>20 M
Au 7.5 nm	123.7
Au 10 nm	11.5
Au 15 nm	3.2

To obtain the necessary built-in potential between the two electrodes, a low work function material, Ca for example, has to be inserted before the cathode. To apply this layer, mostly vacuum deposition techniques are used. That is the reason that in this work, a Ca/Ag electrode of respectively 12 and 17 nm was thermally evaporated on top of the emissive layer. The stack was completed by adding another high barrier encapsulation.

Completed Devices

As stated above, the OLED stack was completed on glass, textile and PET samples.

The degradation, and thus reduced light output in function of the time a manufactured OLED on glass, taken out of the glovebox system after encapsulation, is shown in Fig. 21: Time course of OLED on glass. After deposition of the layer and before encapsulation, the sample shows already some visual defects and pinholes. Subsequently, the sample is encapsulated using plasma techniques and placed outside the glovebox system in ambient conditions. A similar light output is observed right after the sample was brought in ambient conditions. After 19 h, more than half of the light output was lost and eventually after 43 h, only some light-emitting dots could be distinguished. The encapsulation shows a lot of promise, there is, however, plenty of room for improvement.

The PET sample shows a lot of promise as can be seen in Fig. 22. OLED on PET and textile substrates. It has a very nice uniform light output and can be bent in both directions without any loss of light performance. No cracks or other defects can be distinguished even after creasing the sample. Unfortunately, the textile sample is not so successful since only a few dots lit up. This is possibly caused by the effect of chlorobenzene, the solvent used for the emissive layer, on the planarizing layer. This somewhat harmful solvent introduces a lot of defects throughout the OLED layer making it impossible to have a uniform light output.

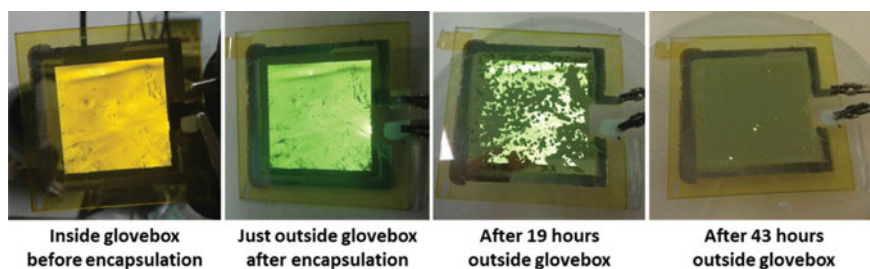


Fig. 21 Time course of OLED on glass

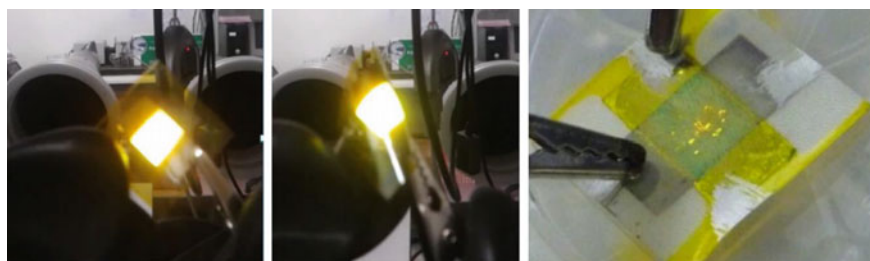


Fig. 22 OLED on PET and textile substrates

4 Conclusion and Outlook

Smart textiles can be obtained by integrating light-emitting devices onto the textile. The two manufactured and examined light-emitting devices, the ACEPEL device and the OLED, show a lot of promise. They are built up with a stack of very thin layers making it possible to be deposited on flexible substrates such as textiles. The ACEPEL device is suited for interior and exterior design due to its high operating voltage of 80–200 V. Different smart designs with a hexagonal structure of the ACEPEL device were screen printed on textile substrates maintaining typical textile properties such as breathability and drapability. Depending on the application, different optimal structures can be indicated. When the emphasis is on maintaining typical textile properties, the optimal structure can be found in the single pixel design with 2 mm diameter dots. If on the other hand, the light output is also of high importance, then the dual pixel design with 1.5 mm diameter dots suits the best. OLEDs, on the other hand, have an operating voltage of 3–5 V and can, therefore, be used in wearable applications. Other advantages of the OLEDs are a very low power supply, a low energy consumption, a good efficacy, a bright and uniform light output and a wide range of vision. There are, however, some challenges such as the necessity of a high barrier encapsulation and the use of non-roll-to-roll compatible and expensive deposition techniques. For now, high barrier encapsulations are still applied using a combination of printing and plasma techniques. To deposit the other OLED layers, innovative printing techniques such as inkjet printing and ultrasonic spray coating are gaining more and more importance. Adequate research into a proper barrier layer, a planarizing layer, a transparent top electrode and roll-to-roll deposition techniques is ongoing and will bring the OLED technology from glass or PET foils towards textiles.

References

1. Krasnov, A. N. (2003). Electroluminescent displays: History and lessons learned. *Displays*, 24(2), 73–79.
2. Destriau, G. (1936). AC electroluminescence in ZnS. *J Chem. Phys.*, 33, 587.
3. Peters, T., Pappalardo, R., & Hunt, R. (1993). Lamp phosphors. *Solid State Luminescence*.
4. Pankove, J. I. (1977). Electroluminescence.
5. Tang, C. W., & Vanslyke, S. A. (1987). Organic electroluminescent diodes. *Applied Physics Letters*, 51(12), 913–915.
6. Burroughes, J. H., et al. (1990). Light-emitting diodes based on conjugated polymers. *Nature*, 347, 539–541.
7. Gustafsson, G., Cao, Y., Treacy, G. M., Klavetter, F., Colaneri, N., & Heeger, A. J. (1992). Flexible light-emitting-diodes made from soluble conducting polymers. *Nature*, 357, 477–479.
8. de Vos, M., Torah, R., & Tudor, J. (2016). Dispenser printed electroluminescent lamps on textiles for smart fabric applications. *Smart Materials and Structures*, 25(4), 45016.
9. Hu, B., Li, D., Ala, O., Manandhar, P., Fan, Q., Kasilingam, D., et al. (2011). Textile-based flexible electroluminescent devices. *Advanced Functional Materials*, 21(2), 305–311.

10. TexOLED: Textile-Integrated and Textile-Based LEDs and OLEDs. (2007).
11. Janietz, S., Gruber, B., Schattauer, S., & Schulze, K. (2012). Integration of OLEDs in textiles. *Advances in Science and Technology*, 80, 14–21.
12. O'Connor, B., An, K. H., Zhao, Y., Pipe, K. P., & Shtein, M. (2007). Fiber Shaped Light Emitting Device. *Advanced Materials*, 19(22), 3897–3900.
13. Cochrane, C., Meunier, L., Kelly, F. M., & Koncar, V. (2011). Flexible displays for smart clothing : Part I—Overview, 36(December), 422–428.
14. Kim, W., Kwon, S., Lee, S.-M., Kim, J. Y., Han, Y., Kim, E., ... Park, B.-C. (2013). Soft fabric-based flexible organic light-emitting diodes. *Organic Electronics*, 14(11), 3007–3013.
15. Withnall, R., Member, S. I. D., Harris, P. G., Ireland, T. G., & Marsh, P. J. (2011). AC powder electroluminescent displays, 798–810.
16. Fischer, A. G. (1963). Electroluminescent Lines in ZnS Powder Particles, II. Models and Comparison with Experience. *Journal of the Electrochemical Society*, 110(7), 733–748.
17. Kitai, A. (2008). *Luminescent materials and applications*. New York: Wiley.
18. Vangerven, T. (2011). *Characterization of printable electroluminescent devices*. XIOS Hogeschool Limburg.
19. Lybye, D. (2004). Coatings technology fundamentals: Screen printing, 1–4.
20. Scott, J. C., Malliaras, G. G., Bozano, L., Carter, S. U. E. A., & Ramos, S. (2000). *The physics of organic light-emitting devices*, 558, 499–505.
21. Fundamentals, O. (n.d.). *OLED fundamentals*.
22. Thompson, B. J. (2005). *Organic diodes*.
23. Troia, M., et al. (2015). T. Hirth Oxygen barrier layers for flexible OLED devices. PT-17 2015, Kiel, Germany.
24. Lybye, D. (2004). Coatings technology fundamentals: Deposition, chemical vapor deposition (pp. 1–30).
25. Martin, P. M. (2009). *Handbook of deposition technologies for films and coatings - Science, applications and technology*.
26. Khouchaf, L., Mehta, R., Renaud Podor, J. R., H.-P. B., Zhongwei Chen, Y. Y., & Kidd, T. E. (2012). *Scanning electron*. In V. Kazmiruk (Ed.).
27. Hugo Knecht, N. F. (2006). FX3300 Luftdurchlässigkeits-Prüfgerät IV, Scherzenbach: Textest AG.
28. Wu, D. S., et al. (2006). Transparent barrier coatings for flexible organic light-emitting diode applications. *Chemical Vapor Deposition*, 12, 220–224.
29. Troia, M., et al. (2015). Oxygen barrier layers for flexible OLED devices. PT-17 2015, Kiel, Germany.
30. Gilissen, K., et al. (2015). Ultrasonic spray coating as deposition technique for the light-emitting layer in polymer LEDs. *Organic Electronics*, 20(February), 31–35.
31. Han, T.-H., Jeong, S.-H., Lee, Y., Seo, H.-K., Kwon, S.-J., Park, M.-H., et al. (2015). Flexible transparent electrodes for organic light-emitting diodes. *Journal of Information Display*, 316 (March 2015).
32. Vandevenne, G., Marchal, W., Verboven, I., ... Drijkoningen, J. (2016). A study on the thermal sintering process of silver nanoparticle inkjet inks to achieve smooth and highly conducting silver layers. *PSSA*, 213(6), 1403–1409.
33. Van Der Pauw, J. (1958). A method of measuring specific resistivity and hall effect of discs of arbitrary shape.pdf.